

A VERY HIGH ENERGY GAMMA-RAY SURVEY OF  
UNIDENTIFIED EGRET SOURCES

By

Stephen Fegan

---

A Dissertation Submitted to the Faculty of the

DEPARTMENT OF PHYSICS

In Partial Fulfillment of the Requirements  
For the Degree of

DOCTOR OF PHILOSOPHY

In the Graduate College

THE UNIVERSITY OF ARIZONA

## **APPROVAL FORM**

Approved by the  
Examining Committee:

---

T.C. Weekes, Dissertation Adviser

---

M. Shupe, Member

---

F. Melia, Member

---

J.D. Garcia, Member

---

K.C. Hsieh, Member

## **STATEMENT BY AUTHOR**

This dissertation has been submitted in partial fulfillment of requirements for an advanced degree at The University of Arizona and is deposited in the University Library to be made available to borrowers under rules of the Library.

Brief quotations from this thesis are allowable without special permission, provided that accurate acknowledgment of source is made. Requests for permission for extended quotation from or reproduction of this manuscript in whole or in part may be granted by the head of the major department or the Dean of the Graduate College when in his or her judgment the proposed use of the material is in the interests of scholarship. In all other instances, however, permission must be obtained from the author.

## ACKNOWLEDGMENTS

As everyone who has gone through the process will know, it is impossible to make such an undertaking without the wisdom and guidance of an adviser who knows all there is to know about the subject. Thank you Trevor for all your patience and encouragement.

I would like to particularly emphasize the formative influence on my first years here of Vladimir Vassiliev and Mike Catanese, two of the best scientists with whom I have had the pleasure of working. Thanks, Mike, for sharing your office and for all your patience with my incessant questioning. Thanks, Vladimir, for involving me in so many interesting projects and for encouraging me to be rigorous in my work. I look forward to working with you again soon.

Many thanks to all the visitors to the Whipple observatory, in particular to John Finley, Stella Bradbury, Stephane LeBohec and Glenn Sembroski. To all the other students and postdocs with whom I had the pleasure of working: Jojo, Andrew, Tony, Mead, Martin and Abe. To Ken who somehow doesn't fit in the last category or the next. To the staff of FLWO past and present: Steve, Karen, Grace, Ginnie, Danny, Roger, Dave, Ceasar, Gene, Emmet and Kevin. To Leslie, Dale and Ann at SAO.

Thanks to all my friends here: Matt, Kelly, Jeff, Taryn, Matty, Janna, Kevin and to Jack for introducing us. Without you all, life in Tucson would not have been any fun. I hope that we all remain friends for a long time to come, and that there are many more trips to Vegas. Thanks Araby, Jenny, Erin and all at the R.G. for the seemingly endless flow of beer. Thanks to all my friends in Ireland, especially to Ronan, for visiting and for putting up with me being out of touch for such long periods.

To Deirdre for being such a good friend for so many years and for all the encouragement throughout the writing of this dissertation.

To my parents, Sylvia and David, who have always supported and encouraged me. It is redundant to say this: without you both I would never have got this far. To Eoin for all the CDs, robots and other strange stuff. Looking forward to watching the classics modern cinema with you again soon, i.e. *Top Secret!* and *Ghostbusters*.

This research has made use of the NASA/IPAC Extragalactic Database (NED) which is operated by the Jet Propulsion Laboratory, California Institute of Technology, under contract with the National Aeronautics and Space Administration. This publication makes use of data products from the Two Micron All Sky Survey, which is a joint project of the University of Massachusetts and the Infrared Processing and Analysis Center/California Institute of Technology, funded by the National Aeronautics and Space Administration and the National Science Foundation. This research has made use of NASA's Astrophysics Data System.

This research was supported by grants from the U.S. Department of Energy, PPARC (U.K.) and Enterprise Ireland. The author acknowledges the support of the Predoctoral Fellowship program at the Smithsonian Astrophysical Observatory.

For my parents.

## TABLE OF CONTENTS

LIST OF TABLES . . . . .	9
LIST OF FIGURES . . . . .	12
ABSTRACT . . . . .	22
1. INTRODUCTION . . . . .	23
1.1 A brief history of observational gamma-ray astronomy . . . . .	23
1.2 The first unidentified HE gamma-ray source . . . . .	28
1.3 The Energetic Gamma-Ray Experiment Telescope . . . . .	29
1.4 Catalogs of EGRET “point” sources . . . . .	31
1.5 Whipple 10 m atmospheric Čerenkov telescope . . . . .	35
1.6 Catalog of VHE gamma-ray sources . . . . .	38
1.7 VHE observations of third EGRET catalog sources . . . . .	42
2. POTENTIAL SOURCES OF HIGH-ENERGY GAMMA-RAYS . . . . .	44
2.1 Blazars . . . . .	44
2.2 Pulsars . . . . .	49
2.3 Supernova Remnants . . . . .	53
2.4 Pulsar Wind Nebulae . . . . .	56
2.5 Other source associations at low Galactic latitudes . . . . .	57
2.6 Possible extra-galactic associations . . . . .	59
2.7 Potential of VHE emission from unidentified 3EG sources . . . . .	61

**TABLE OF CONTENTS – CONTINUED**

3. GROUND-BASED GAMMA-RAY DETECTION . . . . .	65
3.1 Extensive Air-Shower . . . . .	65
3.2 Imaging atmospheric Čerenkov technique . . . . .	67
3.3 Trigger and acquisition electronics . . . . .	71
3.4 Characterization of detector . . . . .	74
4. DATA ANALYSIS . . . . .	76
4.1 Observations . . . . .	76
4.2 Image Conditioning . . . . .	78
4.3 Parameterization . . . . .	86
4.4 Data Selection . . . . .	87
4.5 2D Analysis technique . . . . .	88
4.6 Significance of Observations . . . . .	92
4.7 TRACKING Analysis . . . . .	99
5. OBSERVATIONS . . . . .	100
5.1 Individual observations . . . . .	102
5.2 Summary . . . . .	147

**TABLE OF CONTENTS – CONTINUED**

6. NEXT GENERATION DETECTORS . . . . .	149
6.1 VERITAS . . . . .	150
6.2 Overview of the VERITAS-7 simulations . . . . .	151
6.3 Performance of the four telescope VERITAS sub-array. . . . .	158
6.4 Summary of results . . . . .	171
7. CONCLUSIONS . . . . .	174
APPENDIX A. GLOSSARY . . . . .	177
APPENDIX B. TWO DIMENSIONAL RECONSTRUCTION . . . . .	182
APPENDIX C. PERFORMANCE OF GAUSSIAN SMOOTHING . . . . .	186
APPENDIX D. TRACKING SIGNIFICANCE CALCULATION . . . . .	188
REFERENCES . . . . .	191

## LIST OF TABLES

1.1	Comparison of the characteristics of the EGRET instrument on CGRO and the Whipple 10 m atmospheric Čerenkov imaging telescope. . . . .	39
1.2	Catalog of published VHE sources <sup>1</sup> . Adapted from Horan and Weekes (2004). . . . .	40
4.1	Difference between noise levels for three channels, before and after software noise padding. . . . .	85
4.2	Data selection cuts used in this work. . . . .	88
4.3	Optimized two-dimensional analysis parameters, calculated for observing seasons from 1999 to 2003. . . . .	92
4.4	Estimates for the number of independent bins, $N$ , present in the region of a sky-map of area $\pi R^2$ . Three estimates are given, the first two express the ratio of the areas of the region and the smoothing Gaussian. The final estimate is from a maximum likelihood fit to the distribution of maximum significance. . . . .	98
5.1	Summary of the 3EG and GeV catalog entries for the 19 unidentified sources observed in the survey. . . . .	101
5.2	Upper limits for candidates in 3EG J0010+7309 field. . . . .	104
5.3	Upper limits for candidates in 3EG J0241+6103 field. . . . .	106
5.4	Upper limits for candidates in 3EG J0423+1707 field. . . . .	107
5.5	Upper limits for candidates in 3EG J0433+2908 field. . . . .	109
5.6	Upper limits for candidates in 3EG J0450+1105 field. . . . .	113

**LIST OF TABLES – CONTINUED**

5.7	Upper limits for RX J0509.3+0541. . . . .	114
5.8	Upper limits for candidates in 3EG J0613+4201 field. . . . .	115
5.9	Upper limits for candidates in 3EG J0628+1847 field. . . . .	118
5.10	Upper limits for candidates in the fields of 3EG J0634+0521 and 3EG J0631+0642. . . . .	122
5.11	Upper limits for candidates in 3EG J1009+4855 field. . . . .	123
5.12	Upper limits for candidates in 3EG J1323+2200 field. . . . .	125
5.13	Upper limits for candidates in 3EG J1337+5029 field. . . . .	127
5.14	Upper limits for candidates in 3EG J1826–1302 field. . . . .	132
5.15	Upper limits for candidates in 3EG J1835+5918 field. . . . .	135
5.16	Upper limits for candidates in GeV J1907+0557 field. . . . .	137
5.17	Upper limits for candidates in GeV J2020+3658 field. . . . .	140
5.18	Upper limits for candidates in 3EG J2227+6122 field. . . . .	143
5.19	Upper limits for candidates in 3EG J2248+1745 field. . . . .	146
5.20	Upper limits for candidates in 3EG J2255+1943 field. . . . .	147

**LIST OF TABLES – CONTINUED**

5.21	Summary of upper limits for all 3EG and GeV sources observed in the survey. Some observations result in limits on more than one source. The observations of GeV J0508+0540 were made in a mode incompatible with the two dimensional analysis. In the case of 3EG J2255+1943, the EGRET error box is larger than the field of view of the instrument. . . . .	148
6.1	Trigger requirements for VERITAS-7 simulations. . . . .	152
6.2	Details of the $\gamma$ -ray simulation database. . . . .	161
6.3	Summary of collection area and integral rate from Crab Nebula. . . . .	163
6.4	Summary of angular resolution and optimized aperture cuts for VERITAS-4. . . . .	167
6.5	Summary of the characteristics of the VERITAS-4 sub-array. . . . .	173

## LIST OF FIGURES

1.1	The four identified SAS-2 sources and the 25 sources in the second COS-B catalog. Twenty one COS-B sources were unidentified. The sources are plotted in Galactic coordinates, with the outline of the Milky Way, from optical observations (Vieira, 2000), displayed for comparison. The Galactic-center is in the center of the diagram. . . . .	25
1.2	Schematic of the Energetic Gamma-Ray Experiment Telescope (EGRET) experiment on CGRO. Two levels of spark chamber track pair production $e^-/e^+$ while an NaI scintillator is used as a calorimeter. Figure courtesy of NASA. . . . .	30
1.3	The 271 sources listed in the third EGRET catalog (Hartman et al., 1999), plotted in Galactic coordinates. Sources are displayed by source identification (symbols) and flux (size of the symbol). Sources with a fitted spectrum <i>harder</i> than 2.0 are shown in red, those with a softer spectrum are shown in blue. Those without an estimate of spectral index are shown in gray. Finally, the Gould Belt is shown as a broken green line, with the direction of the center of the Belt, from Stothers and Frogel (1974), shown as a green star. . . . .	32
1.4	Upper limits on $\gamma$ -ray emission at energies $> 100$ MeV from EGRET observations, in units of $10^{-8} \text{ cm}^{-2} \text{ s}^{-1}$ . As noted in Hartman et al. (1999), the regions within $1^\circ$ of the 3EG sources are shown as black. . . . .	33
1.5	Illustration of the Whipple 10m telescope. The mirror consists of 249 spherical mirrors in a Davies-Cotton configuration. The small time-spread introduced between photons reflected from the edge and center of the mirror is evident in the diagram. . . . .	37
1.6	Left: Picture of the Whipple 10 m telescope (courtesy of Dr. R. Lessard). Right: Picture of the high-resolution, 499 pixel camera at the focal plane of the instrument. In normal operation, a reflective light concentrator plate is installed over the face of the inner 379 PMTs to increase photon detection efficiency – the six mounting posts for this plate are visible between the inner and outer parts of the camera. . . . .	37

## LIST OF FIGURES – CONTINUED

<p>1.7 Comparison of upper limit on source luminosity derivable through observations at Whipple with the extrapolated luminosity of a “mean” 100 MeV source. Upper limits for 0.5, 5 and 50 hour observations are shown, assuming a Crab-like spectrum. The hypothetical 100 MeV source, has an integral flux spectrum given by the mean flux and spectral index from 3EG sources chosen for this survey: <math>I(&gt; E) = (30.9 \pm 4.1) \times 10^{-8} (E/100\text{MeV})^{-1.12 \pm 0.21} \text{ cm}^{-2}\text{s}^{-1}</math>. . . . .</p> <p>1.8 The 18 objects reported as <math>\gamma</math>-ray sources in the VHE regime, in Galactic coordinates. Confirmed sources are depicted as solid symbols, unconfirmed sources as outlines. Sources are listed by number, as they appear in the VHE catalog, table 1.2. The thick broken line shows the equatorial plane, separating the northern and southern hemispheres. The thinner broken lines show the 30° and 60° declinations north and south. The data for this figure are taken from Horan and Weekes (2004). . . . .</p> <p>2.1 (Left) Optical path length, <math>\tau(E, z)</math>, for HE <math>\gamma</math>-rays from extra-galactic sources at <math>z = 0.03</math>, <math>z = 0.10</math> and <math>z = 0.30</math> from Stecker and de Jager (1998). (Right) Cut-off in <math>\gamma</math>-ray spectrum due to absorption, <math>\exp\{-\tau(E, z)\}</math>. In each case, two curves are shown, corresponding to the two the IIRF models used by Stecker and de Jager (1998). . . . .</p> <p>3.1 Simulated charged particle tracks in the atmosphere produced by a 100 GeV <math>\gamma</math>-ray (left) and a 1 TeV <math>\gamma</math>-ray (middle) and 1 TeV proton (right). The horizontal and vertical scales are not equal on this plot. Ground level is set for Mt. Hopkins at 2320 m A.S.L. . . . .</p> <p>3.2 Left: Illustration of Čerenkov emission from vertically moving muon. Right: Radial density on the ground of Čerenkov photons with <math>200 \text{ nm} &lt; \lambda &lt; 700 \text{ nm}</math>, showing enhancement at 120 m due to focusing effect of the increasing atmospheric density. Since the intensity of emitted photons is essentially constant as the muon reaches the ground, the radial density diverges like <math>1/r</math>, as <math>r \rightarrow 0</math>. . . . .</p>	<p>39</p> <p>41</p> <p>49</p> <p>66</p> <p>68</p>
---	---

## LIST OF FIGURES – CONTINUED

<p>3.3 Density of photons per unit mirror area in the focal plane of an ideal 10 m telescope for a simulated 350 GeV photon induced shower, in units of <math>\text{m}^{-2} \text{deg}^{-2}</math>. The same shower is shown for three different impact parameters: 0 m, 40 m and 80 m. The axes gives the angular distance in the focal plane from the direction of the primary (which is assumed to be coincident with the center of the camera) in degrees. . . . .</p> <p>3.4 Event rate vs. L-1 trigger threshold with a trigger L-2 requirement (pattern selection trigger) of three adjacent channels exceeding the threshold within the coincidence time. This kind of plot is usually referred to as a “bias curve” . . . . .</p> <p>3.5 Schematic of the major components of the data acquisition system. See text for discussion. . . . .</p> <p>3.6 (Left) Effective collection area vs. energy for trigger and for data selection algorithm. After data selection, the collection area peaks at <math>\sim 4 \times 10^4 \text{ m}^2</math>. (Right) Differential rate of <math>\gamma</math>-rays collection from Crab Nebula. . . . .</p> <p>4.1 A typical event after each stage of image conditioning. (Top left) Raw ADC values. (Top right) After subtraction of injected pedestals. (Bottom Left) After gain equalization. (Bottom right) After cleaning. . . . .</p> <p>4.2 (left) Sample image taken with the high resolution camera, after image conditioning, with image axis and second order moments indicated. (right) Illustration of image parameters. . . . .</p> <p>4.3 Illustration of shower parameter <i>disp</i> in the field of view of camera (left) and from perspective of the shower in the atmosphere (right). . . . .</p> <p>4.4 Observations of the Crab Nebula, offset by varying amounts from the center of the field of view. The contours show detection significance. The observations at an offset of <math>1.3^\circ</math> place the Crab outside of this. . . . .</p>	<p>70</p> <p>72</p> <p>72</p> <p>75</p> <p>79</p> <p>87</p> <p>90</p> <p>93</p>
---	---

## LIST OF FIGURES – CONTINUED

4.5	Relative Crab detection rate as a function of source offset. The off-axis response can be fit by a straight line. . . . .	93
4.6	Significance of excess (deficit) in counts in center bin of 240 background observations. A Gaussian function of unity width, integrated over the binning size, is also shown. . . . .	95
4.7	Probability of at least one from $N$ observations giving a result of $> x\sigma$ as compared with the probability of a single observation giving the same result. Curves with increasing $N$ , from 1 to 600, go from left to right. . .	95
4.8	Experimental and best-fit distributions for $\max(\sigma(\vec{r}) ;  \vec{r}  < R)$ , listed for $R = 0.38^\circ$ , $R = 0.55^\circ$ and $R = 1.10^\circ$ . . . . .	98
4.9	Maximum likelihood fit for $N(R)$ as a function of $A \propto R^2$ . . . . .	98
5.1	The 19 unidentified EGRET sources considered in this survey, plotted in Galactic coordinates. The Milky Way and Gould Belt are also depicted, as described in chapter 1. The candidate sources are labeled by their positions in table 5.1. . . . .	100
5.2	(Left) Limits on emission from 3EG J0010+7309 in units of $10^{-11} \text{ cm}^{-2} \text{ s}^{-1}$ . The 3EG error contours are overlaid as heavy lines, the GeV catalog contour is shown as a broken circle. (right) Spectrum from the on-line version of the 3EG catalog with the limit at 350 GeV. . . . .	104
5.3	(Left) Limits on emission from 3EG J0241+6103 in units of $10^{-11} \text{ cm}^{-2} \text{ s}^{-1}$ . The 3EG error contours are overlaid as heavy lines, the GeV catalog contour is shown as a broken circle. (right) Spectrum from the on-line version of the 3EG catalog with upper limit at 350 GeV. The limit at 500 GeV from Hall et al. (2003a) is also indicated. . . . .	106
5.4	(Left) Limits on emission from 3EG J0423+1707 in units of $10^{-11} \text{ cm}^{-2} \text{ s}^{-1}$ . The 3EG error contours are overlaid as heavy lines. (Right) Spectrum from the on-line version of 3EG catalog with the upper limit at 350 GeV. 107	

## LIST OF FIGURES – CONTINUED

5.5	(Left) Limits on emission from 3EG J0433+2908 in units of $10^{-11} \text{ cm}^{-2} \text{ s}^{-1}$ . The 3EG error contours are overlaid as heavy lines, the GeV catalog contour is shown as a broken circle. (Right) Spectrum from the on-line version of the 3EG catalog with the upper limit at 350 GeV. . . . .	110
5.6	Spectral energy distribution for the radio/x-ray source RX J0433.5+2906. The radio data come from the NASA/IPAC extragalactic database (NED). The IR observations are from the 2 micron all sky survey (2MASS). Optical data are from Halpern et al. (2003). The x-ray flux is from the ROSAT all sky survey bright source catalog (RASS-BSC). Finally, the differential $\gamma$ -ray flux is from the on-line 3EG catalog. . . . .	110
5.7	(Left) Limits on emission from 3EG J0450+1105 in units of $10^{-11} \text{ cm}^{-2} \text{ s}^{-1}$ . The 3EG error contours are overlaid as heavy lines. (Right) Spectrum from the on-line version of the 3EG catalog with the limit at 350 GeV. .	112
5.8	Spectral energy distribution for the radio/x-ray source PKS B0446+112. The data are from the same sources as in figure 5.6. The x-ray source (1RXS J044903.0+112120) was not strong enough to be included in the RASS-BSC, the x-ray flux was estimated from the count rate in the RASS catalog, and should be considered as approximate. . . . .	112
5.9	Spectral energy distribution for the radio/x-ray source RX J0509.3+0541. The data come from the same sources as in figure 5.6 with the 100 MeV upper limit from Hartman et al. (1999) (see figure 1.4), the 1 GeV $\gamma$ -ray flux from Lamb and Macomb (1997), and the preliminary 10 GeV point from Dingus (2001). . . . .	114
5.10	(Left) Limits on emission from 3EG J0613+4201 in units of $10^{-11} \text{ cm}^{-2} \text{ s}^{-1}$ . The 3EG error contours are overlaid as heavy lines, the GeV catalog contour is shown as a broken circle. (Right) Spectrum from the on-line version of the 3EG catalog with the upper limit at 350 GeV. . . . .	116
5.11	(Left) Limits on emission from 3EG J0628+1847 in units of $10^{-11} \text{ cm}^{-2} \text{ s}^{-1}$ . The 3EG error contours are overlaid as heavy lines. (Right) Spectrum from the on-line version of the 3EG catalog with the limit at 350 GeV. .	117

## LIST OF FIGURES – CONTINUED

5.12	Spectral energy distribution for the radio/x-ray source RX J0631.4+1908 (87GB 0628+1911), assuming it is associated with the $\gamma$ -ray source. The data come from the same sources as in figure 5.6. . . . .	117
5.13	Upper limits on emission from 3EG J0634+0521, 3EG J0631+0642 and GeV J0633+0645 in units of $10^{-11} \text{ cm}^{-2} \text{ s}^{-1}$ . The 3EG error contours are overlaid as heavy lines, the GeV error circle as a dashed line toward the top of the diagram. The dash-dotted ellipse toward the bottom of the figure indicates the OB association Mon OB 2A. . . . .	121
5.14	Spectrum for 3EG J0634+0521 (left) and 3EG J0631+0642 (right) from on-line version of the 3EG catalog with the upper limit at 350 GeV. The limit at 500 GeV from Lessard et al. (1999) is also indicated. . . . .	121
5.15	(Left) Limits on emission from 3EG J1009+4855 in units of $10^{-11} \text{ cm}^{-2} \text{ s}^{-1}$ . The 3EG error contours are overlaid as heavy lines. (Right) Spectrum from the on-line version of the 3EG catalog with the limit at 350 GeV. .	123
5.16	(Left) Limits on emission from 3EG J1323+2200 in units of $10^{-11} \text{ cm}^{-2} \text{ s}^{-1}$ . The 3EG error contours are overlaid as heavy lines. (Right) Spectrum from the on-line version of the 3EG catalog with the limit at 350 GeV. .	124
5.17	Significance of excess $\gamma$ -ray-like events detected from the region of 3EG J1337+5029. The cluseter is shown as a dot-dashed circle, and the various other sources in the field as “X” marks. . . . .	128
5.18	(Left) Limits on emission from 3EG J1337+5029 in units of $10^{-11} \text{ cm}^{-2} \text{ s}^{-1}$ . The 3EG error contours are overlaid as heavy lines. (Right) Spectrum from the on-line version of the 3EG catalog with the limit at 350 GeV. .	128
5.19	Upper limits on emission from 3EG J1826–1302, 3EG J1826–1302 and GeV J1825–1310 in units of $10^{-11} \text{ cm}^{-2} \text{ s}^{-1}$ . The SNR, OB association and point source candidates in the field are indicated on the figure and labeled in the key below, as is a third EGRET source 3EG J1824–1514 which partially overlaps the field. . . . .	131

## LIST OF FIGURES – CONTINUED

5.20	Spectrum for 3EG J1826–1302 (left) and 3EG J1823–1314 (right) from on-line version of the 3EG catalog with the upper limit at 350 GeV. . . . .	132
5.21	(Left) Limits on emission from 3EG J1835+5918 in units of $10^{-11} \text{ cm}^{-2} \text{ s}^{-1}$ . The 3EG error contours are overlaid as heavy lines. (Right) Spectrum from the on-line version of 3EG catalog with the limit at 350 GeV. . . . .	135
5.22	Limits on emission from GeV J1907+0557 in units of $10^{-11} \text{ cm}^{-2} \text{ s}^{-1}$ . The GeV error ellipse is shown as a dashed line. The dash-dotted circles correspond to SNR in the field, the heavy “X”-marks indicate the x-ray sources from ASCA and ROSAT. The confidence contours of 3EG J1903+0550 partially overlap the field to the west of the GeV source. . . . .	137
5.23	Upper limits on emission from GeV J2020+3658, 3EG J2021+3716 and 3EG J2016+3657 in units of $10^{-11} \text{ cm}^{-2} \text{ s}^{-1}$ . The SNR, OB association and point source candidates in the field are indicated on the figure and labeled in the key below. . . . .	141
5.24	Spectrum for 3EG J2021+3716 (left) and 3EG J2016+3657 (right) from on-line version of the 3EG catalog with the upper limit at 350 GeV. In each case, the more constraining upper limit for the most likely association: the pulsar AX J2021+3651 and the blazar TXS B2013+370 (or SNR G74.9+1.2 whose limit is almost the same) respectively, is shown.	142
5.25	Significance of excess $\gamma$ -ray-like events, detected from the region of 3EG J2227+6122. . . . .	144
5.26	(Left) Limits on emission from 3EG J2227+6122 in units of $10^{-11} \text{ cm}^{-2} \text{ s}^{-1}$ . The 3EG error contours are overlaid as heavy lines. The dot-dashed ellipse to the west indicates Cep OB 2B. (Right) Spectrum from the COMPTEL catalog (Schönenfelder et al., 2000) and on-line version of the 3EG catalog with the upper limit at 350 GeV. . . . .	144
5.27	(Left) Limits on emission from 3EG J2248+1745 in units of $10^{-11} \text{ cm}^{-2} \text{ s}^{-1}$ . The 3EG error contours are overlaid as heavy lines. (Right) Spectrum from the on-line version of 3EG catalog with the upper limit at 350 GeV. 145	

## LIST OF FIGURES – CONTINUED

5.28 Limits on emission from 3EG J2255+1943 in units of $10^{-11} \text{ cm}^{-2} \text{ s}^{-1}$ . . . . .	146
6.1 (Left) Dimensions of proposed VERITAS telescopes. (Right) Layout of seven telescope VERITAS array with VERITAS-4 sub-array indicated. . . . .	151
6.2 Simulated 300 GeV $\gamma$ -ray events. (Left) The axes of the six images, combined in <i>angular space</i> in the field of view of the array, point toward the origin of the $\gamma$ -ray. (Right) Axes of the images, when combined in <i>2-D space</i> on the ground, indicate the impact location of the shower core. From VERITAS collaboration (1999). . . . .	154
6.3 Shower axis parameters, $(\theta, \phi)$ describe the direction of the reconstructed axis, $(x_0, y_0)$ the point at which the axis intersects the ground. . . . .	156
6.4 (Left) Some of many possible paths for Čerenkov photon detected in PMT. (Right) Shower reconstruction technique. Detected photons are back-propagated from PMT, reflected off the mirror and into space, illustrated as cylinders projected from one of the telescopes. . . . .	156
6.5 Triggering rate for L1 (Channel), L2 (Telescope) and L3 (Array) vs. pixel trigger threshold (in photo-electrons). The rate of background cosmic-rays is also shown. . . . .	160
6.6 Effective areas for various array configurations. . . . .	164
6.7 Differential rate for a Crab Nebula like source. The energy at which the detected rate is maximal is, $E_{\text{peak}}=110 \text{ GeV}$ . . . . .	164
6.8 (Left-Top) Effective area with shape cut applied. (Left-Bottom) Effective area with shape and aperture-cuts applied vs. aperture-cut for three energies. (Right) $A(E, \theta_{\text{cut}})$ , effective area surface with shape and aperture-cuts applied. . . . .	165

## LIST OF FIGURES – CONTINUED

6.9 (Left) $P(E, < \theta_{\text{cut}})$ , probability that a $\gamma$ -ray event with certain energy will be reconstructed closer than $\theta_{\text{cut}}$ to the true origin. (Right) Significance of $\gamma$ -ray events over isotropic background events. . . . .	167
6.10 (Left) Differential rate of background cosmic-ray events, expressed in equivalent $\gamma$ -ray energy. (Right) Fraction of background events passing shape-cuts. . . . .	169
6.11 Minimum observable $\gamma$ -ray flux for 50 and 5 hour observations with the VERITAS-4 array given a required detection significance of $5\sigma$ in each energy bin. The sensitivity is quoted for energy bins separated equally in $\log(\text{energy})$ with four bins per decade. . . . .	172
B.1 Optimization of $disp$ with simulated $\gamma$ -ray events, in two energy bins. The <i>distance</i> of centroid from source is on the y-axis, the ellipticity, $\epsilon$ , on the x-axis. The best fit for eqn. B.1 and B.2 are shown. . . . .	183
B.2 (Left) Best fit of parameter $a_1$ from eqn. B.1 to simulated data. The function $a_1(\text{size})$ can itself be fit by a linear relationship of $a_1(\text{size}) = 1.36^\circ + 0.14^\circ \times \log(\text{size}/U)$ . (Right) $\chi^2$ per degree of freedom for fit of $a_1$ to simulated events. . . . .	183
B.3 Illustration of the longitudinal and transverse errors in reconstructing the arrival direction of $\gamma$ -ray events. . . . .	184
B.4 Distribution of transverse (left) and longitudinal (right) error in reconstructing the arrival direction of simulated events. . . . .	185
B.5 Dependence of longitudinal ( $\sigma_{\parallel}$ ) and transverse ( $\sigma_{\perp}$ ) error on <i>size</i> cut imposed. . . . .	185
C.1 Mean significance after smoothing with Gaussian and Trashcan functions with various smoothing radii. . . . .	187

## LIST OF FIGURES – CONTINUED

## ABSTRACT

A survey of unidentified 100 MeV  $\gamma$ -ray sources is undertaken, with the Whipple 10 m telescope, with the objective of detecting very high energy ( $> 350$  GeV)  $\gamma$ -ray emission. The survey consists of nineteen sets of observations of sources detected by the EGRET instrument on the Compton Gamma-Ray Observatory between 1991 and 1995. Results for 21 EGRET sources are reported; in some cases two EGRET sources are close enough to be viewed in a single observation. For each EGRET source, candidate associations are listed and the implications of each candidate for VHE emission discussed. Finally, a study of the performance of a next-generation ground based instrument, VERITAS, using simulations is presented. The implications of the increased sensitivity of such an instrument for future  $\gamma$ -ray surveys is briefly discussed.

## 1. INTRODUCTION

The scientific objective of this dissertation is a study of very high energy ( $>350$  GeV)  $\gamma$ -ray emission from unidentified 100 MeV sources. EGRET, the Energetic Gamma-Ray Experiment Telescope, a satellite experiment, detected  $\gamma$ -rays from 271 sources at energy  $> 100$  MeV. Of these sources, 170 have yet to be identified with objects at other wavelengths. This chapter presents a brief history of the field of high energy (HE) and very high energy (VHE)  $\gamma$ -ray astronomy and introduces the EGRET experiment and its catalog of point sources. A description of the ground-based, Whipple  $\gamma$ -ray detector is given and the catalog of VHE sources is summarized.

The classes of objects which have been either identified or suggested as HE sources of  $\gamma$ -rays are presented in chapter 2. A brief review of the VHE  $\gamma$ -ray detection technique and of the detector system on the Whipple telescope is given in chapter 3. The two-dimensional reconstruction technique, which is used to infer the origin of  $\gamma$ -ray events and map the VHE emission in the field of view of the telescope is described in chapter 4. The 19 sources chosen for the survey and the VHE sky maps of the neighborhood of these sources is presented in chapter 5. A simulation study of the characteristics of the VERITAS array, a next-generation VHE  $\gamma$ -ray instrument is presented in chapter 6. Finally, the results of this survey are summarized and the potential for future surveys with upcoming  $\gamma$ -ray instruments, such as VERITAS, is discussed in chapter 7.

### 1.1 A brief history of observational gamma-ray astronomy

The field of observational high energy  $\gamma$ -ray astronomy traces its origins to the discovery of emission from the pulsar in the Crab Nebula with large balloon-borne detectors in the late 1960s and early 1970s (see for example Browning et al., 1971; Albats et al., 1972; Parlier et al., 1973; McBreen et al., 1973). The sensitivity of balloon borne

experiments were ultimately limited by the difficulty in separating HE  $\gamma$ -rays originating from the relatively weak  $\gamma$ -ray sources from the overwhelming background of secondary charged particles in the atmosphere. Many source detections were claimed during this period, all with low statistical significance; only the Crab pulsar stood the test of time.

In 1972 NASA launched the second Small Astronomy Satellite (SAS-2), a HE  $\gamma$ -ray satellite, comprising of a set of spark chambers which provided energy and direction estimates for  $\gamma$ -rays with energy  $>35$  MeV. SAS-2 was NASA's second dedicated HE  $\gamma$ -ray telescope, and its fourth to carry HE  $\gamma$ -ray detectors, after Explorer-XI (1961), OSO-3 (1967) and OGO-5 (1968)<sup>1</sup>. These pioneering satellites had demonstrated the existence of a flux of cosmic  $\gamma$ -rays from the Galaxy, tentatively at first (Kraushaar et al., 1965), then conclusively by mapping the correlation of the flux with Galactic latitude and longitude (Clark et al., 1968). They had not, however, been able to identify any isolated  $\gamma$ -ray sources. This changed with the SAS-2 mission, which, in addition to measuring the diffuse Galactic  $\gamma$ -ray emission and finding evidence of emission from the Gould Belt (see chapter 2), detected four isolated sources of  $\gamma$ -rays: the Crab and Vela pulsars, Cygnus X-3 and the first unidentified high energy source,  $\gamma$ 195+5 (Fichtel et al., 1975; Hartman et al., 1979). The  $\gamma$ -ray excesses corresponding to these objects were large but not well localized; the SAS instrument had an angular resolution of  $\sim 2^\circ$ , making identification with known sources impossible on the basis of position alone. Association of these excesses with known sources was done using a timing analysis, by identifying pulsations in the  $\gamma$ -ray signal at the known radio periods from the Crab and Vela pulsars. In the case of Cygnus X-3, the 4.8 hr. orbital period seen in x-rays was used to make the identification. After six months of operation, the satellite incurred a power supply failure and was decommissioned.

The next advance in HE  $\gamma$ -ray astronomy came with the launch of the COS-B satellite, a European Space Agency mission, in 1975. COS-B was most sensitive to  $\gamma$ -rays in the energy range  $\sim 150$  MeV and 5 GeV. The instrument was designed for a two year

---

<sup>1</sup>In addition, two military satellites launched from the USSR contained scientific  $\gamma$ -ray packages which predate SAS-2: COSMOS-208 (1966) and COSMOS-264 (1969).

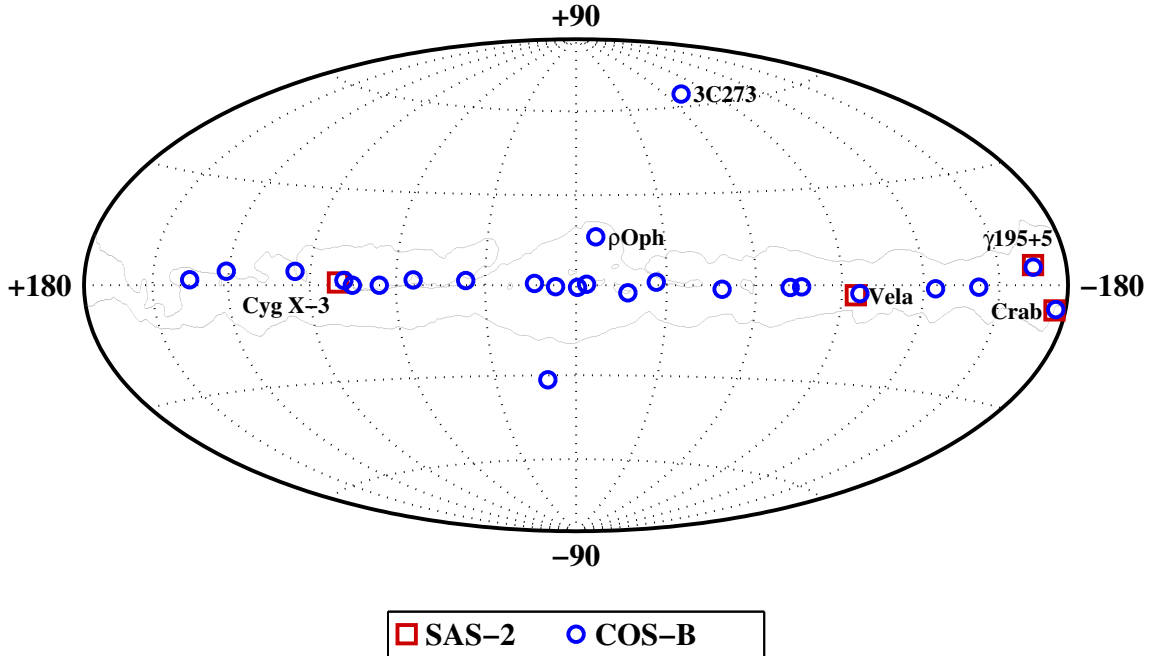


**Figure 1.1:** The four identified SAS-2 sources and the 25 sources in the second COS-B catalog. Twenty one COS-B sources were unidentified. The sources are plotted in Galactic coordinates, with the outline of the Milky Way, from optical observations (Vieira, 2000), displayed for comparison. The Galactic-center is in the center of the diagram.

mission, but operated for close to seven. Data from the first three years of observations were compiled into a catalog of point sources (Swanenburg et al., 1981), illustrated in figure 1.1. The catalog lists 25 sources, mostly on the Galactic plane, with four source identifications (Crab, Vela, 3C273 and the  $\rho$ -Ophiuchi cloud complex), leaving 21 unidentified sources, one of which, 2CG 195+04, corresponds to the unidentified SAS-2 source. Cygnus X-3 is noticeably absent from the COS-B catalog, the 4.8 hr periodicity in the SAS-2 and x-ray data was not detected; Mattox (1990) show that the periodicity was only observed at  $E < 100$  MeV by SAS-2 and would not be visible to COS-B. The identification of 3C273 yielded the first observation of an extra-galactic source in HE  $\gamma$ -rays, a class of object that would be expanded dramatically by the next generation HE  $\gamma$ -ray instrument, EGRET, described in detail in section 1.3. The achievements of the COS-B mission are summarized by Bennett (1990).

Contemporaneous with the development of space-based, HE  $\gamma$ -ray astronomy, the field of very high energy  $\gamma$ -ray astronomy, was being developed (Weekes, 2003). In this energy regime, instruments exploit the fact that the highest energy  $\gamma$ -rays interact in the atmosphere giving rise to extensive air-showers (EAS), electromagnetic cascades of electrons, positrons and  $\gamma$ -rays. At the highest energies,  $> 10 \text{ TeV}$ , arrays of scintillation detectors or water Čerenkov detectors placed at the high altitudes can detect these secondaries directly and, given sufficient ground coverage, can infer the properties of the primary from the distribution of particles on the ground. For example, the Tibet Air-shower Array consists of  $\sim 700$  detectors, distributed over an area of  $36,900 \text{ m}^2$  at an altitude of 4,300 m.

At lower energies, in the range of  $100 \text{ GeV} - 10 \text{ TeV}$ , where energy losses to the atmosphere mean that the air shower does not have a high charged particle density at ground level, an indirect approach to air shower detection is employed. Čerenkov light emitted from the relativistic charged secondaries can be detected at ground level by an optical detector, usually consisting of a large mirror and array of photo-multiplier tubes (PMTs). The diameter of the pool of light, created by an air shower is typically greater than 200 m, dictated largely by the angle of Čerenkov light emission in the atmosphere and by broadening of the shower through multiple Coulomb scattering of the secondaries. Čerenkov radiation is therefore visible at ground level over an area of  $> 10^5 \text{ m}^2$ , giving a huge potential effective area to a detector that can effectively separate  $\gamma$ -ray induced EAS from those that result from the overwhelming background of charged cosmic rays (Jelley and Porter, 1963). Initial experiments employed large “light buckets”, such as recycled military search-lights, to search for excesses of EAS in the direction of potential sources (see previous reference and Chudakov et al., 1963). No statistically significant excesses were found.

To date, two types of ground-based Čerenkov detector have been successful in detecting VHE  $\gamma$ -ray emission at a statistically significant level: instruments based on the optical *imaging* of the Čerenkov photons with a large telescope and *non-imaging* detectors which operate in an analogous way to air shower arrays, by using the density and temporal distribution of Čerenkov light on the ground to infer the properties of

the primary. Both techniques have a long history (Weekes and Turver, 1977; Danaher et al., 1982), and each has resulted in the detection of point sources of  $\gamma$ -rays. The successful non-imaging instruments, such as STACEE and CELESTE, employ solar furnace facilities. In these instruments, an array of large mirrors<sup>2</sup> reflect light from different parts of the Čerenkov pool to a central station which contains a set of PMTs. An electronic trigger system and a set of analog-to-digital converters record the distribution and dispersion in arrival times of photons in the light pool. On the basis of the arrival times and intensities,  $\gamma$ -ray events can be selected over the background. Although this technique was initially investigated over 20 years ago, it was abandoned until more recent times, and has not yet been exploited as fully as the imaging technique.

The imaging atmospheric Čerenkov technique was initially suggested by Weekes and Turver (1977). In essence, a large optical telescope and high resolution camera is used to take a “picture”, in Čerenkov light, of the shower development (Fegan et al., 1983). Although the images of  $\gamma$ -ray induced showers are superficially similar to those of hadronic showers, there are sufficient differences in the development of these showers that the images can be used to differentiate them, at least in a probabilistic sense. The images also allow the energy and arrival direction of the primary  $\gamma$ -rays to be estimated, two of the basic requirements for doing astronomy at any energy. The imaging technique was pioneered at the Fred Lawrence Whipple Observatory in southern Arizona, leading to the first statistically significant detection of a VHE source; the Crab Nebula at a  $9\sigma$  confidence level (Weekes et al., 1989). Details of the atmospheric imaging technique are given in chapter 3, and the Whipple 10 m telescope is described below. Today, ground-based instruments using the imaging technique are operated by six groups around the world, giving coverage in both the northern and southern hemispheres. The number of credible VHE sources has risen to 18, including both galactic and extra-galactic sources. A number of groups are building next-generation ground-based detectors which will come on-line over the next few years and which are expected to increase the number of VHE sources significantly.

---

<sup>2</sup>Usually called *heliostats*, reflecting their origins in the world of solar energy physics.

Details of the design of one such experiment, VERITAS, are given in chapter 6.

## 1.2 The first unidentified HE gamma-ray source

The case of the earliest unidentified  $\gamma$ -ray source, which came to be known as *Geminga*<sup>3</sup>, is an interesting one. A significant excess of events over the expected diffuse Galactic emission was first seen by SAS-2 and subsequently by COS-B. The SAS-2 group reported a pulsation, with period  $\sim 59$  s, in the  $\gamma$ -rays detected, although the limited number events (121 over four months) and the number of degrees of freedom in the blind pulsation search (three: phase, period and its derivative) led them to conclude that the pulsation was not statistically compelling. At the time of publication, four weak radio sources were known within the error box of the data, two supernova remnants bordered it and a known satellite galaxy to the Milky Way lay nearby. None of these associations were convincing, and the team suggested that an undiscovered radio-pulsar was the most likely progenitor (Thompson et al., 1977). Despite the investment of a significant amount of observation time, the source remained unidentified through the COS-B era; their data did, however, rule out the claimed  $\sim 59$  s pulsation. Many claims were made about the source during this time, but its nature remained a complete mystery until the identification of a candidate source by the Einstein x-ray satellite, 1E 0630+178 (Bignami et al., 1983). The characteristics of the x-ray source were unique: large x-ray to optical luminosity, no radio emission detected by the sensitive VLA instrument, point-like emission in the Einstein imager and an estimated distance of  $\sim 100$  pc, placing it within the Galaxy. The association between these objects was not conclusively made until the ROSAT x-ray imager detected a 237 ms pulsation (Halpern and Holt, 1992) which was also seen in  $\gamma$ -rays by the EGRET instrument (Bertsch et al., 1992) and retrospectively in the COS-B and SAS-2 data (Bignami and Caraveo, 1992; Mattox et al., 1992). Geminga is the first example of a radio-quiet pulsar, and serves as an illustration of the difficulty of

---

<sup>3</sup> *Geminga*: its name indicates that it is a  $\gamma$ -ray source in the constellation *Gemini*, but see Bignami et al. (1983) for its coincidental meaning in the Milanese dialect.

associating  $\gamma$ -ray emission with objects known at other wavelengths: either no credible object is detected in the error box of the  $\gamma$ -ray source, or a number are present and some characteristic of the  $\gamma$ -ray source, such as periodicity or variability, must be identified in one of the prospective candidates (or vice versa as in the case of Geminga).

### 1.3 The Energetic Gamma-Ray Experiment Telescope

The Compton Gamma Ray Observatory (CGRO), launched in 1991, was the second of NASA’s “Great Observatories”<sup>4</sup>. The observatory operated continuously until it was de-orbited in 2000. CGRO covered the energy range from 20 keV to 30 GeV with its four on-board instruments: OSSE (60 keV - 10 MeV), COMPTEL (800 keV - 30 MeV), BATSE (30 keV - 1.9 MeV) and EGRET (20 MeV to 30 GeV). Over the course of the mission, each of the instruments produced full sky maps of the  $\gamma$ -ray emission within its energy range.

EGRET employed two thin-plate spark chambers to detect  $\gamma$ -rays by tracking electrons or positrons generated through pair-production in the chamber. The instrument was triggered by requiring a coincident signal to be detected in each of two sets of  $4 \times 4$  scintillator tiles placed under each spark chamber. The incident  $\gamma$ -ray was required to trigger either the corresponding tile, or neighboring tiles at each level, to limit the angle of incidence to less than  $30^\circ$ . A sodium-iodide calorimeter was used to infer the energy of the primary. Energy resolution was  $\sim 20\%$  up to a few GeV, above which the particles were not fully contained in the calorimeter. Background charged particles were eliminated by encasing the instrument in a dome of plastic scintillator acting as an anti-coincidence shield. In addition, upward moving particles were eliminated by measuring the time of flight between the two scintillation layers. Figure 1.2 shows a schematic of the telescope. A detailed description of the instrument can be found in Kanbach et al. (1988); a summary can be found in Esposito et al. (1999).

---

<sup>4</sup>CGRO was launched a year after the Hubble Space Telescope and was followed by the Chandra x-ray satellite in 1999 and recently by the SIRTF infra-red observatory (2003).

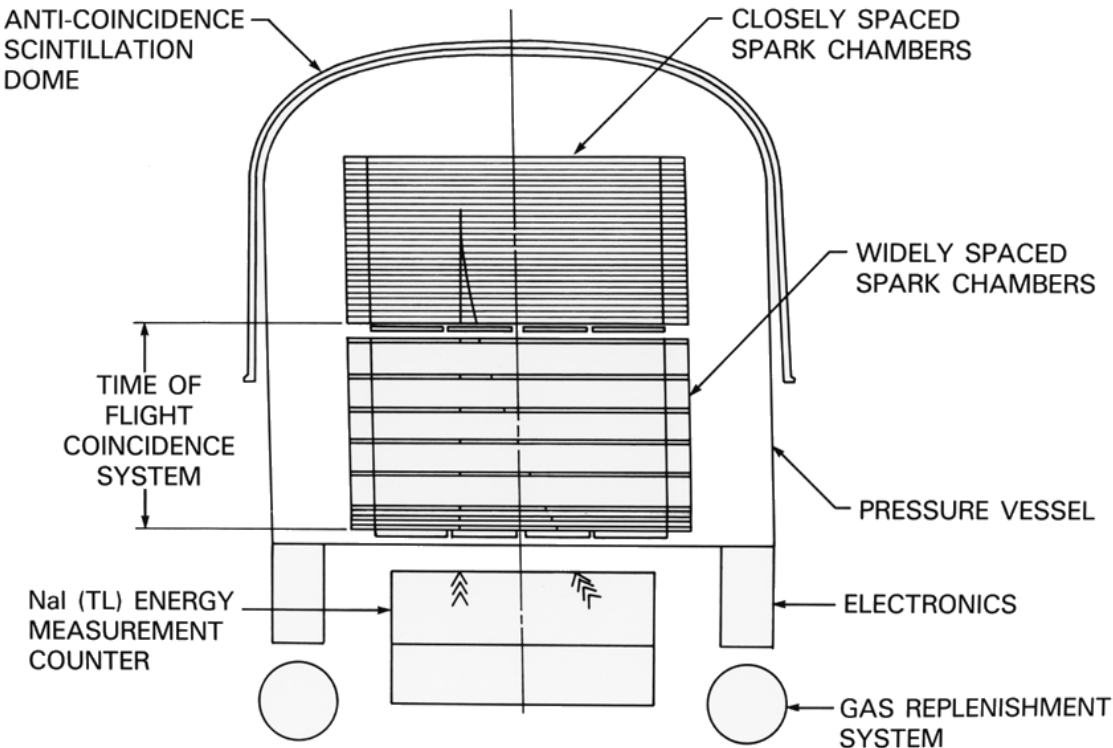


**Figure 1.2:** Schematic of the Energetic Gamma-Ray Experiment Telescope (EGRET) experiment on CGRO. Two levels of spark chamber track pair production  $e^-/e^+$  while an NaI scintillator is used as a calorimeter. Figure courtesy of NASA.

The EGRET instrument was initially planned to function for two years, but was operated, to various degrees of efficiency, for the nine year duration of the CGRO mission. Initially calibrated at SLAC (Thompson et al., 1993), the extended mission, which included five exchanges of the spark chamber gas and numerous equipment failures, required that the instrument be continuously recalibrated in flight using pulsars to measure the point-spread function and the diffuse Galactic background to check the sensitivity (Esposito et al., 1999). From October 1995, EGRET was switched from its wide field, survey mode to a narrow field, pointed mode. In order to conserve spark chamber gas, it spent a large part of its remaining life powered down, awaiting target of opportunity observations of flaring AGN and  $\gamma$ -ray bursts. EGRET's many contributions to the field of HE  $\gamma$ -ray astrophysics are detailed by

Fichtel (1996).

Analysis of the EGRET data for point sources was done with a maximum likelihood method, as described by Mattox et al. (1996). The analysis is dependent on a complicated model of the diffuse Galactic and extra-galactic  $\gamma$ -ray emission which was extrapolated from radio surveys of the Galactic gas density. The energy dependent point-spread function and exposure, which varied by a factor of two across the sky, was also accounted for. An iterative approach to point-source detection was performed; a search was made for significant excesses of  $\gamma$ -rays above a background which included the diffuse  $\gamma$ -ray emission model (as described above) in addition to all those point-sources already discovered.

## 1.4 Catalogs of EGRET “point” sources

The data produced by EGRET have been compiled into a number of catalogs of significantly detected point sources. The EGRET team published three catalogs of point-sources detected at energies greater than 100 MeV, the definitive being the third EGRET Catalog (Hartman et al., 1999), hereafter known as the 3EG catalog. This catalog includes data from the first four viewing periods (until October 1995) when the instrument was in its wide-field triggering mode. Sources are considered significant in this catalog when they are detected above the  $4\sigma$  level far from the Galactic plane, i.e. at Galactic latitudes of  $|b| > 10^\circ$ . In the Galactic plane, at  $|b| < 10^\circ$ , a signal of at least  $5\sigma$  above the background level is required.

Source detection and localization are subject to two possible sources of systematic error. The model of Galactic emission is not completely accurate; errors on small scales may lead to false detections (hence the  $5\sigma$  requirement at  $|b| < 10^\circ$ ), or more likely, lead to systematic errors in the location of genuine sources. The iterative approach to source identification attempts to account for the contribution to the background of the brightest sources in the identification of less bright ones. The large point spread function at 100 MeV means  $\gamma$ -rays from sources separated by distances

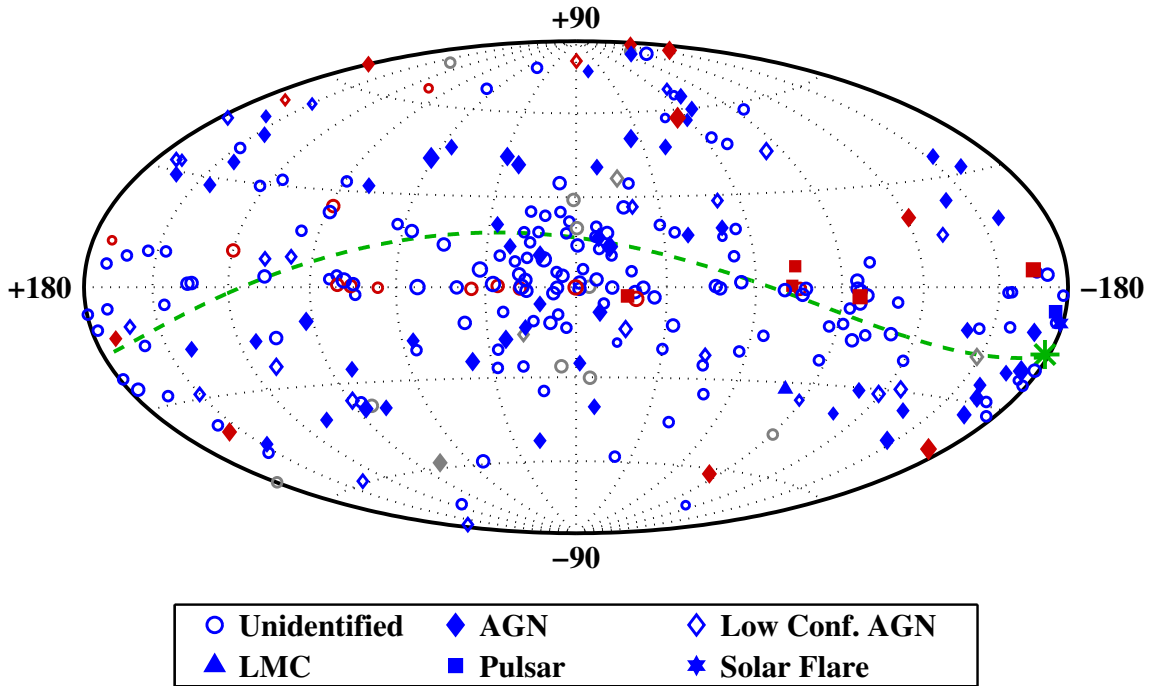
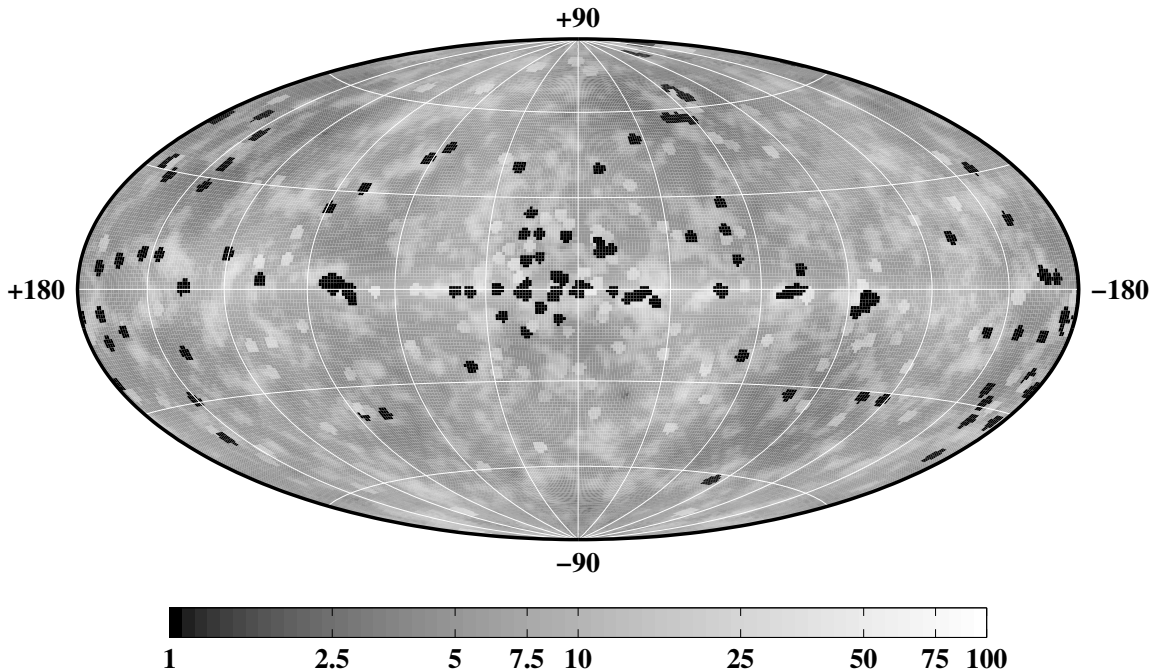


Figure 1.3: The 271 sources listed in the third EGRET catalog (Hartman et al., 1999), plotted in Galactic coordinates. Sources are displayed by source identification (symbols) and flux (size of the symbol). Sources with a fitted spectrum *harder* than 2.0 are shown in red, those with a softer spectrum are shown in blue. Those without an estimate of spectral index are shown in gray. Finally, the Gould Belt is shown as a broken green line, with the direction of the center of the Belt, from Stothers and Frogel (1974), shown as a green star.

of  $< 5^\circ$  will overlap. In the analysis, this implies that sources separated by less than  $1^\circ$  may not be resolved. Overlapping sources can lead to systematic errors in the fitted location of each of the sources, or to phantom sources in the catalog. Such sources are marked as “confused” in the catalog. Some were later interpreted as artifacts of very bright sources such as the Vela pulsar (Thompson et al., 2001).

The catalog contains a total of 271 entries and upper limits on emission for the remainder of the sky. For each source, maps of the *likelihood statistic*<sup>5</sup> are available, which give the probability that the source is within a certain region of the sky at

<sup>5</sup>In a likelihood analysis, the likelihood statistic is analogous to significance. See Mattox et al. (1996) for details.



**Figure 1.4:** Upper limits on  $\gamma$ -ray emission at energies  $> 100$  MeV from EGRET observations, in units of  $10^{-8} \text{ cm}^{-2} \text{ s}^{-1}$ . As noted in Hartman et al. (1999), the regions within  $1^\circ$  of the 3EG sources are shown as black.

various confidence levels. The radius of 95% confidence contour,  $\theta_{95}$ , is quoted in the catalog as a bound on source location. The average point source localization is  $\langle \theta_{95} \rangle = 0.66^\circ$ , large enough that the error-box of many sources contains a large number of possible counterparts at different energies, especially for those sources in the region of the Galactic plane.

At low Galactic latitudes, 80 sources were listed in the 3EG catalog. Five were definitively identified as known pulsars, one corresponded to a solar flare and 74 had no unambiguous counterparts at other energies. The 181 sources at  $|b| > 10^\circ$  include 66 likely identifications with blazars, the Large Magellanic Cloud (LMC), Centaurus A (a giant radio galaxy), 27 low confidence identifications with AGN and 96 unidentified sources. Figure 1.3 shows the sources in the 3EG catalog, by position on the sky, source type, flux and spectral hardness.

The majority of the detected sources are listed with flux estimates from the viewing

periods during which they were detected, and an average flux over the full duration of the database. Many sources were detected in each of the four viewing periods, some, such as the solar flare, were only seen during certain portions of a single viewing period. A systematic variability analysis of the EGRET data is presented in Nolan et al. (2003). Finally, the 3EG catalog presents a power law fit to the spectrum of the detected  $\gamma$ -rays for those sources from which sufficiently large numbers of photons were detected. For those parts of the sky in which no source was detected, upper limits on emission at energies  $>100$  MeV were derived. The limits, reproduced from the online version of the catalog, are shown in figure 1.4. The limits represent the maximum flux a source could have, at the 95% confidence level, without having been detected during the various observations by EGRET.

In addition to the third EGRET catalog, two catalogs of point-sources detected by EGRET at higher energies have been produced. The first, presented in two parts in Lamb and Macomb (1997) and Macomb and Lamb (1999), imposed a requirement that the reconstructed energy of the  $\gamma$ -ray be larger than 1 GeV, and is hereafter referred to as the GeV catalog. The production of this catalog was motivated by the significantly smaller EGRET point spread function at energies above 1 GeV and by the lower background of diffuse  $\gamma$ -rays at these energies. It was hoped that sources could be localized with improved accuracy and that sources with spectra harder than the spectrum of background events would become more significant at higher energies. A similar motivation guided the production of a catalog of  $\gamma$ -ray sources produced from those EGRET events with energies greater than 10 GeV (Dingus and Bertsch, 2001), hereafter the 10 GeV catalog.

The first installment of the GeV catalog lists 57 sources at a significance of  $4\sigma$  and above. Ten of them had not been detected at 100 MeV energies in the *second* EGRET catalog; a total of thirty were listed as unidentified. The second installment of the GeV catalog, which included data from all the EGRET viewing periods, added another 16 sources with three that did not appear in the 3EG catalog. The 10 GeV catalog is based on a database of  $\sim 1000$  photons which were detected at large Galactic latitude; the catalog of Galactic photons was presented at a conference but never appeared in

print. If it is assumed that the  $\gamma$ -rays are uniformly distributed in the sky, only two would be expected to be coincident with blazars by chance within the EGRET point spread function.

## 1.5 Whipple 10 m atmospheric Čerenkov telescope

The Whipple 10 m imaging atmospheric Čerenkov telescope (IACT) is located on Mt. Hopkins in southern Arizona at an elevation of 2,300 m. Built in 1968, it was the first dedicated  $\gamma$ -ray instrument of its type. In design, it has much in common with the large, fully steerable, dish-type solar concentrators of the time and, indeed, it was used as such for a brief period. For most of its life, though, it has been operated as a ground-based  $\gamma$ -ray telescope. The telescope can be operated by a single observer who chooses which sources to look at, manages the data acquisition and analyzes the data to produce a nearly real-time measurement of  $\gamma$ -ray emission. The ability to produce such a quick result has proved to be profitable on many occasions, by prompting the telescope operator to continue to observe objects which are in flaring states. The instrument is operated for 10 months of the year, closing down during the summer to avoid lightning damage to the sensitive electronics during the monsoon season.

The telescope has a total mirror area of  $\sim 75 \text{ m}^2$  and a focal length of 7.3 m. The mirror consists of an array of 249 identical, spherical mirror facets, with radius of curvature 14.6 m. The facets are attached to a spherical optical support structure of radius 7.3 m. This design, suggested by Davies and Cotton (1957), has inferior on-axis performance when compared to a parabolic design but has significantly improved off-axis characteristics. Since the Čerenkov light from an air-shower can be displaced from the direction of the primary particle by the order of a degree or more, good off-axis performance is important to IACT instruments. The design also has the advantage that all mirror facets are identical and can be mass produced. The mirrors are front aluminized at an in-house coating facility, and anodized for protection from the environment. Front coating improves the reflectivity in the UV band, where

significant Čerenkov emission occurs, although it does leave the mirror coating prone to weathering. The facets are aligned by hand at the end of each monsoon season, and checked during the year. Figure 1.5 illustrates the design of the telescope. As can be seen from the figure, the Davies-Cotton design is not isochronous, a small time-spread is introduced between parallel photons reflected from the center and edge of the mirror.

A high resolution camera, consisting of an array of 379 1/2 inch phototubes in a close packed, hexagonal arrangement surrounded by 111 1 inch phototubes, was installed on the instrument in 1999, see figure 1.6. The PMTs have a quartz glass window to extend their sensitivity into the UV. The voltage on each channel is individually controllable with an Ethernet-based LeCroy high-voltage system, allowing the gain on each channel to be equalized across the camera. Signals from the inner 379 channels are transmitted to the acquisition system on coaxial cables. Signals from the outer channels are propagated on a prototype analog optical fiber system designed to have very little dispersion. Due to the somewhat experimental nature of the outer 111 tubes, data from them have not been used in this survey. The inner, high resolution portion of the camera has a field of view of  $\sim 2.2^\circ$ .

The instrument is triggered when three neighboring channels exceed a preset threshold within a given coincidence time. The signals from each channel and other information, such as the absolute time of the event from a GPS clock and time relative to the start of the data run, are then stored on computer for off-line analysis. Details of the trigger electronics and data acquisition system are given in section 3.3.

The data is analyzed off-line and a set of selection criteria (called *super-cuts*) are applied to discard  $> 98\%$  of the background events and retain  $\sim 50\%$  of the  $\gamma$ -ray events. From simulations, it is estimated that the instrument has an effective area of  $4.4 \times 10^4 \text{ m}^2$  at 1 TeV, after data selection has been applied. For a source with a Crab-like power law spectrum,  $dN/dE \propto (E/\text{TeV})^{-2.5}$ , the energy at which the instrument collects most  $\gamma$ -rays, the *peak response energy* is estimated to be  $E_{\text{peak}}=350 \text{ GeV}$ . The analysis technique is described in chapter 4.

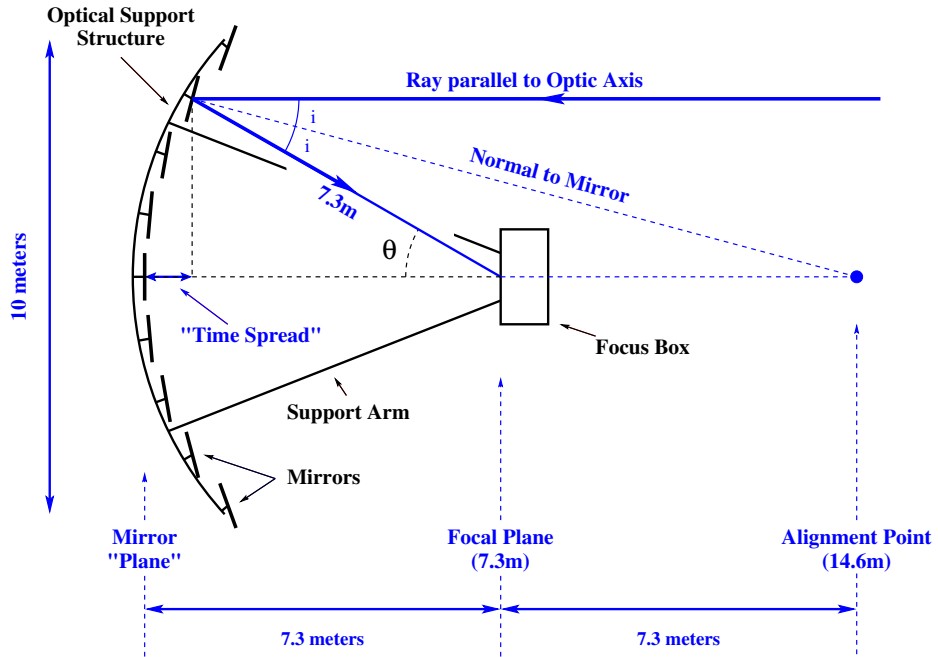


Figure 1.5: Illustration of the Whipple 10 m telescope. The mirror consists of 249 spherical mirrors in a Davies-Cotton configuration. The small time-spread introduced between photons reflected from the edge and center of the mirror is evident in the diagram.

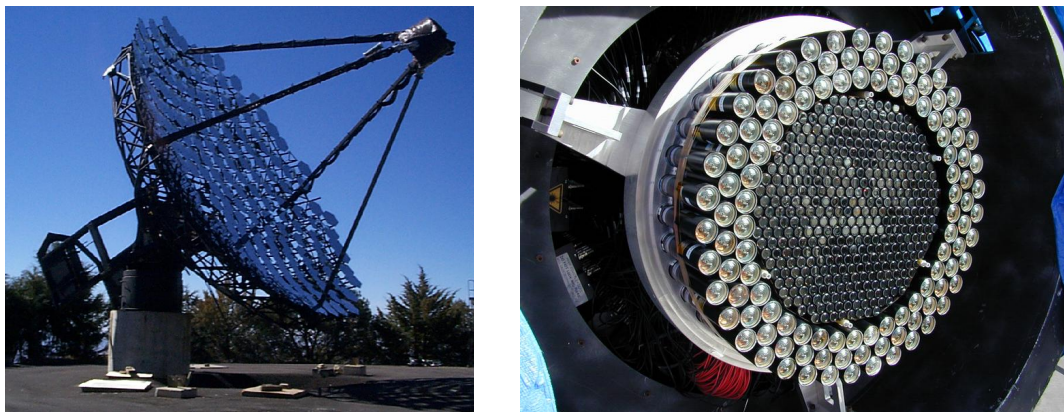


Figure 1.6: Left: Picture of the Whipple 10 m telescope (courtesy of Dr. R. Lessard). Right: Picture of the high-resolution, 499 pixel camera at the focal plane of the instrument. In normal operation, a reflective light concentrator plate is installed over the face of the inner 379 PMTs to increase photon detection efficiency – the six mounting posts for this plate are visible between the inner and outer parts of the camera.

The relatively small field of view of the ground-based Čerenkov instruments dictates that observations be pointed in nature. In general, they are targeted at prospective sources for a certain number of hours in the hope of detecting emission. This is in contrast to satellite instruments which tend to operate in a sky survey mode, at least for the first few years of their life. There have been some exceptions to this rule, such as the sky-survey performed with the Whipple telescope before the adoption of the imaging technique (Weekes et al., 1979) and the recent survey of the Galactic plane region with the HEGRA telescope (Aharonian et al., 2002b).

Table 1.1 contrasts the characteristics of the EGRET and Whipple instruments. Whipple has considerably better point-source localization ability than EGRET and has a field of view comparable to the average error-box of unidentified sources in the 3EG catalog. The Whipple instrument has a detection sensitivity of approximately 30% of the Crab flux in 5 hours of observation – given a required detection at the  $4\sigma$  level. Figure 1.7 shows the upper limit on the luminosity of an object<sup>6</sup>, above 350 GeV, which can be derived from a *non-source*, through observations of 0.5, 5 and 50 hours. The hypothetical EGRET source, is chosen to have the mean flux and spectral index (and  $1\sigma$  errors on each) of the sources chosen for this VHE survey.

## 1.6 Catalog of VHE gamma-ray sources

To date, 18 credible source detections have been made by ground-based  $\gamma$ -ray community. These sources are listed in table 1.2 and are plotted in figure 1.8. Nine have been confirmed by more than one ground-based instrument and are considered to be beyond dispute. The others are, as yet, unconfirmed. In some of these cases the discoveries are so recent that sufficient observations have not been made by an independent group. In others cases it is because there is no longer an independent telescope operating in the correct range of latitude to provide confirmation. In the case of 3C66A, a blazar discovered in 1998, it is possible that the initial discovery was

---

<sup>6</sup>At a 99% confidence level, used throughout this survey.

**Table 1.1: Comparison of the characteristics of the EGRET instrument on CGRO and the Whipple 10 m atmospheric Čerenkov imaging telescope.**

Characteristic	EGRET	Whipple
Energy Range (MeV)	30 to $3 \times 10^4$	$3 \times 10^5$ to $3 \times 10^7$
Effective Area ( $\text{cm}^2$ )	1200 at 100 MeV 1600 at 500 MeV 1400 at 3000 MeV	$2 \times 10^8$ at 350 GeV $4.4 \times 10^8$ at 1 TeV $3.6 \times 10^8$ at 10 TeV
Average error in $\gamma$ -ray origin – $\theta_{68}$ (degrees)	5.85 at 100 MeV 1.71 at 1 GeV 0.50 at 10 GeV	0.42 at 300 GeV 0.25 at 1 TeV
Field of view	$\sim 0.6 \text{ sr}$	0.0012 sr
Sensitivity to Crab like spectrum ( $\text{cm}^{-2}\text{s}^{-1}$ )	$6 \times 10^{-8} > 100 \text{ MeV}$ ( $3\sigma$ after 2 weeks off Galactic plane)	$3.02 \times 10^{-11} > 350 \text{ GeV}$ or $0.294 \times \text{Crab flux}$ ( $4\sigma$ in 5 hrs)

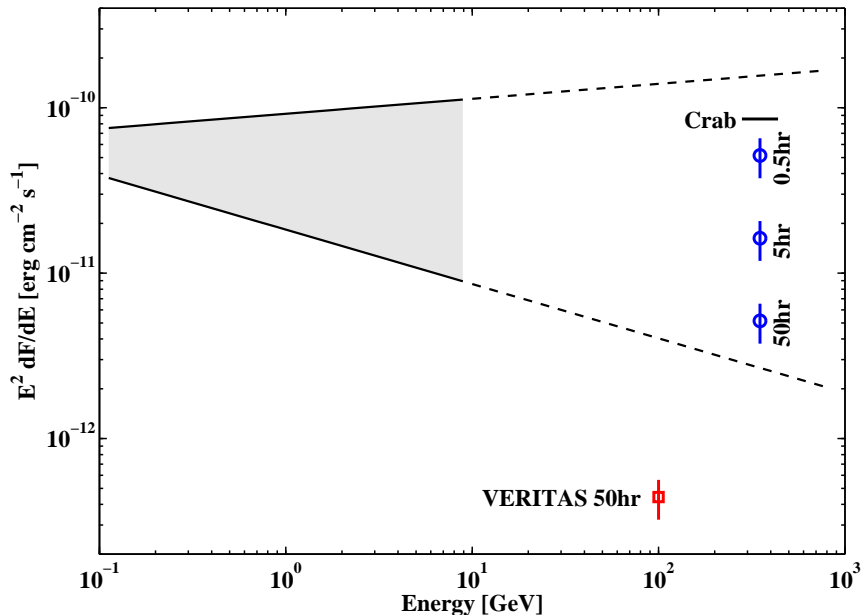


**Figure 1.7:** Comparison of upper limit on source luminosity derivable through observations at Whipple with the extrapolated luminosity of a “mean” 100 MeV source. Upper limits for 0.5, 5 and 50 hour observations are shown, assuming a Crab-like spectrum. The hypothetical 100 MeV source, has an integral flux spectrum given by the mean flux and spectral index from 3EG sources chosen for this survey:  $I(> E) = (30.9 \pm 4.1) \times 10^{-8} (E/100\text{MeV})^{-1.12 \pm 0.21} \text{ cm}^{-2}\text{s}^{-1}$ .

**Table 1.2: Catalog of published VHE sources<sup>1</sup>. Adapted from Horan and Weekes (2004).**

Src. no. <sup>2</sup>	VHE catalog name	Associated source	Source type	Discovery year/group <sup>3</sup>	3EG src.	Indep. conf.
1	TeV 0047–2518	NGC 253	Starburst	2003/C	No	No
2	TeV 0219+4248	3C66A	Blazar	1998/Cr	Yes	No
3	TeV 0535+2200	Crab	SNR/PWN	1989/W	Yes	Yes
4	TeV 0834–4500	Vela	SNR/PWN	1997/C	No	No
5	TeV 1121–6037	Cen X–3	Binary	1998/D	Yes	No
6	TeV 1104+3813	Mrk 421	Blazar	1992/W	Yes	Yes
7	TeV 1231+1224	M87	Radio Gal.	2003/H	No	No
8	TeV 1429+4240	H1426+428	Blazar	2002/W	No	Yes
9	TeV 1503–4157	SN1006	SNR	1997/C	No	Yes
10	TeV 1654+3946	Mrk 501	Blazar	1995/W	No	Yes
11	TeV 1710–4429	PSR 1706–44	SNR/PWN	1995/C	No	Yes
12	TeV 1712–3932	RXJ1713–3946	SNR	1999/C	No	No
13	TeV 2000+6509	1ES1959+650	Blazar	1999/TA	No	Yes
14	TeV 2032+4131	<i>unidentified</i>	<i>unidentified</i> <sup>4</sup>	2002/H	Yes <sup>5</sup>	No
15	TeV 2159–3014	PKS2155–304	Blazar	1999/D	Yes	Yes
16	TeV 2203+4217	BL Lacertae	Blazar	2001/Cr	Yes	No
17	TeV 2323+5849	Cas A	SNR	1999/H	No	No
18	TeV 2347+5142	1ES2344+514	Blazar	1997/W	No	Yes

<sup>1</sup> All VHE sources published in refereed journals are presented here. Recent results from conferences, awaiting publication, are not shown.

<sup>2</sup> Source number from VHE source map, figure 1.8.

<sup>3</sup> C: CANGAROO, Cr: Crimea, D: Durham, H: HEGRA, TA: Telescope Array and W: Whipple.

<sup>4</sup> Butt et al. (2003) suggest that TeV 2032+4131 is associated with an OB association, Cyg OB2. Other associations have also been made (Mukherjee et al., 2003).

<sup>5</sup> VHE source is coincident with 3EG J2033+4118.

made during a period of extreme flaring activity, which has not been repeated. In the case of Cen X-3, flaring outbursts have been noted at other wavelengths, but the VHE emission was reported to be steady over the course of the observation. Since they are expected to be persistent, and have not been confirmed, the discoveries of Vela and Cen X-3 have therefore been regarded as grade “C” (Horan and Weekes, 2004).

The mechanisms responsible for HE and VHE emission are discussed in chapter 2. A brief list of the observational characteristics of the sources and source types are presented below without reference to the emission mechanisms.

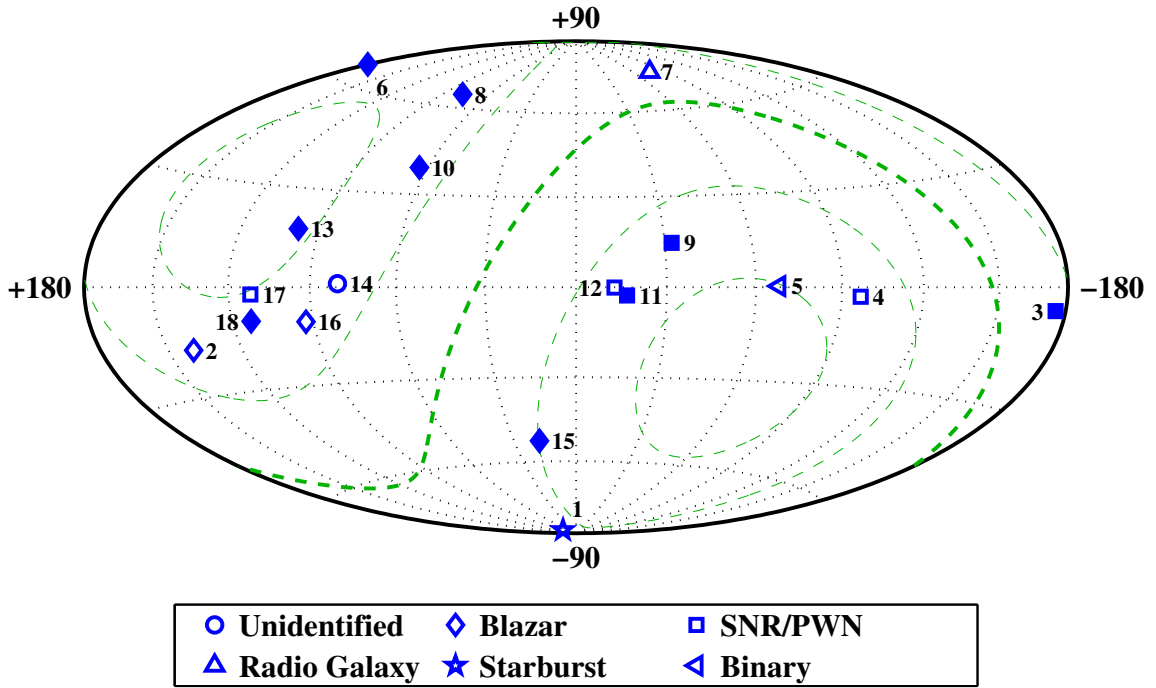


Figure 1.8: The 18 objects reported as  $\gamma$ -ray sources in the VHE regime, in Galactic coordinates. Confirmed sources are depicted as solid symbols, unconfirmed sources as outlines. Sources are listed by number, as they appear in the VHE catalog, table 1.2. The thick broken line shows the equatorial plane, separating the northern and southern hemispheres. The thinner broken lines show the  $30^\circ$  and  $60^\circ$  declinations north and south. The data for this figure are taken from Horan and Weekes (2004).

The first source detected by a ground-based  $\gamma$ -ray instrument was the Crab Nebula (Weekes et al., 1989). The Crab, a class of supernova remnant (SNR) called pulsar wind nebula (or plerion – see section 2.4), was the result of a historical supernova explosion in the year 1054. It is a unique object, one of the brightest in the sky over all wavelengths, with non-thermal emission at radio, optical, x-ray and  $\gamma$ -ray energies. Pulsations from a central pulsar are seen at most energies up to and including the HE  $\gamma$ -ray range. The VHE emission from this object is consistent with being steady over the 15 years for which it has been detected. It has become the “standard candle” in the VHE regime, a source to calibrate new instruments against. Its spectrum is well fitted by a power-law with spectral index of  $-2.49$  (Hillas et al., 1998). No periodicity has been seen in the VHE  $\gamma$ -ray signal, which is not thought to have come

directly from the pulsar, but to emanate from a synchrotron nebula surrounding it. In addition to the Crab, VHE emission has been reported from two other pulsar wind nebulae, both in the southern hemisphere: PSR 1706–44 and Vela.

The remaining SNR belong to the class of shell-type supernova remnant. Two, SN1006 and RXJ1713–3946, are in the southern hemisphere; the third, Cas A, is in the northern hemisphere. As discussed in section 2.3, SNR may be associated with the acceleration of charged particles through diffusive shock acceleration. The shape of the spectra of VHE  $\gamma$ -rays from these objects, in conjunction with observations at other wavelengths, is expected to determine whether hadronic acceleration is occurring at these sites, or whether the emission is the result of electron acceleration. Emission from SN1006 is consistent with a purely leptonic model, while RXJ1713–3946 and Cas A may show evidence for hadronic acceleration, see section 2.3.

The VHE blazars, extra-galactic objects associated with compact super-massive black holes (see section 2.1), are characterized by extreme variability on the time scales of hours and days (Gaidos et al., 1996). Their emission can go from a quiescent state that is at or below the sensitivity of the Whipple instrument to a flaring state with emission at a level of a few times the Crab flux over the course of a single night of observations. During these flaring periods, the spectral index of the source has also been seen to change; in the case of Mrk 421, a hardening of the spectrum from  $-2.7$  to  $-1.9$  was observed in data from the Whipple telescope, taken during 2000/2001 (Krennrich et al., 2002). Flaring activity at TeV energies is usually correlated with increased activity at other wavelengths, in particular significant correlations with x-ray flares have been observed (Maraschi et al., 1999).

## 1.7 VHE observations of third EGRET catalog sources

The 170 unidentified sources in the 3EG catalog have motivated multiwavelength studies at all wavelengths. Studies using the ASCA x-ray satellite have revealed possible counterparts for some of them (Roberts et al., 2001b), as have studies in

the radio and optical bands. In some cases, the multiwavelength approach has been able to narrow the potential candidate associations, leaving a single likely candidate. It is in the spirit of this tradition, that a survey of unidentified sources has been undertaken with the Whipple VHE  $\gamma$ -ray telescope. The unidentified sources provide a catalog of objects whose error-box is well matched to the field of view of an IACT. If VHE emission is present, observations with an IACT would have sufficient angular resolution to narrow down the potential candidates within the error box of the 3EG source and, potentially, provide an unambiguous association. This has been the scientific objective of the research reported in this dissertation.

Objects have been chosen for the survey based upon a number of factors. Preference was given to persistent objects, with hard spectra for which a lack of VHE emission would necessitate a cut-off in the spectrum. In all cases, the location of the source in the sky influenced the choice. It is desirable that sources lie between declinations of  $10^\circ$  south and  $70^\circ$  north so that they can be observed with the Whipple telescope at relatively small angles from the zenith, for which the density of Čerenkov photons on the ground is highest. Additionally, since the telescope is operated by a relatively large collaboration, with diverse research interests, sources were chosen so as not to clash with areas of the sky for which considerable conflicting interests exist, such as the Galactic Center region. Finally, Petry (2001) extrapolated the known EGRET spectrum of the unidentified sources to provide a table of most likely detections with next-generation Čerenkov instruments. A number of the most likely sources from this list were chosen. Chapter 5 lists the 3EG sources chosen in this survey and presents the results of the VHE survey.

## 2. POTENTIAL SOURCES OF HIGH-ENERGY GAMMA-RAYS

To date, EGRET sources have been unambiguously identified with only two major source types: blazars and pulsars (neglecting the LMC, Cen A, the solar flare and  $\gamma$ -ray bursts). Numerous population studies have noted that there are coincidences between the population of unidentified sources and catalogs of other types of sources which exceed what should be expected from chance probability; however these studies do not provide compelling associations for any individual 3EG sources. Some suggested source classes are massive stars, OB associations, supernova remnants (SNR), x-ray binaries and micro-quasars. In addition, it seems likely that there are three independent populations of unidentified source: those associated with the Galactic plane, extra-galactic sources and a population of local sources in the Gould Belt.

### 2.1 Blazars

One of the most unexpected results from the EGRET mission was the discovery of  $\gamma$ -rays from a large number of extra-galactic sources. Before EGRET, only one extra-galactic source had been detected in  $\gamma$ -rays, 3C273, based upon observations with the COS-B satellite (Swanenburg et al., 1978). In total, 67 high-confidence associations of EGRET sources were made with blazars, a type of radio loud active galactic nucleus (AGN). AGN are galaxies with a bright central core which typically outshines the  $\sim 10^{11}$  stars present in the Galaxy by up to three orders of magnitude. AGN are thought to be powered by accretion of material onto a super-massive black hole, (mass  $\sim 10^6 M_\odot$  to  $\sim 10^9 M_\odot$ ). The accreting material forms a disk around the core, at temperatures which can produce continuum emission at UV to soft x-ray energies. AGN can form jets of relativistic charged particles, aligned perpendicular to the plane of the accretion disk. The mechanism responsible for forming the jet is

not completely understood. The accretion disk is surrounded by clouds of hot gas which produce broad line emission. Far out from the core, narrow line emission is produced in clouds of particles, possibly energized by the jet.

AGN have been sub-classified based upon their observational properties, with some classes being more powerful, and therefore better studied, in different energy ranges. At  $\gamma$ -ray energies, the blazar subclass of AGN are powerful emitters. Blazars are characterized by strong emission in radio (they are referred to as radio-loud AGN), continuum emission across the spectrum, very rapid variability on the order of hours to days and weeks, high polarization and the ejection of “blobs” of material at apparent super-luminal velocities, usually visible in radio. The blazar sub-class consists of “BL Lac” type objects, and flat-spectrum radio quasars (FSRQs). These objects are distinguished on the basis of prominent (FSQR) or weak (BL Lac) absorption/emission lines in their spectra. In general, the lack of lines in the spectra of BL Lac objects makes it difficult to determine their redshift, and hence distance. It also means that they are usually identified as AGN at radio or x-ray energies, since they are essentially featureless at optical wavelengths. It has been suggested that all AGN can be unified by a single model (Urry and Padovani, 1995), and that the different observational properties of the AGN classes arise primarily from differences in the viewing angle with respect to the jet and the total power of the accreting object. For example, the presence or absence of broad lines in the spectrum depends on whether the broad line emission region is obscured from sight by other parts of the AGN structure. Blazars are thought to be AGN with jets aligned close to our line-of-sight. The physics behind  $\gamma$ -ray emission in the jet is not well known, and many models exist. The most widely discussed models are leptonic, synchrotron/inverse Compton models, in which synchrotron emission from electrons in the jet produces the low energy emission (radio, optical and soft x-ray) while inverse Compton up-scattering of the soft synchrotron photons by the same population of electrons accounts for the high energy emission. This model, referred to as the synchrotron-self-Compton (SSC) model, predicts that the peak in the power output of the IC component is correlated with the peak in the synchrotron emission, and has been relatively successful in fitting the emission seen

from blazars. A review of leptonic emission models can be found in Boettcher (1999).

The identification of some EGRET sources with blazar objects is presented in detail in von Montigny et al. (1995), Mukherjee et al. (1997), Hartman et al. (1999) and references therein. A recent summary of the EGRET blazars can be found in Mukherjee (2001). In general, identifications were made on the basis of positional coincidence with known radio sources. The blazars listed in the 3EG catalog consist of 50 FSRQs and 17 BL Lacs, with redshift between  $z = 0.03$  and  $z = 2.28$ . For most of these objects the  $\gamma$ -ray emission dominates the total luminosity at all other wavelengths. Their spectra are well fit by a power-law with average spectral index of  $\langle \Gamma \rangle = 2.2$  and no cut-off has been seen up to 10 GeV. The average variability index of the blazars, from Nolan et al. (2003), is  $\langle \delta \rangle = 0.70 \pm 0.08$  with  $\text{RMS}(\delta) = 0.27 \pm 0.05$ , showing that they are consistent with being variable ( $\delta \rightarrow 0$  for persistent sources, and  $\delta \rightarrow 1$  for variable sources).

The GeV and 10 GeV catalogs also contain a number of additional blazar identifications. The 10 GeV catalog suggests that there may be a blazar identification for 3EG J0433+2908 and for GeV J0508+0540. In the time since the 3EG-catalog was published a number of investigations have been made into individual unidentified EGRET sources, leading to possible (or likely) blazar identifications for them. For example, Mukherjee et al. (2000) suggest that 3EG J2016+3657 is associated with a blazar, an especially interesting result as the source is located at low Galactic latitude ( $b = 0.5^\circ$ ), possibly making it the first blazar identified in the direction of the plane.

Of the 3EG blazars, two are confirmed sources of VHE  $\gamma$ -rays: Markarian 421 (usually abbreviated to Mrk 421) and PKS2155–304. A third confirmed VHE source, Mrk 501 is significant only in the EGRET GeV catalog. On the other hand, there are three confirmed VHE blazars not seen by EGRET: H1426+428, 1ES1959+650 and 1ES2344+514, all BL Lac type objects. To date, no FSRQs have been detected by VHE instruments. EGRET largely detected low-frequency peaked BL Lacs (LBL) and FSRQs. These objects have the peak in their synchrotron power emission in the optical, UV or soft x-ray bands. All confirmed BL Lac detections in the VHE band

are high-frequency peaked BL Lacs (HBL), with peak synchrotron power in the hard x-ray band. Correspondingly, the peak in the inverse Compton emission is at higher energies in HBLs, lying in the 300 GeV to 30 TeV range. The energy range in which EGRET was most sensitive fell in that region of the spectrum in which HBLs are least powerful; between the peaks of the synchrotron and inverse-Compton emission. Therefore, EGRET was not sensitive enough to detect many of the TeV selected BL Lacs. The most distant blazar detected in the VHE regime is H1426+428, at a redshift of  $z = 0.129$ . Many models predict that interactions of VHE  $\gamma$ -rays with the extra-galactic background light will attenuate the  $\gamma$ -ray signal to such an extent that sources located at distances much larger than H1426+428 are not be visible in  $\gamma$ -rays at GeV-TeV energies, with current detector sensitivities.

In summary, it seems likely that blazars make up a considerable fraction of the unidentified EGRET sources. Blazars are expected to be uniformly distributed across the sky, to have flat spectra which steepen with distance, and are characterized by extreme variability across the spectrum from radio to TeV energies. Since the known  $\gamma$ -ray blazars have been readily identified with their radio, optical and x-ray counterparts, new identifications would suggest some unusual spectral distributions and/or obscuration, e.g. by the Galactic plane.

### **Intergalactic $\gamma$ -ray absorption**

The spectra of  $\gamma$ -rays detected from all extra-galactic sources are altered from the intrinsic source emission spectrum by absorption of the signal in the ambient field of intergalactic photons. Nikishov (1961) was the first to suggest that high-energy photons would interact with infra-red photons in intergalactic space by photon-photon pair production. At that time, little was known about the strength of the intergalactic infra-red radiation field (IIRF) and the value assumed in the calculation was too large by three orders of magnitude. Shortly after the discovery of the cosmic microwave background (CMB), it was realized by Gould and Schréder (1966) and Jelley (1966) that the universe is effectively opaque to  $\gamma$ -rays with energy greater

than  $\sim 100$  TeV. Gould and Schréder (1967) extended these calculations to account for absorption with radio, microwave, IR and optical photons.

The unexpected discovery of the optically violent variable quasar, 3C279, by EGRET prompted Stecker et al. (1992) to suggest that any subsequent discovery of TeV emission from the object could be used to determine (or at least provide limits on) the density of the IIRF. The discovery of the blazar Mrk 421 at TeV energies (Punch et al., 1992), and the subsequent discovery of other TeV blazars, has produced considerable interest in this subject (see for example Vassiliev, 2000, and references therein).

The threshold for a soft photon with energy  $\epsilon$  (as measured locally) to interact with a  $\gamma$ -ray with energy  $E$  (measured locally) at redshift of  $z$  is

$$\epsilon > \frac{2(m_e c^2)^2}{E(1+z)^2} \approx \frac{0.52}{E/\text{TeV}} \text{ eV.}$$

for small redshifts. For a 1 TeV photon, this corresponds to an IR photon near to the K-band ( $2\mu\text{m}$ ). For energies above 100 TeV the threshold is in the CMB region. The amount of absorption a signal from a distant source undergoes can be calculated from the pair-production cross-section, due to Heitler, given some assumptions for the spectrum of soft-photons (see for example Stecker and de Jager, 1996). Stecker and de Jager (1998) calculated the optical path length (or *opacity*,  $\tau(E, z)$ ) for TeV photons from relatively small redshifts ( $z \leq 0.3$ ), which they presented in parameterized form, valid for  $1 \text{ TeV} < E < 50 \text{ TeV}$  and  $z < 0.3$ . Figure 2.1 shows the opacity, from the parameterized form, as a function of  $\gamma$ -ray energy for three redshifts. The change in the intrinsic source spectrum for these cases is also shown. In each case a strong cut-off<sup>7</sup> in the measured  $\gamma$ -ray spectrum is predicted, independent of the source emission spectrum. For sources at  $z \sim 0.03$ , like Mrk 421, the cut-off occurs at  $\sim 10$  TeV, decreasing to  $\sim 1$  TeV for a more distant source, such as H1426+428 at  $z = 0.129$ .

Predicting VHE emission from the EGRET blazars requires the opacity be known in the energy range  $\sim 1 \text{ GeV} < E < \sim 1 \text{ TeV}$ , and for larger redshifts. For this energy range, the extra-galactic soft photon spectrum must be estimated at optical wave-

---

<sup>7</sup>Defined as the energy at which  $\tau(E, z) = 1$  and the spectrum falls to  $1/e$  of its intrinsic value.

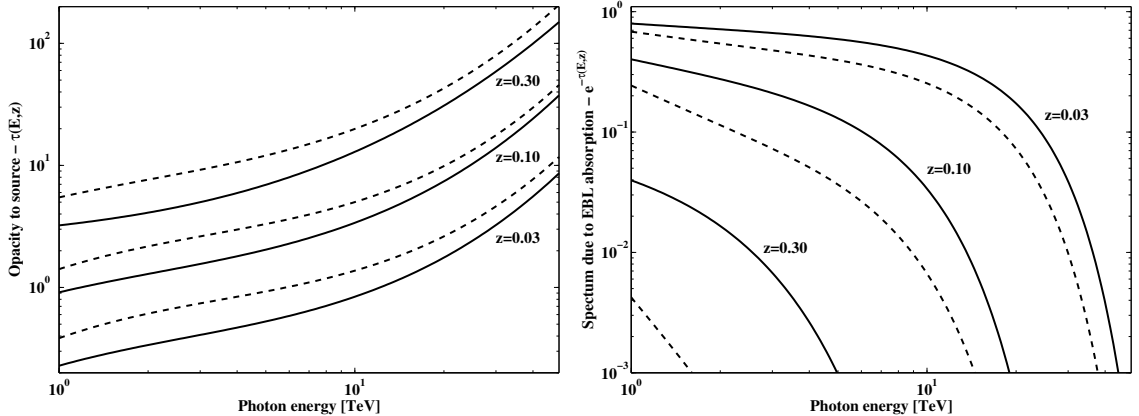


**Figure 2.1:** (Left) Optical path length,  $\tau(E, z)$ , for HE  $\gamma$ -rays from extra-galactic sources at  $z = 0.03$ ,  $z = 0.10$  and  $z = 0.30$  from Stecker and de Jager (1998). (Right) Cut-off in  $\gamma$ -ray spectrum due to absorption,  $\exp\{-\tau(E, z)\}$ . In each case, two curves are shown, corresponding to the two the IIRF models used by Stecker and de Jager (1998).

lengths, where the major contribution comes from starlight. Salamon and Stecker (1998) presented a calculation of this function, and its implication for a number of EGRET blazars. They did not present a parameterized form of the function, which could be plotted here. Qualitatively, the results are similar to the TeV case: the opacity increases with energy and redshift. For a source at  $z = 1$  the opacity increases from  $< 10^{-2}$  at 20 GeV to  $\geq 8$  at 500 GeV. For the EGRET source 3C279 ( $z = 0.54$ ) a spectral cut-off is predicted at  $\sim 90$  GeV; for B1633+382 ( $z = 1.81$ ) it is at  $\sim 25$  GeV.

## 2.2 Pulsars

The second largest category of identified MeV  $\gamma$ -ray point sources is pulsars. The 3EG catalog lists five associations between pulsars and EGRET point sources: Crab, Vela, Geminga, PSR B1706–44 and PSR B1055–52 (Nolan et al., 1996). Kaspi et al. (2000) report evidence of pulsations from PSR B1046–58 (3EG J1048–5840) at the  $3.1\sigma$  level. PSR B1951+32, was identified as a pulsar in EGRET data (Ramana-murthy et al., 1996), although it does not appear in the 3EG catalog<sup>8</sup> (it fell below

<sup>8</sup>The pulsar is depicted at the correct location in the map of sources, figure 4, in Hartman et al. (1999) while it is missing from figure 1.3 in chapter 1, which was generated directly from the electronic version of the 3EG catalog.

the  $5\sigma$  requirement for detection on the Galactic plane). Ramanamurthy et al. (1995) present results of pulsations from PSR B0656+14 at the  $3.6\sigma$  level, although again it is not a 3EG source. In an interesting analysis of a source that contains two possible candidates, Kuiper et al. (2000) show evidence for pulsations from PSR J0218+4232 at the  $3\text{--}4\sigma$  level which is coincident with 3EG J0222+4253, with sufficient  $\gamma$ -ray excess remaining to also accommodate the detection of the blazar 3C66A in that field. Halpern et al. (2001b) report observations of the region near 3EG J2227+6122 in x-ray, optical and radio and suggest an association with an x-ray/radio pulsar PSR J2229+6114. Lacking an appropriate ephemeris covering the EGRET observations, they were not able to perform a pulsed search at MeV energies – but, since no other x-ray counterpart is found to be consistent, they claim it is more conservative to accept the association than to reject it. Finally, PSR B1509–58 is also a  $\gamma$ -ray pulsar; pulsations have been detected at lower energies by the OSSE and BATSE experiments on CGRO but not by EGRET (Ulmer, 1994).

The unambiguous associations, listed above, were made by searching for significant pulsations in the  $\gamma$ -ray data, given a contemporaneous pulsar ephemeris (phase, frequency and frequency derivatives), usually determined from radio observations<sup>9</sup>. Additionally, blind searches for pulsations were performed for those sources with sufficient detected counts. The median number of counts detected from unidentified sources on the plane is  $\sim 400$ , insufficient for a blind search considering that the PSR B1046–58,  $3.1\sigma$  identification was made with  $\sim 350$  counts and a *known* pulsar ephemeris.

Since mid-1997, the sensitive Parkes Multibeam Survey (Manchester et al., 2001) has detected a large number of new radio pulsars at  $|b| < 6^\circ$ . Some of these have been shown to be coincident with unidentified EGRET sources (Manchester et al., 2002). Due to pulsar glitches, the ephemerides for these objects cannot, in general, be extrapolated back to the period of the EGRET observations and definitive associations cannot be made. Other pulsar associations for unidentified 3EG sources have

---

<sup>9</sup>Or from ROSAT x-ray observations in the case of the radio-quiet Geminga pulsar.

also been suggested (Roberts et al., 2002a; Braje et al., 2002; Roberts et al., 2001a; D’Amico et al., 2001). A recent paper by Torres et al. (2003) reviews the current status of pulsars coincident with EGRET sources.

The six identified pulsars listed as sources in the 3EG catalog are all located close to the Galactic plane, at  $|b| < 6^\circ$ . They have hard spectra, with mean  $\langle \Gamma \rangle = 1.89$ ; only the Crab has a  $\Gamma > 2.0$ . The sources are persistent over all viewing periods, and are consistent with having a constant flux, within the 10% systematic errors due to possible errors in the calibration of the instrument over the long duration of the mission. The mean variability index from Nolan et al. (2003) is  $\langle \delta \rangle = 0.11 \pm 0.02$  with  $\text{RMS}(\delta) < 0.07$ .

The power to produce emission from pulsars comes from the slowing of a spinning neutron star. Goldreich and Julian (1969) showed that if a spinning neutron star were to exist in a vacuum, a huge surface electric field would exist parallel to the magnetic field lines ejecting charged particles from the neutron star surface quickly forming a co-rotating plasma, called the magnetosphere, distributed to balance the electric and magnetic fields. Such a co-rotating plasma is not completely possible, however, since portions of the plasma, beyond what is known as the light-cylinder, would be forced to move faster than the speed of light. The field lines become open at this point and particles can be ejected from the magnetosphere. Under certain circumstances, charges cannot be easily replenished from the surface of the neutron star and the out-flow of particles from the system can lead to a deficit in the charge density in certain regions of the magnetosphere; just above the surface of the neutron star at the pole (the “polar cap”) and along the edge of the closed magnetosphere near to the light cylinder (the “outer gap”). In these regions, the electric field is not constrained by the plasma to be perpendicular to the magnetic field and particle acceleration can occur.

Two main models for high-energy  $\gamma$ -ray emission from pulsars have been proposed. Each predicts a different ratio for the populations of radio-loud to radio-quiet pulsars and different levels of emission in the VHE  $\gamma$ -ray regime. The models differ on where

the acceleration takes place, in the *polar cap* or the *outer gap*. Harding (2001) presents an overview of each model and gives references to detailed descriptions. These models fit the hard spectra for those pulsars detected by EGRET from radio through MeV energies, both for young pulsars (such as the Crab) and older pulsars with weaker magnetic fields (such as Vela). They can also account for radio-quiet pulsars such as Geminga.

In the *polar cap* model, the gap forms when the electric field is insufficient to overcome the potential that binds ions to the stellar surface – a low surface temperature also contributes (Ruderman and Sutherland, 1975). If the angular momentum and magnetic field are opposite at the pole, the magnetosphere in the region of the pole contains a positively charged plasma which cannot be replenished with ions from the surface, resulting in a gap. Accelerated particles interact through inverse Compton scattering with thermal x-rays from the surface of the neutron star and curvature radiation (CR) emitted as the charged particles follow the curved field lines. These IC up-scattered photons and CR give rise to particle/photon cascades through pair-production. As the cascade is accelerated further, the density of charged particles increases to the point that the electric field is screened, closing the gap. At this point, no further acceleration is possible. The huge magnetic field in the accelerating region allows single photon pair-production ( $\gamma \rightarrow e^\pm$ ) and photon splitting ( $\gamma \rightarrow 2\gamma$ ) that gives rise to a sharp, super-exponential, cut-off in the spectrum of  $\gamma$ -rays produced. The cut-off occurs at several GeV for most young pulsars and as high as 50 GeV for older pulsars with weaker field strengths. The  $\gamma$ -ray emission forms a beam that is largely coincident with the radio beam; this model does not predict the occurrence of large numbers of radio-quiet pulsars (such as Geminga). Accounting for the size of the beam and making assumptions about the population of pulsars in the Galaxy, the polar cap model predicts 19 radio-loud and 4 radio-quiet pulsars detectable by EGRET (Harding et al., 2003).

In the *outer gap* model, acceleration occurs in a charge depleted region much further from the surface of the neutron star, which cannot be replenished from the stellar surface. Pair-production in the gap must provide the current needed for acceleration.

In young pulsars the pairs are produced by interaction of CR from the accelerated particles and non-thermal synchrotron x-rays from the same pairs. In older pulsars, up-scattering of the flux of thermal x-rays from the hot surface of the neutron star is responsible for pair production. As in the polar cap model, at some point the electric field is screened by the pairs and acceleration stops. Since the magnetic field is orders of magnitude lower than the polar-cap region, single photon interactions are negligible and a slower cut-off in the primary  $\gamma$ -ray spectrum is predicted due to the upper limit in the accelerated particle spectrum. An additional, VHE ( $>100\text{ GeV}$ ) component is predicted from IC up-scattering of infra-red photons, even from pulsars with the highest magnetic fields. Recent predictions give a flux at VHE energies below the sensitivity of current ground-based detectors. The beam of MeV  $\gamma$ -rays is not coincident with the radio beam (which comes from the polar region) but is considerably larger in solid angle. In this model, it is possible for the observer's line-of-sight to intersect either or both (or neither, but that would be uninteresting) of these beams giving a larger population of radio-quiet  $\gamma$ -ray pulsars. Zhang et al. (2000) predict that, 10 radio-loud and 22 radio-quiet pulsars should be detectable by EGRET.

In summary, 6–10 pulsars have been associated with EGRET sources. Their source characteristics are steady (but pulsed) fluxes, flat spectra that steepen above 10 GeV and Galactic distributions. Pulsar models suggest that radio-quiet pulsars could account for a large fraction of the unidentified sources. VHE emission is expected from the outer gap model, but, given the parameters of the EGRET pulsars, the predicted flux is too low to detect at the sensitivity of current VHE observatories. However, this small sample of 100 MeV pulsars may not be typical and given the large uncertainties in pulsar mechanisms, VHE emission is probable at some level.

## 2.3 Supernova Remnants

The 3EG catalog lists a number of possible positional associations with known supernova remnants (SNR), such as IC443, W28, W44,  $\gamma$  Cygni, CTA1 and G347.3–0.5

(Esposito et al., 1996). Additionally, a number of suggestions for SNR associations with unidentified sources have since been made (Combi et al., 2001; Roberts et al., 2001b). Romero et al. (1999) present a list of 27 SNR coincident with 22 EGRET sources (some sources have more than one possible SNR candidate). However, there are no unambiguous identifications of SNR with any individual EGRET sources. Torres et al. (2003) present a recent review of supernova coincident with EGRET sources.

It has long been suspected that SNR could be the acceleration sites of cosmic rays (Ginzburg and Syrovatskii, 1964). The mechanism for producing these high energy particles is diffusive shock acceleration (DSA) of charged particles in the blastwave of the expanding remnant, which can allow acceleration of particles to energies of  $10^{14} - 10^{15}$  eV per nucleon. The flux of cosmic rays observed at the Earth is isotropic; the Galactic magnetic field ensures that no hint of the origin can be inferred from the direction of the particles themselves, except possibly for those of the highest energy. Production of high-energy  $\gamma$ -rays which is expected to accompany the acceleration could finally identify the sites and mechanisms responsible.

A typical supernova ejects a shell of mass  $\sim 1M_{\odot}$  into the interstellar medium (ISM) at speeds of  $\sim 10^4 \text{ km s}^{-1}$ , giving a kinetic energy budget of  $\sim 10^{51}$  erg to the ejecta. The shell moves through the ISM at speeds much greater than the local speed of sound ( $10\text{-}100 \text{ km s}^{-1}$ ), creating a strong shockwave, which sweeps the interstellar material with it. After a relatively short period (typically few hundred years) of uniform expansion, the mass of material swept up becomes comparable to that of the original ejected shell. The blastwave then enters the so-called Sedov-phase, in which radiative losses are small in comparison to the internal energy of the shock, and starts to slow and cool over timescales of  $\sim 10^4$  yr. When the shock reaches speeds of  $\sim 200 \text{ km s}^{-1}$ , radiative processes quickly cool the shell which eventually falls to the density of the ISM and loses its identity (Woltjer, 1972). It is during the Sedov phase that conditions in the shock are correct for particle acceleration to occur. The Green Catalog of SNR (Green, 2001) contains a total of  $\sim 230$  identified SNR, detected through radio and x-ray observations. They generally lie along the plane, but some, such as SN 1006, lie at latitudes up to  $b = 15^\circ$ .

The theory of diffuse shock acceleration seems to have been independently arrived at by Krymskii (1977), Axford et al. (1977), Bell (1978) and Blandford and Ostriker (1978), although the idea was around in less developed forms for some time before that (Fermi, 1949). Drury (1983) presents a review of the process. Charged particles in the plasma on both sides of the shock front are constrained to move along the magnetic field lines and can scatter isotropically from irregularities in the magnetic field. If they are injected into the region of the shock with sufficient velocity such that there is negligible interaction with the shock front, they can be repeatedly scattered across the shock front between the up-stream and down-stream regions. Since an isotropic distribution in one region appears to be relativistically beamed to an observer co-moving with the plasma in the other region, the particle gains energy when it is scattered isotropically in the second region after crossing the shock. The particle gains energy exponentially on each crossing. There is a small probability on each crossing into the downstream region that the particle will not re-cross, since the shock front is advancing through space. The probability of a particle crossing the shock more than  $n$  times falls exponentially with  $n$ . These two exponential relations give rise to the power-law energy distribution that is characteristic of shock acceleration. DSA models have evolved to accommodate spherical shock fronts, various injection models, magnetic field configurations and to account for the reaction of the accelerated particles on the development of the shock.

Accelerated protons are expected to produce a  $\gamma$ -ray signal through intermediate pion production and decay  $p + p \rightarrow \pi^0 \rightarrow 2\gamma$  (Drury et al., 1994). Emission from  $\pi^0$  decay is expected to peak soon after the beginning of the Sedov phase and stays largely constant until the radiative phase dissipates the energy of the shock material. It is expected that in regions where the SNR shock interacts with a medium of higher density than the ISM, such as large, dense molecular clouds, the  $\pi^0$  flux will be enhanced. The spectrum of  $\gamma$ -rays extends from 100 MeV to 10 TeV. Drury et al. (1994) predict that  $\gamma$ -ray emission should be clearly detectable by ground-based instruments at TeV energies. There have been two suggestions, that  $\pi^0$  decay has been seen at TeV energies. Enomoto et al. (2002b) suggest that the broadband spectrum of emission from

the SNR RX J1713.7–3946, including observations at TeV energies by the CANGAROO instrument, is best fitted by a pion spectrum, although the result is controversial (Reimer and Pohl, 2002; Butt et al., 2002). Aharonian et al. (2001) present evidence of a  $\pi^0$  spectrum from observations of the SNR Cassiopeia A, although the spectrum is consistent with an electron induced spectrum at a 15% level.

In addition to  $\gamma$ -ray production through proton interactions, electrons accelerated in the shock are responsible for non-thermal emission, through bremsstrahlung, inverse-Compton up-scattering of the cosmic microwave background, local infra-red/optical photons or radiation from the SNR itself and through synchrotron emission in the magnetic field of the SNR. These processes are generally considered to be responsible for the radio and x-ray emission from shell type supernova remnants. As mentioned above, it can also explain  $\gamma$ -ray emission in the MeV and TeV ranges for some SNR. It is widely believed that the bulk of cosmic radiation below  $10^{14}$  eV originates in supernova remnants in the Galaxy. It would be unexpected if such sources were not apparent as major components of the VHE  $\gamma$ -ray sky. There are major uncertainties in these sources (apart from the total energetics) so that the unidentified EGRET sources may be important pointers to the exact locations of the acceleration sites.

## 2.4 Pulsar Wind Nebulae

Of the > 200 SNR in Green (2001), approximately ten belong to an anomalous class of remnant called Pulsar Wind Nebulae (PWN), and often referred to as *plerions* or *Crab-like* SNR (see Chevalier, 2000). While typical SNR are characterized by a shell-type structure with a steep spectrum of non-thermal radio emission and a shell of x-ray emission, PWN emission is dominated by a central core nebula, with strong non-thermal optical and x-ray emission and a harder radio spectrum. The x-ray and radio emission from the core region is the result of synchrotron radiation from very energetic electrons in the strong magnetic fields that thread the nebula. The short synchrotron cooling time of these electrons requires that the nebula be resupplied by the energetic particles being ejected from the pulsar. The PWN morphology is

complex, with glowing filamentary structures where synchrotron emission is enhanced and cooler outer regions which show evidence of emission lines.  $\gamma$ -ray emission from the synchrotron nebula can occur through inverse-Compton up-scattering of the synchrotron photons (up to TeV energies) by high-energy electrons.  $\gamma$ -ray emission in the MeV range can also result for shock-acceleration of the electron population to higher energies. Roberts et al. (2002b) discuss PWN candidates at MeV energies and possible emission mechanisms. It is unlikely that PWN account for a large number of the unidentified 3EG sources, since so few have been found in the Galaxy; the discovery of a new PWN at VHE energies would be an important first.

## 2.5 Other source associations at low Galactic latitudes

Grenier (2002) and Romero et al. (1999) discuss other possible Galactic sources for unidentified EGRET sources. Some of the possibilities are summarized briefly below.

### 2.5.1 Massive Stars

Particle acceleration through diffusive shock acceleration occurs at the terminal shocks around all stars, including the Sun. Massive stars are expected to accelerate particles to energies at which they could up-scatter the UV radiation from the star to  $\gamma$ -ray energies. None of the many O-type<sup>10</sup> stars in our neighborhood have been observed by EGRET. Binary systems with a massive stars would provide stronger shocks and a larger target of UV radiation. Wolf-Rayet (WR) star systems, with a massive O-type star and companion, where the companion has stripped the star's outer layers are also possibilities. The WR+O system Cyg OB2 No.5 has been suggested as a candidate for 3EG J2022+4317 (Benaglia et al., 2001), a source observed in this TeV survey. Romero et al. (1999) present eleven WR stars which have positional coincidence with six 3EG sources and six Of-type stars coincident with four 3EG sources. As yet, there are no detailed models of VHE emission from massive stars.

---

<sup>10</sup>Stars are classified by their spectral characteristics into classes that reflect their surface temperatures. From hottest (blue) to coolest (red) the sequence goes O-B-A-F-G-K-M.

### 2.5.2 OB Associations

OB associations are collections of massive O- and B-type stars which are the sites of star formation. OB associations have a larger density of pulsars and SNR than the rest of the Galaxy<sup>11</sup>. The strong interstellar winds from the massive O-type stars, possible SNR shock fronts, pulsar winds and massive molecular clouds make OB associations good candidates for  $\gamma$ -ray production (Kaaret and Cottam, 1996). Romero et al. (1999) detail 22 unidentified 3EG sources that have positional coincidences with known OB associations.

### 2.5.3 Gould Belt

The Gould Belt is a local collection of star forming regions (OB associations). The origin of the Gould Belt is not completely understood. It is known that it is a relatively young structure at 30 Myr, which our solar system (age 5 Gyr) happens to be “passing through” – the speed of the solar system in the Galaxy is larger than the average Gould Belt speed, so eventually we will pass beyond the Belt. The Belt was first identified in the mid 1800s, when it was noticed that the bright stars tend to trace a plane inclined to  $20^\circ$  to the Galactic plane. The plane is roughly elliptical in shape with dimensions of  $1000\text{ pc} \times 600\text{ pc}$ . The solar system is  $\sim 150\text{ pc}$  from the center (LeDrew, 1999). The Belt was mapped by Stothers and Frogel (1974), who noted that the density of massive O-type to B2-type stars, within 400 pc, is three times larger in the Belt than in the Galactic plane.

Diffuse  $\gamma$ -ray emission associated with the Gould Belt was first recognised in data from the SAS-2 experiment, in the region of the Galactic anti-center where the Belt lies furthest from the plane (Thompson et al., 1977). More recently, it has been shown that the distributions of all steady, unidentified 3EG sources are best fitted by a combination of three population classes. In addition to the Galactic plane and extra-galactic populations, Gehrels et al. (2000) suggest there is a population

---

<sup>11</sup>In an instance of humorous astrophysical nomenclature, SNR embedded in OB associations are often referred to as SNOBs.

correlated with the Gould Belt, 47 unidentified sources are possibly associated with this population. Nolan et al. (2003) give the mean variability index for the 33 possible Gould Belt sources at  $|b| > 5^\circ$  as  $\langle \delta \rangle = 0.49$ , which they refer to as a “moderately low value”, inconsistent with a purely pulsar population. Not enough is known about these OB sources to make any predictions of VHE emission.

#### 2.5.4 X-ray binaries and micro-quasars

High mass x-ray binaries, consisting of a pulsar and large companion star, can accelerate electrons to TeV energies, resulting in x-ray synchrotron emission and possibly  $\gamma$ -rays up to TeV energies through inverse-Compton up-scattering. Kirk et al. (1999) suggest that TeV  $\gamma$ -ray emission could be present in the PSR B1259–63 system. Kaaret et al. (2000) suggest that 3EG J0634+0521, a source considered in this TeV study, is associated with the source SAX J0635+0533, a system containing a 33 ms x-ray selected pulsar and a large B-type star.

Kniffen et al. (1997) suggest that the *second* EGRET catalog source 2EG J0241+6119 is associated with the x-ray binary source LSI+61°303. This source is remarkable for its periodic radio outbursts, on average every 26.5 days, due to the orbital motion, with a possible modulation every 4.4 yr (Gregory, 2002). The third EGRET catalog source, 3EG J0241+6103 (also in this study) is displaced from the x-ray source to the extent that the association is barely possible at the 95% confidence level.

At TeV energies, Cen X-3 has been recently reported as a  $\gamma$ -ray source at the  $> 6\sigma$  level (Chadwick et al., 1998a). A tentative signal was reported by the HEGRA group from the micro-quasar GRS 1915+105 (Aharonian et al., 1996). Although these claims have not been confirmed, they give credence to the possibility that these classes of source are emitters of VHE  $\gamma$ -rays.

### 2.6 Possible extra-galactic associations

Torres (2003) give a review of possible extragalactic  $\gamma$ -ray sources. Some possible

source types are summarized below.

### 2.6.1 Galaxy Clusters

Recently, Kawasaki and Totani (2002) have suggested that galaxy clusters could be candidates for unidentified EGRET sources at high latitude. Preliminary evidence was presented by Colafrancesco (2001) which suggests that there is a statistical correlation between the 3EG sources at high latitude and the clusters from the Abell catalog of clusters (Abell et al., 1989) at the  $\sim 3\sigma$  level. Scharf and Mukherjee (2002) report a correlation, also at a  $\sim 3\sigma$  level, between the EGRET sky-map of raw photons (they considered only those with  $|b| > 45^\circ$ ) and the Abell catalog. Reimer et al. (2003) stacked (summed) the EGRET excess photon maps for the regions around 58 of the most prominent clusters to form one single map for the population of clusters, which reveals no evidence for emission. They conclude that the Colafrancesco (2001) and Kawasaki and Totani (2002) analysis were likely to explained by systematics and that their analysis must be reconciled with the analysis by Scharf and Mukherjee (2002). The potential for VHE emission from such sources is unclear, but they would certainly be steady sources.

### 2.6.2 Starburst Galaxies

Starburst galaxies are characterized by a significantly enhanced rate of star formation, and hence are rich in supernova explosions, when compared to a normal galaxy such as the Milky Way. As a consequence they are expected to have a high density of cosmic-rays, larger by a factor of two orders of magnitude than the CR density of our galaxy (see Völk, 2003). Consequently, significant  $\gamma$ -ray emission is predicted in the VHE regime. EGRET did not detect any starburst galaxies, but set upper limits on emission on a number of them (Blom et al., 1999). OSSE marginally detected weak emission from NGC 253 (Bhattacharya et al., 1994), a starburst galaxy that has subsequently been shown to emit VHE  $\gamma$ -rays by the CANGAROO collaboration (Itoh et al., 2003). Starburst galaxies are considered as strong candidates for VHE

emission, but, because of their proximity and prominence at other wavelengths, it is unlikely that they could be associated with the unidentified sources.

### 2.6.3 Radio Galaxies

Centaurus A, a radio galaxy at  $z = 0.0018$ , appears in the 3EG catalog as a source. Its flux is listed as  $(13.6 \pm 2.5) \times 10^{-8} \text{ cm}^{-2}\text{s}^{-1}$ , which implies a luminosity of  $\sim 10^{41} \text{ erg s}^{-1}$ , five orders of magnitude lower than the detected blazars. Additionally, Cen A was reported as a VHE source at a  $4.6\sigma$  level by Grindlay et al. (1975). This early report, which predates development of the imaging technique, was made at a time of enhanced emission from Cen A at all wavelengths. No further VHE observations have been made during such an active state, and it is difficult to evaluate the claim (see for example Carramiñana et al., 1990).

Although the population of known radio galaxies is  $\sim 1000$  times larger than that of blazars, the smaller flux, if it is typical of radio galaxies, explains why Cen A is the only radio galaxy in the 3EG catalog; further objects likely have fluxes below the sensitivity of EGRET. Having said that, two other radio galaxies have been suggested as associations for 3EG sources: Mukherjee et al. (2002) suggest that NGC 6251 as a counterpart for 3EG 1621+8203 and Combi et al. (2003) report the discovery of a radio galaxy in the error box of 3EG J1735–1500. At TeV energies, the HEGRA collaboration have recently reported the discovery of M87 at a  $> 4\sigma$  level (Aharonian et al., 2003).

## 2.7 Potential of VHE emission from unidentified 3EG sources

In light of these source classifications, it is possible to make some predictions about the potential of detecting VHE emission from the unidentified EGRET sources.

At low Galactic latitudes, it is likely that a large number of the persistent, non-variable sources are radio-quiet pulsars. The outer-gap model of emission, which

favors a high number of radio-quiet pulsars, suggests that VHE  $\gamma$ -ray emission should take place, but the parameters of the known pulsars place the level of emission below the sensitivity of current IACTs, at least for the amount of observation time that can be devoted to a single source in a survey (typically 5-10 hours). To date, VHE emission has not been seen from the known isolated pulsars. Of course, if a new class of pulsar lies undetected in the population of Galactic EGRET sources, such as was the case with Geminga, then a portion of model phase space could be opened up which would allow for VHE emission.

The most likely Galactic sources of VHE  $\gamma$ -rays, at least on the basis of the known VHE sources, are PWN and supernovae. Three PWN have been detected, they are expected to be persistent and non-variable. Since a relatively small number of PWNs have been identified in x-ray and radio observations, it seems unlikely that they are associated with a large number of the EGRET sources. Shell-type supernova have been identified in the fields of many EGRET sources, and have also been detected by ground-based instruments. The detection of RX J1713.7–3946 at a significant level took a 45 hr. observation with the CANGAROO telescope, (Muraishi et al., 2000), SN1006 was detected with 28 hrs. of data (Tanimori et al., 1998) and Cas A in 232 hrs. of observations with the HEGRA IACT array (Aharonian et al., 2001). These particular sources would not be detectable at a significant level in a survey observation, but there could be other stronger sources not yet identified as PWN.

Recently, the HEGRA group detected the first unidentified VHE source, in the Cygnus region of the sky (Aharonian et al., 2002a). Again, the discovery was made on the basis of a deep observation: 113 hrs. The source has been associated with an OB association in Cygnus (Butt et al., 2003), although other identifications have also been suggested (Mukherjee et al., 2003). This association is intriguing: OB associations have not generally been targeted for HE or VHE emission and their complex morphology suggests that there may be large differences between the VHE emission from one to another, depending on the density and distribution of SNR, large stars and stellar winds they contain. Romero et al. (1999) have listed 22 unidentified 3EG sources that have positional coincidences with known OB associations. Potentially,

some of these may be VHE  $\gamma$ -ray emitters.

Of the variable and non-persistent Galactic sources, high mass x-ray binaries (HMXB) and micro-quasars may be VHE  $\gamma$ -ray sources and several models have been proposed predicting such emission. Indeed, Cen X-3 has been claimed as a VHE source from observations with the Durham Mark 6 telescope (Chadwick et al., 1998b). The VHE signal was consistent with being non-variable (but based on only 10 hrs of observations), in contrast to the EGRET counterpart which was seen to vary significantly in intensity. Taken at face value, this result indicates that HMXBs may be candidates for detection in the survey, but the result has not yet been confirmed. The negative results from ground-based surveys of binary systems, such as Hall et al. (2003a), does not support the earlier optimism that binaries might be an important class of VHE sources.

At all Galactic latitudes, blazars are expected to make up some fraction of the unidentified sources. The EGRET blazar catalog overlaps somewhat with the VHE BL Lacs. No FSRQ, which make up the majority of the EGRET blazars, has been seen in the VHE regime. Of the EGRET BL Lacs, it has been the weaker sources which have been those that are visible to ground-based instruments. Given the extreme spectral and flux variability inherent in that these sources, it is possible that a EGRET blazar may be visible at TeV energies during a flaring episode. Of course, catching a blazar in an extreme flaring episode is unusual without regular monitoring of the source. The data for this survey were not analyzed for flaring during the period of observations, and hence follow-up observations were not made if flaring was present. In addition, BL Lacs at redshifts greater than 0.129 have not been detected at VHE energies, with the exception of 3C66A which some have regarded as spurious.

In summary, on the basis of the known source types, the motivation for the discovery of VHE  $\gamma$ -rays from unidentified EGRET sources is largely exploratory. The unidentified sources have remained largely mysterious since their discovery. The story of the first unidentified source, Geminga, illustrates that new and unexpected source classes may be represented in the 3EG catalog and perhaps in the VHE sky. These

will only be identified by observation in different energy regimes. At very least, the 3EG catalog presents a list of sources which have emission closest in energy to the VHE regime. Unlike radio and x-ray selected sources, they are not too numerous, and present a manageable starting point for VHE observations.

### 3. GROUND-BASED GAMMMA-RAY DETECTION

#### 3.1 Extensive Air-Shower

Discovered in 1938 by Pierre Auger, Extensive Air-Showers (E.A.S.) are cascades of high energy photons, electrons and positrons initiated by cosmic-rays or  $\gamma$ -rays interacting in the upper atmosphere. Typically, the primary particle interacts at an altitude between 15 – 30 km producing secondary particles which continue to interact in the increasingly dense atmosphere through bremsstrahlung and pair-production, producing a cascade of particles in the atmosphere. The number of particles in the cascade continues to increase until their average energy reaches a critical value, at which ionization becomes the dominant interaction mode ( $\sim 100$  MeV in air); the cascade subsequently dies rapidly. The point in the development of the cascade at which ionization becomes dominant at which the number of charged particles in the shower is greatest is referred to as “shower maximum”. In general, very energetic primaries produce showers with larger numbers of secondary particles and the shower maximum occurs deeper into the atmosphere. For primaries with sufficiently large energy the cascade can reach ground level before the critical energy is reached and the shower can be detected directly using charged-particle detectors, such as scintillators, at ground level. Placing these detectors on the highest mountains lowers the energy a primary must have to be detected. Showers from lower energy primaries typically die out completely before they reach ground level, and hence are impossible to detect directly from the ground. Figure 3.1 shows the profile in the atmosphere of the charged particles in two  $\gamma$ -ray-induced air-showers. The first, initiated by a 100 GeV photon, dies out before it reaches ground level. Charged particles from the second, induced by a 1 TeV photon, reach ground level in an area of diameter  $\sim 200$  m. It was the coincidental detection of charged particles at two locations, separated by such large distances on the ground, that led Auger to the discovery of E.A.S. Modern instruments for detecting these cascades directly on the ground consist of arrays of

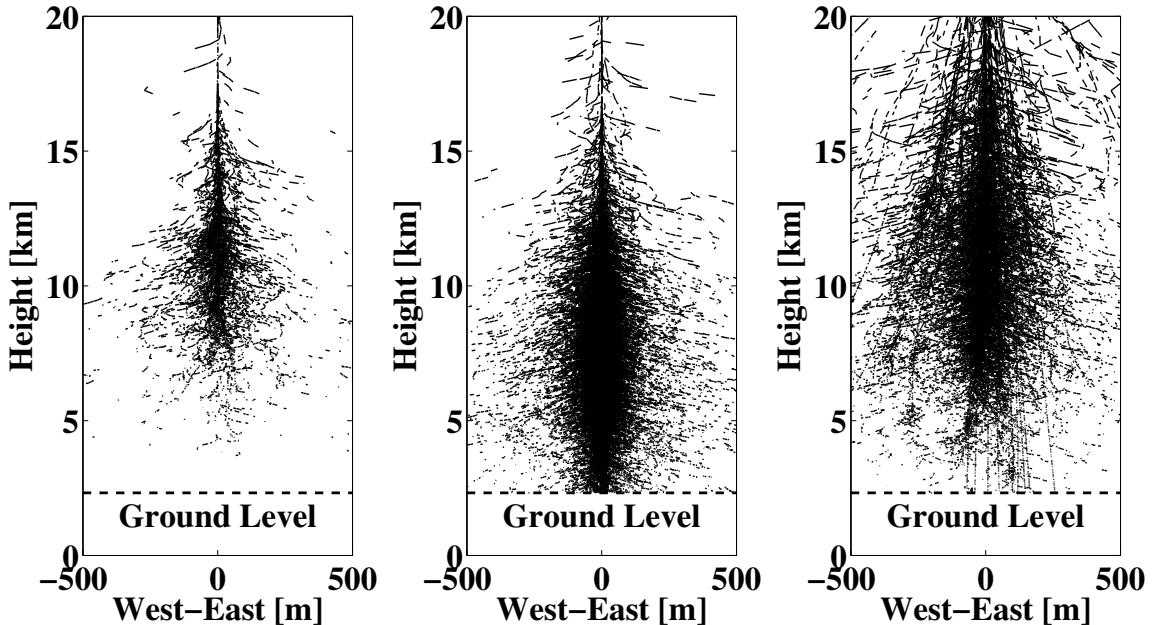


Figure 3.1: Simulated charged particle tracks in the atmosphere produced by a 100 GeV  $\gamma$ -ray (left) and a 1 TeV  $\gamma$ -ray (middle) and 1 TeV proton (right). The horizontal and vertical scales are not equal on this plot. Ground level is set for Mt. Hopkins at 2320 m A.S.L.

charged particle detectors covering a large ground region. One such example is the Pierre Auger Observatory being built in Argentina which will consist of 1600 water Čerenkov detectors distributed over an area of 3,000 km<sup>2</sup> (The Auger collaboration, 1996).

In addition to the electromagnetic component of E.A.S. discussed above, showers initiated by cosmic-rays are dominated by a hadronic component produced during the initial strong interactions in the upper atmosphere. These interactions are violent and unpredictable but the most important end products are neutral and charged pions which decay to a pair of  $\gamma$ -rays or a muon/muon-neutrino pair depending on the charge of the pion. The  $\gamma$ -ray pairs result in electromagnetic cascades as described above. The muons, which were identified as a mysterious “penetrating radiation” by early cosmic ray researchers, reach the ground with little further interaction. Since muons take a considerable amount of the energy of the primary, air-showers produced by hadronic primaries are typically smaller than those produced by a  $\gamma$ -ray of the same

energy. Finally, since the initial strong interactions tend to impart a larger transverse momentum to the secondaries, a hadronic air-shower will typically be broader than a  $\gamma$ -ray induced shower, consisting of overlapping cascades produced by different  $\pi^0$  particles which were initially had slightly different directions of propagation. Figure 3.1 illustrates the distribution of charged particles in a shower produced by a 1 TeV proton. Several muons are visible as straight particle tracks reaching ground level.

## 3.2 Imaging atmospheric Čerenkov technique

A third component of all E.A.S. is Čerenkov radiation (Jelley, 1958), produced as the charged particles in the shower ( $e^\pm$  and  $\mu^\pm$ ) traverse the atmosphere at speeds in excess of the speed of light in air. Čerenkov radiation was first noticed in the early 1900s by the Curies but remained largely a mystery until the 1930s when it was investigated in a series of experiments which exposed very pure liquids to  $\beta$ -radiation (Čerenkov, 1934). The phenomenon was later explained classically as the coherent reinforcement of radiation emitted as the charged particle displaces electrons in the dielectric medium through which it passes (Frank and Tamm, 1937), work for which the three were awarded Nobel prizes in 1958. In a tenuous gas medium such as air, where  $n \approx 1 - \alpha\rho$  (with  $\alpha \ll 1$ ) describes the weak dependence of the index of refraction on the density of the medium, the Čerenkov threshold, characteristic angle and intensity of radiated per unit length of the particle track (Jackson, 1975) may be written

$$\begin{aligned} E_t &\propto \rho^{-1/2} \quad 100 - 20 \text{ MeV for } e^- \text{ between 25km and sea-level} \\ \theta &\propto \rho^{1/2} \quad 0.3 - 1.4^\circ \\ I(\omega) &\propto \rho \quad 2 - 30 \text{ photon m}^{-1} \end{aligned}$$

The profile of Čerenkov light emitted from a very energetic muon traveling vertically through the atmosphere is illustrated in figure 3.2. The effect of the changing atmospheric density along the path of the muon and the resultant change in the Čerenkov emission angle causes a focusing of the Čerenkov light on the ground and an enhance-

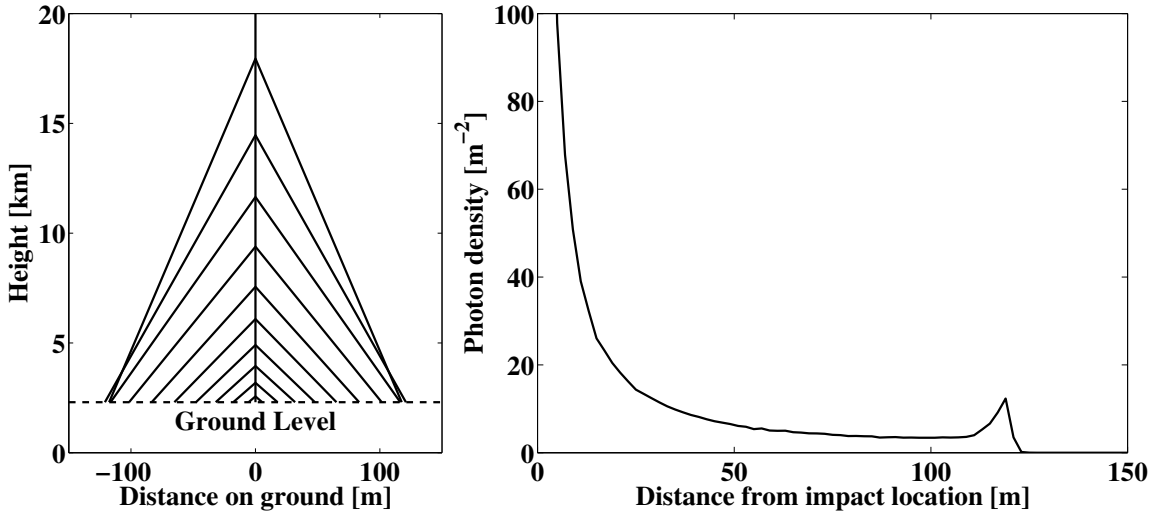


**Figure 3.2:** Left: Illustration of Čerenkov emission from vertically moving muon. Right: Radial density on the ground of Čerenkov photons with  $200 \text{ nm} < \lambda < 700 \text{ nm}$ , showing enhancement at 120 m due to focusing effect of the increasing atmospheric density. Since the intensity of emitted photons is essentially constant as the muon reaches the ground, the radial density diverges like  $1/r$ , as  $r \rightarrow 0$ .

ment of the photon density at distances of  $\sim 120$  m from the muon impact location on the ground. The photons that strike the ground at distances of  $< 30$  m are due to emission from the region of the atmosphere close to ground level. The photon density in this region tends to infinity as  $1/r$  reflecting the essentially constant emission intensity close to the ground level. Since the atmosphere is a strong absorber of light in the U.V. region, such “local” photons tend to have a spectrum with an enhanced U.V. component with respect to emission from higher in the atmosphere. The power of the atmospheric Čerenkov technique is that a sufficiently large and sensitive detector can be placed anywhere in the  $45,000 \text{ m}^2$  light pool to detect the particle.

The profile of Čerenkov light from purely electromagnetic air showers has features similar to the single particle light profile described above. In general, the transverse momentum (with respect to the original primary) imparted to the shower particles is small and the Čerenkov light pool covers approximately the same area as above. The enhancement at 120 m is also prominent since a considerable amount of emission comes from the  $10 - 15$  km region of the atmosphere (see figure 3.2). At distances

greater than 120 m from the shower core, the fall-off in Čerenkov density is slower than single particle case due to multiple Coulomb scattering in the shower. The Čerenkov density typically increases with the energy of the primary as the number of charged particles in the shower core increases and the development of the shower occurs deeper into the atmosphere where the density is higher. In addition, the locally generated Čerenkov component becomes more significant for larger showers; a typical 100 GeV shower, which does not extend to ground level, will have no local light.

The distribution of Čerenkov light from hadronically induced showers is quite different from the electromagnetically induced case above. In general, a number of muons will be present in the shower which give rise to considerable local light distributed around their ground impact locations. Additionally, hadronic showers usually have a number of EM cascades resulting from decay of different  $\pi^0$  particles which can have considerable transverse momenta. The Čerenkov light produced by these photons gives rise to clumps in the distribution on the ground. In some small fraction of cases most of the energy of the primary can go to a single  $\pi^0$  and an essentially electromagnetic shower can arise with properties almost identical to  $\gamma$ -ray-induced showers. Finally, in the hadronic case, there tends to be a large variance in the profile of showers triggered by identical primaries, due to the initial strong force interactions.

The detection of Čerenkov light from air-showers was pioneered by Galbraith and Jelley (1953, 1955) using a ten inch mirror with photomultiplier tube at its focus. Since these early experiments, the desire to discriminate  $\gamma$ -ray-induced air-showers from the overwhelming background of hadronic showers has largely driven the design of atmospheric Čerenkov instruments. The development of the imaging technique by the Whipple collaboration yielded the first detection of very high energy  $\gamma$ -ray emission from an astronomical source (Weekes et al., 1989). The essence of the imaging technique is to take a snapshot of the Čerenkov flash associated with the air-shower using a high resolution camera system consisting of an array of close packed photo-tubes mounted at the focus of a large telescope, fast triggering and readout electronics to digitize the  $\sim 10$  ns signals and a data acquisition system capable of

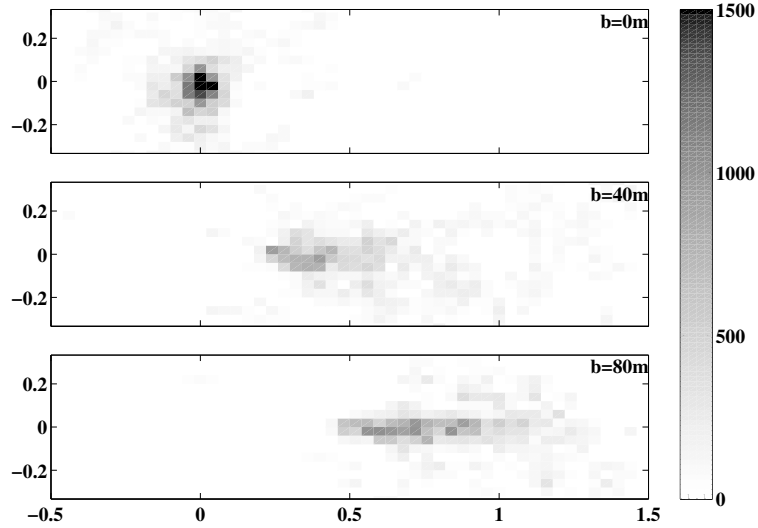


**Figure 3.3:** Density of photons per unit mirror area in the focal plane of an ideal 10 m telescope for a simulated 350 GeV photon induced shower, in units of  $\text{m}^{-2} \text{deg}^{-2}$ . The same shower is shown for three different impact parameters: 0 m, 40 m and 80 m. The axes gives the angular distance in the focal plane from the direction of the primary (which is assumed to be coincident with the center of the camera) in degrees.

recording the data with a minimum of dead time.

In the focal plane of such an instrument, the image traces the development of the shower in the sky. For an EM induced shower the image is largely symmetric around the projection of the shower axis onto the field of view of the instrument, reflecting the symmetry of the shower itself around the axis. The images of EM showers are often described as “cometary”; one side of the shower, in the direction of towards the early stages of the shower development (i.e. towards the upper atmosphere) has a higher photon density. As the shower dies after shower maximum, the image becomes more diffuse with a lower photon density, spread out over a larger area of the image. Higher energy showers produce more secondaries, more Čerenkov photons and extend further into the atmosphere, resulting in an image which has a larger photon density and a larger extent in the field of view. Finally the appearance of the shower in the field of view is dependent to a large extent on the distance between the shower axis and the instrument, usually called the *impact parameter* and denoted as  $b$ . Figure 3.3

illustrates an image of a 350 GeV  $\gamma$ -ray shower viewed at three different impact parameters. The showers become elongated and displaced from the center of the camera as the impact parameter increases. Images of proton induced showers are less compact than  $\gamma$ -ray showers, due largely to the higher transverse momentum imparted by the strong interactions. Data selection criteria, based on these differences, capable of keeping a large fraction of the  $\gamma$ -ray events while discarding the majority of the background cosmic-ray events are described in chapter 4.

### 3.3 Trigger and acquisition electronics

Readout of the 379 channel camera is initiated by a two-level trigger system. At the lowest level (L-1), each of the inner 331 channels are monitored by a constant fraction discriminator (CFD), which triggers when the signal exceeds a pre-programmed level. For a constant pulse profile, the CFD compensates for the time jitter intrinsic to a standard discriminator (i.e. simple voltage comparator), which triggers earlier, relative to the peak in the pulse profile, for signals with large amplitude. The digital outputs of these CFDs are then processed by the second level of trigger (L-2), an electronic system referred to as the *pattern selection trigger* or PST<sup>12</sup>, which is essentially a memory lookup table that can be programmed to discriminate images with two, three or four adjacent channels from those where the triggering channels are non-adjacent. This trigger design, which preferentially records images of compact  $\gamma$ -ray and hadronic showers over the random fluctuations of the night-sky background, is described in detail in Bradbury et al. (1999). In general it is desirable to set the discriminator threshold as low as possible, allowing lower energy events to be recorded. At low trigger levels, the night-sky background light causes an excessive event rate, even with the PST. The trigger is set to ensure that the event rate is below the maximum sustainable rate of the data acquisition system,  $\sim 35$  Hz, even when observing the brightest fields of view. Figure 3.4 shows the trigger rate vs. trigger threshold, as

---

<sup>12</sup>Actually, there are two separate electronic systems involved in the L-2 trigger. The second system, called the multiplicity trigger, has very little time jitter in comparison to the PST, and is used only to set the timing of the L-2 output.

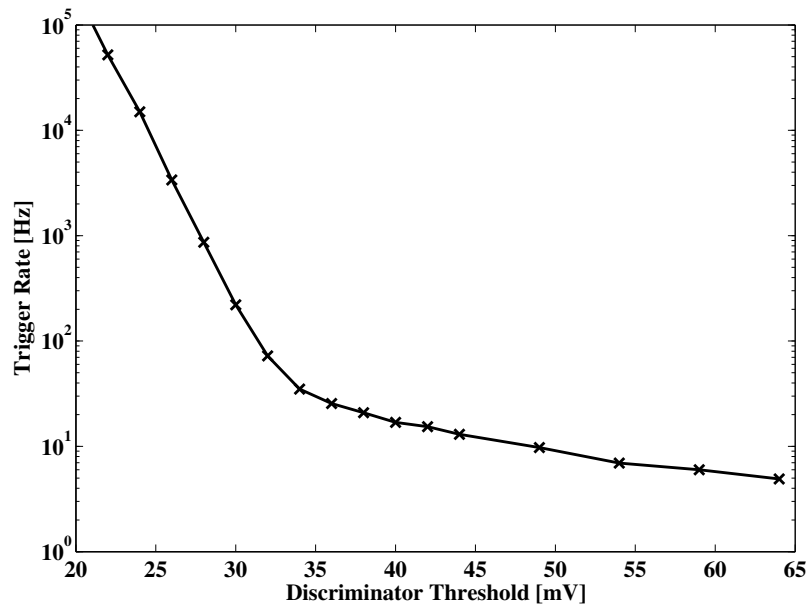


Figure 3.4: Event rate vs. L-1 trigger threshold with a trigger L-2 requirement (pattern selection trigger) of three adjacent channels exceeding the threshold within the coincidence time. This kind of plot is usually referred to as a “bias curve”.

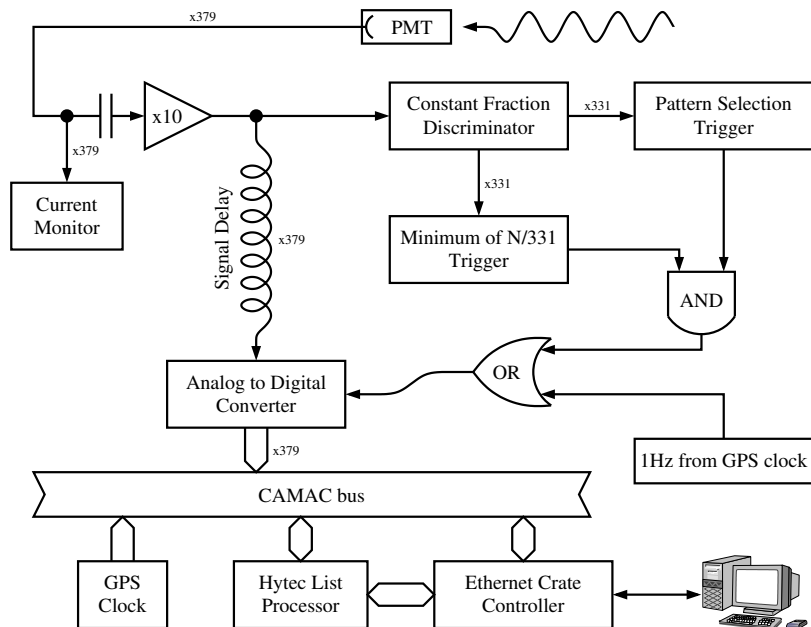


Figure 3.5: Schematic of the major components of the data acquisition system. See text for discussion.

measured in late 2001. At high thresholds, the rate is dominated by the power-law cosmic-ray spectrum; below approximately 35 mV the rate curve becomes very steep, due to random triggers by night-sky noise. A setting of  $\sim 38$  Hz would result in a relatively stable rate, even under the brightest of conditions.

A schematic of the main components of the data acquisition system is shown in figure 3.5. The signal from each channel, after  $\times 10$  amplification, is digitized by a set of LeCroy 2249A 0.25 pC/count charge-to-digital converters (QADC). Conversion is initiated by the L2 trigger; in order to allow for the trigger decision to be formed, the signals are delayed in a length of RG-58 cable, allowing the trigger decision and signals from the PMTs to reach the ADCs coincidentally. The integration time of  $\sim 20$  ns is longer than the intrinsic duration of the Čerenkov flash on the ground, in order to account for the time-spread introduced by the spherical mirror (see figure 1.5) and dispersion in the delay cables. As a consequence, more night-sky noise is integrated in the signal that would otherwise be the case. Future experiments will minimize this noise by having mirrors with longer focal lengths (hence smaller time-spreads) and by eliminating the need for long signal delay cables using electronic delay systems. One approach to the latter is to continually sample the signal with flash ADCs, storing the digitized information in a temporary RAM buffer which can then be read out when the trigger decision is made.

The signal is AC coupled at the input of the amplifier to remove any bias current through the tube, due mainly to the night-sky brightness that the tube is exposed to in addition to the (significantly smaller) dark current in the tube. A small biasing, or pedestal, current is then reintroduced to the signal in the input stage of the QADCs to facilitate the measurement of negative fluctuations of the signal from the mean sky-brightness. This biasing current is removed during the analysis of the data, as described in section 4.2.1. The data is read out over a computer network and stored on disk for offline analysis.

It is estimated that a single photo-electron in the PMTs produces a signal of  $\sim 3.3$  counts in the QADC. This corresponds to a total gain in the system of  $\sim 5 \times 10^6$ .

### 3.4 Characterization of detector

Unlike the lower energy satellite based  $\gamma$ -ray instruments, the response of a ground-based Čerenkov telescopes cannot be measured using an artificial test beam. Characterization of the response of such instruments to  $\gamma$ -rays and cosmic-rays must be done using simulations, by modeling the air-shower development, Čerenkov light production and detector response. For such a study to be accurate, the simulations must correctly account for such factors as: nuclear physics cross-sections (especially for hadronic simulations), atmospheric density profile and response to Čerenkov radiation, wavelength dependent mirror reflectivity and PMT quantum efficiency, dispersion in the cables, response of the trigger and ADCs, and others. Many of these can be accurately measured in the laboratory, others must be extrapolated from standard tables, such as the U.S. standard atmosphere model. It is estimated that the accuracy of such a simulation study  $\sim 20\%$ . This is borne out by the impressive agreement in the spectrum of the Crab Nebula source calculated, from observations, by the various ground-based VHE observatories in the northern hemisphere, such as Whipple, HEGRA and CAT. These groups employ different simulation codes, both for shower physics and detector simulation, yet derive spectra for the Crab that agree to within the limits of statistical and systematic errors.

Chapter 6 describes the study of a next generation ground-based instrument, VERITAS, in some detail. The results of a similar study of the Whipple telescope are presented here, with a brief description of the simulations.

The KASCADE simulation package (Kertzman and Sembroski, 1994) was used to generate sets of  $\gamma$ -ray-induced air shower events. Sets of  $\gamma$ -ray -induced events were generated over a range of energies between 30 GeV and 30 TeV. The energy bins were evenly distributed in  $\log E$  with eight bins per decade of energy. To accommodate the decreasing detection efficiency of the instrument at lower energies, the number of events simulated per bin was chosen to increase sharply at lower energies, to ensure that sufficient events were available so that some of them would survive the simulated trigger requirements and data selection procedure.

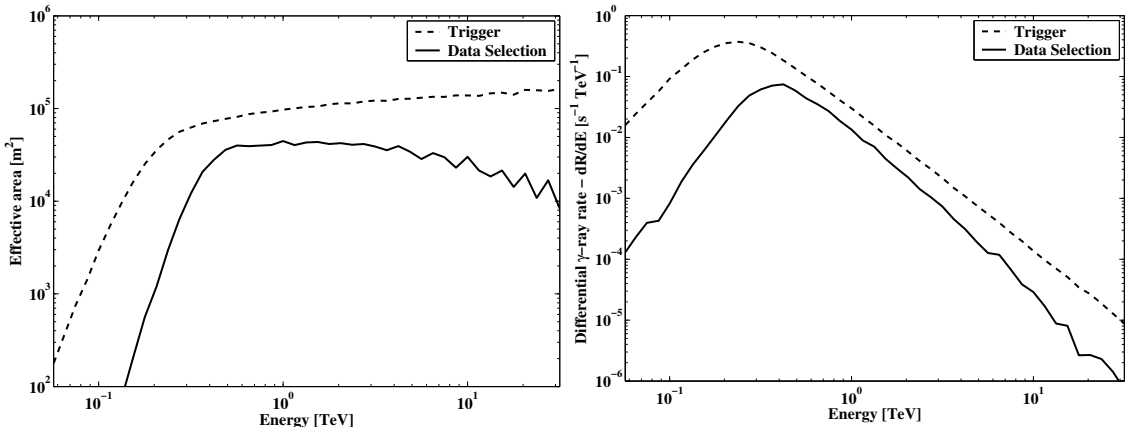


**Figure 3.6:** (Left) Effective collection area vs. energy for trigger and for data selection algorithm. After data selection, the collection area peaks at  $\sim 4 \times 10^4$  m<sup>2</sup>. (Right) Differential rate of  $\gamma$ -rays collection from Crab Nebula.

For each event, the Čerenkov photons generated in the shower were traced to see whether they intersected the mirror. The wavelength dependent reflectivity was accounted for and, if the photon was reflected into a PMT, so also was the quantum efficiency of the tube. The resultant photo-electrons produced by the shower (if there were any) were combined with artificially generated, Poisson distributed, night-sky photo-electrons, producing a realistic image that is comparable to an image of a real  $\gamma$ -ray. The images were subjected to the standard trigger requirement of three neighboring channels above a threshold of  $\sim 7$  photo-electrons. Those events that pass the trigger requirement are then processed using the standard analysis and data selection criteria, as described in chapter 4. Figure 3.6 shows the simulated response of the instrument to on-axis  $\gamma$ -ray primaries at an angle of 20° to the zenith. For a Crab Nebula like spectrum (power law –  $dF/dE \propto E^{-2.5}$ ) the instrument is most sensitive to  $\gamma$ -rays with energy of  $\sim 350$  GeV. It is usual to refer to this as the *peak response energy* of the instrument<sup>13</sup> and to quote fluxes and upper-limits measured with the instrument at that energy.

<sup>13</sup>Or somewhat incorrectly, as the *energy threshold* of the instrument.

## 4. DATA ANALYSIS

A number of data analysis algorithms have been developed by the VHE  $\gamma$ -ray community, some of which are specialized for different classes of instrument or to different classes of candidate  $\gamma$ -ray source. One of the simplest, most effective, single telescope, point-source analysis techniques, dubbed “Supercuts”, was developed for data taken at the Whipple 10 m telescope (Punch et al., 1992). Data selection is based on a set of strict cuts applied to a set of parameters which are calculated for each image. The selection cuts are optimized to preferentially select  $\gamma$ -ray-induced events over background events. This technique typically keeps 50% of  $\gamma$ -ray events and discards  $>99\%$  of background events, significantly improving the signal-to-noise (S/N) ratio. For a bright source such as the Crab Nebula, a S/N ratio corresponding to a  $>4\sigma$  rejection of the null hypothesis that no source is present (with an event rate large enough that Gaussian statistics apply) can be achieved in 30 minutes of observations. This point-source analysis technique has been adapted to sources whose location is not well defined, and to extended sources by Lessard et al. (2001). A refinement of this technique is presented here.

### 4.1 Observations

To avoid damage to the photo-multiplier tubes, observations with the Whipple 10 m telescope are made only during the portion of the night during which the moon is below the horizon. Observations are thus restricted to  $\sim 3$  week periods, called “dark runs”, separated by the period of the full moon. The telescope does not operate during the two month summer monsoon season to protect the sensitive electronics from the frequent lightning strikes on the mountain. The close-down period is used to perform maintenance upgrades to the instrument; hence, its characteristics usually change during this summer period. Observations are divided, therefore, into ten month “observing seasons” when the characteristics of the instrument remain largely

constant. Data for this survey was taken from 1999 to 2003. Significant changes were made to the instrument during the summer and fall of 2001 when a new approach to the alignment of mirror facets was implemented. This new technique corrected for the deformations in the optical support structure which occur as the telescope is elevated from its stow position (Schroedter et al., 2002).

Observations with the instrument are made in one of two modes, termed ON/OFF and TRACKING modes, which have significantly different approaches to background estimation. When operating in the ON/OFF mode, two separate 28 minute scans (ON and OFF) are made. The ON scan is taken while tracking the sky with the candidate object at the center of the field of view and gives an estimate of the  $\gamma$ -ray flux combined with the background rate. The OFF scan is taken in the absence of the candidate object to give an independent estimate of the background rate. The ON and OFF scans are taken such that they are separated by 30 minutes in time and track locations in the sky separated by 30 minutes in Right Ascension. Thus, the scans cover the same range of elevation and azimuth, which helps to minimize differences in the background rate between each scan. In general, ON/OFF mode is only used in the best weather conditions as large differences in the background rate between the two scans are introduced if any cloud drifts through the field of view. ON/OFF mode can be used to test the hypothesis that  $\gamma$ -ray emission is occurring from any location within the field of view of the instrument. This is the case for a candidate source whose location is not known a priori, such as unidentified sources with large error-box locations and for sources whose emission is expected to be extended, such as SNR.

When operating in the TRACKING mode, a single scan is taken tracking the candidate object. An estimate of the background is inferred from the number of events present in the scan which are not consistent with having originated from the candidate source location. The ratio of background events which are consistent with having originated from the source to those which are not, must be calculated independently using data which are known not to have a source present, a process described in section 4.7. TRACKING mode is most applicable when testing the hypothesis that  $\gamma$ -ray emission

is occurring from a point-like object at the center of the field of view, for example, when testing for emission from an extragalactic source or pulsar whose location is well known. Since the background estimate is derived from the observations themselves, twice the amount of on-source data can be collected in a given time than can be collected in ON/OFF mode. The method implicitly assumes that the ratio of events consistent with a candidate source to those which are not is constant across the fields of all potential sources. This may not be the case for fields with bright stars present for observations made over a large range of elevations.

## 4.2 Image Conditioning

Prior to parameterizing the recorded images, five stages of image conditioning are applied, with the aim of minimizing systematic differences across the camera and between the ON and OFF scans, and also to minimize the influence of background night-sky light on the parametrization of the images. Figure 4.1 depicts a typical event after each stage of the image conditioning.

### 4.2.1 Pedestal Removal

The signal chain between the photo-tubes and ADCs is AC coupled at the amplifier to remove any steady current associated with the night-sky background and with any dark currents present in the PMT. To allow negative fluctuations from the mean night-sky background to be measured, a small biasing current is artificially injected into the ADCs in order to yield a positive output for the largest reasonable negative fluctuation, integrated over the 20 ns ADC gate. This small biasing current, dubbed the “pedestal”, is set large enough to accommodate a  $4-5\sigma$  negative fluctuation (with a typical, dark sky, night-sky background rate) by adjusting a trim-potentiometer on the ADC board. Typically the RMS fluctuations due to the night-sky background are  $\sim 4 - 5$  digital counts (DC) when integrated by the ADCs, so a bias current giving an integrated signal of  $\sim 20 - 25$  DC is chosen. The pedestal currents must be

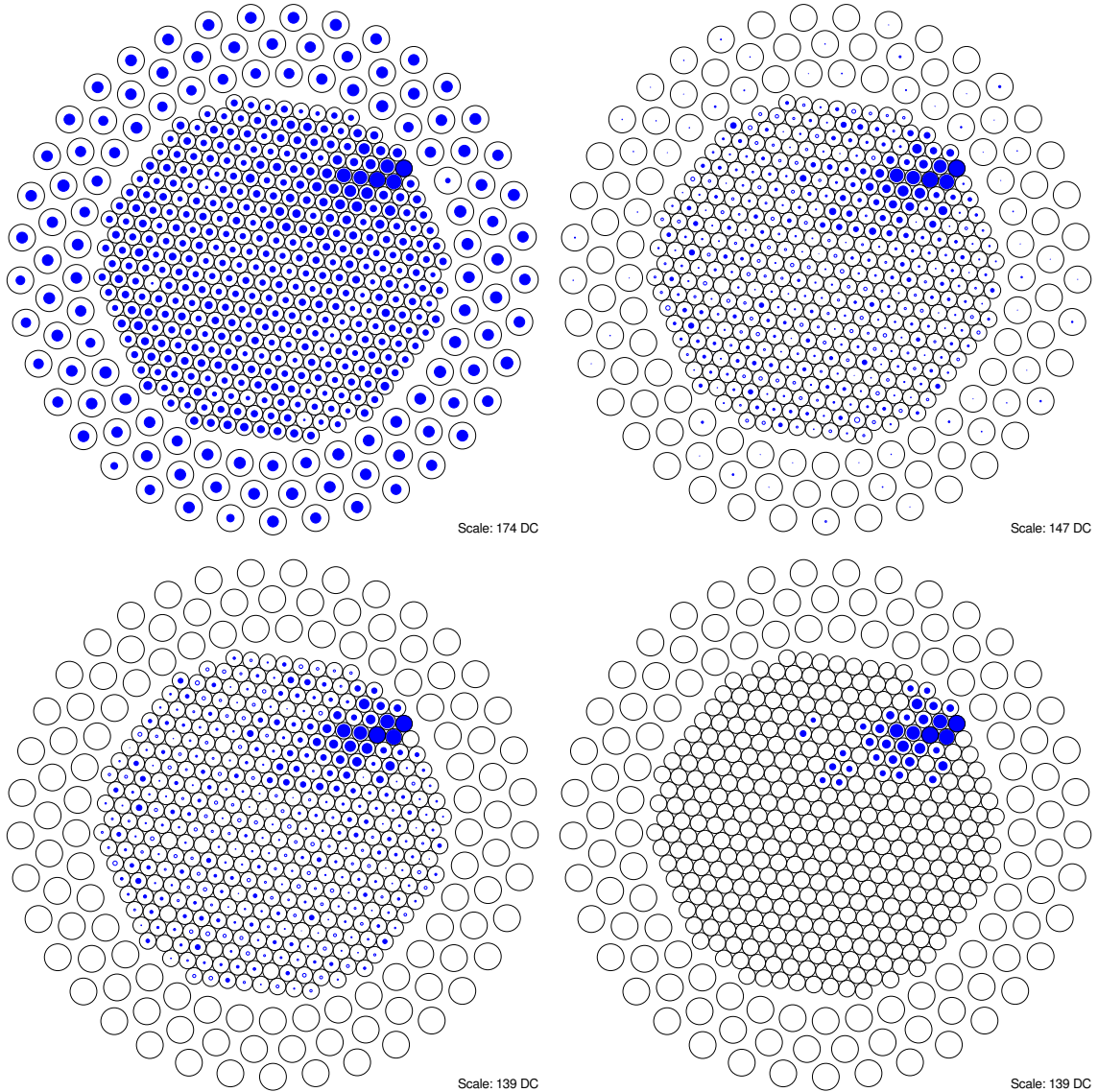


**Figure 4.1:** A typical event after each stage of image conditioning. (Top left) Raw ADC values. (Top right) After subtraction of injected pedestals. (Bottom Left) After gain equalization. (Bottom right) After cleaning.

subtracted from the ADC signals during the analysis to result in a mean of zero for each channel when no signal is present.

In addition to the normal triggering requirement described in section 3.3, an artificial trigger is generated from the 1 Hz signal of the master GPS clock. This causes events, which are flagged as special “pedestal events” in the data stream, to be recorded in the absence of an air-shower. These events record the zero-level point of each ADC in the presence of any night-sky background and the injected pedestal current.

To estimate the level of the integrated pedestal current present in each channel, these events are accumulated over the course of observations (typically 1600 events in a 28 minute scan), and the mean recorded signal in each channel and its variance are calculated. The mean value corresponds to the pedestal current integrated over the gate time, expressed in DC. The variance gives the mean-squared fluctuations in the night-sky background level integrated in the gate, expressed in DC.

For all air-shower triggered events, the value of the pedestal is subtracted from the signal to give the amount of charge recorded in each channel, expressed in DC.

#### 4.2.2 Gain Equalization

At the beginning of every night of observations, a calibration of the relative gain of each channel across the camera is performed. By illuminating the camera uniformly with the flashes from a fast nitrogen arc lamp and recording the results, an estimate of the relative gain in each channel is calculated. The N<sub>2</sub> lamp, which has been demonstrated to illuminate the camera uniformly (Schroedter, 2002), produces fast  $\sim$ 35 ns flashes at a rate of  $\sim$ 750 Hz. Neutral density filters are used to attenuate the flashes so that they produce a manageable signal in the ADCs ( $\sim$ 700 DC from the 10-bit maximum readout).

For any nitrogen arc flash, the signal in each channel<sup>14</sup>,  $s^{(\alpha)}$ , is given by the product of the number of photons which strike the photo-cathode,  $n_{ph}^{(\alpha)}$ , the efficiency of the

---

<sup>14</sup>In this chapter, the channel number is referred to by the index  $\alpha$

PMT at collecting photons,  $\eta^{(\alpha)}$ , and the gain of the channel,  $g^{(\alpha)}$ . The efficiency factor,  $\eta^\alpha$ , accounts for the efficiency of the photo-cathode at converting photons to photo-electrons and for the efficiency of tube at collecting the photo-electrons. This efficiency depends, to some extent, on the voltage across the tube (in particular the voltage across the first dynode). It is convenient to introduce an overall gain factor,  $G$ , to account for the average PMT gain, amplifier gains, cable losses, ADC conversion factor and average PMT efficiency across the camera.  $G$  can be selected such that the mean of  $g^{(\alpha)}\eta^{(\alpha)}$  is unity. The signal can therefore be written,

$$s^{(\alpha)} = G g^{(\alpha)} \eta^{(\alpha)} n_{ph}^{(\alpha)}.$$

To flat-field the camera, i.e. to account for the different gains and efficiencies across the camera, the factor  $g^{(\alpha)}\eta^{(\alpha)}$ , must be calculated for each channel. The efficiency factor is often incorporated into  $g^{(\alpha)}$  at this point, but will be kept in the calculations below. The factor  $g^{(\alpha)}\eta^{(\alpha)}$  is referred to as the “relative gain” of the channel.

Since the mean relative gain is chosen to be unity (i.e. by choice of  $G$ ), the mean signal recorded for any nitrogen flash can be written,

$$\langle s^{(\alpha)} \rangle_\alpha = G \langle g^{(\alpha)} \eta^{(\alpha)} n_{ph}^{(\alpha)} \rangle_\alpha = G \langle g^{(\alpha)} \eta^{(\alpha)} \rangle_\alpha \langle n_{ph}^{(\alpha)} \rangle_\alpha = G \langle n_{ph}^{(\alpha)} \rangle_\alpha,$$

where the mean,  $\langle \cdot \rangle_\alpha$ , is shown explicitly to be taken over all the channels. The signal in each channel can be written relative to the mean as,

$$s^{(\alpha)} / \langle s^{(\alpha)} \rangle_\alpha = g^{(\alpha)} \eta^{(\alpha)} n^{(\alpha)} / \langle n^{(\alpha)} \rangle_\alpha,$$

where the explicit label on  $n_{ph}$  has been dropped. Accumulating a large number of nitrogen flashes (labeled below by the index  $i$ ) and averaging over them for each channel gives the relative gain,

$$\left\langle \frac{s_i^{(\alpha)}}{\langle s_i^{(\alpha)} \rangle_\alpha} \right\rangle_i = g^{(\alpha)} \eta^{(\alpha)} \left\langle \frac{n_i^{(\alpha)}}{\langle n_i^{(\alpha)} \rangle_\alpha} \right\rangle_i = g^{(\alpha)} \eta^{(\alpha)} \frac{\langle n_i^{(\alpha)} \rangle_i}{\langle \langle n_i^{(\alpha)} \rangle_\alpha \rangle_i} = g^{(\alpha)} \eta^{(\alpha)} \frac{\langle n \rangle}{\langle n \rangle} = g^{(\alpha)} \eta^{(\alpha)}.$$

These relative gain estimates are used to scale the signals in each channel for every scan taken during the night.

In practice, gains calculated using this method suffer from a number of deficiencies arising from the fact that the average profile of the nitrogen arc pulses is different from that of Čerenkov pulses from air showers; the duration of the N<sub>2</sub> pulses are significantly longer with a longer decay time. The ADC integration gate is chosen to accommodate all but the largest Čerenkov pulses with a minimum of sky-noise. Because of their fast fall-off, small differences (1-2 ns) in the start time or duration of the gate signal between ADC modules does not significantly effect the signal recorded from Čerenkov pulses, but does have a larger effect on N<sub>2</sub> pulses which have not decayed by the end of the integration time. Another approach to gains calculation is to measure the spectrum of the cosmic-ray background during the course of a night. Over the course of a few hours of observations, sufficient cosmic-ray background events can be collected to allow differences in the spectrum in each channel, due only to a difference in the gain of each channel, to be detected. Since the background events have the same time profile as the  $\gamma$ -ray events of interest, this method does not suffer from the systematic differences as the nitrogen pulser method. The nitrogen method, which is the standard method of gain equalization used when analyzing Whipple data, has been used in this work.

#### 4.2.3 Channel Sanity Checking

In order to minimize the effects of bright stars in or adjoining the field of view, noisy channels and PMTs whose gain is set very high or low, two simple sanity checks are applied to the data. Channels whose RMS pedestal fluctuations are too high, or too low with respect to the median pedestal fluctuation across all the channels in the camera are “turned off in software”, i.e. their signals are disregarded during image parameterization in all events in both the ON and OFF data scans. The requirement for a channel to be included in the parameterization is that,  $0.6 \text{ med}(\sigma^{(\alpha)}) < \sigma^{(\alpha)} < 1.5 \text{ med}(\sigma^{(\alpha)})$ . Additionally, channels whose relative gains are very different from

the median gain across the camera, i.e. those which do not satisfy the following  $0.1 \text{ med}(g^{(\alpha)}\eta^{(\alpha)}) < g^{(\alpha)}\eta^{(\alpha)} < 5.0 \text{ med}(g^{(\alpha)}\eta^{(\alpha)})$ , are also excluded.

#### 4.2.4 Image Cleaning

The parameterization technique employed, based on the principal moments of the light distribution in the image, is sensitive to fluctuations of the night-sky background. In particular, the second order moments of the distribution will be skewed by channels with large night-sky induced signals which lie far from the image of the shower. In order to minimize the effects of these “outliers” a cleaning procedure is applied to the image (Fegan, 1996). Those channels which have a signal larger than a threshold,  $n_{img}$ , times the RMS night-sky fluctuation in that channel are denoted as “image channels”. Those with a signal greater than a different threshold,  $n_{bnd}$ , times the RMS night-sky fluctuation and, in addition, are located adjacent to an “image channel” are denoted “boundary channels”. All channels in the image that are not in either of these categories are discarded. In choosing the thresholds a compromise must be reached between eliminating the noise in the image and keeping channels with a small signal which are part of the air-shower image. This is particularly important to ensure good differentiation between compact  $\gamma$ -ray-like events and broad cosmic-ray-like events. For this work, the values of  $n_{img}=4.25$  and  $n_{bnd}=2.25$  are chosen. These values are standard for the analysis of Whipple 10 m data during this period.

#### 4.2.5 Noise Padding

As described above, when operating in ON/OFF mode, two 28 minute scans are taken, each covering the same range in azimuth and elevation. This ensures that local contributions to the background rate, e.g. due to light pollution from the neighboring cities of Tucson and Nogales, are introduced equally to both scans. Significant differences can still arise due to non-local differences between the ON and OFF scans, such as the presence of bright stars or the Galactic Plane in either of the fields. For candidates that lie near to the Galactic Plane, the field of the OFF scan will not, in

general, also lie on the Plane. The night-sky background flux varies by a factor of two, from  $\langle NSB_{\text{flux}} \rangle \approx 2\text{--}4 \times 10^{12} \text{ s}^{-1} \text{ m}^{-2} \text{ sr}^{-1}$ , between locations away from, and on, the Galactic Plane. There are two major effects of such brightness differences, the first on the image cleaning algorithm described above, the second on the hardware trigger.

As described above, image cleaning discards channels whose signal to noise ratio is smaller than a certain threshold. An air-shower signal recorded in a channel which has a larger noise component will have a smaller S/N ratio and will therefore be more likely to be discarded. This is not a problem for channels in the core of a bright shower, but weak signals from the periphery of a shower will tend to be preferentially discarded by the cleaning algorithm in a region with a bright night-sky background contribution. This has the effect of making the shower image tend to appear smaller. Since the data selection procedure (described below) is based on eliminating all but the most compact images, systematic differences will arise due to cleaning between ON and OFF scans, where large night-sky differences exist. To compensate for this, artificially generated Gaussian noise is added to equalize the noise between the two scans, in a process known as “software padding”.

For each channel, the noise in the ON and OFF fields ( $\sigma_{\text{On}}^{(\alpha)}$  and  $\sigma_{\text{Off}}^{(\alpha)}$ ) are calculated from pedestal events as described above. In general, for each channel, one field will have more noise present than the other, say  $\sigma_{\text{On}}^{(\alpha)} > \sigma_{\text{Off}}^{(\alpha)}$  ( $\sigma_{\text{On}}^{(\alpha)} < \sigma_{\text{Off}}^{(\alpha)}$ ). To compensate, for this channel, Gaussian noise is added to all events of the OFF (ON) scan. Since the noise variance adds in quadrature, the level of padding noise added is given by  $\Delta\sigma_{\text{Pad}}^{(\alpha)} = \sqrt{|\sigma_{\text{On}}^{(\alpha)2} - \sigma_{\text{Off}}^{(\alpha)2}|}$ . For well matched ON and OFF fields, small amounts of noise will be added to both fields. For scans where there is a large systematic difference, one field will have more noise added to it than the other. During cleaning, the S/N ratio of channels in both the ON and OFF scans is calculated using the common value of  $\sigma_{\text{Pad}}^{(\alpha)} = \max(\sigma_{\text{On}}^{(\alpha)}, \sigma_{\text{Off}}^{(\alpha)})$  for the noise level.

The padding technique, introduced in Cawley (1993), has been employed successfully for a decade when analyzing Whipple data. Previous generations of the Whipple

**Table 4.1:** Difference between noise levels for three channels, before and after software noise padding.

Relative $\sigma_{\text{Pad}}^{(\alpha)}$	Before Padding		$\sigma_{\text{Pad}}^{(\alpha)}$	After Padding	
	$\sigma_{\text{On}}^{(\alpha)}$	$\sigma_{\text{Off}}^{(\alpha)}$		$\sigma_{\text{On}}^{(\alpha)}$	$\sigma_{\text{Off}}^{(\alpha)}$
Smallest	4.21 DC	4.03 DC	1.21 DC	4.21 DC	4.37 DC
Intermediate <sup>1</sup>	6.36 DC	4.43 DC	4.56 DC	6.36 DC	6.40 DC
Largest	9.03 DC	4.34 DC	7.92 DC	9.03 DC	8.69 DC

<sup>1</sup> Intermediate value corresponds to channel with largest night-sky noise which would survive sanity check, as described above.

instrument were fitted with 1 inch diameter photo-tubes whereas the high-resolution camera, with which the data in this survey was collected, employs 0.5 inch PMTs. This corresponds to a decrease in the collected night-sky background by a factor of four, from  $\sim 8$  photo-electrons (PE) in a 20 ns gate to  $\sim 1.8$  PE. With previous cameras it was assumed that this background could be approximated by a Gaussian distribution; this assumption is no longer valid, except in the brightest regions of the sky. Therefore, it could be argued that padding should be performed with a non-Gaussian noise distribution. Table 4.1 shows the measured width of the noise distribution for three channels selected from an ON/OFF mode observation before and after padding. The channels were chosen to have the smallest and largest differences in noise between the ON and OFF scans. An intermediate value was also chosen, corresponding to the channel with the largest difference that would have passed the sanity check described above. It can be seen from the table that the difference between the noise levels after padding is not large in any of the cases, the maximum being 4%. Any improvement to be gained from padding with a more realistic modeling of the noise distribution is expected to be small and was not undertaken for the data analyzed in this work.

Finally, as mentioned above, differences in the background sky brightness will also influence the triggering rate of the instrument. Individual stars in the field of view can usually effect a number of neighboring channels and essentially decrease the triggering threshold in one small region of the camera. This star-induced effect is not serious as the “hot” channels will usually be eliminated from the analysis by the sanity checks.

More troublesome is a large scale brightness difference between the ON and OFF fields which can decrease the effective triggering threshold across the camera causing more events to be recorded in the brighter field. It is possible to compensate for this effect during analysis by imposing a higher triggering threshold. Another approach which can be adopted is to scale the number of counts recorded in the calculation of the background estimate.

### 4.3 Parameterization

Events are parameterized by the moments of the light distribution in the image. The zeroth, first and second moments describe the total light in the image, the “center of mass” of the light distribution in the camera and the length, width and orientation of the distribution. Given that each channel is located at coordinates  $x_i^{(\alpha)}$  in the camera and records a signal  $s^{(\alpha)}$ , the first three orders of moments are,

$$\begin{aligned} S = X^{(0)} &= \sum_{\alpha} s^{(\alpha)} \\ (x_c, y_c) = \bar{x}_i = X_i^{(1)} &= \sum_{\alpha} s^{(\alpha)} x_i^{(\alpha)} / S \\ \sigma_{ij} = X_{ij}^{(2)} &= \sum_{\alpha} s^{(\alpha)} (x_i^{(\alpha)} - \bar{x}_i)(x_j^{(\alpha)} - \bar{x}_j) / S \end{aligned}$$

It is usual to refer to the parameter  $S$  as the *size* of the image and to define a parameter describing the distance between the center of the camera and the image centroid as  $distance = \sqrt{x_c^2 + y_c^2}$ . The *length*, *width* and *orientation* of the image are derived by diagonalizing the matrix of second order moments, i.e. by finding the value of  $\theta$  such that,

$$\begin{pmatrix} \sigma_{11} & \sigma_{12} \\ \sigma_{21} & \sigma_{22} \end{pmatrix} = \begin{pmatrix} \cos \theta & \sin \theta \\ -\sin \theta & \cos \theta \end{pmatrix} \begin{pmatrix} length^2 & 0 \\ 0 & width^2 \end{pmatrix} \begin{pmatrix} \cos \theta & -\sin \theta \\ \sin \theta & \cos \theta \end{pmatrix}.$$

From these moments a number of useful parameters are calculated (see appendices of Reynolds et al., 1993). In particular, the *alpha* parameter is important to the

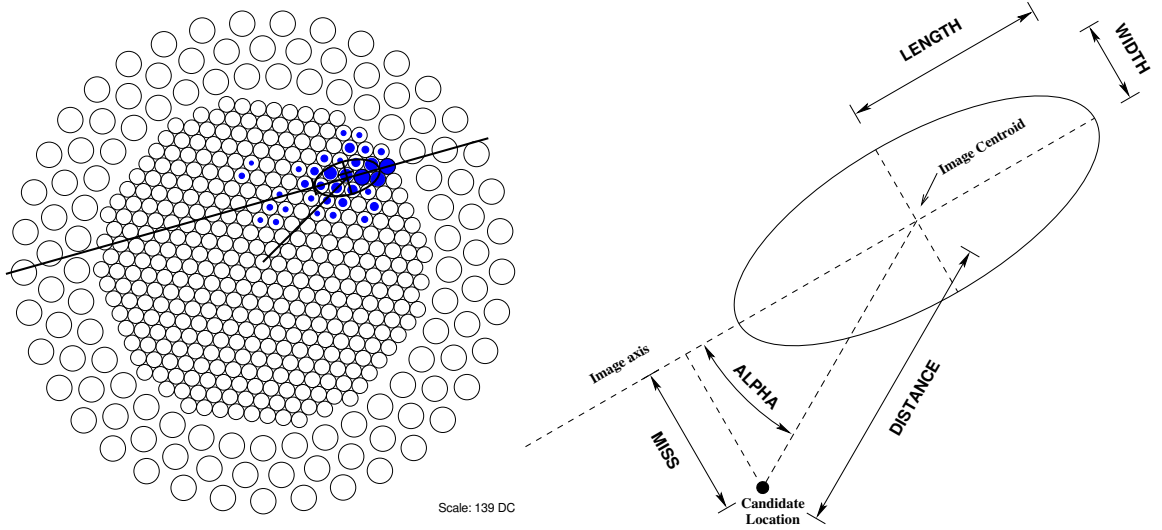


**Figure 4.2:** (left) Sample image taken with the high resolution camera, after image conditioning, with image axis and second order moments indicated. (right) Illustration of image parameters.

analysis of data from a candidate point-source object at the center of the field of view. As illustrated in figure 4.2, *alpha* describes the orientation of the shower image with respect to the line joining the source location and the centroid of the image distribution. Images with a small value of *alpha* (usually  $\alpha < 15^\circ$ ) are considered to be consistent with having originated from the source location; those with a large value of *alpha* are not. In a standard point source analysis, a histogram is made of the alpha parameter for all events which pass the data selection criteria. An excess of events with small *alpha* is indicative of a source at the center of the field of view.

#### 4.4 Data Selection

Data selection is based on strict cuts of the parameter values described above. Cuts can be considered as belonging to two categories. The first set is used to address undesirable effects that arise due to the instrument itself, the second to preferentially retain  $\gamma$ -ray events while eliminating the background. The values that parameters must have to survive the cuts are chosen by optimizing the response of the system to a known  $\gamma$ -ray source, usually the steady flux from the Crab Nebula. The standard

**Table 4.2: Data selection cuts used in this work.**

Parameter	Supercuts	Loosercuts	1 TeV Loosercuts
<i>distance</i>	$> 0.40^\circ$	$< 1.00^\circ$	$< 1.00^\circ$
<i>length</i>	$> 0.05^\circ$	$< 0.12^\circ$	$< 0.14^\circ$
<i>width</i>	$> 0.13^\circ$	$< 0.25^\circ$	$< 0.35^\circ$
<i>size</i>	n/a	n/a	$> 1500 \text{ DC}$

set of cuts used on Whipple data is known as “Supercuts”. Since “Supercuts” were optimized for point source detection, a new set of cuts were developed for this work, termed “Loosercuts”. They were chosen to accept more events, relying on the 2-dimensional reconstruction to increase the S/N ratio. Additionally a set of cuts optimized to keep only events with energy  $>\sim 1 \text{ TeV}$  has been developed.

Cuts in the first category are largely the same for both sets. They consist of three cuts, known as *trigger*, *distance* and *size*. The *trigger* cut reduces the effects of unevenness in the hardware trigger by requiring that the two largest signals recorded in the event are greater than 30 DC. The *distance* cut, which eliminates those events occurring at the edge of the camera and which may be truncated, is listed in table 4.2. The *size* cut, a cut on the total signal recorded in the image, is not applied in Supercuts, but can be used to adjust the peak response energy (P.R.E.) of the instrument. For example a cut requiring  $\text{size} > 1500 \text{ DC}$  gives a P.R.E. of  $\sim 1 \text{ TeV}$ .

The second category of cuts are based largely on the shape (*length* and *width*) of the image. The shape cuts are listed in table 4.2. The bulk of the background is eliminated by the strict *width* cut which is optimized to keep the compact  $\gamma$ -ray events while eliminating the broader cosmic-ray images. Additionally a cut on the ratio of the length of the image to the amount of light present,  $\text{length}/\text{size} < 0.0004$ , is used to eliminate a large fraction of the background muon images.

## 4.5 2D Analysis technique

For extended sources or sources where the source location is not well determined, it is essential to reconstruct the arrival direction of the primary. This can be done

naturally using systems of telescopes observing the shower from a number of different positions on the ground, as described in chapter 6. For a single telescope, the arrival direction must be inferred from the *shape* and *orientation* of the single observed image. The approach taken here is based on Lessard et al. (2001).

Although the shower processes are stochastic in nature, there is a statistical relationship between the parameters of the recorded image and a set of parameters, denoted  $\Theta$ , which describe the energy and path of the incident  $\gamma$ -ray,  $\Theta = \{E, x_0, y_0, b, \psi\}$ . The parameter  $E$  refers to the energy of the primary  $\gamma$ -ray. The pair,  $(x_0, y_0)$  denote the direction of propagation of the  $\gamma$ -ray with respect to the axis of the telescope, i.e. the location in the field of view of the source of the  $\gamma$ -ray. The final two parameters,  $(b, \psi)$ , denote the point of closest approach of the propagation of the primary  $\gamma$ -ray to the camera;  $b$  is conventionally called the impact parameter,  $\psi$  denotes the direction to the point of closest approach.

The following relationships exist, in a statistical sense, between the image parameters and the shower parameters

$$\text{length} = \text{length}(E, b) \quad (4.1)$$

$$\text{width} = \text{width}(E, b) \quad (4.2)$$

$$\text{size} = \text{size}(E, b) \quad (4.3)$$

$$(x_c, y_c) = (x_c(E, x_0, y_0, b, \psi), y_c(E, x_0, y_0, b, \psi)) \quad (4.4)$$

$$\theta = \theta(x_0, y_0, \psi) \quad (4.5)$$

where any contribution to the parameters due to optical aberrations and clipping of the image due to the finite size of the camera have been ignored. The requirement of two-dimensional reconstruction is to find a relationship between the image parameters and the direction of propagation of the  $\gamma$ -ray , i.e. to find,

$$x_0 = x_0(\text{size}, \text{length}, \text{width}, x_c, y_c)$$

$$y_0 = y_0(\text{size}, \text{length}, \text{width}, x_c, y_c)$$

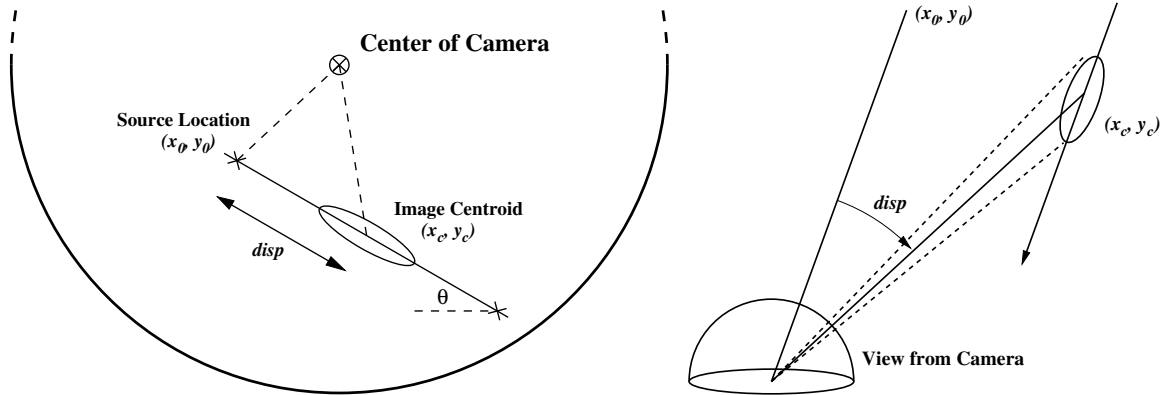


**Figure 4.3:** Illustration of shower parameter  $disp$  in the field of view of camera (left) and from perspective of the shower in the atmosphere (right).

In practice, it is more convenient to estimate the arrival direction of the primary with respect to the image centroid,  $\Delta x = x_c - x_0, \Delta y = y_c - y_0$ . As illustrated in figure 4.3, the  $\gamma$ -ray source location lies along the shower axis (disregarding errors in axis reconstruction), whose direction in the camera is described by  $\theta$ . It is convenient to define a new shower parameter,  $disp$ , as the distance between the image centroid and the source location, by  $\Delta x = disp \cos \theta, \Delta y = disp \sin \theta$ . In general,  $disp = disp(E, b)$ , i.e. is dependent only on the energy and impact parameter of the primary. If the relationships, equations 4.1–4.5, are valid, then  $disp$  can be written in terms of the shower image parameters,  $disp = disp(size, length, width)$ .

When the shower impact location is zero, there is no preferred direction in the shower image, i.e.  $length = width$ , and the image centroid and source location coincide, i.e.  $disp = 0$ . This suggests that  $disp$  should be expanded in terms of the shower ellipticity,  $\epsilon = 1 - width/length$ ,

$$disp = a_1(size, length) \times \epsilon + a_2(size, length) \times \epsilon^2 + \dots$$

Simulations, detailed in appendix B, which assume that the dependence of  $a_i$  on  $length$  is of secondary importance, indicate that the quadratic term,  $a_2$ , is unnecessary and the  $a_1$  can be reasonably approximated as

$$a_1 = 1.36^\circ + 0.14^\circ \log(size/1622\ DC).$$

For this work, a simpler assumption was made, following Lessard et al. (2001). The dependence on *size* was neglected completely and the displacement between source location and image centroid was assumed to be given simply as the product of a constant,  $\xi$  and the ellipticity,

$$disp = \xi \times \left(1 - \frac{width}{length}\right) \quad (4.6)$$

This approach is justified empirically using observations of the Crab Nebula, deliberately offset from the center of the camera by various degrees, as detailed below.

A sky map is produced by constructing a 2-dimensional histogram of the reconstructed arrival direction with respect to the center of the camera. Errors in reconstructing both the image axis and *disp* are accounted for by convolving the final 2D map with a Gaussian smoothing function  $g(\vec{r}; r_0) = \exp(-r^2/2r_0^2)$ , where  $r_0$  is a scaling parameter chosen to maximize the significance of an excess. Appendix C discusses the advantage of Gaussian smoothing over that of Lessard et al. (2001).

This method yields two possible arrival directions for each event, each of which is on the major axis of the shower image, separated from the centroid by the calculated parameter, *disp*. In creating a 2D map of the detected events, the origin of each event is assigned to both possible directions in the hope that one will have an excess as the event origins are superimposed.

Calculation of excess signal, significance and upper-limit maps ( $S(\vec{r})$ ,  $\sigma(\vec{r})$  and  $UL(\vec{r})$  respectively) is then done by convolving the ON and OFF counts with the smoothing function  $g(\vec{r})$  in the appropriate manner,

$$S(\vec{r}) = \sum_{\vec{r}'} [(ON(\vec{r}') - OFF(\vec{r}'))]g(\vec{r}' - \vec{r}) \quad (4.7)$$

$$\Delta S(\vec{r})^2 = \sum_{\vec{r}'} [ON(\vec{r}') + OFF(\vec{r}')]g^2(\vec{r}' - \vec{r}) \quad (4.8)$$

Then  $\sigma(\vec{r}) = S(\vec{r})/\Delta S(\vec{r})$  and  $UL(\vec{r})$  is calculated from  $S(\vec{r})$  and  $\Delta S(\vec{r})$  by the method of Helene (1983).

**Table 4.3: Optimized two-dimensional analysis parameters, calculated for observing seasons from 1999 to 2003.**

	1999-2000	2000-2001	2001-2002	2002-2003
$\xi$	1.5°	1.5°	1.5°	1.5°
$r_0$	0.175°	0.175°	0.175°	0.175°
Relative Crab Rate	0.86	1.00	0.91	0.80

Calibration of the two dimensional analysis method was done using sets of observations of the Crab Nebula, in which its location was deliberately offset from the center of the field of view by various degrees. Calculating the relative  $\gamma$ -ray rate allows a model of the detector response for off-axis and extended sources to be made. Table 4.3 lists the values of  $\xi$  and  $r_0$  found to be optimal. It also lists the rate of  $\gamma$ -rays detected from the Crab Nebula, normalized to 1.0 for the 2000-2001 season.

Figure 4.4 shows significance maps for the Crab Nebula offset by three different amounts. In each of them the Crab is clearly visible. At an offset of 0.3° the  $\gamma$ -ray collection efficiency is 84% of what it is on axis. At an offset of 1.3°, with the source outside of the geometrical extent of the camera, the efficiency is 30%. The significance map for this data shows appreciable background contamination over the field due to the simple reconstruction approach of assigning the arrival direction of each photon to two points on the shower axis. More sophisticated approaches can reduce such false sources (Lessard et al., 2001).

Figure 4.5 shows the relative collecting efficiency for offset sources. This curve is used to normalize detected emission rates or upper limits to the Crab flux.

## 4.6 Significance of Observations

The calculated significance,  $\sigma(\vec{r})$ , described above, corresponds to the confidence that the null hypothesis, i.e. that no source is present at that point in the sky, is false. A large value of significance can be thought of as giving a high confidence that a source is present at the location. In the absence of any source,  $\sigma(\vec{r})$  should be distributed as

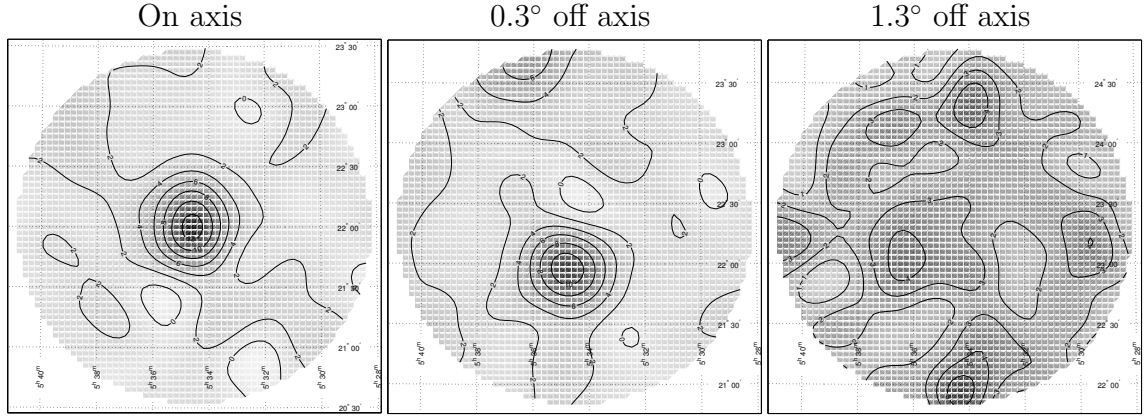


Figure 4.4: Observations of the Crab Nebula, offset by varying amounts from the center of the field of view. The contours show detection significance. The observations at an offset of  $1.3^\circ$  place the Crab outside of this.

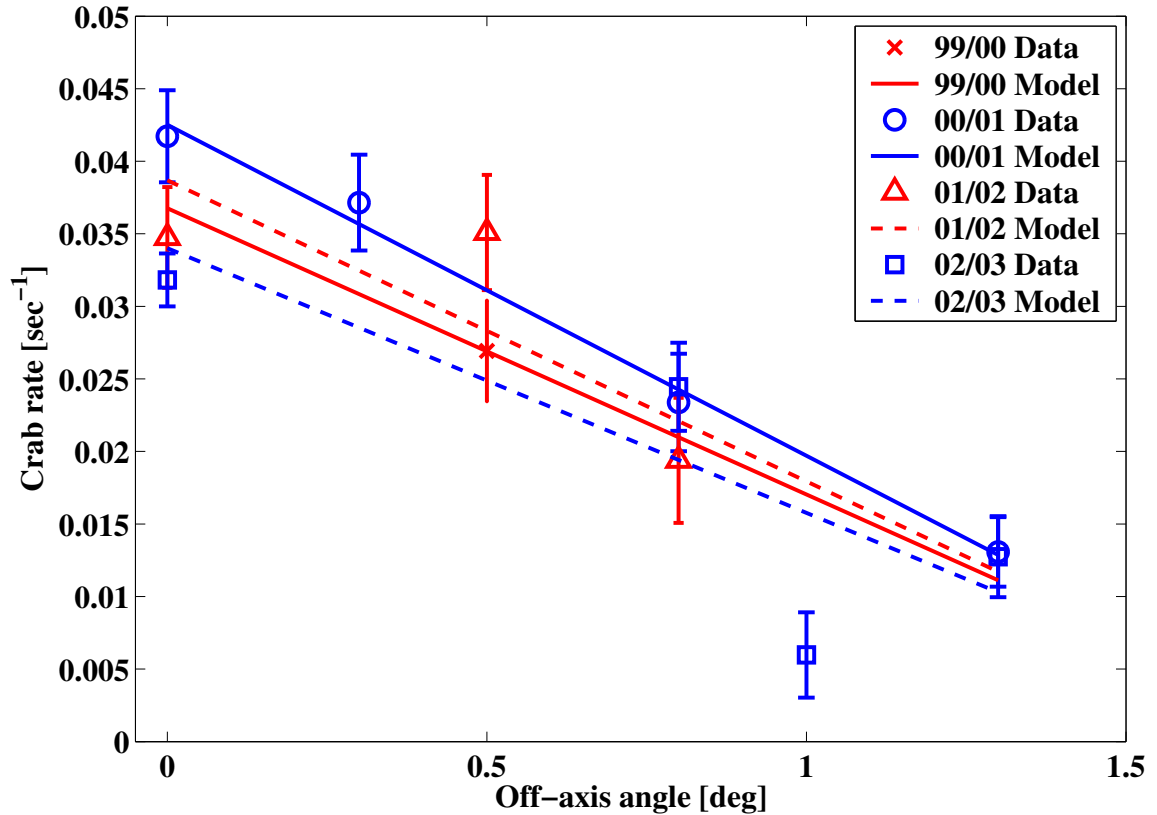


Figure 4.5: Relative Crab detection rate as a function of source offset. The off-axis response can be fit by a straight line.

Gaussian with unity width, for any location in the field of view ( $\vec{r}$ ) chosen a priori. To ensure that the measurement of sigma is not biased, “dark-field” observations were analyzed. The analysis was applied to 240 observations from 1999 to 2003 which were taken on regions of the sky which are assumed to have no source present in them, i.e. observations on candidate point-source objects whose analysis did not result in any significant excess. The significance of any excess (or deficit) found in the center bin,  $\sigma(\vec{0})$ , of the sky map from each of the observations is displayed in figure 4.6.

When the location of the source within the field of view is not known in advance, the null hypothesis must be modified to require that no source be present anywhere within the field of interest. To reject this hypothesis a number of independent bins must be calculated and the “true significance” of the largest observed excess must be determined. This “true significance” is different from the a priori significance  $\sigma(\vec{r})$  discussed up to this point. The distribution of the function  $\max \sigma(\vec{r})$  is not Gaussian for maps which contain more than one independent bin. Since the term “significance” is usually associated with the Gaussian distribution it is less confusing to refer instead to the probability that the null hypothesis be true or false.

For a single observation, with Gaussian distribution, the probability that a result of  $> x\sigma$  will be observed, in the absence of a  $\gamma$ -ray source, is given by the error function,

$$P_1(> x\sigma) = \frac{1}{\sqrt{2\pi}} \int_x^\infty e^{-x'^2/2} dx' = \{1 - \text{erf}(x/\sqrt{2})\}/2.$$

The probability of observing at least one result of  $> x\sigma$  in  $N$  independent observations, denoted  $P_{\geq 1/N}(> x\sigma)$ , is calculated by noting that if such a result is not observed, it must be the case that **all**  $N$  observations have a result of  $\leq x\sigma$ , which is simply the product of  $N$  individual probabilities  $P_1(\leq x\sigma)$ ,

$$P_{\geq 1/N}(> x\sigma) = 1 - \{1 - P_1(> x\sigma)\}^N.$$

It is conventional to claim the detection of a source when the null hypothesis has been rejected at a  $> 4\sigma$  level (Weekes, 1999), assuming a Gaussian distribution. Figure 4.7

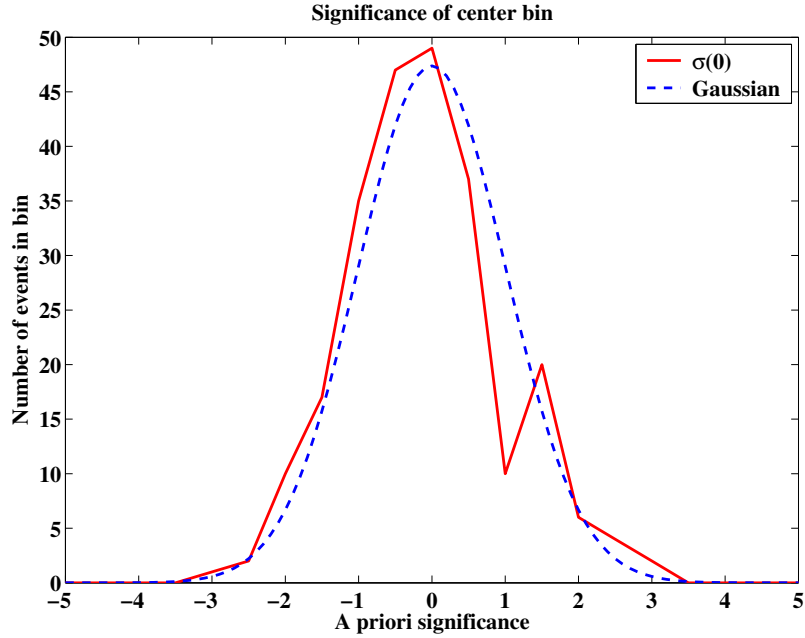


Figure 4.6: Significance of excess (deficit) in counts in center bin of 240 background observations. A Gaussian function of unity width, integrated over the binning size, is also shown.

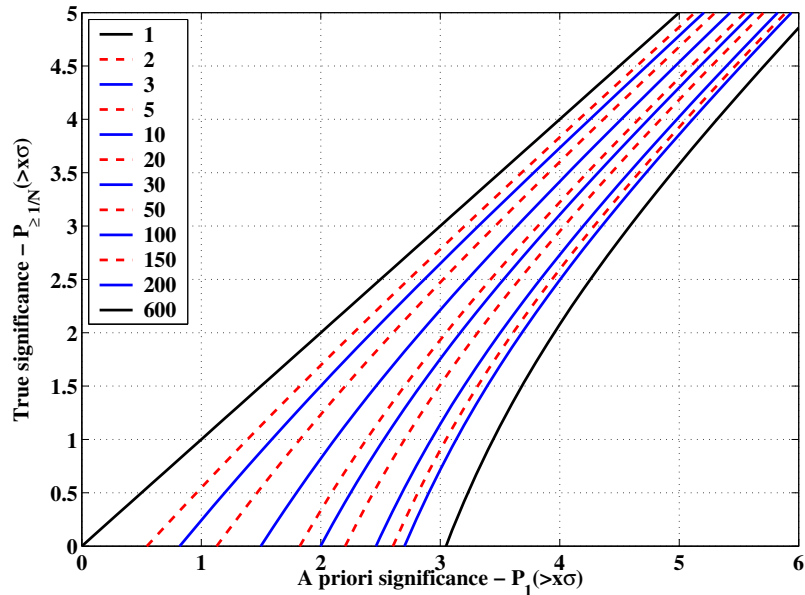


Figure 4.7: Probability of at least one from  $N$  observations giving a result of  $> x\sigma$  as compared with the probability of a single observation giving the same result. Curves with increasing  $N$ , from 1 to 600, go from left to right.

shows how  $P_{\geq 1/N}(> x\sigma)$  relates to  $P_1(> x\sigma)$ . It can be seen from the figure that a  $4\sigma$  Gaussian confidence level (on the y-axis) corresponds to the probability of detecting at least one  $\sim 4.6\sigma$  result with  $N = 10$  and increases to  $\sim 5.3\sigma$  for  $N = 600$ .

To relate the curves in figure 4.7 to the sky maps generated from real data, an equivalent number of independent bins must be calculated. The individual bins in the 2-d histogram are highly correlated, both through the smoothing applied to the image and the inaccuracy in the reconstruction method. Since the reconstruction method is difficult to characterize, as are the effects of the edge of the camera, the number of independent bins in the image is difficult to calculate. Two estimates can be made, the first by considering the width of the smoothing and the size of the camera, the second by fitting for  $N$  in the distribution,  $P_{\geq 1/N}(> x\sigma)$ , of maximum significances from the dark-field data described above.

For a 2-dimensional Gaussian smoothing function,  $g(\vec{r}; r_0) = \exp(-r^2/2r_0^2)$ , 50% of the counts are contained in a region of radius  $r = 0.206^\circ$  for  $r_0 = 0.175^\circ$ . An estimate of the number of independent bins can be made for regions of the sky map of various widths, given by  $2R$ , by taking the ratio of the area of the region and the area under the Gaussian. To account for effects at the border of the region of interest, a border of  $0.206^\circ$  can be added, so

$$N \sim \frac{\pi \times (R + 0.206^\circ)^2}{\pi \times (0.206^\circ)^2} = \left( \frac{R}{0.206^\circ} + 1 \right)^2$$

The estimates for  $N$  from this method, with and without the border effect are shown in table 4.4.

To estimate the number of independent bins from the distribution of the maximum significance in the dark field data,  $\max(\sigma(\vec{r}) ; |\vec{r}| < R)$ , a maximum likelihood approach is used. For any value of  $R$ , the size of the region of interest, analysis of the 240 dark fields result in a set of maximum significances,  $\{x_i^{(R)}\} = \{ \max(\sigma_i(\vec{r}) ; |\vec{r}| < R) \}$ . The likelihood that this set of observations are drawn from the probability distribution

for  $N$  independent Gaussian observations is given by,

$$L(x_i^{(R)} | N) = \prod_{i=1}^{240} \left[ \frac{dP_{\geq 1/N}(> x\sigma)}{dx} \right]_{x=x_i^{(R)}}$$

Maximizing the log likelihood,  $\Lambda = \ln L$ , gives the best estimate of the number of independent bins for each region size,  $N(R)$ .

Figure 4.8 shows the experimental distributions for  $R = 0.38^\circ$ ,  $R = 0.55^\circ$  and  $R = 1.10^\circ$ . The theoretical distribution based on the most likely value of  $N(R)$  is also shown. It can be seen that in the  $R = 1.1^\circ$  case, the fit is not particularly good, a result of the broad tails on the experimental distribution. Also displayed on these figures is the results of a simple Monte Carlo (MC) simulation of the smoothing, as described in appendix C. It can be seen that the likelihood fit to the experimental results matches the MC distributions well, with the MC distributions being slightly wider. Figure 4.9 shows the function  $N(R)$  plotted against the area of the region,  $A \propto R^2$ . It can be seen that there is a roughly linear increase of  $N$  with  $A$ , at least for  $R < 0.9^\circ$ . Table 4.4 lists the values of  $N$  for the cases considered above.

When data from an unidentified EGRET source is analyzed, a map of (a priori) significance is produced and the EGRET 95% contour level overlaid. The area of the region inside the contour can then be used to calculate an equivalent number of independent bins, using figure 4.9. This value can then be used to calculate a significance level which is equivalent to the accepted Gaussian  $4\sigma$  confidence level. The map can then be checked for emission from within the region of interest.

Additionally, the data can be tested to see whether they are consistent with the null hypothesis that no emission is present in any of the 18 candidate fields considered in the survey. The value of  $N$  appropriate is  $18 \times N(1.1^\circ) \approx 600$ , the number of independent bins in the regions of the sky within  $1.1^\circ$  of the center (the region defined by the edge of the camera) of each 18 field. A significance level, from figure 4.7, of  $\sim 5.3\sigma$  is required to claim the null hypothesis is false with the required confidence.

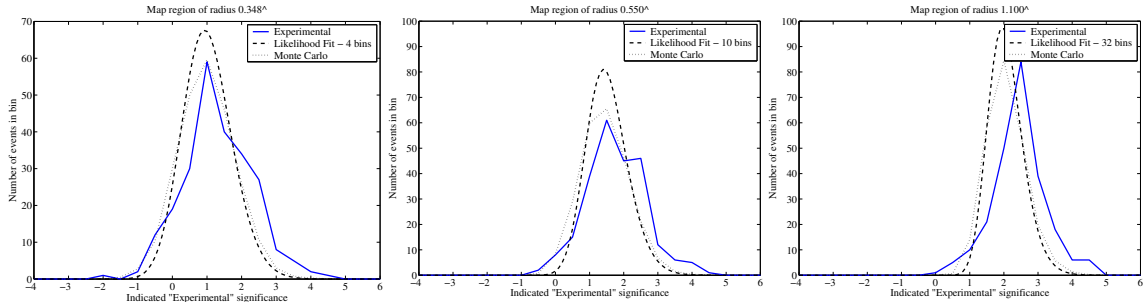


Figure 4.8: Experimental and best-fit distributions for  $\max(\sigma(\vec{r}) ; |\vec{r}| < R)$ , listed for  $R = 0.38^\circ$ ,  $R = 0.55^\circ$  and  $R = 1.10^\circ$ .

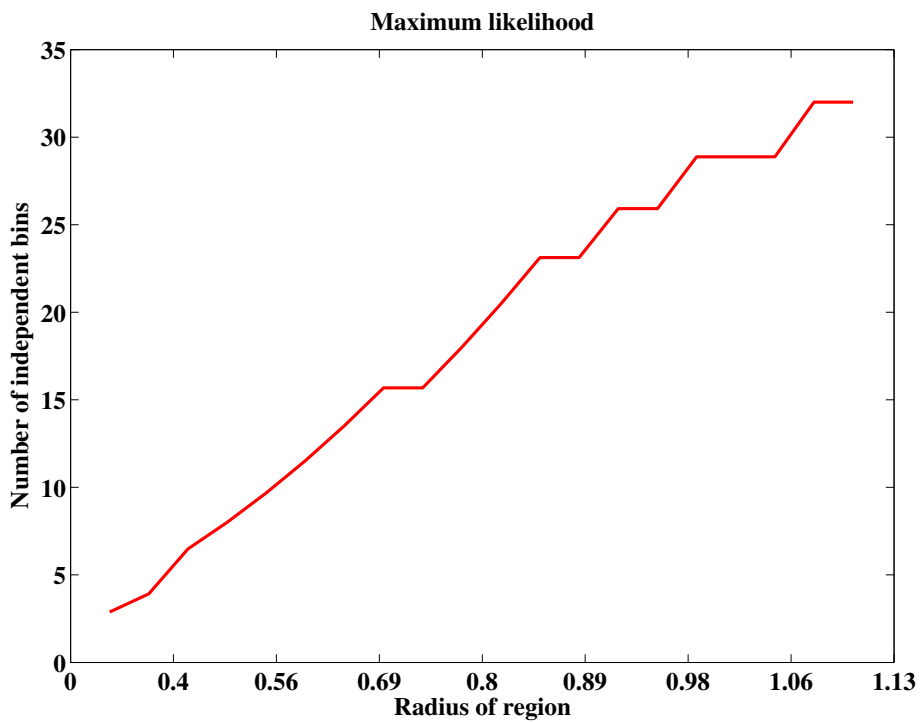


Figure 4.9: Maximum likelihood fit for  $N(R)$  as a function of  $A \propto R^2$ .

Table 4.4: Estimates for the number of independent bins,  $N$ , present in the region of a sky-map of area  $\pi R^2$ . Three estimates are given, the first two express the ratio of the areas of the region and the smoothing Gaussian. The final estimate is from a maximum likelihood fit to the distribution of maximum significance.

Method	$R = 0.35^\circ$	$R = 0.55^\circ$	$R = 1.1^\circ$
Ratio of areas $(R/0.206)^2$	3	7	29
Ratio of areas $(R/0.206 + 1)^2$	7	13	40
Maximum likelihood fit	4	10	32

## 4.7 Tracking Analysis

For objects whose location is well known, a simpler analysis technique can be applied. The analysis can take advantage of the TRACKING mode of observation, giving twice the amount of on-source data over the ON/OFF mode. As described above, the analysis takes advantage of the fact that the candidate source is at the center of the field of view, which allows events which are not consistent with having originated at the center of the field of view to be eliminated. The selection is done on the basis of the *alpha* parameter; a cut of  $\alpha < 15^\circ$  was been found to be optimal. An estimate of the background is made from the number of events which are not aligned with the center of the field of view; those with  $20^\circ < \alpha < 65^\circ$  are chosen. Assuming there are  $N_{On}$  events with  $\alpha < 15^\circ$  and  $N_{Off}$  with  $20^\circ < \alpha < 65^\circ$ , the excess counts is given by,

$$\Delta N = N_{On} - \rho N_{Off} \quad (4.9)$$

The constant  $\rho$ , termed the “tracking ratio”, relates the number of counts with  $\alpha < 15^\circ$  to the number with  $20^\circ < \alpha < 65^\circ$  in the absence of a source. This constant must be calculated independently with dark field observations. The significance of the excess is given by propagation of errors,

$$\sigma = \frac{N_{On} - \rho N_{Off}}{\sqrt{N_{On} + \rho^2 N_{Off}}} \quad (4.10)$$

This equation for significance is not completely correct for a number of reasons. First, the value of  $\rho$  calculated from dark field data has an error associated with it,  $\rho \pm \Delta\rho$ . The calculation of significance equation must account for this error, lowering the significance somewhat. Additionally, as described in Li and Ma (1983), calculation of significance should be based on a likelihood approach rather than the simple propagation of errors above, which systematically underestimates the significance (in the absence of  $\Delta\rho$ ). The corrected equations for significance are listed in appendix D. In practice, the differences between the calculated values are small, and equation 4.10 can be employed.

## 5. OBSERVATIONS

VHE observations of 19 unidentified EGRET sources are presented in this chapter. The sources, listed in table 5.1, and depicted in figure 5.1, are distributed across the portion of the sky visible from southern Arizona, with seven at low Galactic latitude ( $b < 5^\circ$ ), three at mid latitudes ( $5^\circ < b < 15^\circ$ ) and nine at high latitude. Eight have entries in both the 3EG and GeV catalogs, two are listed only in the GeV catalog, the remainder only in the 3EG catalog. The sample includes 3EG J1835+5918 (#14 in the table and figure), which has the hardest spectrum among all unidentified 3EG sources (fifth hardest from all 3EG sources), a large 100 MeV flux and a low variability index. Included also is 3EG J1337+5029 (#12), which has the fourth hardest spectrum from the unidentified sources. Five objects are consistent with being in the Gould Belt, in particular #4, #5 and #6 lie approximately in the direction of the center of the Belt and are each  $> 10^\circ$  from the Galactic plane.

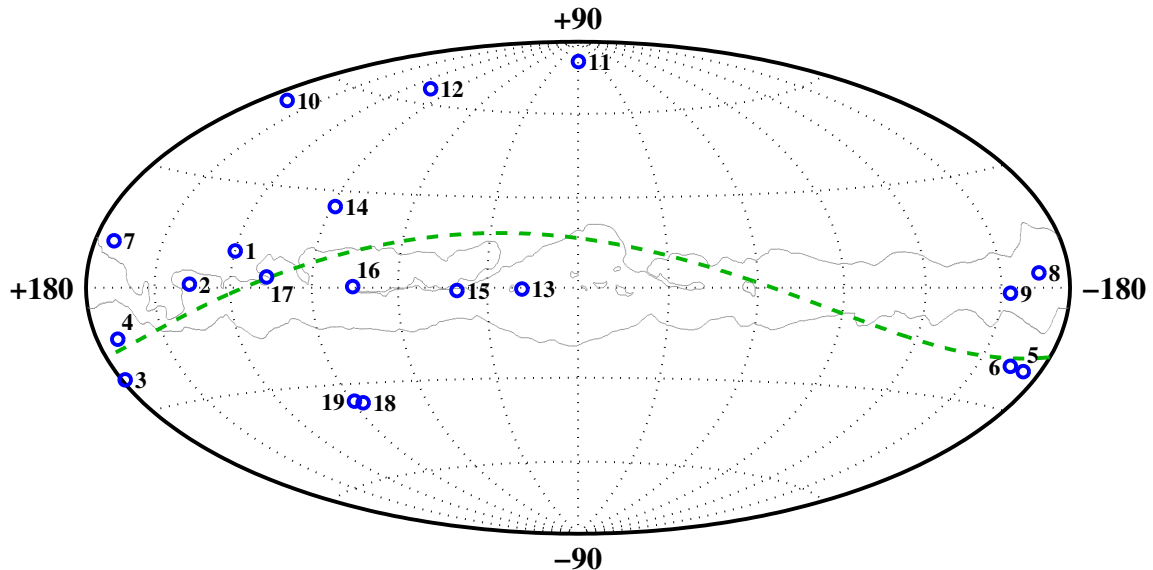


**Figure 5.1:** The 19 unidentified EGRET sources considered in this survey, plotted in Galactic coordinates. The Milky Way and Gould Belt are also depicted, as described in chapter 1. The candidate sources are labeled by their positions in table 5.1.

**Table 5.1: Summary of the 3EG and GeV catalog entries for the 19 unidentified sources observed in the survey.**

	Source Name	Coordinates <sup>1</sup>		Third EGRET Catalog				GeV Catalog				Var. <sup>4</sup>
		<i>b</i>	<i>l</i>	Error <sup>2</sup> $\theta_{95}$ [deg]	$F \pm \Delta F$	Spectrum <sup>3a</sup> $\Gamma \pm \Delta\Gamma$	Error $\theta_{95}$ [deg]	$F \pm \Delta F$	Flux <sup>3b</sup>	$F \pm \Delta F$	Indx. <sup>4</sup>	
1	3EG J0010+7309	10.56	119.87	0.25×0.22	42.3±5.5	1.85±0.10	0.43	-	5.8±1.2	0.26	-	-
2	3EG J0241+6103	0.99	135.85	0.21×0.15	69.3±6.1	2.21±0.07	0.31	-	6.9±1.3	0.38	-	-
3	3EG J0423+1707	-22.21	178.68	0.88×0.65	15.8±2.7	2.43±0.21	-	-	-	0.42	-	-
4	GeV J0433+2907	-12.58	170.50	0.19×0.16	22.0±2.8	1.90±0.10	0.35	-	3.3±0.7	0.40	-	-
5	3EG J0450+1105	-20.55	187.89	0.65×0.61	14.9±2.5	2.27±0.16	-	-	-	1.13	-	-
6	GeV J0508+0540	-19.81	195.32	-	-	-	-	0.62	1.4±0.4 <sup>6</sup>	-	-	-
7	3EG J0613+4201	11.45	171.38	0.66×0.46	9.0±2.3	1.92±0.26	0.65	-	1.8±0.6 <sup>6</sup>	0.72	-	-
8	3EG J0628+1847	3.64	193.60	0.66×0.49	23.9±4.0	2.30±0.10	-	-	-	-	-	-
9	3EG J0634+0521	-1.22	206.15	0.85×0.50	15.0±3.5	2.03±0.26	-	-	-	<0.88	-	-
10	3EG J1009+4855	52.15	166.93	1.12×0.80	4.8±1.4	1.90±0.37	-	-	-	<0.94	-	-
11	3EG J1323+2200	81.15	359.63	0.52×0.43	5.2±1.6	1.86±0.35	-	-	-	1.09	-	-
12	3EG J1337+5029	65.06	105.18	0.77×0.66	9.2±2.6	1.83±0.29	-	-	-	0.53	-	-
13	3EG J1826-1302	-0.42	18.41	0.55×0.39	46.3±7.3	2.00±0.11	0.32	-	9.9±1.7	0.88	-	-
14	3EG J1835+5918	25.08	88.74	0.16×0.13	60.6±4.4	1.69±0.07	0.27	-	10.2±1.4	0.15	-	-
15	GeV J1907+0557	-0.88	40.08	-	-	-	-	0.38×0.28	9.2±1.9	-	-	-
16	Gev J2020+3658	0.24	75.29	0.35×0.26	59.1±6.2	1.86±0.10	0.28×0.21	-	11.2±1.5	0.36	-	-
17	3EG J2227+6122	3.19	106.55	0.50×0.41	41.3±6.1	2.24±0.14	0.54	-	3.9±1.2 <sup>6</sup>	0.20	-	-
18	3EG J2248+1745	-36.15	86.00	1.14×0.78	12.9±3.5	2.11±0.39	-	-	-	0.65	-	-
19	3EG J2255+1943	-34.35	89.85	2.67×2.33	5.8±2.8	2.36±0.61	-	-	-	1.18	-	-

<sup>1</sup> Galactic coordinates from the 3EG or GeV catalog as appropriate.

<sup>2</sup> Elliptical fits to 95% error contours for 3EG sources from Mattox et al. (2001).

<sup>3</sup> Flux at energies greater than (a) 100 MeV and (b) 1 GeV in units of  $10^{-8} \text{ cm}^{-2} \text{s}^{-1}$ .

<sup>4</sup> Variability index from Nolan et al. (2003), higher values indicate more source variability.

<sup>5</sup> Listed as source of repeating weak outbursts of GeV  $\gamma$ -rays (Table 2 of Macomb and Lamb, 1999).

<sup>6</sup> Listed as a low-significance source of GeV  $\gamma$ -rays in table 2 or 3 of Lamb and Macomb (1997).

<sup>7</sup> Nolan et al. (2003) present variability indices for 3EG sources only.

<sup>8</sup> As noted in Nolan et al. (2003), 3EG J0628+1847 failed a consistency check during the analysis.

## 5.1 Individual observations

Details and results of the observations are presented below, with a discussion of each candidate source and possible counterparts in the fields of view. For each object, with the exception of GeV J0508+0540, a two dimensional analysis has been performed and a map of the excess (or deficit) of  $\gamma$ -ray-like events produced. For objects where a significant excess of events is detected, a map of the significance of the emission is presented. For those without a significant excess, i.e. those which do not have an excess at a  $3\sigma$  level or higher, a map of the upper limit of VHE  $\gamma$ -ray emission is presented, at a 99% confidence level. The maps are overlayed with the 3EG error contours<sup>15</sup> at the 50%, 69%, 95% and 99% confidence level, as described by Mattox et al. (1996). For GeV sources, the 95% error ellipse is shown, based on the parameters in the catalog. From each of these maps, the maximum upper limit within the 3EG (or GeV) error-box is presented, corresponding to a conservative VHE upper limit for the HE  $\gamma$ -ray source. For each object that has potentially interesting counterparts at other wavelengths, such as radio and x-ray counterparts suggested in the literature, upper limits are also presented for emission from the location of the possible counterparts; these limits are generally lower than the limit on emission from the entire error-box. Finally, for the sources with an entry in the 3EG catalog, the  $\gamma$ -ray spectrum is shown, extrapolated to 1 TeV, with the VHE upper limit for the error-box overlaid.

### 5.1.1 3EG J0010+7309

The 3EG source J0010+7309 has long been suggested as possibly associated with the supernova CTA 1, G119.5+10.2 in Green (2001), on the basis of its position. The first images of CTA 1 at x-ray energies were recorded with the ROSAT instrument; the source has been well studied with later x-ray instruments, such as ASCA and XMM-Newton (Seward et al., 1995; Slane et al., 1997, 2004). The observations indicate that the x-ray emission from CTA 1 must be described by three components; the first is a

---

<sup>15</sup>The contours were extracted from the on-line version of the catalog which contains maps of the  $(TS)^{1/2}$  likelihood statistic

thermal, shell-type, component associated with the Sedov expansion of the remnant into the inter-stellar medium (ISM), which appears to be occurring in a region of low density. The shell-type nebula is large,  $\sim 107$  arcmin in diameter, and  $1.4 \pm 0.3$  kpc. in distance. There is a “blow-out” region in the north of the nebula where the nebula has evidently expanded quickly into a region of particularly low density. The second x-ray component is evident as a region of bright, non-thermal emission at the center of the nebula. This emission is consistent with synchrotron emission from a central PWN, with a power-law spectral index of 2.3 and total x-ray luminosity of  $L_X = 5.6 \times 10^{33}$  erg s $^{-1}$ . Finally, ROSAT detected a non-thermal compact point source, RX J0007.0+7302, which may be associated with a pulsar at the center of the nebula, although no pulsations have been detected in radio or x-rays. Slane et al. (2004) report on XMM observations of the compact source; its spectrum is best fit by a power-law with index of 1.5 and total luminosity of  $L_X = 4.7 \times 10^{31}$  erg s $^{-1}$ .

The  $\gamma$ -ray source has a large, steady  $>100$  MeV flux, a hard spectrum of  $\Gamma = 1.85$ , with possible evidence of softening above 2 GeV and a low variability index of  $\delta = 0.26$ . Brazier et al. (1998) suggest that the  $\gamma$ -rays are most likely associated with the compact source which lies within the 95% confidence contour of the EGRET observations. As noted by Slane et al. (2004), the power-law x-ray spectrum of the compact source can be extrapolated to  $\gamma$ -ray energies without a spectral break. Other compact x-ray sources in the region are suggested as possible counterparts by Seward et al. (1995); Brazier et al. (1998) dismiss all but RX J0010+7309.

The VHE observations reported here consist of a combined 195 min. exposure on the source, pointed at the center of the nebula, offset by 0.27 degrees from the center of the 3EG source. The data were taken during late 1999. No emission is detected at a significant level, an upper limit on emission from anywhere within the 95% error circle of  $F_{(>350\text{GeV})} < 2.2 \times 10^{-11}$  cm $^{-2}$  s $^{-1}$  is calculated. Figure 5.2 shows the map of the upper limit of point source emission from the region and the 3EG power-law spectrum extrapolated to 350 GeV, with the upper limit superimposed. It is clear from the diagram that extrapolating the EGRET power-law to the VHE regime is in conflict with these observations by an order of magnitude. A cut-off

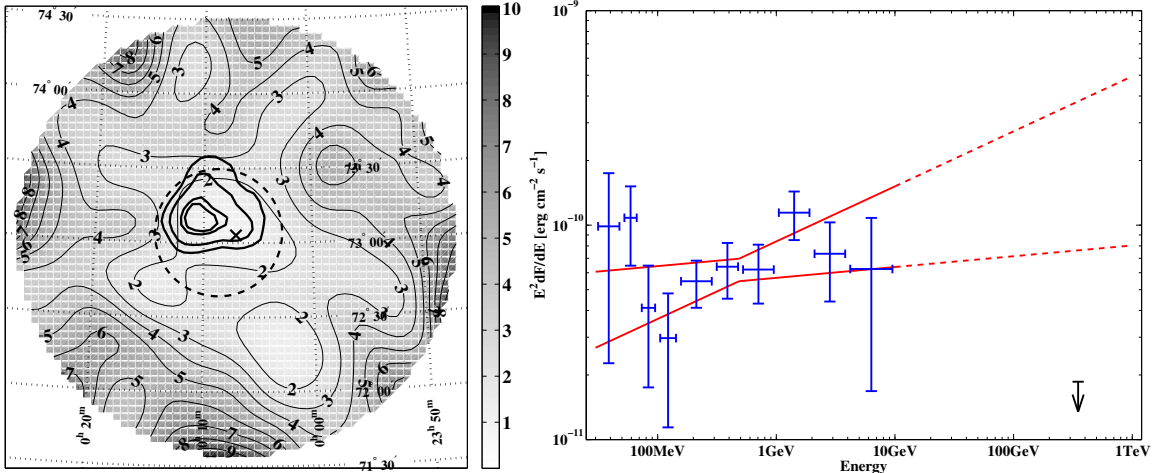


**Figure 5.2:** (Left) Limits on emission from 3EG J0010+7309 in units of  $10^{-11} \text{ cm}^{-2} \text{ s}^{-1}$ . The 3EG error contours are overlaid as heavy lines, the GeV catalog contour is shown as a broken circle. (right) Spectrum from the on-line version of the 3EG catalog with the limit at 350 GeV.

**Table 5.2: Upper limits for candidates in 3EG J0010+7309 field.**

Source Name	Coordinates	Extent	Upper Limit
	$\alpha_{2000}$	$\delta_{2000}$	$\times 10^{-11} \text{ cm}^{-2} \text{ s}^{-1}$
3EG J0010+7309	$00^h 09^m 36.6^s$	$+73^\circ 10' 57.4''$	$0.25 \times 0.22$
RX J0007.0+7302	$00^h 07^m 02.2^s$	$+73^\circ 03' 07.1''$	1.1

in the spectrum is required to reconcile the observations. Some evidence for this cut-off is also visible in the highest energy bins of the EGRET spectrum. The cut-off supports the supposition that the  $\gamma$ -rays originate from a pulsar. The upper limit from RX J0007.0+7302, whose location is marked with an “X” in figure 5.2, is  $F_{(>350 \text{ GeV})} < 1.1 \times 10^{-11} \text{ cm}^{-2} \text{ s}^{-1}$ .

### 5.1.2 3EG J0241+6103

First detected by the COS-B instrument, and designated as 2CG 135+01, the  $\gamma$ -ray source 3EG J0241+6103 has been the subject of much study over the past 25 years. On the basis of the COS-B position, the source was been associated with the quasar QSO 4U0241+61, at redshift  $z = 0.0438$ , (Maraschi et al., 1978; Apparao et al., 1978) and with the non thermal radio source GT 0236+610 (Gregory and Taylor, 1978;

(Hermsen et al., 1977). Observations with EGRET refined the position estimate, and eliminated the possible association with the quasar (Kniffen et al., 1997), which lies over a degree away. The non-thermal radio source quickly came to be associated with the binary system LSI +61°303 (Gregory et al., 1979), an unusual object which has been identified at radio, optical and x-ray energies. LSI +61°303 exhibits periodic radio outbursts at a period of  $\sim$ 26.5 days (Taylor and Gregory, 1982). The outbursts do not occur at a constant phase relative to this period; there is evidence that both the phase and amplitude of the outbursts vary slowly with a  $\sim$ 4.6 yr. phase modulation period (Gregory et al., 1999; Gregory, 2002). Paredes et al. (1997) report a periodic modulation of the x-ray light-curve from the ASM satellite, which appears to occur at a constant orbital phase, corresponding to the periastron. No pulsations have been detected in the x-ray signal, suggesting that the x-ray emission is not directly from the neutron star companion. Massi et al. (2001) report the existence of a one-sided jet from the object on a milli-arcsecond scale. A number of models have been suggested to explain the radio and x-ray emission and to account for the possibility of  $\gamma$ -ray emission. Gregory and Neish (2002) provide an introduction to the observational status of this object and provide references to the various emission models.

The 3EG source has a spectral index of  $\Gamma = 2.21$ , a large 100 MeV flux and shows evidence of variability. Kniffen et al. (1997) show that the variations in the  $\gamma$ -ray flux are not correlated with the radio outbursts. An exposure of 524 min. was taken with the Whipple telescope between November 2000 and February 2001, centered on the binary system, offset by  $\sim$ 0.25° from the center of the 3EG source. No significant emission is detected and an upper limit of  $F_{(>350\text{ GeV})} < 2.2 \times 10^{-11} \text{ cm}^{-2} \text{ s}^{-1}$  is derived for emission within the 3EG 95% contour. Figure 5.3 shows a map of upper limits of emission from the region with the location of LSI +61°303 and QSO 4U0241+61 indicated with an “X” (near the center and displaced by a degree to the north respectively). It is evident from the figure that the binary system lies outside of the 95% confidence contour of the EGRET data, although it does lie within the considerably larger 95% confidence circle from the GeV catalog. As noted by Roberts et al. (2001b) based on an image of the region with the ASCA instrument, there are no good x-ray

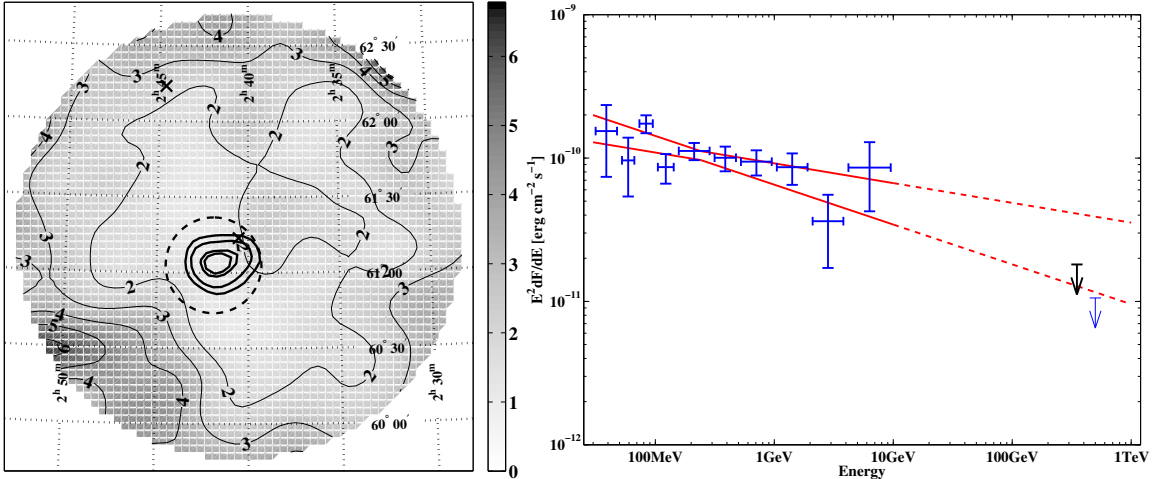


**Figure 5.3:** (Left) Limits on emission from 3EG J0241+6103 in units of  $10^{-11} \text{ cm}^{-2} \text{ s}^{-1}$ . The 3EG error contours are overlaid as heavy lines, the GeV catalog contour is shown as a broken circle. (right) Spectrum from the on-line version of the 3EG catalog with upper limit at 350 GeV. The limit at 500 GeV from Hall et al. (2003a) is also indicated.

**Table 5.3: Upper limits for candidates in 3EG J0241+6103 field.**

Source Name	Coordinates $\alpha_{2000}$	$\delta_{2000}$	Extent deg	Upper Limit $\times 10^{-11} \text{ cm}^{-2} \text{ s}^{-1}$
3EG J0241+6103	$02^h 41^m 31.3^s$	$+61^\circ 04' 12.3''$	$0.21 \times 0.15$	2.2
LSI +61°303	$02^h 40^m 31.4^s$	$+61^\circ 13' 45.6''$	-	1.7
QSO 4U0241+61	$02^h 44^m 37.3^s$	$+62^\circ 13' 57.0''$	-	2.3

candidates within the 95% confidence contour for this source. Table 5.3 shows the upper limits derived for these candidate sources.

LSI +61°303 was previously observed with the Whipple telescope between 1996 and 1999, with no significant excess of  $\gamma$ -rays being observed; a limit of  $F_{(>500 \text{ GeV})} < 0.88 \times 10^{-11} \text{ cm}^{-2} \text{ s}^{-1}$  was reported by Hall et al. (2003a). Assuming that the 3EG source corresponds to the LSI +61°303, this paper shows that an exponential cutoff is required in the extrapolated EGRET spectrum to accommodate the VHE observations. Almost all of the flux phase space at 350 GeV allowed by extrapolating the EGRET spectrum is ruled out by the upper limit reported here. After a quarter century of study, 2CG 135+01 remains one of the most puzzling of all  $\gamma$ -ray sources.

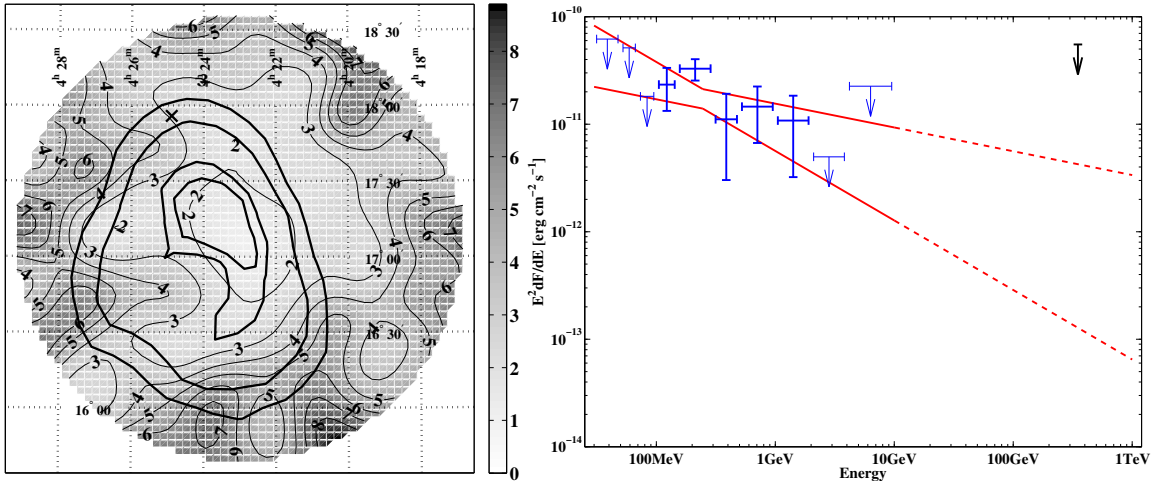


**Figure 5.4:** (Left) Limits on emission from 3EG J0423+1707 in units of  $10^{-11} \text{ cm}^{-2} \text{ s}^{-1}$ . The 3EG error contours are overlaid as heavy lines. (Right) Spectrum from the on-line version of 3EG catalog with the upper limit at 350 GeV.

**Table 5.4: Upper limits for candidates in 3EG J0423+1707 field.**

Source Name	Coordinates	Extent	Upper Limit
	$\alpha_{2000}$	$\delta_{2000}$	$\times 10^{-11} \text{ cm}^{-2} \text{ s}^{-1}$
3EG J0423+1707	$04^h 23^m 56.5^s$	$+16^\circ 56' 27.4''$	$0.88 \times 0.65$
B0422+1749	$04^h 24^m 53.4^s$	$+17^\circ 55' 49.9''$	-

### 5.1.3 3EG J0423+1707

3EG J0423+1707 is an EGRET source about which very little is known at other wavelengths. The 3EG error circle is large, at  $0.88^\circ \times 0.65^\circ$ , and it has the softest spectrum among all of the sources chosen for this survey. Mattox et al. (2001) suggest the radio source B0422+1749 as a possible, but unlikely, counterpart, with a probability of  $2 \times 10^{-4}$ .

The VHE observation consists of 193 min. of data pointed at the center of the 3EG source. No significant emission is observed, and an upper limit of  $F_{(>350\text{GeV})} < 6.6 \times 10^{-11} \text{ cm}^{-2} \text{ s}^{-1}$  is derived for VHE emission within the 95% confidence contour. A limit of  $F_{(>350\text{GeV})} < 2.8 \times 10^{-11} \text{ cm}^{-2} \text{ s}^{-1}$  applies to the radio source B0422+1749. As is clear from figure 5.4, this limit does not constrain the extrapolated EGRET spectrum.

### 5.1.4 GeV J0433+2907

The  $\gamma$ -ray source 3EG J0433+2908 is listed as possibly being associated with the radio source 87GB 0430+2859 in the 3EG catalog, and was assumed to be an AGN. The  $\gamma$ -ray source is unusual for an EGRET AGN; the spectrum is particularly hard with no indication of a break at energies up to 10 GeV. Dingus and Bertsch (2001), analyzed all of the EGRET photons at energies above 10 GeV and show that three are consistent with having originated from the location of the radio source. At these energies the EGRET point-spread function is considerably better than at 100 MeV; given this improved PSF, they calculate a probability of  $1.9 \times 10^{-6}$  that three photons could be associated with the source location purely by chance. Wallace et al. (2001) gather together compelling evidence that the radio source corresponds to an AGN: optical observations show a featureless optical spectrum typical of a BL Lac and the spectral energy distribution<sup>16</sup>, or SED, shows a clear two-peaked distribution, indicating synchrotron/inverse-Compton (IC) emission that is typical for AGN. Assuming that the  $\gamma$ -ray source corresponds to the radio/x-ray source, the SED for 3EG J0433+2908 is shown in figure 5.6, and will be discussed further below. No successful redshift measurements have been made for this object, Halpern et al. (2003) report on repeated attempts to determine the redshift and argue that  $z > 0.3$  for this object.

Between November 1999 and January 2002 a total of 1900 min. of data were taken with the Whipple instrument pointed at the GeV catalog source location, which is coincident with the radio/x-ray source. Prior to the publication of Dingus and Bertsch (2001), 500 min. of data were collected in the ON/OFF mode, suitable for analysis using the two-dimensional reconstruction technique. No significant emission was detected; figure 5.5 shows the upper limits of emission that can be derived from these data. The upper limit within the 3EG 95% error contour is  $F_{(>350\text{GeV})} < 1.6 \times 10^{-11} \text{ cm}^{-2} \text{ s}^{-1}$ . This limit is displayed with the 3EG spectrum in figure 5.5. To

---

<sup>16</sup>An SED, or  $\nu F_\nu$  plot, for an object is a graphical representation of the power an instrument would receive across the spectrum given the assumption that its bandwidth is proportional to the frequency. SEDs are usually displayed in units of  $\text{Jy Hz}$ ,  $\text{W m}^{-2}$  or  $\text{erg cm}^{-2} \text{ s}^{-1}$  and are equivalent to the  $E^2 dF/dE$  plots presented in this chapter.

**Table 5.5:** Upper limits for candidates in 3EG J0433+2908 field.

Source Name	Coordinates		Extent	Upper Limit $\times 10^{-11} \text{ cm}^{-2} \text{ s}^{-1}$
	$\alpha_{2000}$	$\delta_{2000}$	deg	
3EG J0433+2908	$04^h 33^m 35.1^s$	$+29^\circ 07' 42.2''$	$0.19 \times 0.16$	1.6
87GB 0430+2859	$04^h 33^m 37.5^s$	$+29^\circ 05' 53.0''$	-	0.8

reconcile the limit with the increasing EGRET spectrum a cut-off in the spectrum at an energy greater than 10 GeV is required. The remainder of the VHE data was taken in the TRACKING mode, and is not suitable for 2D analysis but can provide a more sensitive limit on emission from the radio/x-ray source. A limit of  $F_{(>350 \text{ GeV})} < 0.76 \times 10^{-11} \text{ cm}^{-2} \text{ s}^{-1}$  is derived from all of the data combined. This limit is shown on a SED for the object in figure 5.6. It must be noted that the distribution was produced with *non-contemporaneous* data; since the SED of an AGN can change considerably as the sources goes from a quiescent to a flaring state, figure 5.6 should be considered as approximate. The double peaked structure is clearly visible, with the peak in the synchrotron emission occurring somewhere in the optical to x-ray band and the peak in the IC emission occurring between the HE and VHE  $\gamma$ -ray regimes.

Typically, for a low-frequency peaked BL Lac (LBL) the peak in the synchrotron emission occurs in the far-infrared to optical bands, with the IC peak below 100 MeV, so that the emission is falling through the EGRET energy range. Conversely, for an HBL (high frequency peaked BL Lac) the peak in the synchrotron emission occurs at UV to soft x-ray energies. The IC component then peaks at GeV to TeV energies. The SED for this object resembles most that of an HBL. The object seems to be intermediate between the typical EGRET BL Lac and the VHE selected extreme HBLs. It is reasonable to conclude that a cutoff is required between 10 GeV and  $\sim 100$  GeV, either due to a feature intrinsic to the source spectrum or due to absorption of the  $\gamma$ -ray signal in the extra-galactic background light, especially if the object is at a distance of  $z > 0.3$ . On the other hand, it is also possible that the state of the object was different when the various observations were made, i.e. flaring when EGRET observed it and quiescent during the VHE observations, in which case a cutoff may not be required. However, since the EGRET spectrum represents a mean spectrum over all viewing periods, this is unlikely.

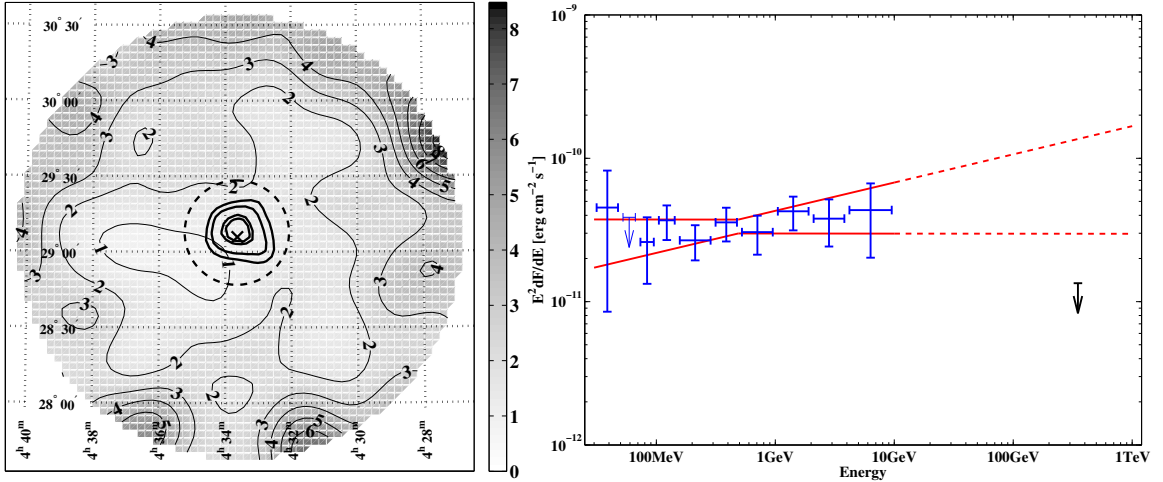


Figure 5.5: (Left) Limits on emission from 3EG J0433+2908 in units of  $10^{-11} \text{ cm}^{-2} \text{ s}^{-1}$ . The 3EG error contours are overlaid as heavy lines, the GeV catalog contour is shown as a broken circle. (Right) Spectrum from the on-line version of the 3EG catalog with the upper limit at 350 GeV.

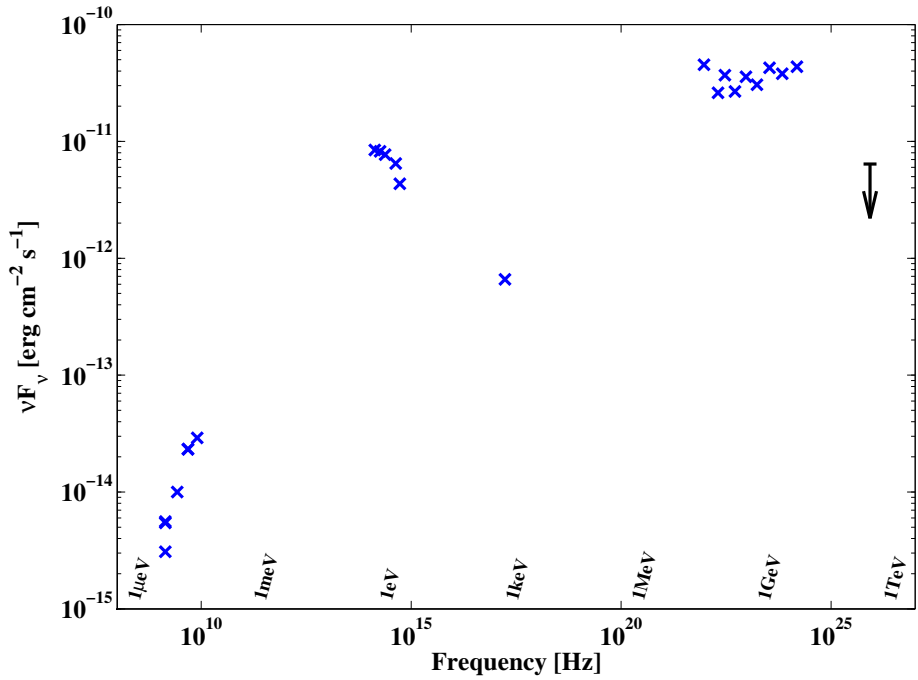


Figure 5.6: Spectral energy distribution for the radio/x-ray source RX J0433.5+2906. The radio data come from the NASA/IPAC extragalactic database (NED). The IR observations are from the 2 micron all sky survey (2MASS). Optical data are from Halpern et al. (2003). The x-ray flux is from the ROSAT all sky survey bright source catalog (RASS-BSC). Finally, the differential  $\gamma$ -ray flux is from the on-line 3EG catalog.

### 5.1.5 3EG J0450+1105

With a spectral index of 2.27, 3EG J0450+1105 has one of the softer spectra of the sources chosen in this survey. The source is not detected as a significant source in the GeV catalog, although it is listed as a “source of GeV gamma rays based upon the search for repeating, weak outbursts” in the second part of the catalog (Macomb and Lamb, 1999). The source is consistent with being highly variable: it has a variability index of 1.13 and its flux is listed in the 3EG catalog as having a maximum of  $109.5 \times 10^{-8} \text{ cm}^{-2} \text{ s}^{-1}$  during EGRET viewing period #36 while its average flux over all viewing periods is  $14.9 \times 10^{-8} \text{ cm}^{-2} \text{ s}^{-1}$ .

Mattox et al. (2001) suggest that the  $\gamma$ -ray source is associated with the radio source B0446+1116, an AGN, with a probability level of 0.14. Halpern et al. (2003) confirm this association, and present their attempts to resolve a redshift for the object. They claim that the accepted redshift of  $z = 1.207$  is likely incorrect, and that the featureless spectrum they obtained makes it impossible to derive an unambiguous redshift. Depending on how the minor features in the spectrum are interpreted, they suggest  $z = 0.74$  or  $z = 0.21$  as possible values, with the lower value being less likely.

A total of 264 min. of VHE observations were made between November 2000 and February 2001. No significant excess was seen, although there was a  $3\sigma$  deficit of events at one location. Given the large number of fields viewed in this survey, a  $3\sigma$  deficit (or excess) is not statistically significant, see figure 4.7. The upper limits derived from the observations are shown in figure 5.7 and summarized in table 5.6. The limit for emission within the large EGRET error-box is  $F_{(>350 \text{ GeV})} < 5.0 \times 10^{-11} \text{ cm}^{-2} \text{ s}^{-1}$ .

Figure 5.8 shows an SED for the radio source obtained from published data. The source was only weakly detected by ROSAT, it is absent from the ROSAT bright source catalog (RASS-BSC) but is present in the electronic version of the ROSAT all sky survey (RASS). The SED clearly shows the two peaked structure, typical of an LBL, with the synchrotron emission peaking in the IR-optical band and the IC

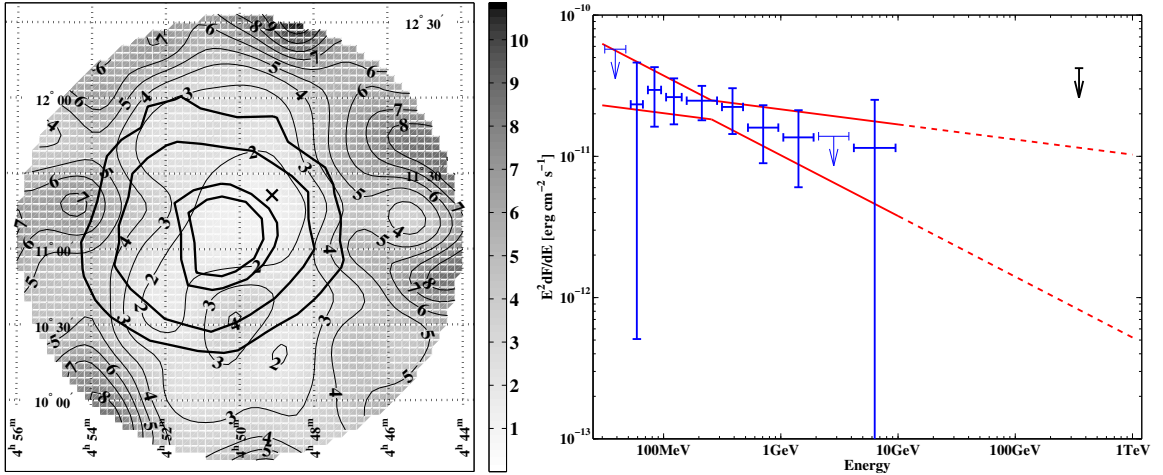


Figure 5.7: (Left) Limits on emission from 3EG J0450+1105 in units of  $10^{-11} \text{ cm}^{-2} \text{ s}^{-1}$ . The 3EG error contours are overlaid as heavy lines. (Right) Spectrum from the on-line version of the 3EG catalog with the limit at 350 GeV.

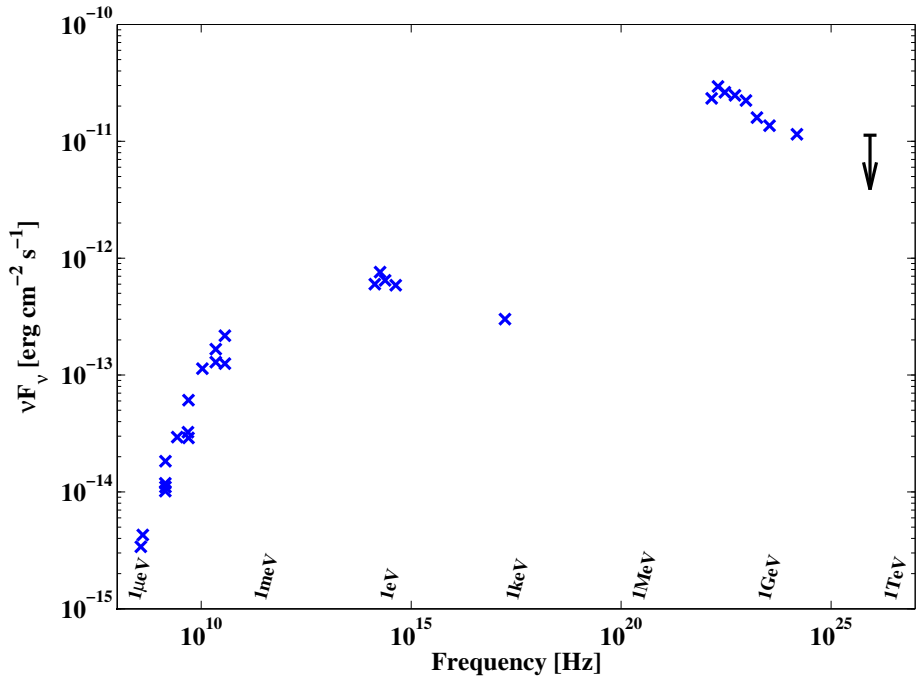


Figure 5.8: Spectral energy distribution for the radio/x-ray source PKS B0446+112. The data are from the same sources as in figure 5.6. The x-ray source (1RXS J044903.0+112120) was not strong enough to be included in the RASS-BSC, the x-ray flux was estimated from the count rate in the RASS catalog, and should be considered as approximate.

**Table 5.6:** Upper limits for candidates in 3EG J0450+1105 field.

Source Name	Coordinates		Extent	Upper Limit $\times 10^{-11} \text{ cm}^{-2} \text{ s}^{-1}$
	$\alpha_{2000}$	$\delta_{2000}$	deg	
3EG J0450+1105	$22^h 15^m 06.5^s$	$+31^\circ 28' 55.7''$	$0.65 \times 0.61$	5.0
B0446+1116	$04^h 49^m 07.7^s$	$+11^\circ 21' 28.6''$	-	1.3

component peaking below 100 MeV. The upper limit derived for the location of the radio source is also shown; it is clear from the figure that, due to the soft spectrum, the VHE upper limit does not constrain the emission significantly.

### 5.1.6 GeV J0508+0540

The  $\gamma$ -ray source GeV J0508+0540 is listed in the GeV catalog as a “low-significance source”, with  $23 \pm 7$  photons detected from the source at  $E > 1 \text{ GeV}$ . It was not seen significantly at 100 MeV, and consequently had no corresponding 3EG entry. Dingus and Bertsch (2001) list two EGRET photons with energies greater than 40 GeV from the object. The two photons are consistent with having originated from the BL Lac 0509+056, to within 4 arcmin, with probability of  $1.3 \times 10^{-8}$  of occurring by chance. Halpern et al. (2003) report several unsuccessful attempts to measure the redshift of this object; the optical spectra they recorded were featureless and no host galaxy could be resolved.

The VHE observations of this source consist of 842 min. of data taken between October and December 2001, pointing at the radio/x-ray source. The data were recorded in the TRACKING mode, under the assumption that the  $\gamma$ -ray source was the AGN, and are unsuitable for analysis with the two-dimensional method. For this source alone, no source maps are presented. No significant excess was observed, the limit on emission from the AGN is  $F_{(>350 \text{ GeV})} < 0.73 \times 10^{-11} \text{ cm}^{-2} \text{ s}^{-1}$ .

An approximate SED for this object is presented in figure 5.9. Since no 3EG detection was achieved, a differential spectrum is not available for this source; an upper limit at 100 MeV and the integral flux from the GeV catalog, transformed into a differential

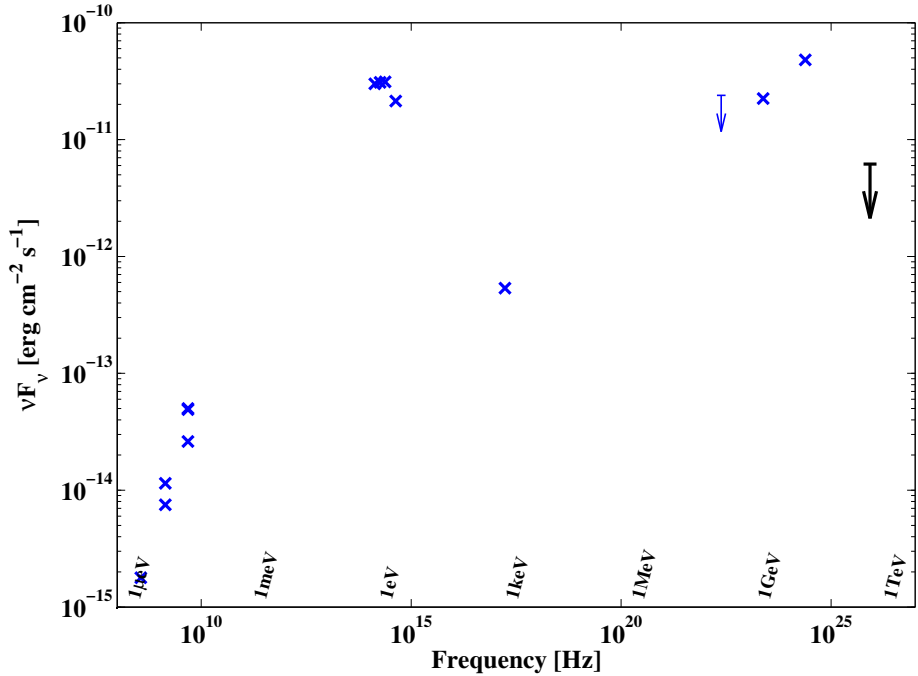


Figure 5.9: Spectral energy distribution for the radio/x-ray source RX J0509.3+0541. The data come from the same sources as in figure 5.6 with the 100 MeV upper limit from Hartman et al. (1999) (see figure 1.4), the 1 GeV  $\gamma$ -ray flux from Lamb and Macomb (1997), and the preliminary 10 GeV point from Dingus (2001).

**Table 5.7: Upper limits for RX J0509.3+0541.**

Source Name	Coordinates $\alpha_{2000}$	$\delta_{2000}$	Extent deg	Upper Limit $\times 10^{-11} \text{ cm}^{-2} \text{ s}^{-1}$
RX J0509.3+0541	$05^h 09^m 26.0^s$	$+05^\circ 41' 35.4''$	-	0.73

flux assuming a differential power-law spectrum of index 2.0<sup>17</sup>, are displayed. No flux at  $>10$  GeV is listed in Dingus and Bertsch (2001), due to the small number of photons detected and a lack of understanding of the performance of anti-coincidence shield at these energies. A preliminary flux was obtained from the author (Dingus, 2001) and is plotted in figure 5.9.

EGRET did not resolve the peak in the high energy component of the emission below 10 GeV, suggesting that the object resembles an HBL. There is insufficient data at

<sup>17</sup>The spectrum is probably harder than 2.0 so the fluxes may be a little *higher* than plotted.

lower energies to resolve the peak in the low energy component; it is possible that the synchrotron emission peaks at or below the IR/optical points in the SED, in which case the x-ray emission results from IC up-scattering. Alternatively, the low energy emission may peak between the optical and x-ray energies with the x-rays resulting from synchrotron emission. Although it is not possible to definitely rule out either scenario, usual SSC models would have difficulty in explaining the  $\gamma$ -ray emission (both lack of 100 MeV emission and increasing emission through 10 GeV) in the former case. It was the fact that, like many VHE selected HBLs, the source was not seen in the 3EG catalog that initially suggested that this source would be an interesting one to study in the VHE regime. Based on the preliminary 10 GeV point, a strong cutoff in the emission is required to accommodate the VHE upper limit. The cutoff may be from absorption in the extragalactic background light if the source is at a large redshift, or may be intrinsic to the source spectrum.

### 5.1.7 3EG J0613+4201

3EG J0613+4201 is a 100 MeV and 1 GeV  $\gamma$ -ray source at mid-Galactic latitude with a relatively hard spectrum, weak flux, large error-box and a high variability index. Mattox et al. (2001) list three possible radio counterparts for the source, all outside of the 95% 3EG contour. None of the potential associations are very compelling, in each case the probability of the association being correct is listed as  $\leq 10^{-4}$ .

The VHE observations of this source, which were made over two observing seasons, between November 2001 and January 2003, consist of 275 min. of data taken pointed at the center of the 3EG source. No significant emission was detected and a limit

**Table 5.8: Upper limits for candidates in 3EG J0613+4201 field.**

Source Name	Coordinates		Extent	Upper Limit
	$\alpha_{2000}$	$\delta_{2000}$	deg	$\times 10^{-11} \text{ cm}^{-2} \text{ s}^{-1}$
3EG J0613+4201	$06^h 14^m 20.6^s$	$+41^\circ 59' 51''$	$0.66 \times 0.46$	4.3
87GB 0609+4123	$06^h 12^m 51.2^s$	$+41^\circ 22' 37''$	-	1.9
87GB 0612+4131	$06^h 16^m 22.4^s$	$+41^\circ 30' 48''$	-	3.1
87GB 0614+4209	$06^h 18^m 08.6^s$	$+41^\circ 08' 00''$	-	2.9

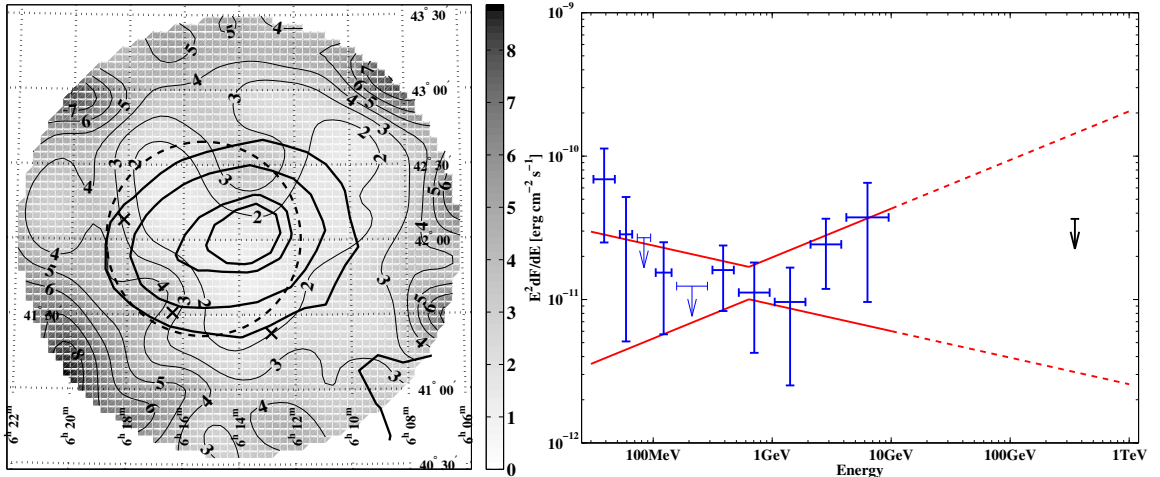


**Figure 5.10:** (Left) Limits on emission from 3EG J0613+4201 in units of  $10^{-11} \text{ cm}^{-2} \text{ s}^{-1}$ . The 3EG error contours are overlaid as heavy lines, the GeV catalog contour is shown as a broken circle. (Right) Spectrum from the on-line version of the 3EG catalog with the upper limit at 350 GeV.

of  $F_{(>350\text{GeV})} < 4.3 \times 10^{-11} \text{ cm}^{-2} \text{ s}^{-1}$  is placed on emission from within the 95% confidence contour. Upper limits for the region are presented in figure 5.10, with the locations of the three potential candidates marked. The limits derived for these locations are presented in table 5.8. The limit is not sensitive enough to rule out a simple extrapolation of the EGRET spectrum into the VHE regime.

### 5.1.8 3EG J0628+1847

The  $\gamma$ -ray source 3EG J0628+1847 has a relatively weak spectral index, an average 100 MeV flux and lies at a low Galactic latitude. Its variability index could not be determined by Nolan et al. (2003), since the source failed a consistency check during their analysis. Despite being close to the Galactic plane, Romero et al. (1999) report no positional associations with known SNR, OB associations or WR- and O-type stars. Mattox et al. (2001) list two radio sources from the Green Bank catalog in the field, one just inside the 95% confidence contour, the other just inside the 99% contour; these are listed as having probabilities of  $2 \times 10^{-4}$  and  $9 \times 10^{-4}$ , respectively, of being counterparts. The second radio source, 87GB 0628+1971, is listed as coincident with

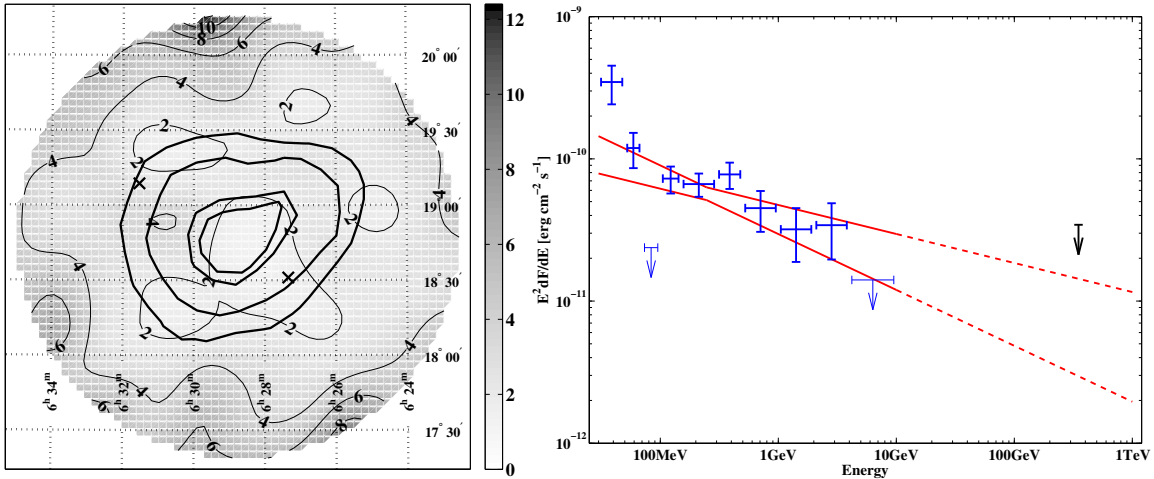


Figure 5.11: (Left) Limits on emission from 3EG J0628+1847 in units of  $10^{-11} \text{ cm}^{-2} \text{ s}^{-1}$ . The 3EG error contours are overlaid as heavy lines. (Right) Spectrum from the on-line version of the 3EG catalog with the limit at 350 GeV.

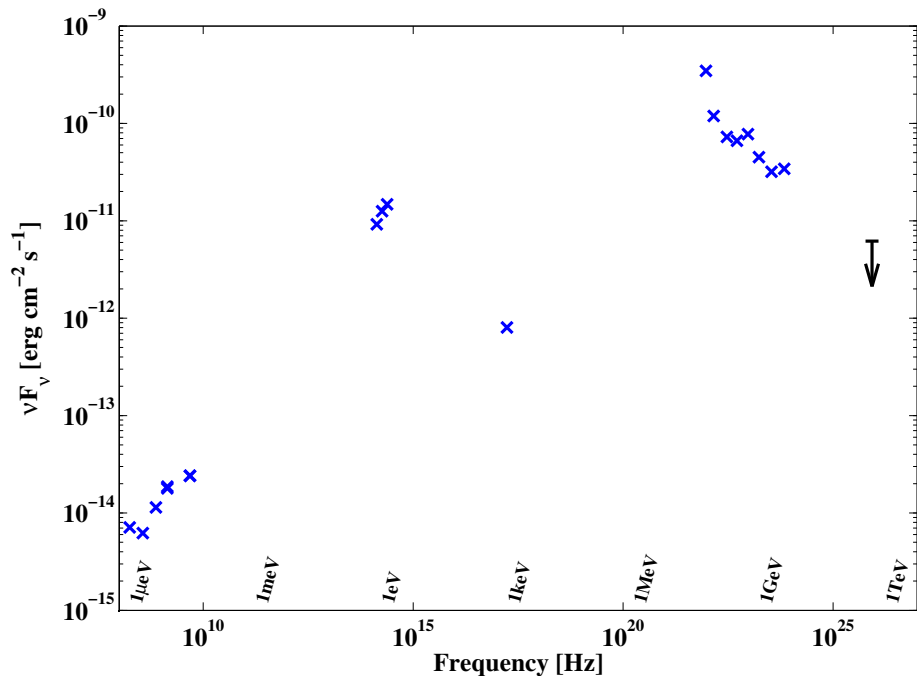


Figure 5.12: Spectral energy distribution for the radio/x-ray source RX J0631.4+1908 (87GB 0628+1911), assuming it is associated with the  $\gamma$ -ray source. The data come from the same sources as in figure 5.6.

**Table 5.9:** Upper limits for candidates in 3EG J0628+1847 field.

Source Name	Coordinates $\alpha_{2000}$	$\delta_{2000}$	Extent deg	Upper Limit $\times 10^{-11} \text{ cm}^{-2} \text{ s}^{-1}$
3EG J0628+1847	$06^h 28^m 36.1^s$	$+18^\circ 50' 35''$	$0.66 \times 0.49$	4.1
87GB 0624+1833	$06^h 27^m 20.5^s$	$+18^\circ 31' 04''$	-	1.5
87GB 0628+1911	$06^h 31^m 32.3^s$	$+19^\circ 08' 41''$	-	2.6

a ROSAT x-ray source by Laurent-Muehleisen et al. (1997) and has an associated IR point source in the 2MASS catalog.

VHE observations of the 3EG source were made between December 2001 and February 2003. A total of 331 min. of usable data were collected and analyzed using the two-dimensional technique. No significant emission was seen in the field; the upper limits on emission that are derived from the data are presented in figure 5.11. The upper limit from within the 95% error contour is  $F_{(>350\text{ GeV})} < 4.1 \times 10^{-11} \text{ cm}^{-2} \text{ s}^{-1}$ , and is displayed with the EGRET spectrum on the right hand side of figure 5.11. The VHE upper limit does not constrain an extrapolation of the EGRET spectrum to 350 GeV.

The upper limits for the two candidates from Mattox et al. (2001), are presented in table 5.9. Assuming that the  $\gamma$ -ray source is associated with 87GB 0628+1911, an approximate SED for the object is shown in figure 5.12. The distribution shows a bimodal structure, typical of an AGN. Since the HE component peaks somewhere below 100 MeV, the source is likely an LBL. The VHE limit appropriate to the source location does not significantly constrain the spectrum above 10 GeV.

### 5.1.9 3EG J0634+0521 and 3EG J0631+0642

The  $\gamma$ -ray sources J0634+0521 and J0631+0642 both lie in the region of the Monoceros supernova remnant, although neither is explicitly associated with it in the 3EG catalog. In addition, the GeV source J0633+0645 partially overlaps 3EG J0631+0642 and is listed as a possible counterpart to the SNR in Lamb and Macomb (1997).

The large shell-type SNR G205.5+0.5, or Monoceros Loop Nebula, is 220 arcmin in diameter, the fifth largest SNR in Green (2001). The SNR is thought to be

$1.39 \pm 0.1$  kpc distant, and approximately  $3 - 20 \times 10^4$  yr in age, i.e. in the Sedov expansion phase. Monoceros was first recognized as a source of 100 MeV  $\gamma$ -rays by Esposito et al. (1996). Jaffe et al. (1997) presented a map of EGRET  $\gamma$ -ray emission over a large area around the SNR, where they found evidence for an extended emission feature in the direction of the Rosette nebula. They suggest that, since  $\gamma$ -ray emission was not seen uniformly across the remnant, the  $\gamma$ -rays are produced in a region of enhanced shock acceleration at the interaction between the remnant and the nebula. Kaaret et al. (1999) used the Beppo-SAX narrow-field instruments to image the region around J0634+0521 and discovered a point source with a hard spectrum, SAX J0635+0553. They report an optical counterpart, which is likely a B-type companion star, and conclude that if the  $\gamma$ -ray emission is associated with the system (or a portion of it is), then it is a  $\gamma$ -ray emitting x-ray binary. When the x-ray observations were subsequently revisited, a 33.8 ms pulsation was discovered (Kaaret et al., 2000). In a recent study of all potential EGRET SNR counterparts, Torres et al. (2003), suggest that the source of the  $\gamma$ -ray emission is far from resolved. The fact that Beppo-SAX did not discover extended emission from the region, as would be expected in a shock acceleration scenario, suggests that the binary may be responsible for the  $\gamma$ -ray emission. On the other hand, no orbital variations are seen in the  $\gamma$ -ray signal, arguing against an origin in the binary system. Analysis of the pulsar energetics and accretion rate further confuses the issue, see Torres et al. (2003) for review. Lucarelli et al. (2001) report preliminary evidence for VHE  $\gamma$ -ray emission from the region with the HEGRA telescope system<sup>18</sup>. The VHE emission was extended and was not coincidental with the Beppo-SAX source. No flux was reported for the observations.

Torres et al. (2003) suggest that 3EG J0643+0521 might be a composite source, with the Beppo-SAX source being responsible for a portion of the EGRET  $\gamma$ -ray flux and the bulk of the x-ray emission, while interactions between the SNR and the Rosette nebula may contribute to the 3EG flux and account for any VHE emission. They

---

<sup>18</sup>At a  $5.7\sigma$  level for emission based on 120 hrs. at  $E > 500$  GeV from four  $0.2^\circ \times 0.2^\circ$  bins in the region of the Rosette nebula.

predict that, if a composite source is responsible, a spectral break should be detected between the EGRET and ground-based  $\gamma$ -ray regimes. For 3EG J0631+0642 a pure shock acceleration model is sufficient to explain the 3EG flux.

Romero et al. (1999) studied potential positional associations between 3EG sources and SNR, OB associations, WR-type and O-type stars. In addition to the Monoceros SNR, they report two O-type stars and two OB associations in the region: from a catalog of O-type stars (Cruz-González et al., 1974) HD46150 and HD46223 and from a catalog of OB-associations (Mel'Nik and Efremov, 1995) Mon OB 2A and Mon OB 1B<sup>19</sup>. Mon OB 1B lies just outside of the region studied in this work.

The VHE observations of this source consist of 248 min. of data. In order to accommodate the 95% confidence contours of both 3EG sources and the GeV source, the telescope was pointed close to the coordinates listed for the Monoceros nebula in Green (2001), approximately half way between the two 3EG sources. Although both EGRET sources were in the field of view they lie toward the edge of the camera, which is less sensitive to  $\gamma$ -rays than the center.

No significant emission was detected in the field; figure 5.13 presents the upper limits derived from the observations. The figure shows the EGRET contours for both sources, with 3EG J0634+0521 toward the lower left. The GeV source is indicated as a dashed circle overlapping 3EG J0631+0642. The dash-dotted circle towards the bottom of the figure indicates the location of Mon OB 2A, with the two O-type stars, each marked by an “X” within. Finally, the location of SAX J0635+0533 is marked as an “X” near the center of 3EG J0634+0521. Table 5.10 summarizes the upper limits derived for the EGRET error-boxes and for the various candidate sources.

The extrapolated EGRET spectra for both sources are shown in figure 5.14 with the upper limits at 350 GeV. These observations do not require a break in the spectrum of either source and cannot substantiate (or refute) the two component model of Torres et al. (2003). Although the previous upper limits derived from observations with the

---

<sup>19</sup>Romero et al. (1999) refer to Mon OB 2B which is not in the catalog. Mon OB 1B is the correct source association.

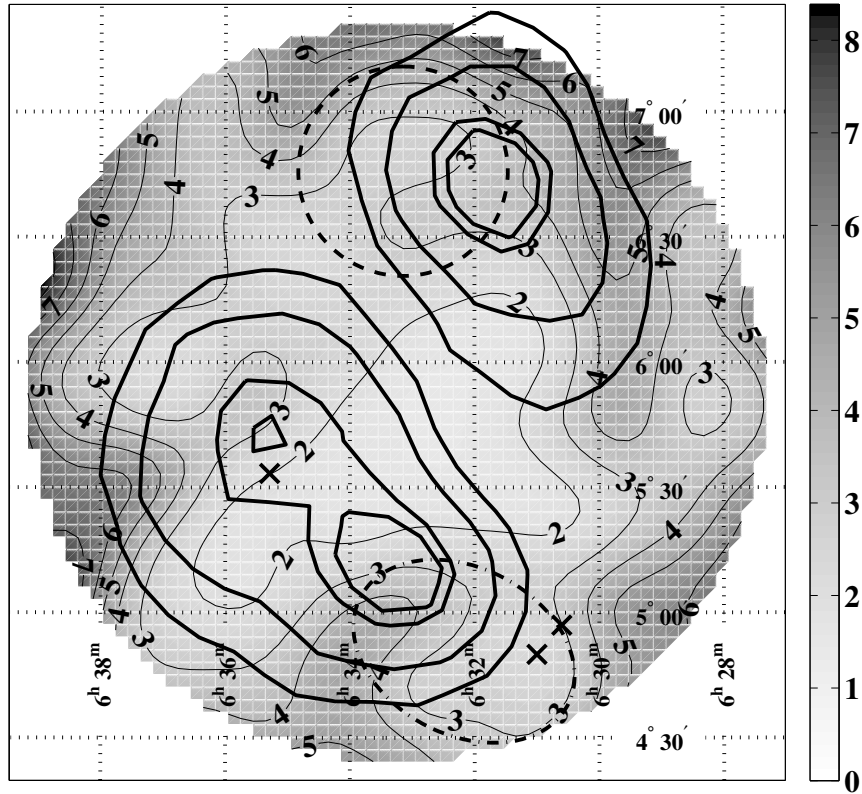


Figure 5.13: Upper limits on emission from 3EG J0634+0521, 3EG J0631+0642 and GeV J0633+0645 in units of  $10^{-11} \text{ cm}^{-2} \text{ s}^{-1}$ . The 3EG error contours are overlaid as heavy lines, the GeV error circle as a dashed line toward the top of the diagram. The dash-dotted ellipse toward the bottom of the figure indicates the OB association Mon OB 2A.

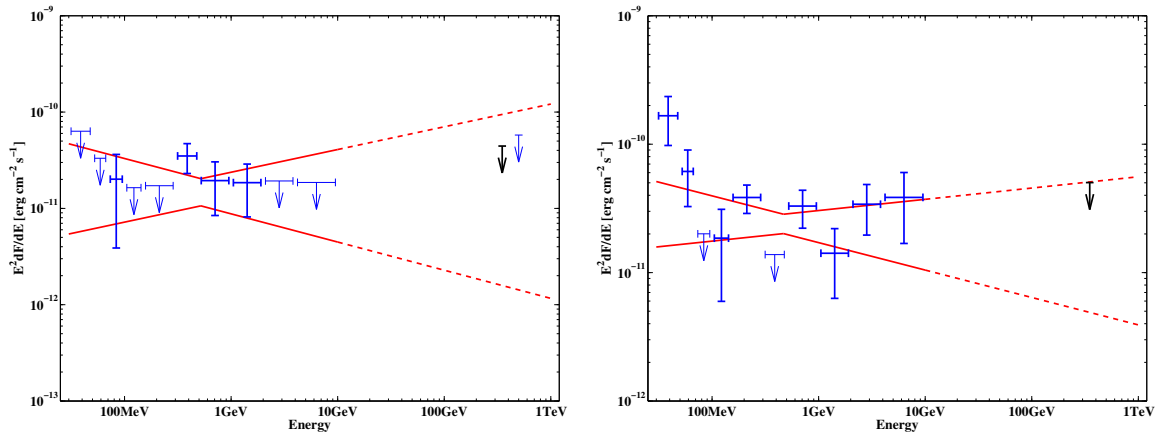


Figure 5.14: Spectrum for 3EG J0634+0521 (left) and 3EG J0631+0642 (right) from on-line version of the 3EG catalog with the upper limit at 350 GeV. The limit at 500 GeV from Lessard et al. (1999) is also indicated.

**Table 5.10: Upper limits for candidates in the fields of 3EG J0634+0521 and 3EG J0631+0642.**

Source Name	Coordinates		Extent	Upper Limit
	$\alpha_{2000}$	$\delta_{2000}$	deg	$\times 10^{-11} \text{ cm}^{-2} \text{ s}^{-1}$
3EG J0634+0521	$06^h 34^m 39.9^s$	$+05^\circ 28' 21''$	$0.85 \times 0.50$	5.3
3EG J0631+0642	$06^h 31^m 39.4^s$	$+06^\circ 41' 42''$	$0.55 \times 0.39$	6.0
GeV J0633+0645	$06^h 33^m 08.8^s$	$+06^\circ 45' 49''$	$0.42 \times 0.42$	4.9
SAX J0635+0533	$06^h 35^m 17.4^s$	$+05^\circ 33' 21''$	-	2.0
Mon OB 2A	$06^h 32^m 10.2^s$	$+04^\circ 50' 46''$	$0.33 \times 0.47$	4.7
HD46150	$06^h 30^m 36.0^s$	$+04^\circ 57' 00''$	-	3.1
HD46223	$06^h 31^m 00.0^s$	$+04^\circ 50' 00''$	-	2.4

Whipple telescope (Lessard et al., 1999) had a lower flux value, the observations were made at higher energy, and do not constrain the extrapolated EGRET spectrum any more than these observations. The previous limits are shown on the figure at 500 GeV, at approximately the same level. This source is a prime candidate for observation with the next generation of ground-based instruments, such as VERITAS, which will have an order of magnitude increase in sensitivity over the current generation, and will operate at energies  $\sim 100$  GeV. These instruments will have the ability to accurately reconstruct the origin of the  $\gamma$ -rays, and will have the ability to resolve the  $\gamma$ -ray emission from unidentified EGRET sources such as this one.

### 5.1.10 3EG J1009+4855

In the 3EG catalog, J1009+4855 is listed as having a low flux and a hard, but relatively ill defined, spectral index. Nolan et al. (2003) present only an upper limit for the variability index, not surprising given the low mean flux from the source and that it was not seen at a particularly high flux state during any of the EGRET viewing periods. The source is also listed in the GeV catalog as a low significance source. Very little is known about this source at other wavelengths, the EGRET catalog suggests a weak association with the radio/x-ray source B1011+496, a known AGN at redshift of  $z = 0.2$ . Mattox et al. (2001) lists the probability of that association as  $2 \times 10^{-4}$ ; the

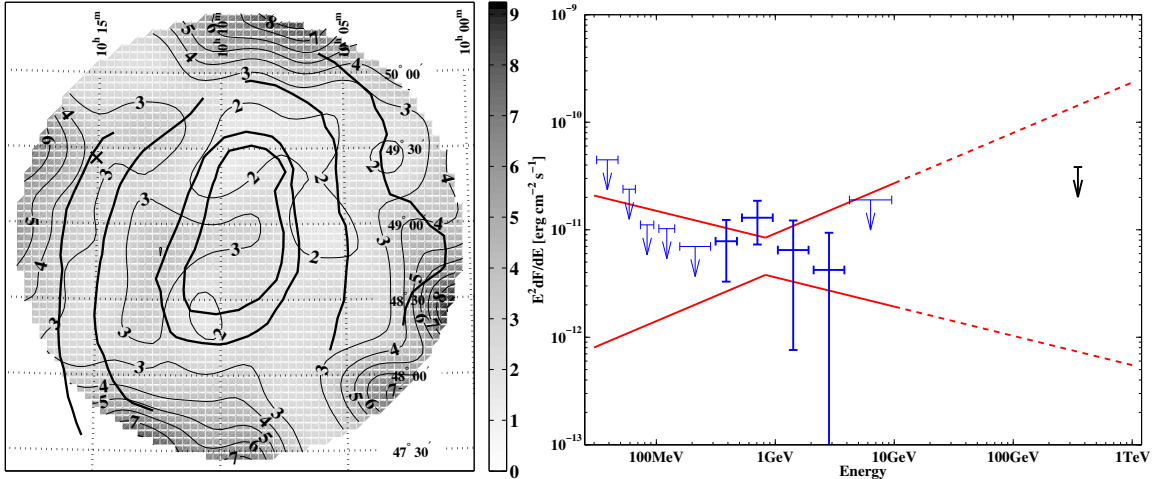


**Figure 5.15:** (Left) Limits on emission from 3EG J1009+4855 in units of  $10^{-11} \text{ cm}^{-2} \text{ s}^{-1}$ . The 3EG error contours are overlaid as heavy lines. (Right) Spectrum from the on-line version of the 3EG catalog with the limit at 350 GeV.

**Table 5.11: Upper limits for candidates in 3EG J1009+4855 field.**

Source Name	Coordinates $\alpha_{2000}$	Coordinates $\delta_{2000}$	Extent deg	Upper Limit $\times 10^{-11} \text{ cm}^{-2} \text{ s}^{-1}$
3EG J1009+4855	$10^h 09^m 59.3^s$	$+48^\circ 50' 30''$	$1.12 \times 0.80$	4.6
87GB 1011+4941	$10^h 15^m 04.1^s$	$+49^\circ 26' 01''$	-	3.3

radio-source lies outside of the large 99% error contour<sup>20</sup> and the association seems unlikely.

VHE observations of the source were made between December 2001 and March 2002. A total of 248 min. of usable data were obtained, pointed at the center of the 3EG source. No significant emission was detected, a map of the upper limits on emission from the region is presented in figure 5.15. A limit of  $F_{(>350 \text{ GeV})} < 4.6 \times 10^{-11} \text{ cm}^{-2} \text{ s}^{-1}$  is placed on emission within the 95% error contour, shown with an extrapolation of the EGRET spectrum in figure 5.15. The upper limit does not significantly constrain the wide range of fluxes allowed by the large uncertainties in the 3EG spectrum.

<sup>20</sup>The EGRET contours are derived from rectangular likelihood maps in Galactic or equatorial coordinates (see Mattox et al., 1996). The 95% and 99% confidence contours are not bounded within the map for this source and hence are not closed in figure 5.15.

### 5.1.11 3EG J1323+2200

EGRET detected variable emission from the high latitude source J1323+2200, with an average flux of  $5.2 \pm 1.6 \times 10^{-8} \text{ cm}^{-2} \text{ s}^{-1}$ . During most of the viewing periods (VP) for which it was in the field of view no emission was detected; during VP 308.0 a flux of  $68.4 \pm 22.6 \times 10^{-8} \text{ cm}^{-2} \text{ s}^{-1}$  was measured. The source is listed in the GeV catalog as a “source of GeV gamma rays based upon the search for repeating, weak outbursts”. Nolan et al. (2003) calculate the variability index to be 1.09, consistent with a highly variable source. Its 100 MeV spectral index is hard, with a relatively large error,  $\Gamma = 1.86 \pm 0.35$ . Mattox et al. (2001) lists four potential associations with radio sources, two of which (with the lowest 5 GHz fluxes) are within the 95% confidence contour. The most likely association, just outside of the 95% contour, is listed as having a probability of  $\sim 1\%$ .

VHE observations during the first five months of 2001 resulted in 276 min. of usable data centered on the 3EG catalog position. The data were analyzed using the two dimensional reconstruction technique and no significant emission was detected from the source. Upper limits on emission are presented in figure 5.16. A limit of

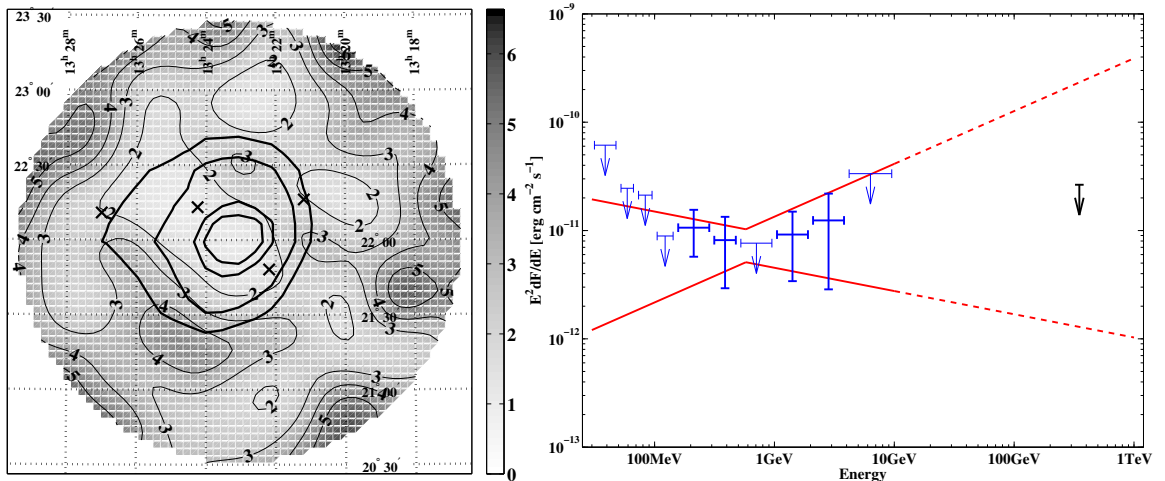


**Figure 5.16:** (Left) Limits on emission from 3EG J1323+2200 in units of  $10^{-11} \text{ cm}^{-2} \text{ s}^{-1}$ . The 3EG error contours are overlaid as heavy lines. (Right) Spectrum from the on-line version of the 3EG catalog with the limit at 350 GeV.

**Table 5.12:** Upper limits for candidates in 3EG J1323+2200 field.

Source Name	Coordinates		Extent	Upper Limit $\times 10^{-11} \text{ cm}^{-2} \text{ s}^{-1}$
	$\alpha_{2000}$	$\delta_{2000}$	deg	
3EG J1323+2200	$13^h 23^m 20.1^s$	$+22^\circ 02' 52''$	$0.52 \times 0.43$	3.1
87GB 1324+2226	$13^h 27^m 00.8^s$	$+22^\circ 10' 50''$	-	2.1
87GB 1318+2231	$13^h 21^m 11.2^s$	$+22^\circ 16' 12''$	-	2.1
87GB 1319+2203	$13^h 22^m 11.4^s$	$+21^\circ 48' 12''$	-	1.6
87GB 1321+2229	$13^h 24^m 14.9^s$	$+22^\circ 13' 08''$	-	1.2

$F_{(>350\text{ GeV})} < 3.1 \times 10^{-11} \text{ cm}^{-2} \text{ s}^{-1}$  is placed on emission within the 95% error contour, limits on the four radio sources, which are displayed as crosses in the figure, are listed in table 5.12. The limits do not significantly constrain an extrapolation of the EGRET spectrum to 350 GeV.

### 5.1.12 3EG J1337+5029

The  $\gamma$ -ray source 3EG J1337+5029, at Galactic latitude of  $+65^\circ$ , was detected by EGRET with a relatively low flux of  $9.2 \pm 2.6 \times 10^{-8} \text{ cm}^{-2} \text{ s}^{-1}$  and a hard spectrum of  $1.83 \pm 0.29$ , the fourth hardest among the unidentified sources. Nolan et al. (2003) list a variability index of 0.53, indicating a variable source; it was detected significantly in four of the six viewing periods that it was in the EGRET field of view.

Colafrancesco (2002) suggests that the  $\gamma$ -ray source is associated with the galaxy cluster Abell 1758 (Abell et al., 1989), with diameter of 22 arcmin and redshift of  $z = 0.279$ . The cluster is coincident with two ROSAT x-ray sources RX J1332.5+5024 and RX J1332.7+5032, both of which show evidence of being extended, each with a radius of approximately 75 arcsec. Böhringer et al. (2000) present a reanalysis of the x-ray data for all extended RASS-BSC sources, accounting properly for the extended nature of the source in the flux calculation. They calculate a flux of  $F_X(0.1 - 2.4 \text{ keV}) = 5.6 \pm 0.53 \times 10^{-12} \text{ erg cm}^{-2} \text{ s}^{-1}$  for the cluster<sup>21</sup>, corresponding to a luminosity of  $L_X(0.1 - 2.4 \text{ keV}) \sim 1.8 \times 10^{45} \text{ erg s}^{-1}$ . Additionally, four radio sources from the

<sup>21</sup>They label the source as RXC 1332+5032; seemingly it corresponds to both of the RASS-BSC sources. The x-ray flux they quote was been integrated over a radius of 11.5 arcmin, covering the whole extent of the cluster.

NRAO VLA Sky Survey (NVSS) are coincident with the cluster. Colafrancesco (2002) concludes that since the cluster “falls within the 95% confidence level position error contour of the source” and, given the x-ray/radio sources listed above, this source represents a “probable candidate for the correlation of galaxy clusters and EGRET unidentified  $\gamma$ -ray sources”. Analysis of the 3EG significance maps performed for this study shows that the cluster location, as listed in Abell et al. (1989) and the NED database, does not lie within the 95% contour, even taking into account the diameter of the cluster. Figure 5.17 shows that the cluster lies just outside the 95% contour to the west<sup>22</sup>, approximately  $0.8^\circ$  from the 3EG catalog position.

There are five additional RASS-BSC x-ray sources in the field, four within the 95% contour; some have radio counterparts in the NVSS. The RASS catalog lists some potential associations for the x-ray sources, two with stars, and one with an AGN and a star. Limits are presented for each of the x-ray sources irrespective of these associations. Mattox et al. (2001) list two unlikely radio associations from the Green Bank catalog, one outside of the 99% contour, the other just inside. These seven sources are shown on figure 5.17. The two x-ray sources inside the cluster have been omitted in light of the combined, extended source discussed above (Böhringer et al., 2000).

VHE observations during the first six months of 2002 yielded 166 min. of data. Figure 5.17 shows the significance of excess (or deficit)  $\gamma$ -ray-like events within the field of view. A broad excess, approximately  $1.0^\circ \times 0.5^\circ$  in extent, lies along the 99% contour to the north-west of the 3EG catalog position. The peak in the excess has an a priori statistical significance of  $\sim 4\sigma$ , making it the most significant of all the observations in this survey. Since emission was not predicted from this particular location a priori, the true probability of obtaining such a result by chance, given the number of sources observed in this survey and the combined size of the EGRET error-boxes must be evaluated. This is done by first calculating the number of “independent”  $0.1^\circ \times 0.1^\circ$

---

<sup>22</sup>By convention, astronomical maps have west and east reversed with respect to the usual mapping convention. They are oriented to coincide with what someone on the ground looking up at the sky would see, with north pointed up.

**Table 5.13:** Upper limits for candidates in 3EG J1337+5029 field.

Source Name	Coordinates		Extent	Upper Limit
	$\alpha_{2000}$	$\delta_{2000}$	deg	$\times 10^{-11} \text{ cm}^{-2} \text{ s}^{-1}$
3EG J1337+5029	$13^h 38^m 00.8^s$	$+50^\circ 25' 57''$	$0.77 \times 0.66$	5.9
Abell 1758	$13^h 32^m 31.7^s$	$+50^\circ 30' 41''$	$0.18 \times 0.18$	6.9
87GB 1329+5023	$13^h 31^m 37.2^s$	$+50^\circ 07' 55''$	-	3.6
87GB 1340+5125	$13^h 42^m 23.5^s$	$+51^\circ 10' 18''$	-	3.9
*J133510.2+503920	$13^h 35^m 10.2^s$	$+50^\circ 39' 20''$	-	3.5
RX J1335.3+5015	$13^h 35^m 19.6^s$	$+50^\circ 15' 04''$	-	3.0
RX J1337.3+5032	$13^h 37^m 20.0^s$	$+50^\circ 32' 52''$	-	2.5
*J134023.3+503113	$13^h 40^m 23.3^s$	$+50^\circ 31' 13''$	-	2.1
*J134350.8+503016	$13^h 43^m 50.8^s$	$+50^\circ 30' 16''$	-	3.0

\* The standard RASS-BSC catalog prefix of 1RXS is omitted for formatting purposes.

bins represented by the sources using figure 4.9. It is estimated that  $\sim 200$  bins lie within the 95% contours for the 18 sources analyzed using the two dimensional technique. Figure 4.7 can then be used to calculate an equivalent Gaussian significance of the probability of obtaining such a result by chance. In the case of a  $4\sigma$  excess with 200 trials, the equivalent significance is  $\sim 2.5\sigma^{23}$ . Given this conservative approach and that the dataset for this source is so small ( $\sim 2.5$  hrs), we do not claim to have seen emission from this source. However, the excess gives an a priori expectation of emission from this location, and is a strong reason to make followup observations. Results from these independent observations will then not have to pay a “statistical penalty”. Based on these results, the source has been awarded 20 hrs of observations with the Whipple telescope during spring 2004.

Since VHE emission is not claimed, upper limits for the region and potential associations are presented in figure 5.18 and table 5.13. An upper limit of  $F_{(>350 \text{ GeV})} < 5.9 \times 10^{-11} \text{ cm}^{-2} \text{ s}^{-1}$  is derived for the EGRET source. Figure 5.18 (right) shows the upper limit, which rules out half of the flux space allowed by extrapolating the EGRET spectrum to 350 GeV. Upcoming observations will either detect emission from this source or further constrain its spectrum.

<sup>23</sup>Strictly, the excess seen here is not within the 95% contour; a similar calculation for all of the bins within  $1.1^\circ$  of the center of the 18 sources gives 600 trials and a significance of  $\sim 2.1\sigma$ .

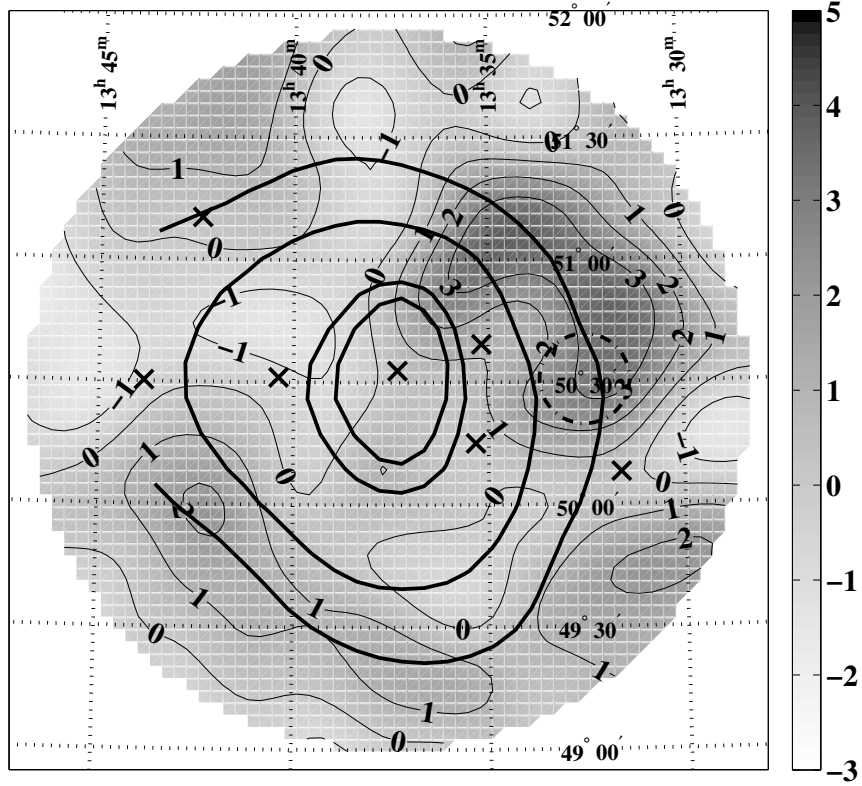


Figure 5.17: Significance of excess  $\gamma$ -ray-like events detected from the region of 3EG J1337+5029. The cluseter is shown as a dot-dashed circle, and the various other sources in the field as “X” marks.

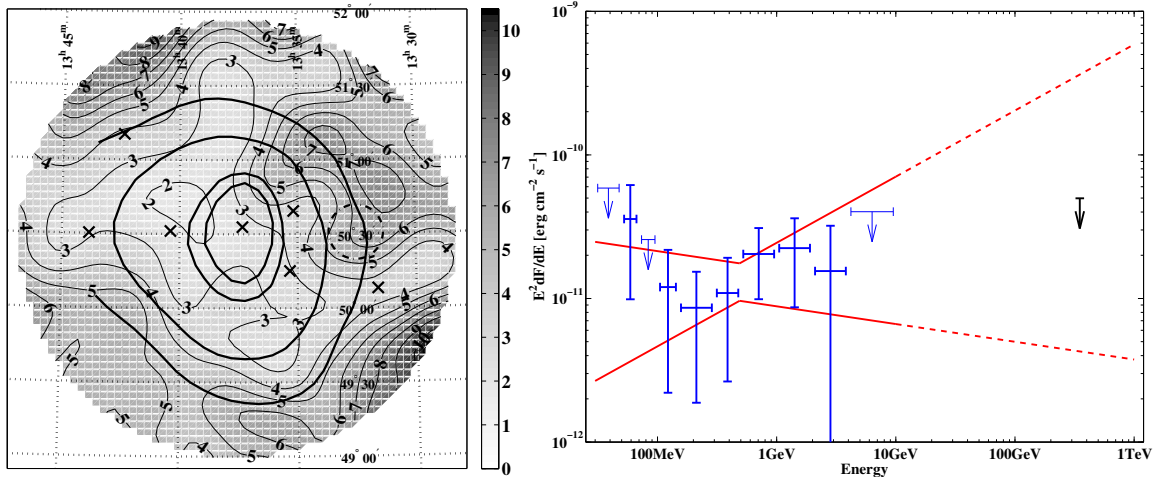


Figure 5.18: (Left) Limits on emission from 3EG J1337+5029 in units of  $10^{-11} \text{ cm}^{-2} \text{s}^{-1}$ . The 3EG error contours are overlaid as heavy lines. (Right) Spectrum from the on-line version of the 3EG catalog with the limit at 350 GeV.

### 5.1.13 3EG J1826–1302 and 3EG J1823–1314

The low latitude  $\gamma$ -ray sources 3EG J1826–1302 and 3EG J1823–1314 are the closest sources to the Galactic center to be studied in this survey. 3EG J1826–1302 has a relatively hard, well determined spectrum ( $\Gamma = 2.00 \pm 0.11$ ), a large 100 MeV flux, and shows evidence of being variable ( $\delta = 0.88$  from Nolan et al. 2003). 3EG J1823–1314 has a softer spectrum ( $\Gamma = 2.69 \pm 0.19$ ), a large flux and a variability index of  $\delta = 0.60$ . The center of the sources lie approximately  $0.8^\circ$  apart, a separation that is considerably smaller than the EGRET point-spread function at 100 MeV; they are listed in the 3EG catalog as having positions, fluxes and significances that could be affected by source confusion. Their 99% confidence contours overlap considerably, their 95% contours overlap to a smaller degree. The GeV catalog lists a source, GeV J1825–1310 which overlaps both of the 3EG sources but is more consistent with being associated with 3EG J1826–1302. Finally, a third EGRET source 3EG J1824–1514 is also close to these sources ( $\sim 2^\circ$ ) and is partially within the field of view of the VHE observations, as described below.

Roberts et al. (2001b) present x-ray observations of the  $\gamma$ -ray error-box in their catalog of ASCA observations of the bright GeV sources. Their image revealed a previously unknown extended x-ray source, denoted AX J1826.1–1300, which they conclude is a PWN. The putative PWN is centered on the 3EG source J1826–1302, and makes a good potential counterpart for the  $\gamma$ -ray source. A pulsar/PWN origin would account for the hardness of the EGRET spectrum, and the variability index of  $\delta = 0.88$  is consistent with the value of  $0.66 \pm 0.29$  which Nolan et al. (2003) calculate as the mean for the class of six potential pulsar/PWN associations suggested by Grenier (2002). Roberts et al. (2001b) also report extended emission near the non thermal radio source SNR 18.1-0.2, reported as a possible SNR by Odegard (1986) (but not adopted as such by Green 2001), and remark that it is consistent with the 100 MeV source 3EG J1823–1314.

The much studied PSR B1823–13, a young, energetic, Vela-like pulsar, is contained within the 95% error contour of 3EG J1826–1302. The source has been targeted for

VHE observations with the Whipple (see Hall et al., 2001, and its references) and HEGRA (Aharonian et al., 2002b, identified as PSR J1826-1334) telescopes, with limits of  $F_{(>520\text{ GeV})} < 0.91 \times 10^{-11} \text{ cm}^{-2} \text{ s}^{-1}$  and  $F_{(>1700\text{ GeV})} < 0.48 \times 10^{-11} \text{ cm}^{-2} \text{ s}^{-1}$  being derived respectively. Gaensler et al. (2003) present deep XMM-Newton observations of the pulsar, in which they discover two components of emission, a core of hard x-ray emission of 5 arcsec extent surrounded by an asymmetric region of fainter, softer, diffuse emission toward the south of the pulsar. They do not detect the radio pulsar, either as a compact point source or through pulsations. No associated SNR is seen.

Green (2001) contains three SNR within the field of view of the VHE observations, one of which, G18.8-0.3 (or Kes 67), was suggested by Sturner and Dermer (1995) as a candidate for a source in the first EGRET catalog (GRO 1923-12 from Fichtel et al. 1994). None of the SNR are within the 95% confidence contours of the two EGRET sources reported on here. Romero et al. (1999) lists a positional coincidence between the three EGRET sources in the field and the OB association Sct OB 3. The association does not significantly overlap 3EG J1826-1302 or 3EG J1823-1314 but does show some overlap with 3EG J1826-1302 and with the SNR G16.8-11. Previous VHE limits for the three SNR (and for many other Galactic SNR) have been presented by the HEGRA collaboration (Aharonian et al., 2002b). Mattox et al. (2001) do not have potential radio candidates for these 3EG sources. The RASS-BSC contains two x-ray sources, listed in table 5.14, in the field.

Clearly, the source region is dense with potential counterparts. It is also possible that the correct association for the sources has not yet been resolved at other energies, e.g. the SNR counterparts for PSR B1823-13 and for AX J1826-1300 have not been identified, this could be the case for other SNR in the field.

The VHE observations of these sources were made as part of a search for emission from the pulsar, consequently the field is centered on PSR B1823-13. A total of 416 min. of data were collected between April and July 2000. The results of a point source analysis of the data have been previously published in Hall et al. (2001, 2003b). The

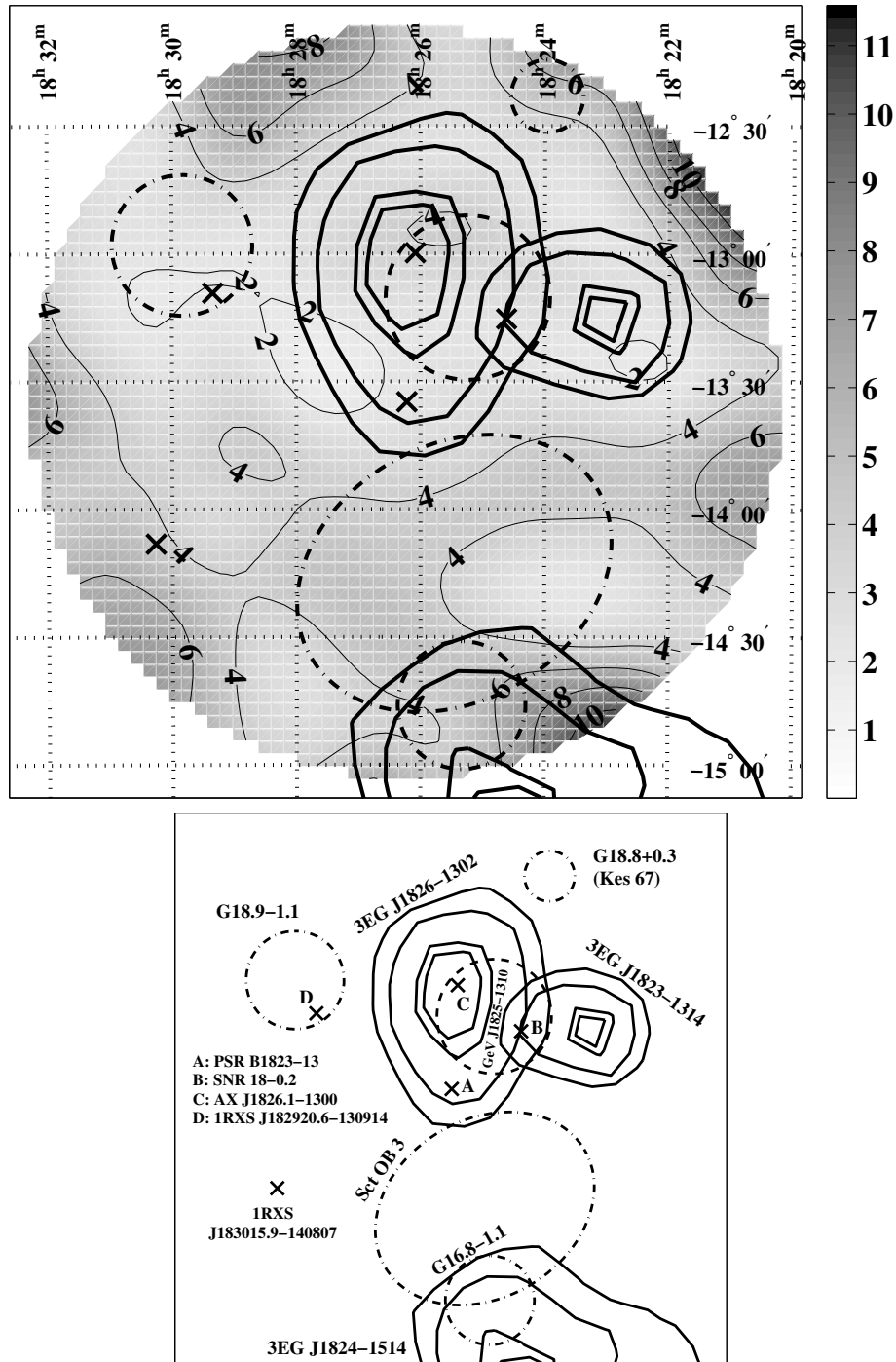
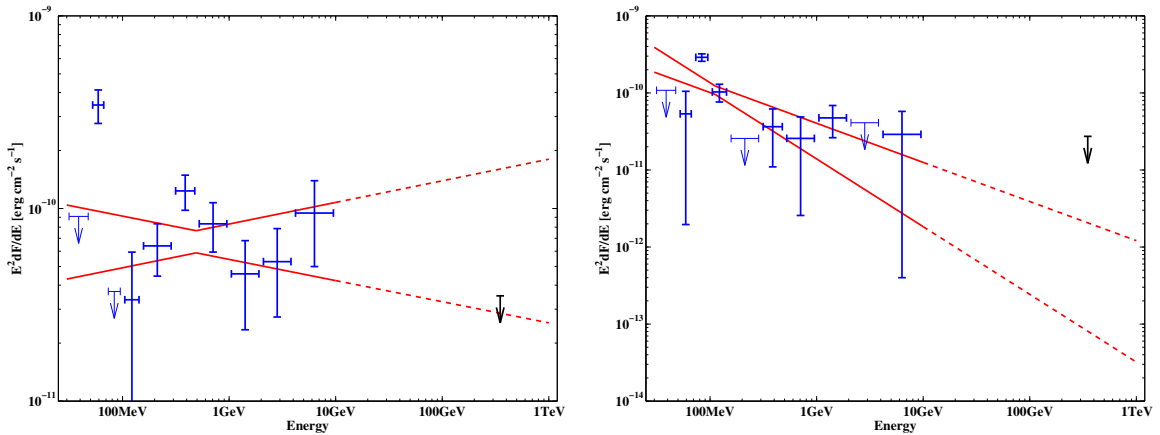


Figure 5.19: Upper limits on emission from 3EG J1826–1302, 3EG J1826–1302 and GeV J1825–1310 in units of  $10^{-11} \text{ cm}^{-2} \text{ s}^{-1}$ . The SNR, OB association and point source candidates in the field are indicated on the figure and labeled in the key below, as is a third EGRET source 3EG J1824–1514 which partially overlaps the field.

**Table 5.14: Upper limits for candidates in 3EG J1826–1302 field.**

Source Name	Coordinates	Extent	Upper Limit
	$\alpha_{2000}$	$\delta_{2000}$	$\times 10^{-11} \text{ cm}^{-2} \text{ s}^{-1}$
3EG J1826–1302	$18^h 26^m 01.0^s$	$-13^\circ 05' 28''$	$0.55 \times 0.39$ 4.2
3EG J1823–1314	$18^h 23^m 24.7^s$	$-13^\circ 14' 32''$	$0.33 \times 0.23$ 3.2
GeV J1825–1310	$18^h 25^m 14.3^s$	$-13^\circ 10' 19''$	$0.32 \times 0.32$ 4.2
PSR B1823–13	$18^h 26^m 13.2^s$	$-13^\circ 34' 47''$	- 2.4
SNR 18.1–0.2	$18^h 24^m 37.0^s$	$-13^\circ 15' 18''$	$0.03 \times 0.01$ 2.6
AX J1826.1–1300	$18^h 26^m 04.9^s$	$-12^\circ 59' 48''$	- 3.7
G16.8–1.1	$18^h 25^m 20.0^s$	$-14^\circ 46' 00''$	$0.25 \times 0.25$ 6.9
G18.8–0.3 (Kes 67)	$18^h 23^m 58.0^s$	$-12^\circ 23' 00''$	$0.14 \times 0.14$ 6.8
G18.9–1.1	$18^h 29^m 50.0^s$	$-12^\circ 58' 00''$	$0.28 \times 0.28$ 3.6
Sct OB 3	$18^h 25^m 27.2^s$	$-14^\circ 15' 04''$	$1.30 \times 1.00$ 6.2
*J183015.9–140807	$18^h 30^m 15.9^s$	$-14^\circ 08' 07''$	- 4.6
*J182920.6–130914	$18^h 29^m 20.6^s$	$-13^\circ 09' 14''$	- 2.0

\* The standard RASS-BSC catalog prefix of 1RXS is omitted for formatting purposes.



**Figure 5.20:** Spectrum for 3EG J1826–1302 (left) and 3EG J1823–1314 (right) from on-line version of the 3EG catalog with the upper limit at 350 GeV.

two dimensional analysis did not reveal any significant emission. Upper limits for the region and various potential associations are presented in figure 5.19, which includes a key to the complex field, and summarized in table 5.14. A limit of  $F_{(>350\text{ GeV})} < 4.2 \times 10^{-11} \text{ cm}^{-2} \text{ s}^{-1}$  is derived for the hard  $\gamma$ -ray source 3EG J1826–1302. A somewhat lower limit of  $F_{(>350\text{ GeV})} < 3.2 \times 10^{-11} \text{ cm}^{-2} \text{ s}^{-1}$  is derived for the smaller, softer 3EG J1823–1314.

The VHE upper limits are displayed in figure 5.20 with an extrapolation of the EGRET spectrum. The limit derived for the region of 3EG J1826–1302 constrains the hard EGRET spectrum to the softest spectrum allowed by the errors in the 100 MeV flux and spectral index. It is likely that a cutoff in the spectrum occurs between the highest EGRET flux point, at 6 GeV, and the VHE observations. In the case of 3EG J1823–1314, the softer EGRET spectrum is not constrained by the VHE upper limit.

### 5.1.14 3EG J1835+5918

The bright  $\gamma$ -ray source 3EG J1835+5918 has the hardest spectral index and smallest error circle among all of the EGRET sources classified as unidentified. The source was detected consistently throughout the EGRET mission; Nolan et al. (2003) calculate a variability index of  $\delta = 0.15$ . The hard spectrum and low variability suggest an association with a pulsar, although none have been definitively identified in the field.

The source has been extensively studied at radio, optical and x-ray energies by two independent groups (see Reimer et al., 2002; Halpern et al., 2002, and references therein), who present compelling evidence that the source is associated with an isolated neutron star, possibly a radio-quiet, Geminga-like pulsar. Taking just one of these groups' work (Halpern et al.): Mirabal et al. (2000) report on a series of observations with many different instruments across the spectrum, which narrowed the list of potential ROSAT and ASCA x-ray candidate associations in the 95% error contour from ten to one: RX J1836.2+5925. Optical/UV photometry uncovered 40 possible AGN in the field, based on a search for broad UV continuum emission. Twenty radio

sources were found in archival VLA observations or standard radio catalogs. In particular, no flat-spectrum radio sources, which could correspond to FSRQs and BL Lacs, the only AGN identified as EGRET sources to date, were identified in the field. Follow-up optical spectra of the candidates revealed that most of the x-ray sources were distant AGN or G- to M-type stars. Only RX J1836.2+5925, the brightest of the ROSAT sources, was unidentified in the initial optical survey, and was selected as the mostly likely counterpart for the  $\gamma$ -ray source, although its properties were unlike any other known EGRET source. Mirabal and Halpern (2001) report a reanalysis of the ROSAT data in which soft x-ray emission below 0.4 keV became apparent, which they conclude is thermal emission from the surface of an isolated neutron star. Subsequent observations with the Chandra x-ray satellite and Hubble space telescope (Halpern et al., 2002) make this conclusion very compelling, the excellent resolution of the Chandra instrument rules out all possible optical counterparts in the HST image, down to the limiting magnitude of  $V > 28.5$ . These observations make an association with an AGN very unlikely and constrain the distance and temperature of a neutron star (NS) candidate. They conclude that it must have temperature of  $T \approx 3 \times 10^5$  K, be very distant (compared with the Geminga pulsar),  $d \approx 800$  pc. Given a standard model for NS cooling, they calculate an age of  $\sim 10^6$  yr. No SNR was detected around the pulsar in sensitive VLA observations, it seems likely that the NS was ejected from the remnant at birth and traveled to its present location. If the NS started in (or near) the Galactic plane and the putative distance of 800 pc is correct, the NS must have traveled a distance of 340 pc to reach its present location (latitude of  $b = 25^\circ$ ); Halpern et al. (2002) conclude this is not unreasonable, given its age of one million years.

VHE observations of this source during May and June 2000 resulted in 110 min. of data, pointed at the center of the 3EG source. The data were analyzed with the two dimensional technique and no statistically significant emission was detected. Limits for the region are presented in figure 5.21 and summarized in table 5.15. A limit of  $F_{(>350\text{ GeV})} < 3.8 \times 10^{-11} \text{ cm}^{-2} \text{ s}^{-1}$  is derived for the field, which clearly constrains an extrapolation of the EGRET spectrum to the VHE regime (see figure 5.21). A

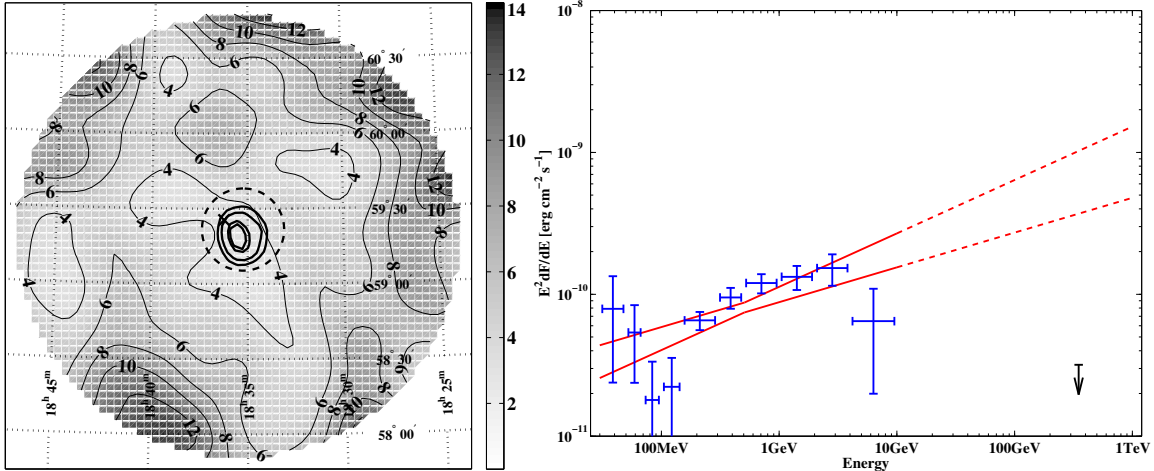


**Figure 5.21:** (Left) Limits on emission from 3EG J1835+5918 in units of  $10^{-11} \text{ cm}^{-2} \text{ s}^{-1}$ . The 3EG error contours are overlaid as heavy lines. (Right) Spectrum from the on-line version of 3EG catalog with the limit at 350 GeV.

**Table 5.15: Upper limits for candidates in 3EG J1835+5918 field.**

Source Name	Coordinates	Extent	Upper Limit
	$\alpha_{2000}$	$\delta_{2000}$	$\times 10^{-11} \text{ cm}^{-2} \text{ s}^{-1}$
3EG J1835+5918	$18^h 35^m 24.9^s$	$+59^\circ 19' 15.3''$	$0.16 \times 0.13$
RX J1836.2+5925	$18^h 36^m 13.7^s$	$+59^\circ 25' 30.1''$	3.7

cutoff is required in the spectrum between the highest EGRET energies and 350 GeV, supporting the case for a pulsar origin of the  $\gamma$ -rays. Halpern et al. (2002) suggest that this cutoff is visible in the 4 GeV EGRET point, which is considerably below the expected power law flux, although the deficit may also be the result of low photon statistics.

### 5.1.15 GeV J1907+0557

The GeV source J1907+0557 does not have a counterpart 100 MeV EGRET source, although 3EG J1903+0550 is listed incorrectly in the 3EG catalog as being associated with it; there is very little overlap at the 95% confidence level. Sturner and Dermer (1995) suggest that a first EGRET catalog source in the region is associated with the SNR G40.5–0.5; an association of the SNR with the revised positions of the GeV

and 3EG sources seems unlikely. There are two additional SNR in the region listed by Green (2001), neither is a likely counterpart for the GeV source. One of them (G39.2–0.3) is listed by Torres et al. (2003) as a counterpart to the 3EG source. Roberts et al. (2001b) present an ASCA image of the GeV source in which they discover an extended x-ray source, AX J1907.4+0557. No other x-ray source appears in the ASCA image, which covers approximately half of the region within the GeV 95% contour.

The center of the GeV source was observed with the Whipple instrument for 277 min. between May and June 2000. The data shows a large excess of  $\gamma$ -ray-like events whose reconstructed origins are distributed across the ON source region, from the center of the field to a distance of  $> 1.8^\circ$  from the center, by which point the number of events drops quickly due to the limited field of view of the instrument. It is unlikely that such a broad excess is the result of  $\gamma$ -ray emission from a large, extended source; rather it is likely to be the result of a difference in brightness between the ON and OFF source regions which is not completely compensated for by the data selection algorithm. In order to remove this systematic effect, the number of events in an annulus defined by  $1.4^\circ < dist < 1.8^\circ$  is calculated from the ON-source and OFF-source data and their ratio used to scale number of OFF-source counts to the ON-source region. After this rescaling, no significant excess or deficit is present, upper limits on  $\gamma$ -ray emission are presented in figure 5.22 and summarized in table 5.16. A limit of  $F_{(>350\text{ GeV})} < 3.0 \times 10^{-11} \text{ cm}^{-2} \text{ s}^{-1}$  is placed on emission from within the GeV error circle. A limit cannot be placed on VHE emission from the 3EG source, since it is not fully contained within the field of view. No spectral information is available for this object at EGRET energies, therefore an extrapolated spectrum is not shown.

A limit on VHE emission has been obtained by the HEGRA group (Rowell et al., 2003); based on an exposure of  $\sim 1725$  min. they derive a limit of  $F_{(>700\text{ GeV})} < 0.03 \times 10^{-11} \text{ cm}^{-2} \text{ s}^{-1}$ , for emission from the GeV source, approximately 35 times lower than the limit presented here for an energy threshold that is twice as high (assuming a standard  $\Gamma = 2.5$  spectrum). The lower limit is partly due to the longer exposure, but is also the result of the multi-telescope technique which enhances background rejection

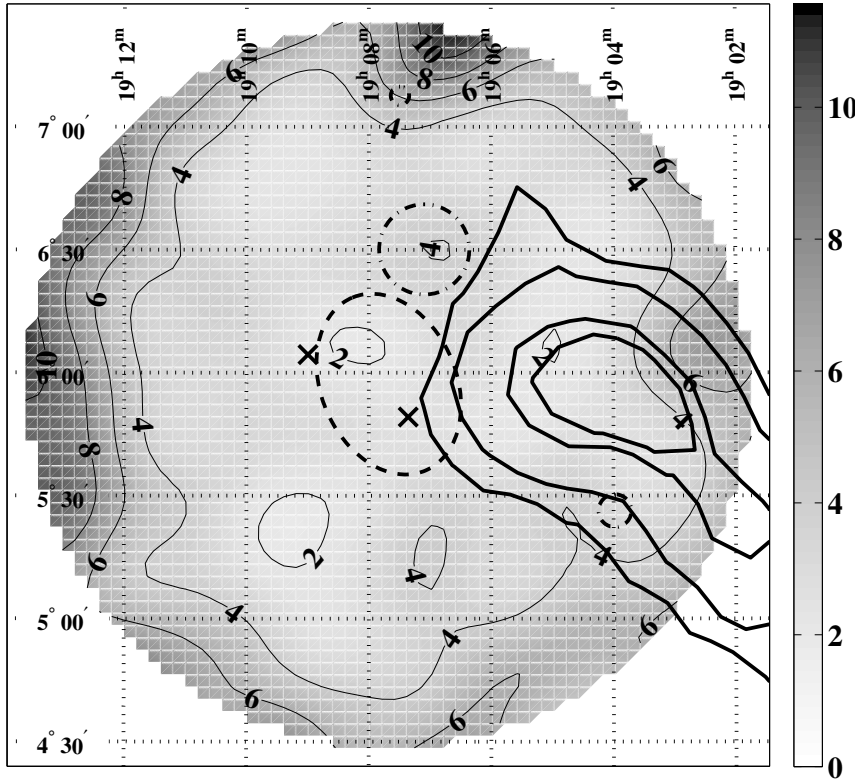


**Figure 5.22:** Limits on emission from GeV J1907+0557 in units of  $10^{-11} \text{ cm}^{-2} \text{ s}^{-1}$ . The GeV error ellipse is shown as a dashed line. The dash-dotted circles correspond to SNR in the field, the heavy “X”-marks indicate the x-ray sources from ASCA and ROSAT. The confidence contours of 3EG J1903+0550 partially overlap the field to the west of the GeV source.

**Table 5.16: Upper limits for candidates in GeV J1907+0557 field.**

Source Name	Coordinates $\alpha_{2000}$	$\delta_{2000}$	Extent deg	Upper Limit $\times 10^{-11} \text{ cm}^{-2} \text{ s}^{-1}$
GeV J1907+0557	$19^h 07^m 40.4^s$	$+05^\circ 57' 14''$	$0.38 \times 0.28$	3.0
AX J1907.1+0549	$19^h 07^m 21.3^s$ *	$+05^\circ 49' 14''$	-	2.6
G39.2–0.3	$19^h 03^m 58.7^s$	$+05^\circ 26' 19''$	$0.07 \times 0.07$	3.6
G40.5–0.5	$19^h 07^m 05.6^s$	$+06^\circ 30' 06''$	$0.18 \times 0.18$	4.0
G41.1–0.3	$19^h 07^m 29.4^s$	$+07^\circ 07' 35''$	$0.04 \times 0.04$	6.3
*J190859.7+060426	$19^h 08^m 59.7^s$	$+06^\circ 04' 26''$	-	2,3

\* The standard RASS-BSC catalog prefix of 1RXS is omitted for formatting purposes.

and allows the  $\gamma$ -ray origin to be reconstructed more accurately, which decreases the amount of smoothing that is required, reducing the number of background events in each bin of the map, and hence allowing a stronger upper limit to be derived.

### 5.1.16 GeV J2020+3658 (3EG J2021+3716 and 3EG J2016+3657)

The first two catalogs of EGRET point sources listed a  $\gamma$ -ray source in the region of the field of the COS-B source 2CG 075+00. Further data resolved two separate sources, 3EG J2021+3716 and 3EG J2016+3657, each with a spectrum of  $\sim 2.0$ . The GeV catalog also lists a source in the region, GeV J2020+3658, which is suggested in the 3EG catalog as a counterpart for 3EG J2016+3657. Roberts et al. (2001b) note that this association is probably incorrect, and that the GeV source is more likely to be associated with 3EG J2021+3716, with which it has considerable overlap. Of the two 3EG sources, J2021+3716, has a larger 100 MeV flux ( $F = 59.1 \pm 6.2 \times 10^{-8} \text{ cm}^{-2} \text{ s}^{-1}$ ), harder spectrum ( $\Gamma = 1.86 \pm 0.10$ ) and lower variability index ( $\delta = 0.36$ ). The other has a flux of  $34.7 \pm 5.7 \text{ cm}^{-2} \text{ s}^{-1}$ , spectral index of  $2.09 \pm 0.11$  and shows more evidence of variability, with  $\delta = 0.44$ .

An ASCA image of the GeV source region revealed two bright x-ray sources, one corresponding to a massive Wolf Rayet binary star system with a 21.6 day periodicity (WR 141), whose x-ray emission is consistent with a thermal spectrum at  $kT \sim 5 \text{ keV}$  (Roberts et al., 2001b). The second, identified as AX J2021.1+3651 was seen to have a non-thermal spectrum; subsequent investigations with the Arecibo radio receiver revealed a young, energetic pulsar with period of 104 ms (Roberts et al., 2002a). The ASCA image also reveals extended x-ray emission, which may be thermal emission from an SNR or a nearby massive star. The pulsar is an intriguing candidate for the  $\gamma$ -ray source, especially in light of the hard 3EG spectrum and relatively low variability of the source. The pulsar is located well within the 95% confidence region of the GeV source; its positional association with the 3EG source is less clear, it lies just outside of the 99% contour. If the 3EG and GeV sources correspond to the same object, the WR star system is a better positional association, although it is not

contained within the 95% contour of the 3EG source. Finally, a second WR-type star, WR 142 is located north of the 3EG catalog position, well within the 95% region. Source confusion between the adjacent EGRET sources probably means that there are systematic errors in the positions of the confidence contours for both 3EG sources and the GeV source; none of the above candidates should be considered as ruled out based on their position alone. Roberts et al. (2002a) conclude that the pulsar is the most conservative association, being a member of the only class of Galactic  $\gamma$ -ray sources to be unambiguously identified to date.

Mukherjee et al. (2000) and Halpern et al. (2001a) present detailed multiwavelength observations of 19 x-ray sources from the ROSAT faint source catalog consistent with 3EG J2016+3657. Most have stellar associations: WR-type systems, binaries, cataclysmic variables<sup>24</sup> and O- and B-type stars that are members of the OB association Cyg OB 1. These candidates are generally dismissed by Halpern et al. (2001a). Two ROSAT sources appear to be plausible candidates for the  $\gamma$ -ray emission, one an SNR G74.9+1.2 (or CTB 87), the other a flat spectrum radio source TXS B2013+370 (or G74.87+1.22), which overlaps the position of the SNR but is not related with it. The SNR has a filled center morphology, flat radio spectrum and high polarization, typical of a synchrotron nebula. No associated pulsar has been detected. Based on its low x-ray luminosity and large distance of 12 kpc, Halpern et al. (2001a) argue that the energetics of the system are not sufficient to account for the  $\gamma$ -ray source. Multiwavelength observations of TXS B2013+370 (Mukherjee et al., 2000) reveal that it has the properties of a blazar at radio, optical and x-ray wavelengths. The flux variability seen in the EGRET data was also seen in optical observations of the radio source. Halpern et al. (2001a) conclude that, based on the population of 66 well identified blazars at higher galactic latitudes, it would be expected to find at least one in the region of  $-1^\circ < b < +1^\circ$ . A redshift is not known for this object.

Romero et al. (1999) list four WR-type stars in the field, these have been discussed

---

<sup>24</sup>A binary system with a white dwarf and red dwarf in a close orbit of less than 1 solar radius which has an accretion disk an/or magnetically restricted flow of matter onto the white dwarf. Some undergo novae events, thermonuclear runaway in their accretion disks during which the luminosity can increase by factors of  $10^6$ .

**Table 5.17:** Upper limits for candidates in GeV J2020+3658 field.

Source Name	Coordinates		Extent	Upper Limit $\times 10^{-11} \text{ cm}^{-2} \text{ s}^{-1}$
	$\alpha_{2000}$	$\delta_{2000}$	deg	
GeV J2020+3658	$20^h 20^m 45.1^s$	$+36^\circ 58' 50''$	$0.28 \times 0.21$	3.7
3EG J2021+3716	$20^h 21^m 19.9^s$	$+37^\circ 15' 12''$	$0.35 \times 0.26$	3.7
3EG J2016+3657	$20^h 16^m 34.1^s$	$+36^\circ 52' 22''$	$0.68 \times 0.44$	5.8
AX J2021+3651 (PSR)	$20^h 21^m 07.8^s$	$+36^\circ 51' 19''$	-	2.0
TXS B2013+370	$20^h 15^m 28.4^s$	$+37^\circ 11' 02''$	-	2.0
G74.9+1.2 (CTB 87)	$20^h 15^m 40.3^s$	$+37^\circ 11' 52''$	$0.07 \times 0.07$	2.1
WR 137	$20^h 14^m 32.7^s$	$+36^\circ 39' 46''$	-	5.5
WR 138	$20^h 17^m 00.4^s$	$+37^\circ 25' 24''$	-	2.0
WR 141	$20^h 21^m 33.2^s$	$+36^\circ 55' 36''$	-	2.1
WR 142	$20^h 21^m 38.2^s$	$+37^\circ 23' 38''$	-	1.9
*J202509.2+363121	$20^h 25^m 09.2^s$	$+36^\circ 31' 21''$	-	4.4

\* The standard RASS-BSC catalog prefix of 1RXS is omitted for formatting purposes.

above. They also suggest that the  $\gamma$ -ray emission may be associated with the large OB-association listed as Cyg OB 1,8,9 in the catalog of Mel’Nik and Efremov (1995). The OB association, whose mysterious name denotes that it is an amalgamation of three previously known OB associations, is large ( $\sim 6.5^\circ \times 3.5^\circ$ ) and is listed as a possible counterpart to six EGRET sources, including the two of concern here. Finally, the RASS-BSC lists two bright x-ray sources. One corresponds to WR 138, the other is located far from the EGRET sources, but is displayed in figure 5.23 for completeness.

VHE observations of this source, centered on the GeV source, were made during October and November 1999. A total of 223 min. of data were collected. No significant emission was detected and upper limits for the region are presented in figure 5.23 and summarized in table 5.17. The spectra for the 3EG sources are shown in figure 5.24, with the limits at 350 GeV from the observations. In the case of 3EG J2021+3716 (left), the hard spectrum is constrained by the limit from within the 95% contour of the source. If the association with the pulsar is correct, the upper limit for the pulsar constrains the emission further, as indicated in the figure by the lighter upper limit at 350 GeV. A cut-off in the spectrum above the 10 GeV is required to accommodate either limit, which is consistent with a pulsar source. In the case of 3EG J2016+3657

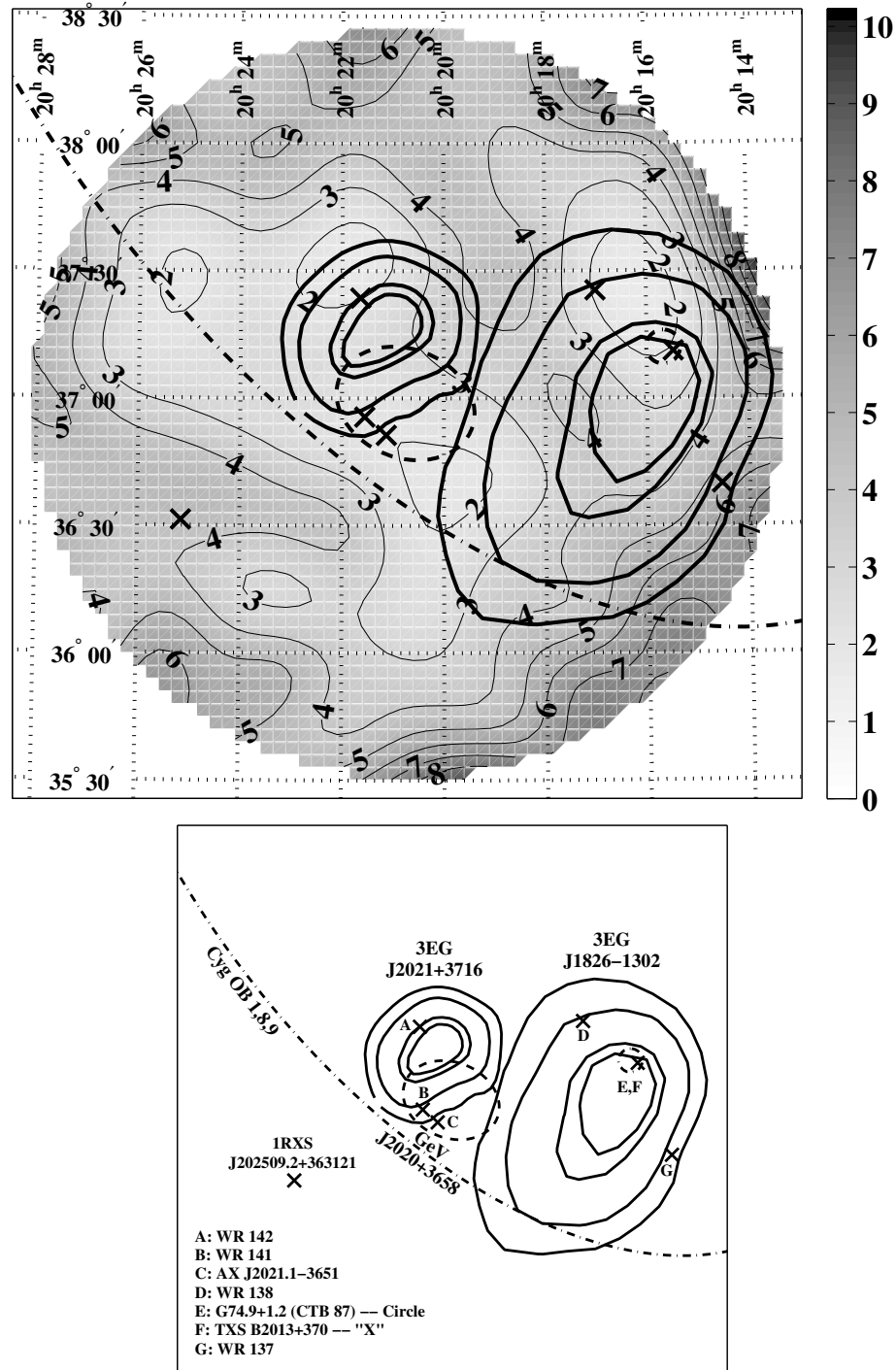
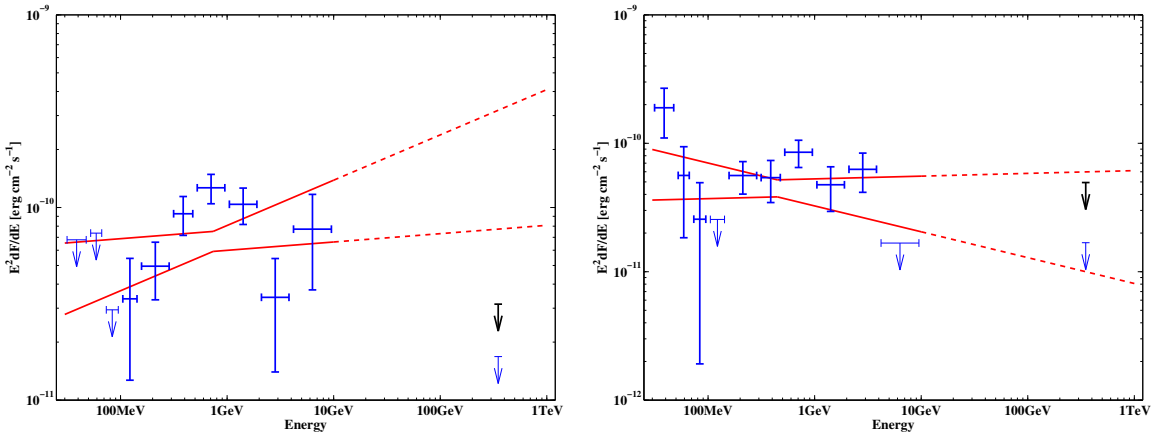


Figure 5.23: Upper limits on emission from GeV J2020+3658, 3EG J2021+3716 and 3EG J2016+3657 in units of  $10^{-11} \text{ cm}^{-2} \text{ s}^{-1}$ . The SNR, OB association and point source candidates in the field are indicated on the figure and labeled in the key below.



**Figure 5.24:** Spectrum for 3EG J2021+3716 (left) and 3EG J2016+3657 (right) from on-line version of the 3EG catalog with the upper limit at 350 GeV. In each case, the more constraining upper limit for the most likely association: the pulsar AX J2021+3651 and the blazar TXS B2013+370 (or SNR G74.9+1.2 whose limit is almost the same) respectively, is shown.

(right), the emission is not well constrained by the limit for the large 3EG error box, which extends close to the edge of the field of view of the VHE observations, where the instrument is significantly less sensitive. If the blazar or SNR association is correct the emission is somewhat constrained by the limit, although not significantly.

### 5.1.17 3EG J2227+6122

The low latitude  $\gamma$ -ray source 3EG J2227+6122 was first detected by the COS-B satellite (2CG 106+1.5) and subsequently by the CGRO instruments EGRET and COMPTEL between 0.75 MeV and 10 GeV. It has a relatively strong flux, spectral index of 2.24 and low variability index of  $\delta = 0.20$ .

Halpern et al. (2001c) and Halpern et al. (2001b) report on multiwavelength observations of six possible x-ray counterparts in the region of 3EG J2227+6122. Optical observations identified five of the sources with stars, the sixth remained unidentified. Radio observations revealed only one radio source, coincident with the unidentified x-ray source, which was subsequently identified as a young, 55 ms radio pulsar:

**Table 5.18:** Upper limits for candidates in 3EG J2227+6122 field.

Source Name	Coordinates		Extent	Upper Limit
	$\alpha_{2000}$	$\delta_{2000}$	deg	$\times 10^{-11} \text{ cm}^{-2} \text{ s}^{-1}$
3EG J2227+6122	$22^h 27^m 20.8^s$	$+61^\circ 23' 28.9''$	$0.50 \times 0.41$	4.1
GeV J2227+6101	$22^h 27^m 45.9^s$	$+61^\circ 01' 22.7''$	$0.54 \times 0.54$	3.5
PSR J2229+6144	$22^h 29^m 05.3^s$	$+61^\circ 14' 09.3''$	-	2.2
87GB B2226+6122	$22^h 28^m 38.0^s$	$+61^\circ 37' 42.0''$	-	2.8
*J223500.5+604935	$22^h 35^m 00.5^s$	$+60^\circ 49' 35.0''$	-	2.7

\* The standard RASS-BSC catalog prefix of 1RXS is omitted for formatting purposes.

PSR J2229+6144. Since the radio and  $\gamma$ -ray observations were non-contemporaneous, and the timing ephemeris for a young pulsar cannot be extrapolated back in time as the pulsations are unstable, a search for pulsations in the EGRET data could not be performed. Halpern et al. (2001b) conclude that since no other x-ray or radio counterpart is found to be consistent with the  $\gamma$ -ray source, it is more conservative to accept the association with the pulsar, than to reject it.

Mattox et al. (2001) suggest a possible association with 87GB B2226+6122, a radio source which corresponds to a Galactic H<sub>II</sub> region. In addition, Romero et al. (1999) lists the OB-association Cep OB 2B as a possible counterpart, although there is no overlap between the 95% contour of the 3EG source and the OB association; their centers are separated by  $\sim 3.8^\circ$ .

VHE observations of this object were made in September and October 2000, resulting in 360 min. of data pointed at the center of the 3EG source. The map of excess  $\gamma$ -ray-like events shows an excess within the 95% confidence contour, at an a priori significance of  $3.2\sigma$  (figure 5.25). The excess does not coincide with the pulsar or with the only RASS-BSC x-ray source in the region (1RXS J223500.5+604935). Given there is no a priori reason to expect emission from the location of the excess, the true probability of obtaining such an excess by chance must be calculated using figure 4.7. For 200 independent trials, appropriate to all the independent bins in the 95% contour of all sources, this probability is equivalent to a Gaussian distribution at  $\sim 1.2\sigma$  level. As in the case of 3EG J1337+5029, the probability is below what is required to claim a detection. Upper limits on emission are presented in figure 5.26 and summarized in

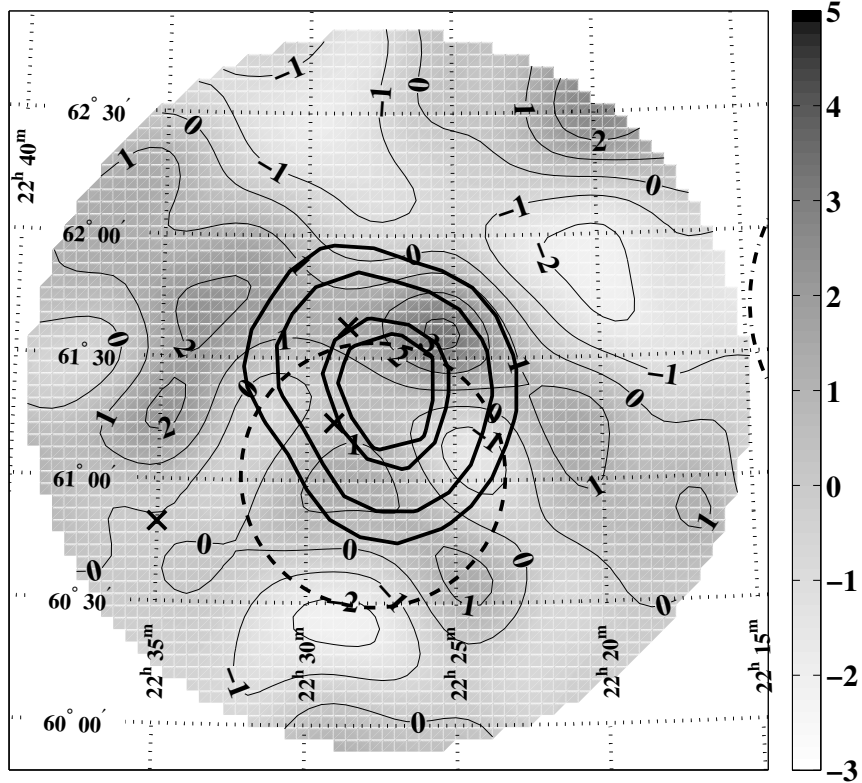


Figure 5.25: Significance of excess  $\gamma$ -ray-like events, detected from the region of 3EG J2227+6122.

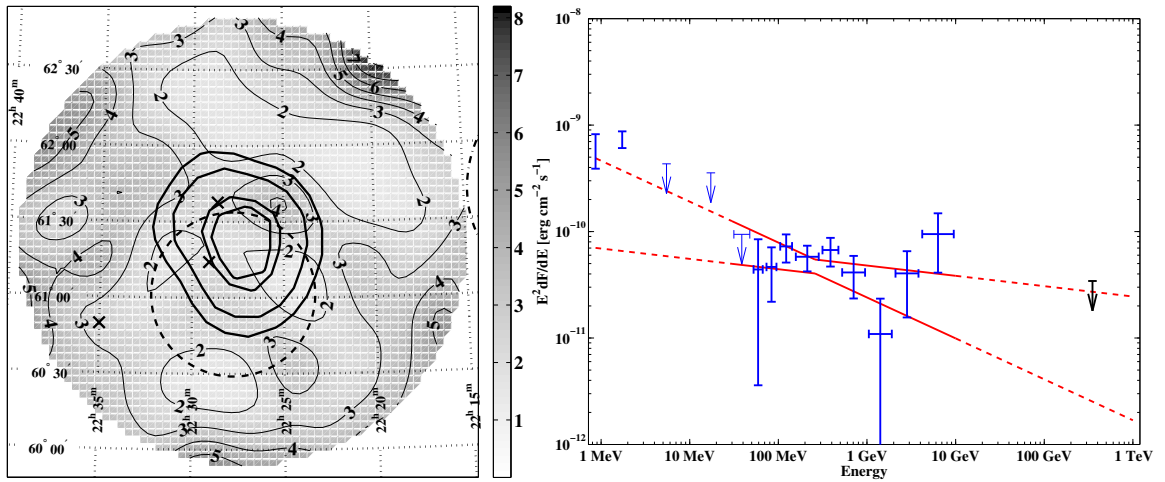


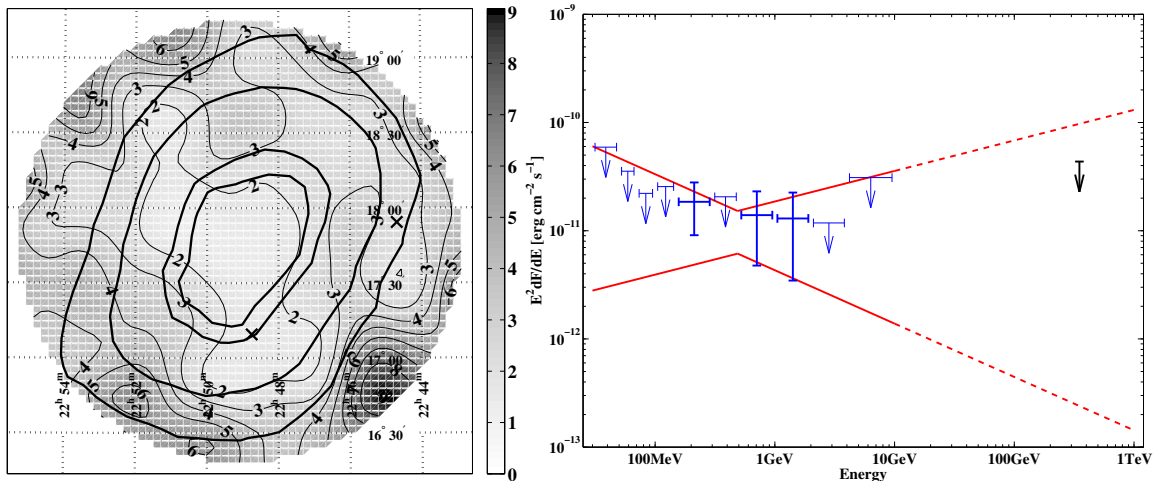
Figure 5.26: (Left) Limits on emission from 3EG J2227+6122 in units of  $10^{-11} \text{ cm}^{-2} \text{ s}^{-1}$ . The 3EG error contours are overlaid as heavy lines. The dot-dashed ellipse to the west indicates Cep OB 2B. (Right) Spectrum from the COMPTEL catalog (Schönfelder et al., 2000) and on-line version of the 3EG catalog with the upper limit at 350 GeV.

table 5.18. The limits for the 95% contour region do not significantly constrain the extrapolated EGRET spectrum.

### 5.1.18 3EG J2248+1745

The EGRET  $\gamma$ -ray source 3EG J2248+1745 lies  $\sim 36^\circ$  from the Galactic plane, has a relatively low flux, shows considerable variability ( $\delta = 0.65$ ) and has a large positional uncertainty. Very little is known about the source, Colafrancesco (2002) note that the cluster Abell 2248, at redshift of  $z = 0.143$ , lies within the 95% contour, but is a unlikely counterpart due to the variability of the EGRET source. Mattox et al. (2001) list the well studied flat spectrum radio source 87GB B2251+1552 (3C454.3, an AGN at  $z = 0.86$ ) as an unlikely association. The radio source lies well outside of the 99% contour and is a far more likely counterpart for 3EG J2254+1601. The RASS-BSC contains one bright x-ray source with the EGRET 99% contour: 1RXS J224441.6+175418.

The VHE data were taken over two observing seasons between October 2001 and November 2002. In total, 304 min. of data were obtained, pointing at the center of



**Figure 5.27:** (Left) Limits on emission from 3EG J2248+1745 in units of  $10^{-11} \text{ cm}^{-2} \text{ s}^{-1}$ . The 3EG error contours are overlaid as heavy lines. (Right) Spectrum from the on-line version of 3EG catalog with the upper limit at 350 GeV.

**Table 5.19:** Upper limits for candidates in 3EG J2248+1745 field.

Source Name	Coordinates		Extent	Upper Limit
	$\alpha_{2000}$	$\delta_{2000}$	deg	$\times 10^{-11} \text{ cm}^{-2} \text{ s}^{-1}$
3EG J2248+1745	$22^h 48^m 54.3^s$	$+17^\circ 47' 09.5''$	$1.13 \times 0.78$	5.2
Abell 2486	$22^h 48^m 45.0^s$	$+17^\circ 09' 30.0''$	-	1.7
*J224441.6+175418	$22^h 44^m 41.1^s$	$+17^\circ 54' 18.0''$	-	2.6

\* The standard RASS-BSC catalog prefix of 1RXS is omitted for formatting purposes.

the 3EG source. No significant excess of events were seen, upper limits are presented in figure 5.27 and summarized in table 5.27. Due to the large uncertainty in the EGRET location, the upper limit for the region within the 95% contour is not very sensitive. An extrapolation of the EGRET spectrum to 350 GeV is not significantly constrained by the limits.

### 5.1.19 3EG J2255+1943

The EGRET source 3EG J2255+1943 has the largest positional error and variability index of all sources considered in this survey. The diameter of the 95% error contour is larger than the field of view of the Whipple instrument, and is not closed in the significance map from the on-line version of the 3EG catalog. The source has a low flux and soft spectrum of  $\Gamma = 2.24 \pm 0.14$ . Little is known about this source, no counterparts have been suggested at other energies. Two x-ray sources in the region

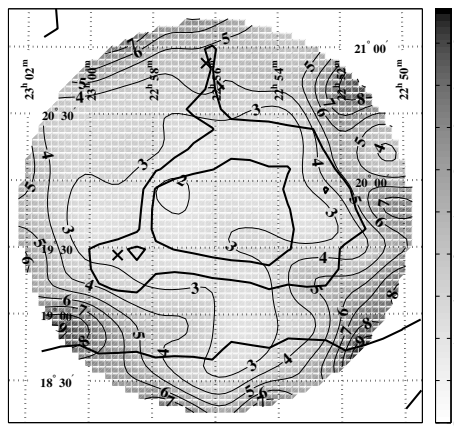


**Figure 5.28:** Limits on emission from 3EG J2255+1943 in units of  $10^{-11} \text{ cm}^{-2} \text{ s}^{-1}$ .

**Table 5.20:** Upper limits for candidates in 3EG J2255+1943 field.

Source Name	Coordinates		Extent	Upper Limit
	$\alpha_{2000}$	$\delta_{2000}$	deg	$\times 10^{-11} \text{ cm}^{-2} \text{ s}^{-1}$
*J225617.9+205257	22 <sup>h</sup> 56 <sup>m</sup> 17.9 <sup>s</sup>	+20°52'57.0"	-	4.4
*J225906.4+192637	22 <sup>h</sup> 59 <sup>m</sup> 06.4 <sup>s</sup>	+19°26'37.0"	-	2.7

\* The standard RASS-BSC catalog prefix of 1RXS is omitted for formatting purposes.

are listed in the RASS-BSC. VHE observations during the winter of 2001 and 2002 yielded a total of 250 min. of data which show no significant excess of  $\gamma$ -ray-like events. Since the total error box is not contained within the field of view of the instrument an upper limit is not presented for the 3EG source. Limits for the portion of the source within the field of view of the VHE observations are presented in figure 5.28. Limits for the two RASS-BSC sources are summarized in table 5.20.

## 5.2 Summary

Results from the 19 sets of observations are presented in table 5.21. The results represent  $\sim 100$  hrs of on-source observations and approximately the same amount of off-source control data, a large program undertaken over four years with the Whipple 10 m IACT. Upper limits for the 95% confidence regions of 24 EGRET  $\gamma$ -ray sources are presented in the table. The limits range from 15% of the Crab Nebula flux above 350 GeV in the case of 3EG J0433+2908 to 65% of the Crab flux for 3EG J0423+1707. These limits are conservative since they represent the maximum derivable limit from anywhere in the field. In each case, where a counterpart has been suggested, more sensitive limits are presented elsewhere in this chapter.

In the cases of 3EG J0433+2908 and GeV J0508+0540, some (or all) of the observations were made in the in the TRACKING mode, which are incompatible with the two dimensional analysis technique. The observations resulted in sensitive limits on the point source AGNs suggested as associations for the EGRET emission.

**Table 5.21:** Summary of upper limits for all 3EG and GeV sources observed in the survey. Some observations result in limits on more than one source. The observations of GeV J0508+0540 were made in a mode incompatible with the two dimensional analysis. In the case of 3EG J2255+1943, the EGRET error box is larger than the field of view of the instrument.

Source Name	Exposure [min]	Upper Limit $\times 10^{-11} \text{ cm}^{-2} \text{ s}^{-1}$
3EG J0010+7309	194.6	2.2
3EG J0241+6103	524.4	2.2
3EG J0423+1707	193.0	6.6
3EG J0433+2908	499.9	1.6
3EG J0450+1105	273.9	5.0
GeV J0508+0540	842.0	-
3EG J0613+4201	276.5	4.3
3EG J0628+1847	332.1	4.1
3EG J0634+0521	248.0	5.3
3EG J0631+0642	248.0	6.0
GeV J0633+0645	248.0	4.9
3EG J1009+4855	248.4	4.6
3EG J1323+2200	275.6	3.1
3EG J1337+5029	165.7	5.9
3EG J1826–1302	416.3	4.2
3EG J1823–1314	416.3	3.2
GeV J1825–1310	416.3	4.2
3EG J1835+5918	110.9	3.8
GeV J1907+0557	277.1	3.0
3EG J2021+3716	222.5	3.7
3EG J2016+3657	222.5	5.8
GeV J2020+3658	222.5	3.7
3EG J2227+6122	360.1	4.1
GeV J2227+6101	360.1	3.5
3EG J2248+1745	304.4	5.2
3EG J2255+1943	248.9	-

## 6. NEXT GENERATION DETECTORS

The success of the current generation of ground-based detectors in the 300 GeV to 10 TeV energy range has motivated the construction of a next generation of experiments. The design of these next generation VHE  $\gamma$ -ray detectors is guided by the desire to improve the flux sensitivity over this range of energies and to reach lower energies where there will be overlap with the energy range accessible to upcoming satellite based experiments. Increased sensitivity will be achieved by increasing the number of  $\gamma$ -rays collected and improving the discrimination of  $\gamma$ -rays from background cosmic-rays.

The former is achieved by having larger light collection area, the ultimate being to collect all of the light from the air shower with a detector whose mirror area is comparable to the size of the Čerenkov light pool on the ground. The amount of light recorded from an air shower increases more quickly with mirror area ( $\propto A$ ) than the fluctuations in the background light recorded from the night sky ( $\propto A^{1/2}$ ), the principal background determining the triggering threshold. Collecting more light allows this threshold to be lowered and hence lower energy events to be collected. Two large area detector designs have been adopted, the first employs a large steerable telescope, exemplified by the MAGIC telescope (Lorenz, 1996) being built on La Palma which is a 17 m carbon-fiber frame telescope with a  $234 \text{ m}^2$  mirror area. The second are converted solar furnace experiments such as STACEE in New Mexico (Covault et al., 2001) and CELESTE (Smith et al., 1996) in the French Pyrenees, which comprise large fields of heliostats with area  $\sim 2400 \text{ m}^2$  and a central light collecting tower which houses secondary optics and the photon detectors. All of the upcoming experiments have, at minimum,  $75 \text{ m}^2$  of mirror area, equivalent to a 10 m diameter dish.

Inability to discriminate  $\gamma$ -rays from background cosmic-rays, cosmic electrons and local muons is ultimately the factor that limits the sensitivity of all ground-based experiments. The ability of a system to discriminate between a  $\gamma$ -ray signal and

background events depends on many factors, from the design of the instrument and the analysis technique. Some of these factors can change during the lifetime of the experiment, e.g. improved analysis algorithms, upgraded photon detectors etc. It is the design of the instrument itself that contributes, in the largest degree, to the elimination of background events. An instrument that is designed to take advantage of the inherent difference between signal events and background events can achieve good intrinsic discrimination by its very nature. One such design is an array of multiple telescopes viewing the air shower stereoscopically from different points on the ground. Signals from multiple telescopes, placed close enough that they all lie within the Čerenkov light pool of an air shower, can be combined in such a way that  $\gamma$ -ray-like events produce a very different signal from cosmic-ray events. The array can be triggered in a fashion that eliminates local muon events and reduced accidental night-sky triggers. Examples of such systems are VERITAS (Weekes et al., 2002), a system of seven 12 m telescopes in southern Arizona, which will be the largest array in the northern hemisphere. HESS (HESS collaboration, 2002) an array of four 12 m telescopes being built in Namibia and CANGAROO (Enomoto et al., 2002a) a four, 10 m telescope array in Australia will survey the sources in the skies of the southern hemisphere. The array technique has been successfully demonstrated, albeit with small telescopes, by the HEGRA collaboration (Konopelko, 1999).

## 6.1 VERITAS

The VERITAS experiment, which began construction in 2002, will be an array of seven 12 m telescopes, located in southern Arizona, USA. The seven f/1.0 telescopes will be situated at the vertices and center of a regular hexagon of side 80 m. The Čerenkov light pool of  $\gamma$ -ray induced showers that impact close to the center of the array will encompass all seven telescopes, each of which will have a different view of the shower development which can be combined to give a more accurate reconstruction of the properties of the primary than those previously available to single telescope ground-based  $\gamma$ -ray instruments.

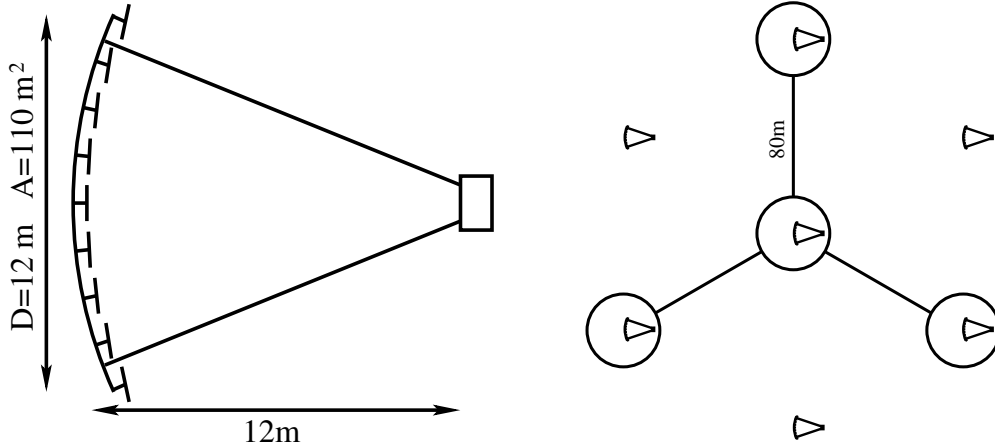


**Figure 6.1:** (Left) Dimensions of proposed VERITAS telescopes. (Right) Layout of seven telescope VERITAS array with VERITAS-4 sub-array indicated.

VERITAS will be built in three stages between 2002 and 2007. After a single prototype telescope is completed in 2003 and operated for a number of months, the second stage, a four telescope array will be completed in 2005. The final stage, bringing the full seven telescope array on-line, will then be completed in 2007. An evaluation of the characteristics of the four telescope array is presented in detail in this chapter.

## 6.2 Overview of the VERITAS-7 simulations

The results of a detailed simulation of the VERITAS array, as performed by V. Vasilev, are presented in the original proposal by the VERITAS collaboration to DOE and NSF (VERITAS collaboration, 1999). Two sub-array layouts were simulated in detail, the complete system of seven 10 m telescopes separated by 80 m and a sub-array of three telescopes separated by  $80 \times \sqrt{3} \approx 140 \text{ m}$ .

In the time since this original work was performed, the proposed design of the array has changed, the telescope diameter has been increased to 12 m and the initial configuration will be a 4 telescope sub-array with an 80 m separation. Each telescope will have 499 channels with a field of view of  $3.5^\circ$ , as in the original proposal. This chapter presents an extrapolation of the characteristics of the four telescope array (VERITAS-4) from the results of the original simulation. This was done by the au-

thor as part of this dissertation; the details are presented in this chapter. A brief overview of the original work is discussed first.

### 6.2.1 Trigger conditions

The VERITAS system uses multi-level trigger hardware to eliminate much of the accidental triggers, mostly due to the night-sky background light. This allows the trigger level to be set as low as possible yet keep the array trigger rate below 1 kHz, as required by the data acquisition system. The first level (L1), or “channel-level” trigger is a discriminator set to trigger when the signal in the channel exceeds a certain voltage, which is usually expressed in terms of a number of photo-electrons (p.e.) detected within a certain time, assuming a known single p.e. voltage pulse profile. The L2, or “telescope-level” trigger is a pattern recognition system which can be programmed to require two, three or four neighboring channels trigger in the camera within a certain coincidence time. This trigger preferentially selects air-shower events over night-sky noise events since the Čerenkov light from an air-shower originates largely from the same region of the sky, whereas night-sky fluctuations are distributed randomly in the camera. The L3, or “array-level” trigger is programmed to require that a certain number of telescope-level triggers occur within a coincidence time. The L3 trigger is responsible for initiating the data readout. The trigger requirements used in the original VERITAS-7 simulations, for both the full array and the three telescope sub-array, are listed in table 6.1.

**Table 6.1: Trigger requirements for VERITAS-7 simulations.**

(Sub-)Array	L1 trigger level	L2 (Telescope)	L3 (Array)
Seven telescope array	4.2 p.e.	3 neighbors	3 out of 7 (3/7)
Three telescope sub-array	3.8 p.e.	3 neighbors	3 out of 3 (3/3)

### 6.2.2 Reconstruction

Stereoscopic imaging of the air-shower with an array of imaging telescopes allows the nature of the primary particle to be inferred more accurately than with a single

telescope. Reconstruction of the parameters of a primary  $\gamma$ -ray, its energy, arrival direction and impact parameter can be estimated by combining the images from the individual telescopes.

The images of a compact air-shower, such as those from a  $\gamma$ -ray primary, tend to be aligned toward the arrival direction of the primary. This tendency, when employed to a set of stereoscopic views of an air-shower, allow the arrival direction to be determined by overlapping the images from all telescopes and tracing the axes of the individual images to a common point. For less compact showers, such as those that are hadronic in origin, a single point of origin for all of the images cannot usually be identified. In addition, by tracing the axes of the images from their origin at the site of each telescope on the ground, the location of the shower core impact with the ground can be found. This simple geometrical reconstruction technique, as illustrated in figure 6.2, demonstrates the stereoscopic approach. Although this simple approach is powerful, there are additional properties of the air-shower that can be inferred from the images if a more sophisticated algorithm is adopted. One such approach, described below, additionally provides an estimate of the width of the shower emission region in space, a parameter that is different for  $\gamma$ -ray- and background-induced events.

The most likely origin of the  $\gamma$ -ray is estimated by a least-squares approach. A simple model of the shower is constructed and the parameters of the model adjusted to best fit the data from all telescopes. It is assumed that the shower can be represented by an “emission-region” in the sky which is distributed around a shower-axis, a line in 3-D space represented by two direction angles ( $\theta, \phi$ ) and a shower impact location on the ground ( $x_0, y_0$ ). For convenience,  $\theta$  and  $\phi$  are taken as the direction the shower-axis makes to the optical axis of the array, figure 6.3. The impact location is taken relative to the center of the array on the ground. As the shower progresses through the atmosphere, Čerenkov photons are emitted from the emission region and these may be detected by the telescopes. The density of Čerenkov emission is proportional to the charged particle density in the emission region. This region can be considered, to first order, as an ellipsoid, symmetrically distributed around the shower-axis with particular RMS width and length, the mean values of which depend

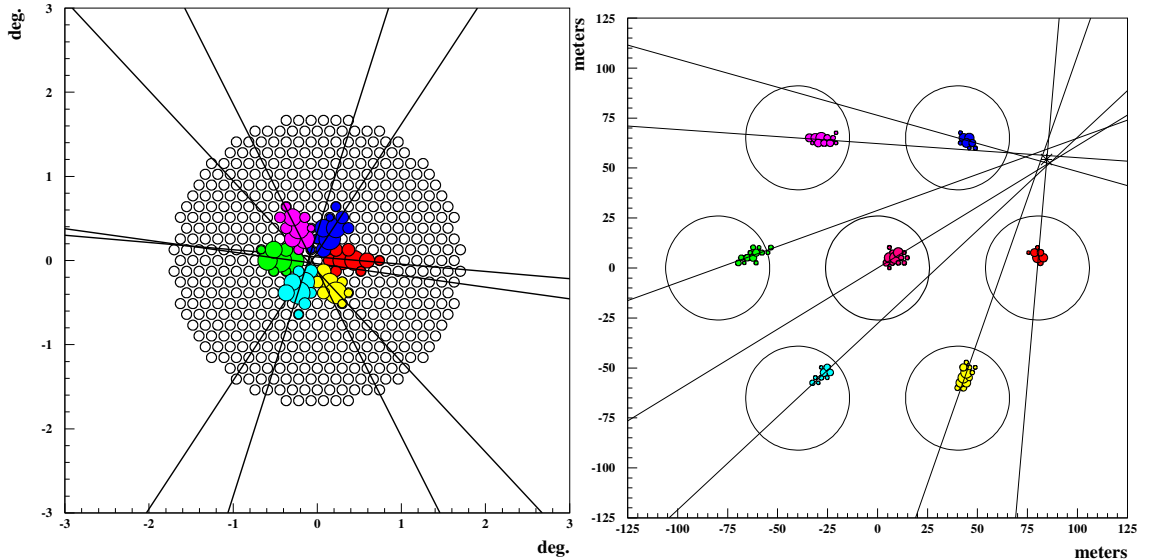


**Figure 6.2:** Simulated 300 GeV  $\gamma$ -ray events. (Left) The axes of the six images, combined in *angular space* in the field of view of the array, point toward the origin of the  $\gamma$ -ray. (Right) Axes of the images, when combined in *2-D space* on the ground, indicate the impact location of the shower core. From VERITAS collaboration (1999).

on the type of particle that initiated the shower and its energy. Photons detected by a telescope will have taken an unknown path from this region to the camera, having been reflected from some portion of the telescope mirror. Ideally, one would like to reconstruct the width of the emission-region, by tracing the detected photons exactly back along their path in space, a process known as back-propagation. It would then be possible to find the RMS width of the emission region by calculating the mean square distance between the photon paths and the shower axis. Of course, in reality this is not possible for a number of reasons. First, it is not possible to record every emitted photon, due to the limited telescope size and inefficiencies in the detector, so any estimate will be statistical in nature, with errors decreasing as the number of detected photons increases. A more significant factor is the finite, non-zero size of the PMTs in the focal plane. Since these detectors then subtend a non-zero solid angle in space, there is inherent pixelation in the arrival directions of the detected photons (figure 6.4). Finally, it is impossible to determine which portion of the  $110\text{ m}^2$  mirror any particular photon was reflected from. Essentially this means that no single path

through space can be assigned to any detected Čerenkov photon; an infinite number of possible paths must be considered.

Ideally, for each channel that records a signal, an infinite number of back-propagated rays are constructed, each reflected off a different part of the telescope mirror and propagated out into space, giving every possible path for every Čerenkov photon that was detected in each of the PMTs. For each ray, the minimum square distance,  $d_i^2$ , between the  $i$ 'th ray and the shower axis is calculated. These squared distances are summed to give  $D^2(\theta, \phi, x_0, y_0)$ , and the result minimized over all possible axis parameters. Those parameters which minimize the total square distance is then taken as the best “fit” of the shower-axis to the data, since it requires an emission region with the smallest width. In practice, an infinite number of back-projected rays are not constructed for every PMT, a sample are used, distributed evenly over the mirror area and over the area subtended in space by the PMT. The actual value of  $D_{\min}$ , reflects the size of the emission region but is also dependent on the PMT pixelation and mirror size.

### 6.2.3 Background rejection

Rejection of the isotropic cosmic-ray and cosmic-electron background come from two separate selection techniques. The first, based on the reconstructed arrival direction of the  $\gamma$ -ray, is applicable only to point sources of  $\gamma$ -rays, such as AGN and pulsar candidates. The second, based on the “shape” of the air-shower is applicable to point source and extended  $\gamma$ -ray sources. In evaluating the performance of the VERITAS array, only point source candidates are considered here, for which the instrument will operate in its most sensitive mode.

The goal of any selection technique is to eliminate as many background events as possible while keeping as many of the  $\gamma$ -rays as possible. It is quite acceptable to eliminate up to  $\sim 50\%$  of the  $\gamma$ -rays in order to have an efficient background ( $> 99.99\%$ ) rejection. In general, the efficiency of background rejection is dependent

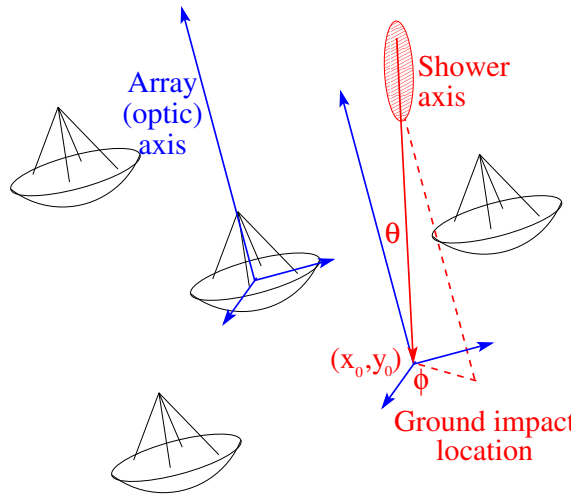


Figure 6.3: Shower axis parameters,  $(\theta, \phi)$  describe the direction of the reconstructed axis,  $(x_0, y_0)$  the point at which the axis intersects the ground.

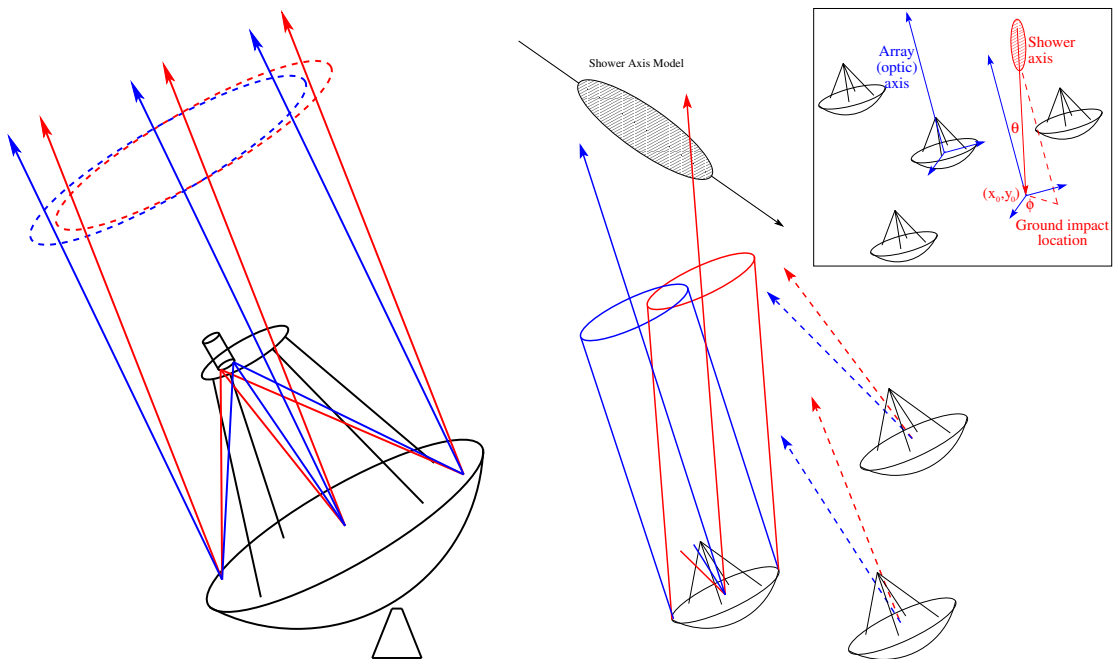


Figure 6.4: (Left) Some of many possible paths for Čerenkov photon detected in PMT. (Right) Shower reconstruction technique. Detected photons are back-propagated from PMT, reflected off the mirror and into space, illustrated as cylinders projected from one of the telescopes.

on the energy of the primary. Showers resulting from high energy primaries can be imaged accurately, allowing the primary to be identified with a high degree of certainty. At these energies, background events can be eliminated effectively. Low energy events are imaged less well, identification of the primary is less certain and rejection is less effective.

The first rejection technique, the “aperture-cut”, exploits the fact that, for a point source, only those events which are reconstructed as having arrived from a point in space that lies close to the candidate source need be considered. All other events can be rejected as part of the isotropic background. Assuming the array is pointing directly at a candidate  $\gamma$ -ray source, the reconstructed shower axis parameter,  $\theta$ , gives the distance between  $\gamma$ -ray and the candidate source. To reject a large part of the isotropic background it is sufficient to define a maximum value,  $\theta_{\text{cut}}$ , and consider only events with  $\theta < \theta_{\text{cut}}$ .

From simulations, it is found that the dispersion in the reconstructed arrival direction of  $\gamma$ -rays from a point source, depends on the energy of the  $\gamma$ -ray. The instrument has a small dispersion for high energy events, i.e. high energy events tend to be reconstructed as having arrived from a small region of space surrounding their true origin. The opposite is true for low energy events, which tend to be reconstructed in a larger area surrounding the true origin.

The second rejection technique comes from consideration of the physical meaning of  $D_{\min}(\theta, \phi, x_0, y_0)$ .  $D$ , the RMS distance from the shower axis of the photons detected on the ground, is related to the physical width of the Čerenkov emission region in space, and is generally larger for a hadronic shower than for a compact  $\gamma$ -ray shower, since the transverse momentum of an average hadronic shower particle is larger in the former case, as discussed in section 3.1.

By simply choosing a “shape-cut”,  $D_{\text{cut}}$  on the value of  $D_{\min}$  for a shower, one can preferentially keep  $\gamma$ -ray events, i.e. require that  $D_{\min} < D_{\text{cut}}$ . In practice, it is better to make the cut a function of the primary photon energy,  $D_{\text{cut}}(E_\gamma)$ . It is found

that the rejection is most efficient for very energetic  $\gamma$ -rays and almost completely ineffective for low energy  $\gamma$ -rays.

To estimate the energy of the primary  $\gamma$ -ray, an “energy estimator” function, must be found. The estimator must relate the measured image parameters, denoted as  $\Theta = \{D, \theta, \phi, x_0, y_0, S_i, z\}$ , where  $S_i$  is the signal recorded by the  $i$ 'th telescope and  $z$  is the angle between the zenith and the axis of the array, to the energy of the primary. Many approaches to energy estimation are possible. One approach is to find, from simulations, an analytic function that estimates the average amount of light collected in the array, given the energy of the primary, the impact parameter,  $b=\sqrt{x_0^2 + y_0^2}$ , and the zenith angle. This function can then be inverted to give an energy estimator. Another approach is to determine the probability density function  $p(\Theta; E)$  describing the likelihood that the observed parameters,  $\Theta$ , arose from an event of energy  $E$ . For any given event, the probability density can be searched to give the most likely energy of the particle. Energy estimation techniques applicable to an array of telescopes are discussed in more detail in Hofmann et al. (1997) and Aharonian et al. (1999).

Given an energy-estimator function, it is possible to calculate the best value for the shape-cut,  $D_{\text{cut}}(E_\gamma)$ , and aperture-cut,  $\theta_{\text{cut}}(E)$ , as a function of energy. Since the shape-cut is applied to all data (from point- and extended-sources), an optimum value is chosen for this function in the absence of any aperture-cut. With these values chosen, optimum values for the aperture-cut are chosen, with the shape-cut applied. This process, originally done for the VERITAS-7 configuration, was repeated for the VERITAS-4 evaluation and will be described in detail in section 6.3.4.

### 6.3 Performance of the four telescope VERITAS sub-array.

Evaluation of the VERITAS-4 sub-array was done by interpolation from the full VERITAS-7 characteristics introduced above. This was done in two steps, first the results of the original analysis for the 3/3;10m (3 triggering out of an array of 3, 10 m telescopes) and 3/7;10m configurations were scaled from the original 10 m diameter

case to a 12 m case. These scaled results are designated 3/3;12m and 3/7;12m. Finally an interpolation to the required 3/4;12m array was made between the scaled 3/3;12m and 3/7;12m characteristics.

### 6.3.1 Trigger level

At the time this work was performed, it was planned to locate the VERITAS array under the dark skies of Montosa canyon in southern Arizona. The mean background photon rate from the night sky was taken to be,  $\langle NSB_{\text{flux}} \rangle \approx 2-4 \times 10^{12} \text{ s}^{-1} \text{ m}^{-2} \text{ sr}^{-1}$ , the factor of two in range corresponding to the variation from a patch of dark sky to the bright Galactic Plane region. For a telescope with  $110 \text{ m}^2$  mirror area and PMTs of angular diameter  $0.15^\circ$  in the focal plane, and after factoring in the mirror reflectivity and efficiency of the PMTs, this corresponds to a detected photon rate of  $\langle NSB \rangle \approx 0.16-0.32 \text{ ns}^{-1} \text{ channel}^{-1}$ . The L2, telescope-trigger coincidence time is taken to be 8 ns., i.e., a requirement that three neighboring channels to trigger within 8 ns. The L3, array-trigger coincidence time is 40 ns., i.e. requiring that three telescopes trigger within 40 ns. Determining the various trigger rates (L1, L2, L3) given the night-sky background rate and given a L1 pixel trigger threshold requires that the response of the various components of the trigger be simulated and subjected to random, Poisson distributed, background photons. This was done by J. Hall from the University of Utah, and the results are presented in figure 6.5 for completeness. The rate of triggering due to background cosmic ray events is also displayed; this is discussed in more detail in section 6.3.6.

A threshold of 5.6 p.e. was chosen as appropriate for 3/4;12m, corresponding to a trigger rate of  $\sim 1 \text{ Hz}$  due to background light. The array is designed to operate at rates up to 1 kHz, corresponding to a threshold of  $\sim 5.0 \text{ p.e.}$  However, it can be seen that the array rate increases rapidly as the trigger threshold is decreased. The threshold of 5.6 p.e. is chosen for stability and in order that the simulations will remain largely valid in regions of the sky where the mean background photon rate is slightly higher than the  $0.16 \text{ ns}^{-1} \text{ channel}^{-1}$  assumed valid for dark sky.

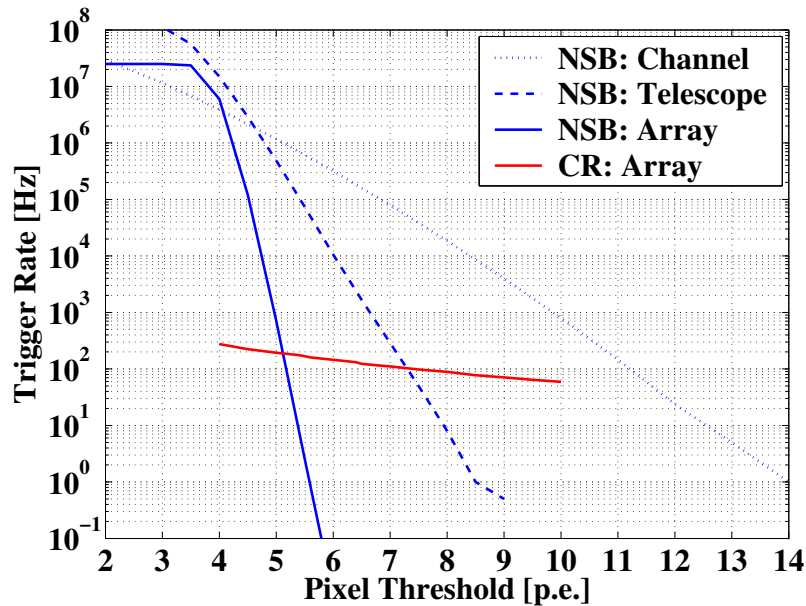


Figure 6.5: Triggering rate for L1 (Channel), L2 (Telescope) and L3 (Array) vs. pixel trigger threshold (in photo-electrons). The rate of background cosmic-rays is also shown.

### 6.3.2 Simulations database

Shower simulations, both  $\gamma$ -ray and proton induced, were generated using the KASCADE simulation package (Kertzman and Semborski, 1994). Producing simulated images in the focal plane of an instrument is a three stage process. In the first stage, KASCADE simulates the evolution of air-showers initiated by a set of mono-energetic particles (usually,  $\gamma$ -rays or protons) which are randomly injected into the upper-atmosphere within a certain distance from the center of the instrument (the “sampling radius”) at a determined zenith angle. The package records the particle tracks that join the random interaction sites in the atmosphere. In the second stage of the simulation, Čerenkov light is produced along the particle tracks (if the particle was charged and had energy above the Čerenkov threshold) and propagated through the atmosphere to ground level where all the surviving photons are recorded. The final stage is to process this photon database through a simulation of the instrument itself, accounting for randomly distributed mirror mis-alignments, the reflectivity of aluminum, mirror weathering, characteristics of the light concentrators and

the wavelength dependent efficiency of the PMTs. This final stage results in a list of photo-electrons for each channel and the relative times that they were detected.

The  $\gamma$ -ray database for the 12 m VERITAS array consists of 25 mono-energetic bins, distributed evenly in  $\log(\text{energy})$  between 10 GeV and 10 TeV with eight bins per decade in energy. The number of events simulated at each energy decreases with energy reflecting the fact that many more events are needed at low energies to obtain good statistics since the triggering efficiency is much lower and hence most events are not seen by the array. This will be shown in section 6.3.3. Conversely, the sampling radius is increased with energy as large, energetic events are visible further from the array, the lateral spread of particles in an energetic air-shower being larger. The sampling radius must be chosen large enough that a significant fraction of events fail the selection criteria, in this work the sampling radius was chosen so that a maximum of  $\sim 85\%$  of events passed the selection criteria. If this requirement failed at any energy the sampling radius was increased. All energy bins are produced at a zenith angle of  $z = 20^\circ$ , which is considered to be representative of typical observing conditions. Table 6.2 lists the details of four representative energy bins.

**Table 6.2: Details of the  $\gamma$ -ray simulation database.**

Energy [TeV]	Sampling Radius [m]	Number of Events
0.01	157.164	1197031
0.1	209.551	146334
1.0	304.897	14091
10.0	376.145	1323

The proton-induced database was produced in a similar manner, although there is an important difference from the  $\gamma$ -ray database. The proton database has four energy bins per decade of energy and each energy bin consists of 36 sub-bins. This is done to account for the fact that the cosmic-ray background events are distributed isotropically. For a  $\gamma$ -ray point-source with the telescope pointing directly at the source, all primaries propagate parallel to the optical-axis of the array. This is not true for proton events, so sub-bins are produced with events originating with angle  $\theta$  to the optical axis of the array. These 36 sub-bins are distributed evenly in  $\theta^2$  with

$0^\circ < \theta < 6^\circ$ . For each of the sub-bins, events are injected into the atmosphere within a sampling radius, in a similar manner to the  $\gamma$ -ray database.

### 6.3.3 Gamma-ray trigger rate

To extrapolate from the original work with 10 m telescopes, the trigger criteria were applied to the two original configurations (seven and three telescopes) and to the four telescope array, but with 12 m aperture instruments: 3/7;12m, 3/3;12m and 3/4;12m. Hence, the efficiency of each configuration was evaluated over the range of energies under consideration. In this work, each event was required to pass the L1, L2 and L3 trigger requirements and was subjected to an additional requirement aimed at ensuring there is sufficient light in the image to process it further. To meet this requirement, the events were conditioned, as described in section 4.2, and the conditioned images were required to have at least 25 p.e. in each of the triggering telescopes.

Multiplying the area over which the events were sampled,  $A_{\text{samp}} = \pi r_{\text{samp}}^2$ , by the fraction of events passing the criteria above, leads to an important characteristic of the array configuration, the *effective collection area* for  $\gamma$ -rays. This characteristic is essentially the detector area that an equivalent, 100% efficient, “space-based” instrument would require to detect the same flux of  $\gamma$ -rays directly. Figure 6.6 shows how the effective area depends on energy for the three configurations. After the hadronic rejection cuts are applied the effective area is suppressed by a factor of approx. 30%–70%, as shown in section 6.3.4.

Another characteristic of interest is the energy at which most  $\gamma$ -rays are detected, for a given  $\gamma$ -ray source spectrum, typically the Crab Nebula spectrum (Hillas et al., 1998), approximated here by a power-law over the energy range of 10 GeV to 100 TeV:

$$\frac{dF}{dE} = 3.2 \times 10^{-7} \left( \frac{E}{\text{TeV}} \right)^{-2.5} \text{m}^{-2} \text{s}^{-1} \text{TeV}^{-1}$$

**Table 6.3: Summary of collection area and integral rate from Crab Nebula.**

Energy	Collection area [m <sup>2</sup> ]	$\gamma$ -ray rate $> E$ [min <sup>-1</sup> ]
30 GeV	$2.0 \times 10^2$	45
100 GeV	$3.3 \times 10^4$	40
300 GeV	$2.2 \times 10^5$	15
1 TeV	$3.0 \times 10^5$	4

The *differential rate*, given by,

$$\frac{dR}{dE}(E) = A(E) \frac{dF}{dE} = 3.2 \times 10^{-7} A(E) \left( \frac{E}{\text{TeV}} \right)^{-2.5} \text{s}^{-1} \text{TeV}^{-1}$$

is shown for the 3/4;12m array criterion in figure 6.7. The energy at which this curve reaches a maximum, often called the peak detection energy, or  $E_{\text{peak}}$ , is 110 GeV. Integrating the curve gives a total triggering rate of  $\sim 45 \text{ min}^{-1}$  from the Crab Nebula. Approximately 10% of the detected events have energies less than 100 GeV, and 10% have energy greater than 1 TeV. These results are summarized in table 6.3.

### 6.3.4 Effect of shape- and aperture-cuts

The effects of the shape- and aperture-cuts are interpolated from the full analysis of the 3/3;10m and 3/7;10m configurations. For each of these two cases a function  $A(E, \theta_{\text{cut}})$ , corresponding to the effective area of the array at energy  $E$  with optimum shape-cut and aperture-cut given by  $\theta_{\text{cut}}$ , is shown in figure 6.8. This surface was derived by polynomial interpolation from four curves available from the full analysis. These are  $A(E, \pi)$ , the effective area with no aperture-cuts applied, i.e. trigger and optimized shape-cut only. This curve is shown as the top-left plot of figure 6.8. The remaining three curves used to interpolate the surface were  $A(100 \text{ GeV}, \theta_{\text{cut}})$ ,  $A(1 \text{ TeV}, \theta_{\text{cut}})$  and  $A(10 \text{ TeV}, \theta_{\text{cut}})$ , the effective area for three energy bins with trigger, optimized shape-cut and an aperture-cut of varying degrees applied. These three curves are shown for both array configurations in the bottom-left plot in figure 6.8.

The  $A(E, \theta_{\text{cut}})$  surface applicable to the 3/4;12m configuration is interpolated from

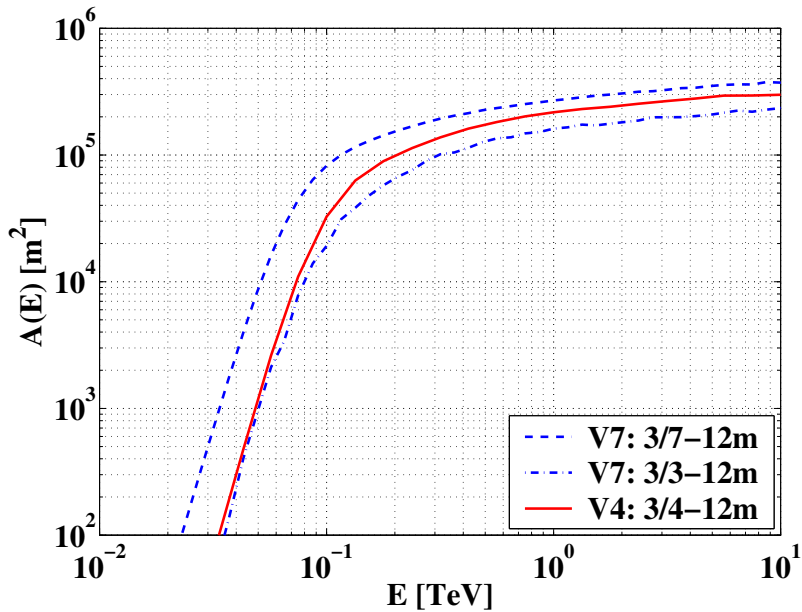


Figure 6.6: Effective areas for various array configurations.

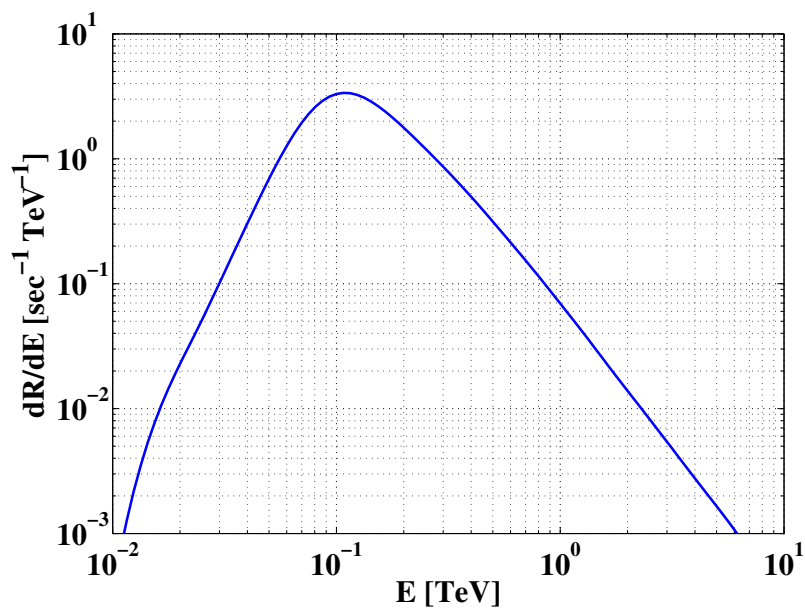
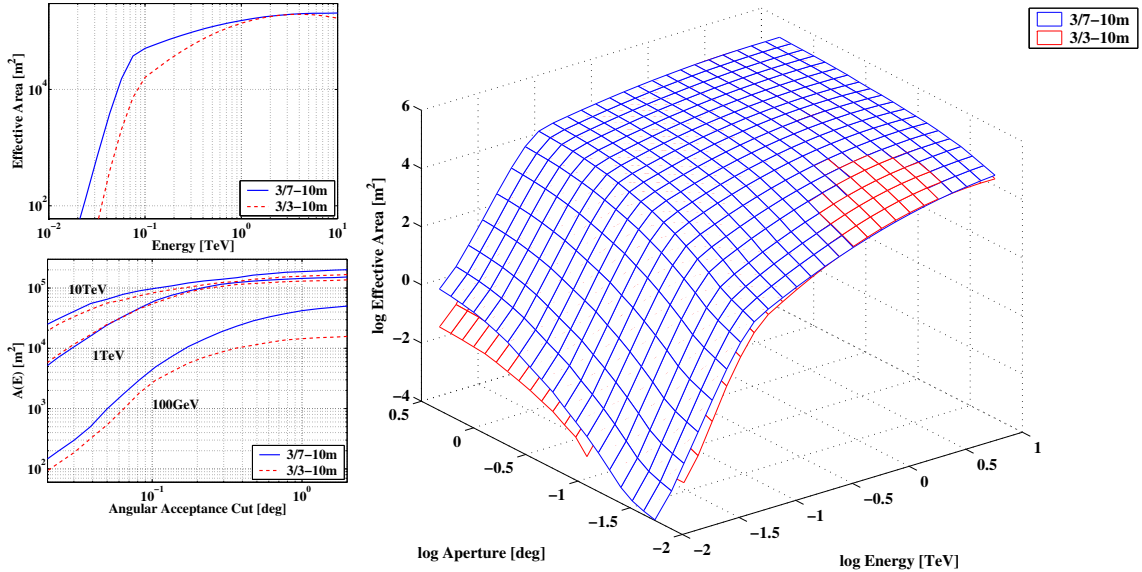


Figure 6.7: Differential rate for a Crab Nebula like source. The energy at which the detected rate is maximal is,  $E_{\text{peak}}=110$  GeV.



**Figure 6.8:** (Left-Top) Effective area with shape cut applied. (Left-Bottom) Effective area with shape and aperture-cuts applied vs. aperture-cut for three energies. (Right)  $A(E, \theta_{\text{cut}})$ , effective area surface with shape and aperture-cuts applied.

the 3/3;10m and 3/7;10m by scaling using the trigger effective area curves on figure 6.6 and the equivalent curves for the 10 m case. From here on the effective area curve for the 10 m case with only the trigger cut applied is referred to as  $A_{X;10m}^{\text{TR}}(E)$  (with  $X=3/3$ , 3/7 or 3/7), with a similar expression for the 12 m case. The effective area surface with trigger, shape-cut and aperture-cuts applied is similarly referred to as  $A_{X;10m}^{\text{SA}}(E, \theta_{\text{cut}})$ .

Defining the ratio of the trigger-only effective areas in the 12 m and 10 m cases as  $R_X(E)$ , i.e.

$$R_X(E) = \frac{A_{X;12m}^{\text{TR}}}{A_{X;10m}^{\text{TR}}}$$

and  $x(E)$  as the interpolation factor between the 3/4 trigger-only curve and the 3/3 and 3/7 trigger-only curve in log space,

$$x(E) = \frac{\log A_{3/4;12m}^{\text{TR}}(E) - \log A_{3/3;12m}^{\text{TR}}(E)}{\log A_{3/7;12m}^{\text{TR}}(E) - \log A_{3/3;12m}^{\text{TR}}(E)}$$

Then the 3/4;12m effective area with trigger, shape-cut and aperture-cut applied is the interpolation between the 3/3;10m and 3/7;10m cases,

$$\log A_{3/4;12m}^{\text{SA}}(E, \theta_{\text{cut}}) = x(E) \log \left\{ R_{3/3}(E) A_{3/3;10m}^{\text{SA}}(E, \theta_{\text{cut}}) \right\} + (1 - x(E)) \log \left\{ R_{3/7}(E) A_{3/7;10m}^{\text{SA}}(E, \theta_{\text{cut}}) \right\}$$

### 6.3.5 Angular resolution

The optimum aperture cut,  $\theta_{\text{cut}}(E)$ , is calculated by maximizing the detected  $\gamma$ -ray significance (signal-to-noise ratio) at each energy. Figure 6.9 (left) shows a plot of the probability for event reconstruction, based on collection area  $A(E, \theta_{\text{cut}})$ , for three different energies. This corresponds to the probability of reconstructing a  $\gamma$ -ray within  $\theta_{\text{cut}}$  of its arrival direction, denoted  $P_\gamma(< \theta_{\text{cut}})$ . The probability of reconstructing the event within  $\pi$  is unity, dropping off as tighter cuts are made. It can be seen from the probability curves that high energy events are reconstructed more accurately than low-energy events. A cut of 1 arc minute excludes 90% of 10 TeV events, 97% of 1 TeV events and >99% of 100 GeV events. Interestingly, there is a range of aperture cut for which mid-energy  $\gamma$ -rays have higher probability to pass than the highest energy events. This is likely a result of “clipping” of the shower image in the camera, an effect of the higher energy showers developing deeper into the atmosphere and being longer in angular extent than the low energy showers.

The number of isotropic background cosmic-ray events passing an angular cut is,  $P_p(< \theta_{\text{cut}}) \propto \theta_{\text{cut}}^2$ , to first order in  $\theta_{\text{cut}}$ . The detection significance ratio is therefore,

$$\sigma(\theta_{\text{cut}}) \propto \frac{P_\gamma(< \theta_{\text{cut}})}{\sqrt{P_p(< \theta_{\text{cut}})}} \propto \frac{P_\gamma(< \theta_{\text{cut}})}{\theta_{\text{cut}}}$$

Figure 6.9 (right) shows the significance at three energies. Maximizing the detection significance at every energy gives the optimized values for the aperture cut,  $\theta_{\text{cut}}^*(E)$ . To evaluate the angular resolution of the instrument, a fit is made to  $dP_\gamma(< \theta_{\text{cut}})/d\theta_{\text{cut}}$  in the region of  $\theta_{\text{cut}}(E) < \theta_{\text{cut}}^*(E)$  with the assumption that the reconstructed events

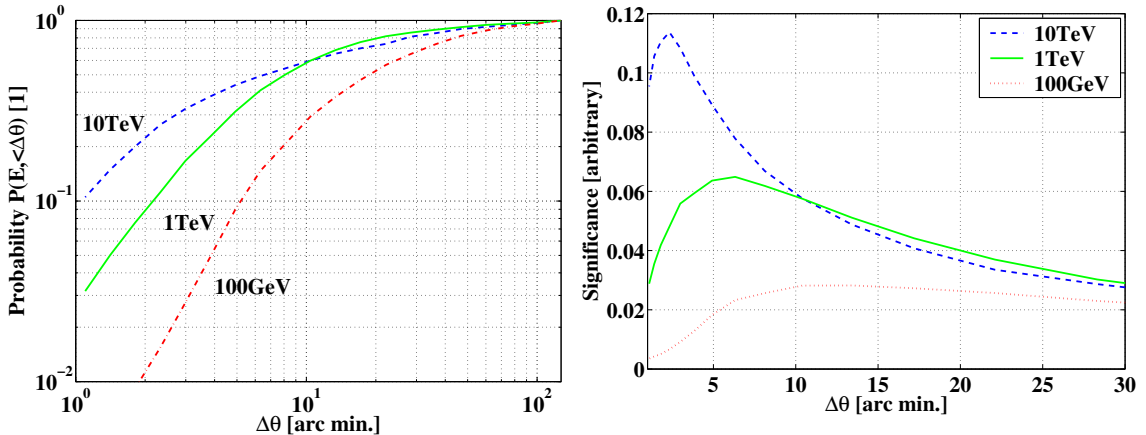


**Figure 6.9:** (Left)  $P(E, < \theta_{\text{cut}})$ , probability that a  $\gamma$ -ray event with certain energy will be reconstructed closer than  $\theta_{\text{cut}}$  to the true origin. (Right) Significance of  $\gamma$ -ray events over isotropic background events.

**Table 6.4: Summary of angular resolution and optimized aperture cuts for VERITAS-4.**

Energy	Optimized aperture cut		Angular resolution	
	[arc. min]	[degrees]	[arc. min]	[degrees]
10 TeV	2'	0.03°	1.6'	0.03°
1 TeV	6'	0.10°	4.3'	0.07°
100 GeV	11'	0.18°	7.5'	0.13°

are distributed as a two-dimensional Gaussian. The half-width of the fitted Gaussian is defined as the angular-resolution of the instrument. Table 6.4 gives the optimized aperture-cut and the angular resolution of three  $\gamma$ -ray energies. In section 6.3.7 a more useful method of calculating the optimum aperture-cut by directly maximizing the sensitivity of the instrument to  $\gamma$ -rays is described. It is similar to the method shown here, the main difference being a more accurate treatment of the background.

### 6.3.6 Cosmic-ray events

As noted in section 6.2.3 the energy-estimator function is chosen and optimized with  $\gamma$ -ray images, with the requirement that  $E_{\text{est}} \approx E_\gamma$ . This will not, in general, be the case for hadronic showers whose images are inherently different from  $\gamma$ -ray images of the same energy. In a full simulation of the array performance where the reconstruc-

tion technique is applied to hadronically-induced events, the energy-estimator will assign a “ $\gamma$ -ray-energy estimate”,  $E_{est}$  to each hadronic event of energy  $E_p$ . These events will then naturally be counted toward the background in the energy bin containing  $E_{est}$ , when the instrument sensitivity is calculated.

For this work, since the full reconstruction is not applied to the data, a different approach to finding the equivalent  $\gamma$ -ray-energy is adopted. An assumption is made that, for those hadronic showers that result in  $\gamma$ -ray-like images, the energy estimate is, to first order, a function of the amount of light collected relative to the amount of light an equivalent  $\gamma$ -ray event would produce. It is found that the following relationship holds, except possibly at the lowest energies,

$$\frac{E_{est}}{\text{TeV}} \approx 0.4 \frac{E_p}{\text{TeV}}^{0.88}$$

Using this expression the proton spectrum of

$$\frac{dF}{dE_p} = 1.1 \times 10^{-5} \frac{E_p}{\text{TeV}}^{-2.75} \text{ m}^{-2} \text{ s}^{-1} \text{ TeV}^{-1} \text{ sr}^{-1}$$

can be converted into a spectrum in equivalent  $\gamma$ -ray energy,  $E_\gamma$ . By folding this spectrum with the collecting area for protons, also expressed in equivalent  $\gamma$ -ray energy the differential rate of detected cosmic-ray events is calculated, figure 6.10.

The fraction of background events passing the “shape-cut” was determined during the comprehensive evaluation of VERITAS characteristics and is plotted in figure 6.10 (right) for completeness. It is assumed that this curve is applicable to the updated VERITAS configuration. This assumption, although not completely accurate, is reasonable, since the shape cut on  $D$  (as explained in section 6.2.3) does not depend strongly on mirror size. The absolute value of  $D$  for any event has a dependence on mirror diameter from its definition as the RMS distance from the back-traced rays to the image axis, with the back-traced rays being reflected off the entire mirror area. The average value of  $D$ , for events of any given energy, will increase from the 10 m to the 12 m case. The dispersion in  $D$  will also increase for events of a given  $\gamma$ -ray

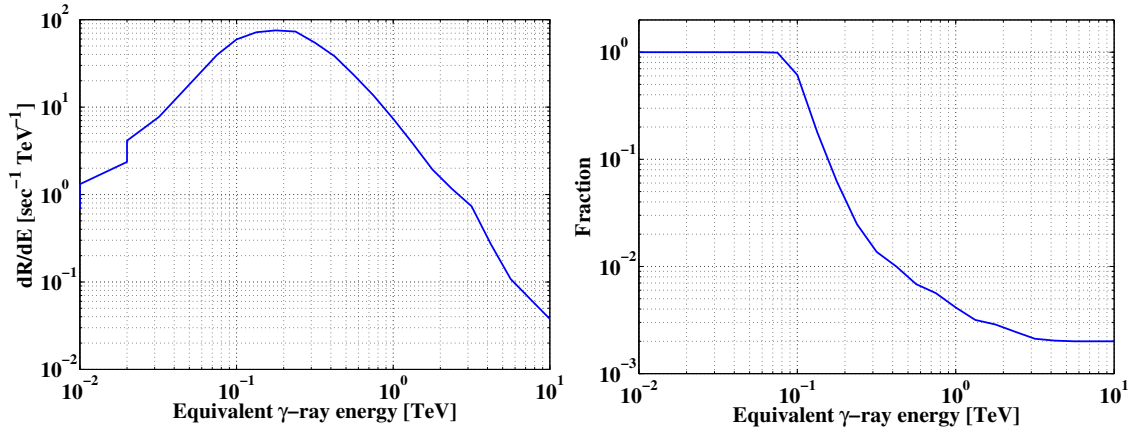


**Figure 6.10:** (Left) Differential rate of background cosmic-ray events, expressed in equivalent  $\gamma$ -ray energy. (Right) Fraction of background events passing shape-cuts.

energy, decreasing the efficiency of any cut on  $D$ . However this will be compensated for, to some extent, by an increase in the amount of light collected for each event, giving more collected photons and a better estimate of  $D$ .

### 6.3.7 Sensitivity

The sensitivity of an atmospheric Čerenkov imaging telescope to a  $\gamma$ -ray source is usually expressed as the minimum observable flux the source must have to be detected with a certain significance in a certain exposure time. A minimum flux sensitivity is calculated for a range of energy bins, separated equally in  $\log(\text{energy})$  with four bins per decade. This configuration of energy bins is the same as that used when attempting to reconstruct the energy spectrum of a detected source.

Given an exposure of duration  $\Delta T$  and  $\gamma$ -ray detection rate of  $R_\gamma$  with background event rate of  $R_B$ , the number of counts collected while observing the source is  $N_{ON} = (R_\gamma + R_B)T$ . The number of events collected while taking a control observation, in the absence of the source is  $N_{OFF} = R_B T$ . The significance of the detection is therefore

$$\sigma = \frac{N_{ON} - N_{OFF}}{\sqrt{N_{ON} + N_{OFF}}} = \frac{R_\gamma T}{\sqrt{(R_\gamma + 2R_B)T}}$$

Given any required significance, this expression can be solved for  $R_\gamma$  (the positive root) giving,

$$R_\gamma = \sigma^2 \left\{ \frac{1 + \sqrt{1 + 8R_B T / \sigma^2}}{2T} \right\}$$

The background has two significant components; cosmic-rays and cosmic-electrons. The cosmic-ray flux is calculated by integrating the differential proton rate, figure 6.10 (left), multiplied by the fraction of cosmic-ray events passing the shape cuts, figure 6.10 (right). The rate of detected electrons is given by integrating the differential flux of the cosmic-electrons,

$$\frac{dF}{dE_{e^\pm}} = 9.5 \times 10^{-9} \frac{E_{e^\pm}}{\text{TeV}}^{-3.26} \text{ m}^{-2} \text{ s}^{-1} \text{ TeV}^{-1} \text{ sr}^{-1}$$

multiplied by the  $\gamma$ -ray collecting area and by the angular-extent of the aperture-cut,  $\pi\theta_{\text{cut}}^2$ .

The minimum observable rate in an energy bin centered at  $E_c$ , given by  $R_\gamma(E_c)$  can then be converted into a minimum observable flux,  $F_\gamma(10^{-1/8}E_c \rightarrow 10^{+1/8}E_c)$ , by dividing by the  $\gamma$ -ray collection area. The flux is usually expressed differentially in flux units as  $E dF/dE$  or in power units as  $E^2 dF/dE$  by assuming a power-law spectrum  $dF/dE = F^* E^{-(\Gamma+1)}$ ,

$$R_\gamma(E_c) = \int_{10^{-1/8}E_c}^{10^{+1/8}E_c} A(E') F^* E'^{-(\Gamma+1)} dE' \approx F^*(E_c) A(E_c) E_c^{-\Gamma} \left( \frac{10^{+1/8\Gamma} - 10^{-1/8\Gamma}}{\Gamma} \right)$$

assuming four bins per decade of energy, whose edges ( $10^{-1/8}E_c$  and  $10^{+1/8}E_c$ ) are equally spaced around  $E_c$  in log space. It is also assumed that the collecting area  $A(E')$  changes slowly within each bin and can be replaced in the integration with its value at the center of the bin. The expression in the parentheses, a product of the binning and the assumed power-law index, can be written as the constant  $B$ . Hence,

$$E \frac{dF}{dE} = F^* E^{-\Gamma} \approx \frac{R_\gamma(E)}{B \times A(E)}$$

In the original VERITAS-7 work, the sensitivity was derived as a function of energy, shape-cut and aperture-cut, i.e. as  $E \frac{dF}{dE}(E, D_{\text{cut}}, \theta_{\text{cut}})$ . It was by maximizing this function for every energy bin that the optimum values of  $D_{\text{cut}}(E)$  and  $\theta_{\text{cut}}(E)$  were found. For this analysis, the value of the optimum shape-cut was taken implicitly from the previous analysis. The optimum aperture-cut was calculated by maximizing the sensitivity, taken as a function of energy and aperture-cut,  $E \frac{dF}{dE}(E, \theta_{\text{cut}} | D_{\text{cut}}(E))$ , with the shape-cut fixed as described above.

Figure 6.11 shows the sensitivity of the VERITAS-4 array to  $\gamma$ -ray sources. In each region of this plot a different background dominates. For the case of 50 hrs exposure, in the region  $E > 2 \text{ TeV}$  the limitation is  $\gamma$ -ray statistics, a minimum of 25 counts are needed for a  $5\sigma$  detection. At  $\sim 1 \text{ TeV}$  the most prominent background is cosmic-ray interactions producing only  $\pi^0$  particles which decay and initiate purely electromagnetic showers. These events cannot be differentiated from  $\gamma$ -ray events. At  $200 \text{ GeV} < E < \sim 1 \text{ TeV}$  cosmic-ray and cosmic-electron initiated events dominate approximately equally. At low energies, night sky noise affects the images of all events strongly degrading the performance of the  $\gamma$ -ray separation.

It can be seen from the diagram that VERITAS will be sensitive to a source as bright as the Crab Nebula between 30 GeV and  $> 30 \text{ TeV}$  in 50 hours of observations. This will provide a large overlap with next generation satellite-based instruments which are expected to operate up to energies of 300 GeV (NASA, 2001).

## 6.4 Summary of results

These results were presented to the VERITAS funding agencies to show the worthiness of a first stage, four telescope instrument. The configuration, with 12 m telescopes, performs well in comparison to the full VERITAS  $7 \times 10 \text{ m}$  instrument although there is an inevitable loss of sensitivity at the lowest energies (below 100 GeV) and less flexibility to split the instrument into sub-array configurations. Partially on the basis of these results, the four telescope instrument has been funded; a prototype is being

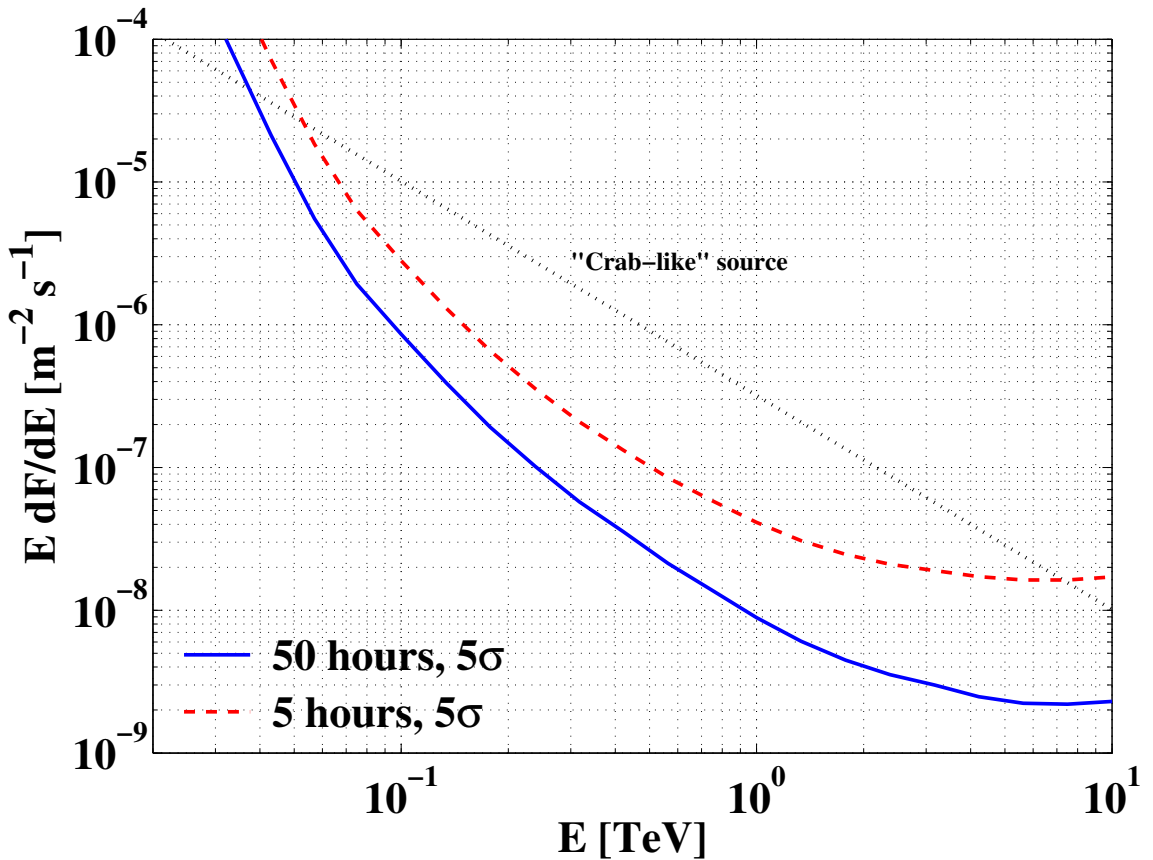


Figure 6.11: Minimum observable  $\gamma$ -ray flux for 50 and 5 hour observations with the VERITAS-4 array given a required detection significance of  $5\sigma$  in each energy bin. The sensitivity is quoted for energy bins separated equally in  $\log(\text{energy})$  with four bins per decade.

built at the Smithsonian Astrophysical Observatory facility close to the original Mon-tosa canyon site. Construction of the full instrument will begin at Horseshoe canyon on Kitt Peak in 2004. This new site, at higher elevation, will allow the instrument to exceed the specifications calculated here and summarized in table 6.5.

**Table 6.5: Summary of the characteristics of the VERITAS-4 sub-array.**

Characteristic	E	Value
Peak Energy <sup>a</sup>		110 GeV
Flux sensitivity <sup>b</sup>	at 100 GeV	$3.4 \times 10^{-11} \text{ cm}^{-2} \text{ s}^{-1}$
	at 1 TeV	$6.5 \times 10^{-13} \text{ cm}^{-2} \text{ s}^{-1}$
	at 10 TeV	$2.1 \times 10^{-13} \text{ cm}^{-2} \text{ s}^{-1}$
Angular resolution <sup>c</sup>	100 GeV	7.5 arc min
	1 TeV	4.3 arc min
	10 TeV	1.6 arc min
Collection area <sup>d</sup>	100 GeV	$3.3 \times 10^8 \text{ cm}^2$
	1 TeV	$2.2 \times 10^9 \text{ cm}^2$
	10 TeV	$3.0 \times 10^9 \text{ cm}^2$
Crab Nebula	>30 GeV	45/minute
$\gamma$ -ray rates <sup>e</sup>	>100 GeV	40/minute
	>300 GeV	15/minute
	>1 TeV	4/minute
Energy resolution <sup>f</sup>		<15%

<sup>a</sup>Energy at which the differential trigger rate of photons from a “Crab Nebula - like” source is maximal for the given trigger conditions (see text for details).

<sup>b</sup> Minimum differential flux,  $E dF/dE$  for a  $5\sigma$  excess in 50 hours of observations within each energy bin with  $\log_{10}(E_{i+1}/E_i) = 1/4$ .

<sup>c</sup> Half-width of a two-dimensional Gaussian distribution which describes the central part of the distribution of reconstructed photon arrival directions. Actual acceptance aperture for photons may be larger (e.g. for spectroscopy), or smaller (e.g. for maximal significance detection) than this value.

<sup>d</sup> Collection area for 3/4 telescopes with a telescope trigger requiring 3 adjacent PMTs to detect >5.6 p.e. within an 8 nsec window.

<sup>e</sup>  $\gamma$ -ray rates for photons which trigger the VERITAS (Phase I) array. Depending on the science requirement, such as spectroscopy or new source detection, a data analysis strategy is chosen which will reduce  $\gamma$ -ray rates by 30–70% while suppressing dramatically the CR background.

<sup>f</sup>RMS  $\Delta E/E$ .

## 7. CONCLUSIONS

In the time since the end of the CGRO mission, multiwavelength observations have proved to be the most powerful tool available to investigate the origin of the high energy emission from the unidentified sources. For a number of such sources, some of which were discussed in chapter 5, x-ray, radio and optical observations have narrowed the list of scientifically viable, potential candidates. In some cases, such observations have ruled out all but one candidate. This survey was undertaken in the hope that VHE emission would be detected from one of the sources chosen, and that the higher spatial resolution achievable with the ground-based technique would allow the source of the  $\gamma$ -ray emission to be identified. There is significant overlap between the VHE source catalog and the EGRET sources; seven of the eighteen credible VHE sources were also seen by EGRET at some level. Of the two categories of sources unambiguously identified by EGRET, blazars and pulsars, detections of eight BL Lac type blazars have been claimed at TeV energies. No pulsars have been directly detected by ground-based instruments, but some EGRET pulsars are associated with PWN which, like the Crab, Vela and PSR 1706, may be visible to VHE  $\gamma$ -ray instruments.

In total, results from VHE observations of 21 EGRET sources are reported, more than 10% of the unidentified source population. The observations yielded an average of 5 hours of data from each source. The decision to obtain this amount of data on a relatively large number of sources was partly made so that the survey could co-exist with other observing programs using the Whipple instrument, i.e. a request was not made for a large quantity of data from any one location in the sky, which would preclude other observation programs in that area. It was anticipated that this level of observations would be sufficient to provide upper-limits on emission that would constrain the spectrum of a mean EGRET source (figure 1.7).

When the survey was initiated, little was known about many of the observed sources, outside of what was published in the 3EG catalog. Since this time, our understanding

of these sources has advanced considerably, both through work on the population as a whole and through multiwavelength observations of individual sources. Of particular note in the first category is the calculation of source variability by Nolan et al. (2003) and the systematic correlation of the sources with radio sources (Mattox et al., 2001) and SNR, OB-associations and massive stars (Romero et al., 1999). That so many of the sources chosen here now have potential associations, as discussed in chapter 5, is a testament to the ongoing interest in multiwavelength observations of these sources, such as the work of Roberts et al. (2001b), Mukherjee et al. (2000) and Kaaret et al. (1999), to mention just a few.

Based on the number of observations made (i.e. the number of sources surveyed and the number of independent bins in each two-dimensional image) it cannot be claimed that VHE  $\gamma$ -ray emission was detected from any of the sources, at a significant level. Two of these sources, 3EG J1337+5029 and 3EG J2227+6122, have excesses with sufficiently low chance probability that they would be considered as suggestive of  $\gamma$ -ray emission, if the observations are taken in isolation from the rest of the survey. In the case of J1337+5029, the excess corresponds to the location of a cluster, Abell 1758. If excess is the result of  $\gamma$ -ray emission from the cluster, it would represent a new class of VHE emission and be the most distant source of VHE emission to date (at  $z = 0.279$ , considerably more distant than H1426+428, the most distant VHE blazar, at  $z = 0.129$ ) and have important implications for the density of the IIRF. The excess in the case of J2227+6122 does not correspond to any of the suggested associations for the EGRET source. To confirm (or refute) any emission, independent follow-up observations will be made. The excesses correspond to fluxes of 0.40 and 0.33 of the integral Crab Nebula flux, at energies  $> 350$  GeV, respectively. At this level, a five to ten hour exposure on each will be sufficient for confirmation.

The next generation of ground-based instruments, such as VERITAS, will be  $> 10$  times more sensitive than the Whipple 10 m instrument (figure 1.7 and 6.11). They will be most sensitive to  $\gamma$ -rays at approximately  $\sim 100$  GeV, with some sensitivity even below this energy (table 6.3). A survey of EGRET sources with one of these instruments, should have considerable success in detecting  $\gamma$ -ray emission.

The EGRET sources J0010+7309 and J0634+0521, which are associated with the CTA 1 and Monoceros SNR, are prime candidates for observation with a next generation instrument. In particular, in conjunction with the next generation of space-based instruments, VERITAS may resolve two components of emission from J0634+0521, and confirm the model of Torres et al. (2003). Some models suggest that the  $\gamma$ -ray source 3EG J0241+6103 (the COS-B source 2CG 135), which likely corresponds to the x-ray binary system LSI +61°303, may be detectable in the VHE regime.

Of the likely AGN surveyed, 3EG J0433+2908 and GeV J0508+0540, from which  $> 10$  GeV photons were detected by EGRET, are worthy of follow-up observations with VERITAS, especially as part of a broad spectrum multiwavelength campaign. Even if not detected in the VHE regime, the spectra of  $\gamma$ -rays from these sources may have implications for models of the intergalactic infra-red field.

The pulsar candidates surveyed represent another class of objects that may be detectable with VERITAS, especially if they are associated with PWN. These sources are probably not good candidates for an initial round of unidentified EGRET observations; instead observations of other well known, bright pulsars will hopefully resolve between the two models of HE pulsar emission. If it is the case that VHE emission is observed from these objects, 3EG J2227+6122 and J1826–1302 would represent good candidates for observation.

The population of unidentified sources represent an important enduring legacy of the EGRET mission, and will remain somewhat of a mystery for a number of years to come. The next NASA  $\gamma$ -ray instrument, GLAST, scheduled for launch in 2007, will have a point-source flux sensitivity greater than 50 times that of EGRET ( $1.6 \times 10^{-9} \text{ cm}^{-2} \text{ s}^{-1}$  at energies  $> 100$  MeV in all-sky survey mode) and a localization accuracy between 0.4 and 5.0 arcmin. GLAST will undoubtedly identify some fraction of the unidentified sources but will almost certainly produce a population of its own unidentified sources close to its flux sensitivity. In the mean time, the role of multiwavelength observations in studying the EGRET sources, including more sensitive x-ray, radio, optical and VHE  $\gamma$ -ray observations, cannot be overstated.

## APPENDIX A

### GLOSSARY

**ACT** — *Atmospheric Čerenkov Telescope*, ground-based  $\gamma$ -ray detection technique utilizing the production of Čerenkov radiation by charged secondaries (largely  $e^\pm$ ) in the extensive air-showers that result from interaction of the primary in the atmosphere.

**AGN** — *Active Galactic Nucleus*, a galaxy with a powerful central core which is typically more luminous than the stars of the host galaxy combined. AGN are sub-categorized by their observational characteristics, such as the strength of radio emission, variability and presence or absence of broad emission line. In the unified theory of AGN, emission is the result of accretion onto a super-massive black hole, the various classes arising largely through differences in the orientation with respect to the line of sight of the observer.

**ASCA** — Japanese x-ray satellite (1993–2000).

**Blazar** — Sub-class of AGN characterized by strong radio emission, extreme variability, polarization at radio and optical wavelengths, and strong continuum emission. Blazars are classified as either FSRQ or BL Lac objects, distinguished by the presence (FSRQ) or absence (BL Lac) of absorption and emission lines. It is thought that blazars are AGN with a jet emanating from the core, oriented in the direction of the observer. They have a two peaked emission spectra, with correlated synchrotron and inverse-Compton components.

**BL Lac** — A type of blazar characterized by the absence of absorption and emission lines which makes the determination of redshift difficult. Their featureless spectra at optical wavelengths mean that BL Lacs are usually identified at x-ray or radio energies. Traditionally BL Lacs have been classified as low-frequency (LBL) or high-frequency (HBL) depending on the energy of the peak of synchrotron emission. There

is probably a sequence of intermediate BL Lacs which are more difficult to identify as they do not stand out at radio or x-ray energies. All extragalactic VHE  $\gamma$ -ray sources detected to date are extreme HBLs.

**CANGAROO** — *Collaboration between Australia and Nippon for a Gamma Ray Observatory in the Outback*, arguably the most contrived of astronomical acronyms. An ACT experiment operating in the Australian outback. The group is upgrading their single telescope to an array of four 10 m instruments.

**CGRO** — *Compton Gamma-Ray Observatory*, second in NASA’s program of “great observatories”. Launched in 1991 with four experiments covering the energy range from 60 keV to 30 GeV, it operated for nine years.

**Chandra** — Third of NASA’s “great observatories”, an x-ray instrument named for Subrahmanyan Chandrasekhar (1999-present).

**COS-B** — First dedicated European  $\gamma$ -ray satellite (1975–1982). Successful mission, operated in the energy range of 2 keV to 5 GeV, producing a catalog of sources and detailed observations of Geminga.

**DSA** — *Diffusive Shock Acceleration*, acceleration of a charged particle which repeatedly crosses of a shock-front due to scattering in the plasma.

**EGRET** — *Energetic Gamma-Ray Experiment Telescope*, an instrument on the CGRO satellite, which operated in the energy range of 30 MeV to 30 GeV. The most successful  $\gamma$ -ray mission to date, its many achievements included a catalog of 271 point sources. EGRET sources are conventionally prefixed by 3EG.

**erg** — unit of energy in the CGS system equaling  $10^{-7}$  J.

**HBL** — see BL Lac.

**HE** — *High Energy*, in the context of this work, refers to the energy range accessible to satellite based  $\gamma$ -ray instruments, 30 MeV to 30 GeV.

**HEGRA** — *High-Energy Gamma Ray Astronomy*, European ACT and air-shower array experiment on La Palma. The HEGRA group were the first to successfully employ the stereoscopic technique to discriminate between  $\gamma$ -rays and cosmic-rays.

**IC** — *inverse-Compton* scattering.

**IIRF** — *Intergalactic Infra-Red Radiation Field*, ambient field of infra-red photons that permeates the universe.

**ISM** — *Interstellar Medium*, low density material that permeates the regions between stars in the galaxy.

**LBL** — see BL Lac.

**MC** — *Monte Carlo*.

**O-type star** — Massive, hot star. Stellar sequence goes O-B-A-F-G-K-M in order of decreasing surface temperature.

**OB association** — Region of the galaxy which has a significant enhancement in the density of O- and B-type stars. Region has accelerated rate of star formation and supernovae.

**PMT** — *Photo-Multiplier Tube*.

**PSR** — prefix used frequently to designate pulsars, e.g. PSR 1959+650, pulsar at sky coordinates  $\alpha = 19^h 59^m$ ,  $\delta = +65.0^\circ$ .

**PWN** — *Pulsar Wind Nebula*, synchrotron nebula or plerion. A supernova remnant which is being resupplied with high energy electrons by a central pulsar. The electrons cool quickly through synchrotron emission. For example: The Crab Nebula.

**RASS-BSC (-FSC)** — *ROSAT All Sky Survey - Bright (Faint) Source Catalog*.

**ROSAT** — *Röntgen Satellite*, a German-US x-ray satellite which operated from 1990 to 1999. Its principal instrument, denoted HRI, operated in the energy range

of 0.12 keV to 2.4 keV. The main aim mission was the first all-sky survey with a sensitivity 1000 higher than that of UHURU. ROSAT sources are conventionally prefixed by RX or 1RXS.

**RXTE** — *Rossi X-ray Timing Explorer*, NASA x-ray satellite (1995–present).

**SAS-2, Second Small Astronomy Satellite**, the first dedicated NASA  $\gamma$ -ray instrument (1972–1973). Mission ended early due to failure of power supply. First observation of the radio-quiet Geminga pulsar.

**SAX or Beppo-SAX**, *Satellite per Astronomia X*, an Italian x-ray satellite (1996–2002).

**SED** — *Spectral Energy Distribution*, the power an instrument would receive as a function of frequency, given the assumption that its bandwidth is proportional to the frequency.

**SNR** — *Super Nova Remnant*, hot material thrown off as blast wave in supernova explosion. Shocks formed in interaction with ISM may give rise to particle acceleration, possibly resulting in a population of charged particles with energies up to  $10^{15}$  eV.

**TeV** — *Terra Electron-Volts*, unit of energy equivalent to  $\sim 1.6 \times 10^{-7}$  J and 1.6 erg.

**UHURU** — Early NASA x-ray satellite, also known as SAS-1, (1970–1973).

**VHE** — *Very High Energy*, in the context of this work, the energy range of 300 GeV to 30 TeV, accessible to ground-based  $\gamma$ -ray instruments.

**VLA** — *Very Large Array*, interferometer consisting of 27 radio telescopes, each with 25 m diameter, near Socorro, NM. The array has four configurations, the largest of which spans an area of diameter 35 km.

**WR-type** — *Wolf-Rayet*, a star system in with a massive O-type star and companion, in which the companion has stripped the star’s outer layers. Spectrum shows high metallicity.

**XMM-Newton** — *X-ray Multi-Mirror* mission, a high resolution, x-ray instrument operated by the European Space Agency (1999-present).

**XR<sub>B</sub>** — *X-ray Binary*, a binary system consisting of a pulsar and a large companion star. Often they are sub-classified as high-mass (HMXB) or low-mass (LMXB).

## APPENDIX B

### TWO DIMENSIONAL RECONSTRUCTION

As shown in section 4.5, the expression for  $disp(size, length, width)$  can be expanded in terms of the ellipticity parameter  $\epsilon = 1 - width/length$ ,

$$disp = a_1(size, length) \times \epsilon + a_2(size, length) \times \epsilon^2 + \dots$$

We further assume that the dependence on  $length$  is of secondary importance with respect to  $size$ ,

$$disp = \sum_1^\infty a_i(size) \times \epsilon^i$$

Optimization of  $a_i(size)$  is done with simulated  $\gamma$ -ray events, selected with energy in proportion to the Crab Nebula spectrum. The images have artificial night-sky noise added and are analyzed in the same manner as real events as described in sections 4.2, 4.3 and 4.4. Events are binned in terms of  $\log(size/U)$ , where  $U = 1622\ DC/deg$  describes the characteristic light density per unit arc length in a muon image (Horan, 2001). For each bin, the best fit for the following two functions are found,

$$disp^{(1)} = a_1 \times \epsilon \tag{B.1}$$

$$disp^{(2)} = a_1 \times \epsilon + a_2 \times \epsilon^2 \tag{B.2}$$

Figure B.1 shows the distribution of  $distance$  vs.  $\epsilon$  for simulated events in two  $size$  bins. It can be seen from the diagrams that the quadratic fit, eqn. B.2, is not reasonable as  $\epsilon$  increases, as it turns over and begins to decrease. The fitted function  $a_1(size)$  and the quality of the fits are shown in figure B.2. It can be seen that,  $a_1(size)$  can be approximated by

$$a_1(size) = 1.36^\circ + 0.14^\circ \times \log(size/U) \tag{B.3}$$

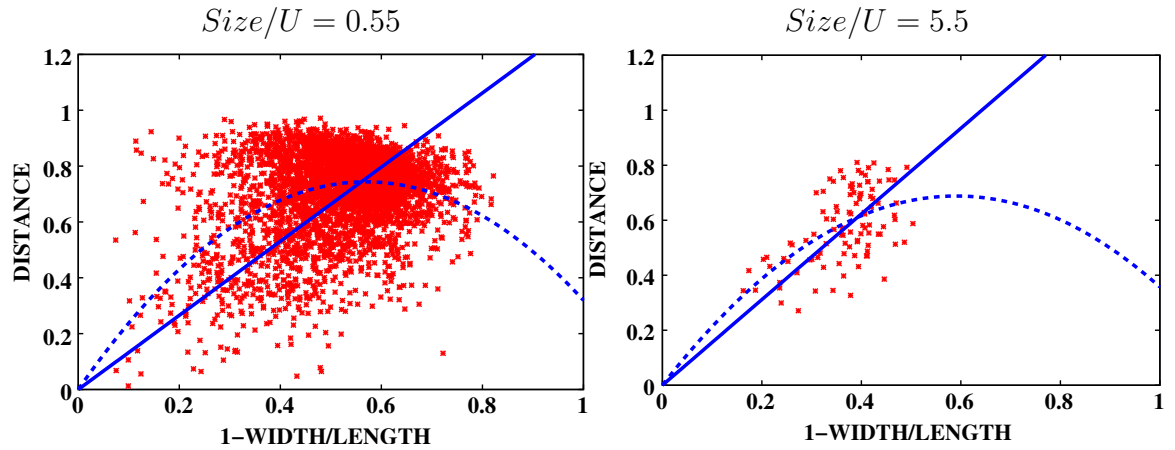


Figure B.1: Optimization of  $disp$  with simulated  $\gamma$ -ray events, in two energy bins. The *distance* of centroid from source is on the y-axis, the ellipticity,  $\epsilon$ , on the x-axis. The best fit for eqn. B.1 and B.2 are shown.

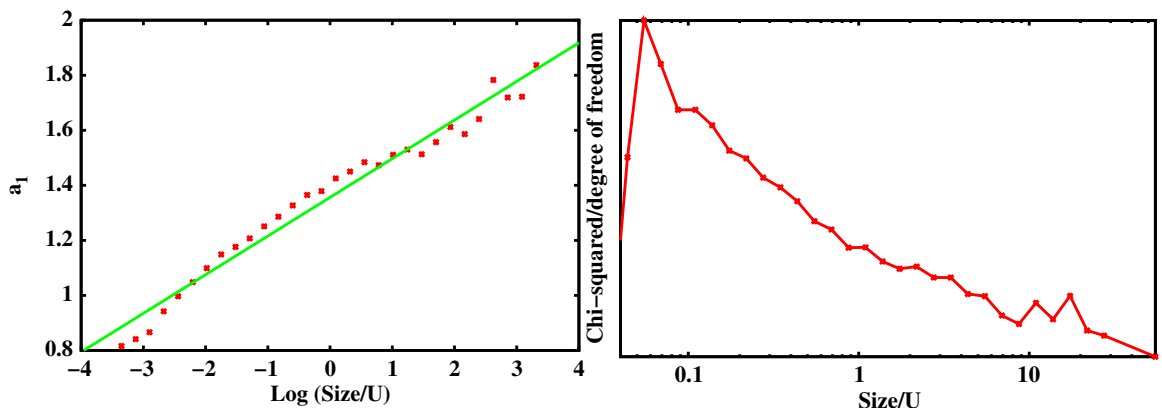
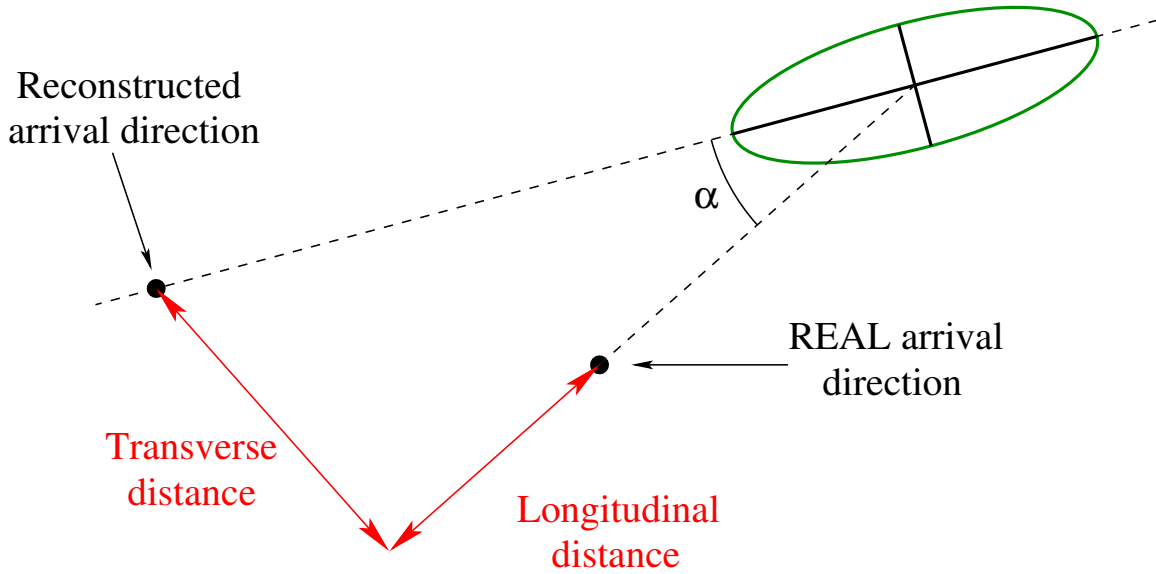


Figure B.2: (Left) Best fit of parameter  $a_1$  from eqn. B.1 to simulated data. The function  $a_1(size)$  can itself be fit by a linear relationship of  $a_1(size) = 1.36^\circ + 0.14^\circ \times \log(size/U)$ . (Right)  $\chi^2$  per degree of freedom for fit of  $a_1$  to simulated events.



**Figure B.3:** Illustration of the longitudinal and transverse errors in reconstructing the arrival direction of  $\gamma$ -ray events.

Using the relationship given in eqn. B.3, the arrival direction of the simulated events can be reconstructed using the two dimensional technique. Since the origin of the simulated  $\gamma$ -rays is known, the performance of the reconstruction can be evaluated. Distributions of the longitudinal and transverse error in the reconstructed arrival direction (as illustrated in figure B.3) are shown in figure B.4. The distribution of longitudinal error has an r.m.s. width of  $\sigma_{\parallel} \approx 0.23^\circ$  and can be fit by a Gaussian with  $\sigma_G \approx 0.19^\circ$ . The distribution of transverse error has width of  $\sigma_{\perp} \approx 0.22^\circ$ .

High energy events have considerably better reconstruction characteristics, a cut of  $\log(size/U) > 1.0$ , which keeps only 1% of the events, gives  $\sigma_{\parallel} \approx 0.15^\circ$  and  $\sigma_{\perp} \approx 0.05^\circ$ , as shown in figure B.5. This suggests that a high energy cut will result in a sky-map with better angular resolution.

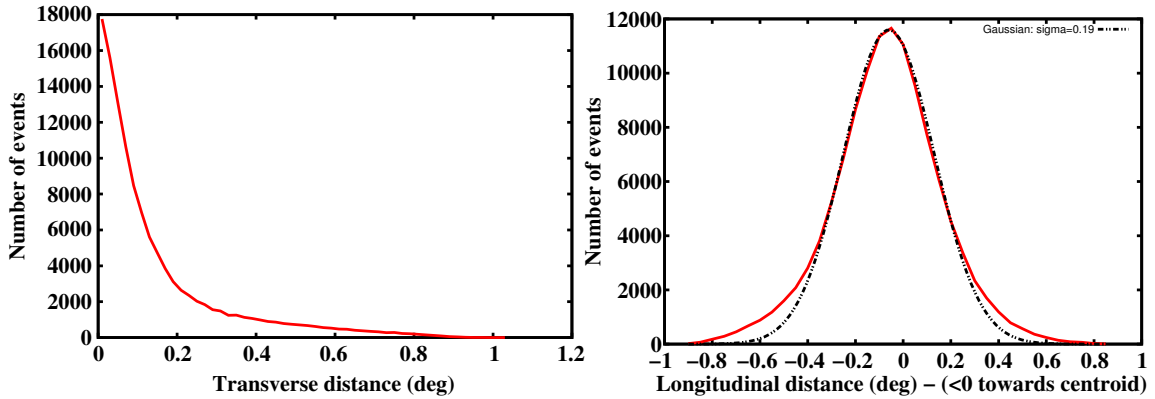


Figure B.4: Distribution of transverse (left) and longitudinal (right) error in reconstructing the arrival direction of simulated events.

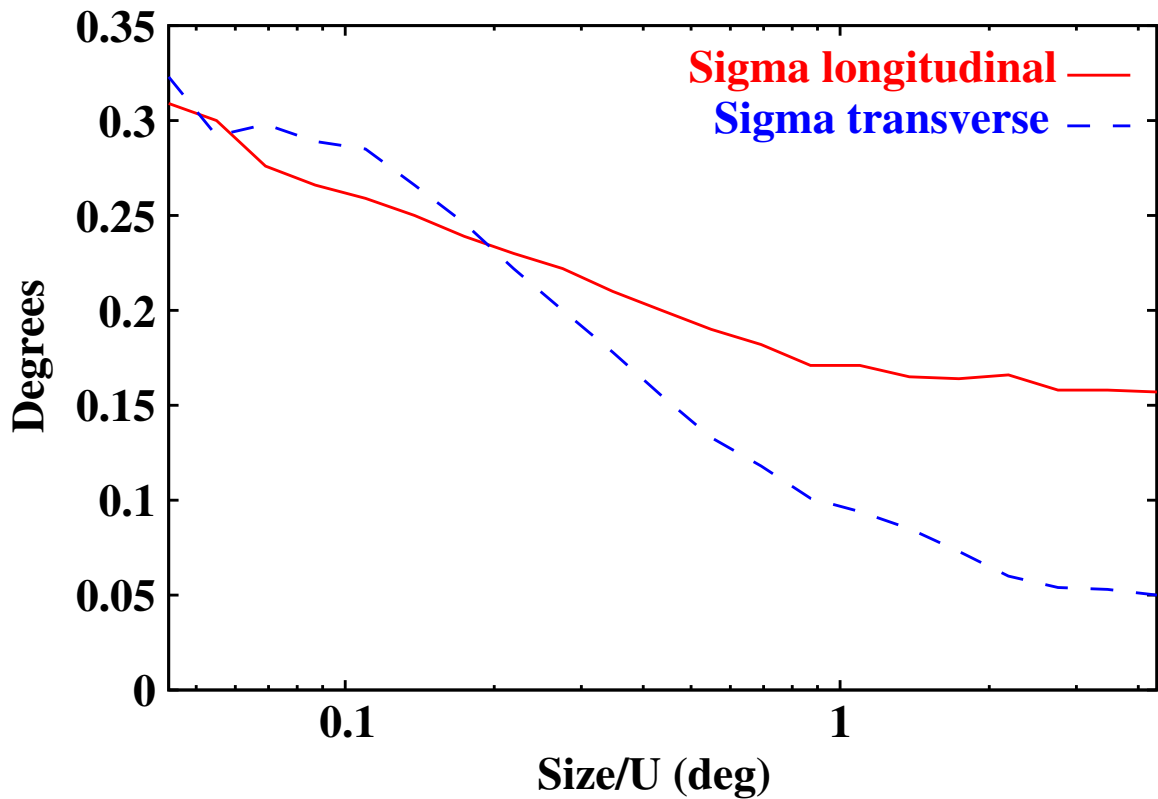


Figure B.5: Dependence of longitudinal ( $\sigma_{||}$ ) and transverse ( $\sigma_{\perp}$ ) error on size cut imposed.

## APPENDIX C

### PERFORMANCE OF GAUSSIAN SMOOTHING

The performance of the Gaussian smoothing,  $g(\vec{r})$ , and the “Trashcan” smoothing,  $t(\vec{r})$  from Lessard et al. (2001) can be evaluated using a simple Monte Carlo simulation. The smoothing functions are given by,

$$\begin{aligned} g(\vec{r}) &= \exp(-r^2/2r_0^2) \\ t(\vec{r}) &= \begin{cases} 1(r < r_0) \\ 0(r > r_0) \end{cases} \end{aligned}$$

A simple sky-map can be produced given a background rate ( $r_b$ ), a  $\gamma$ -ray signal rate ( $r_s$ ), and a value for the intrinsic angular resolution of the two dimensional reconstruction method before smoothing ( $\sigma_{2D}$ ). Appendix B indicates that  $\sigma_{2D} = 0.2^\circ$  is reasonable. The background and signal in each bin of the sky-map are given by a Poisson distributed random deviate with appropriate mean, denoted  $B(\mu_B)$  and  $S(\mu_S)$  for the case of mean background  $\mu_B$  and mean signal  $\mu_S$ . The background is distributed uniformly over both the ON and OFF maps, while the signal appears only in the ON source map and is smeared over a number of bins by the point-spread function. A simple Monte Carlo simulation of a typical sky-map is as follows,

$$\begin{aligned} OFF(\vec{r}) &= B(r_b) \\ ON(\vec{r}) &= B(r_b) + S\left(\frac{r_s}{2\pi\sigma_{2D}^2} e^{-r^2/2\sigma_{2D}^2}\right) \end{aligned}$$

To evaluate the performance of the smoothing algorithms, the sky-map is smoothed with both smoothing functions ( $g(\vec{r})$  and  $t(\vec{r})$ ), and the significance calculated from equations 4.7 and 4.8. Figure C.1 shows the average, maximum significance calculated over a large number of smoothed sky-maps, as a function of the smoothing radius,

$r_0$ . Values of  $r_b = 30$  count/bin and  $r_s = 1000$  counts were used, which are reasonable for a bright source.

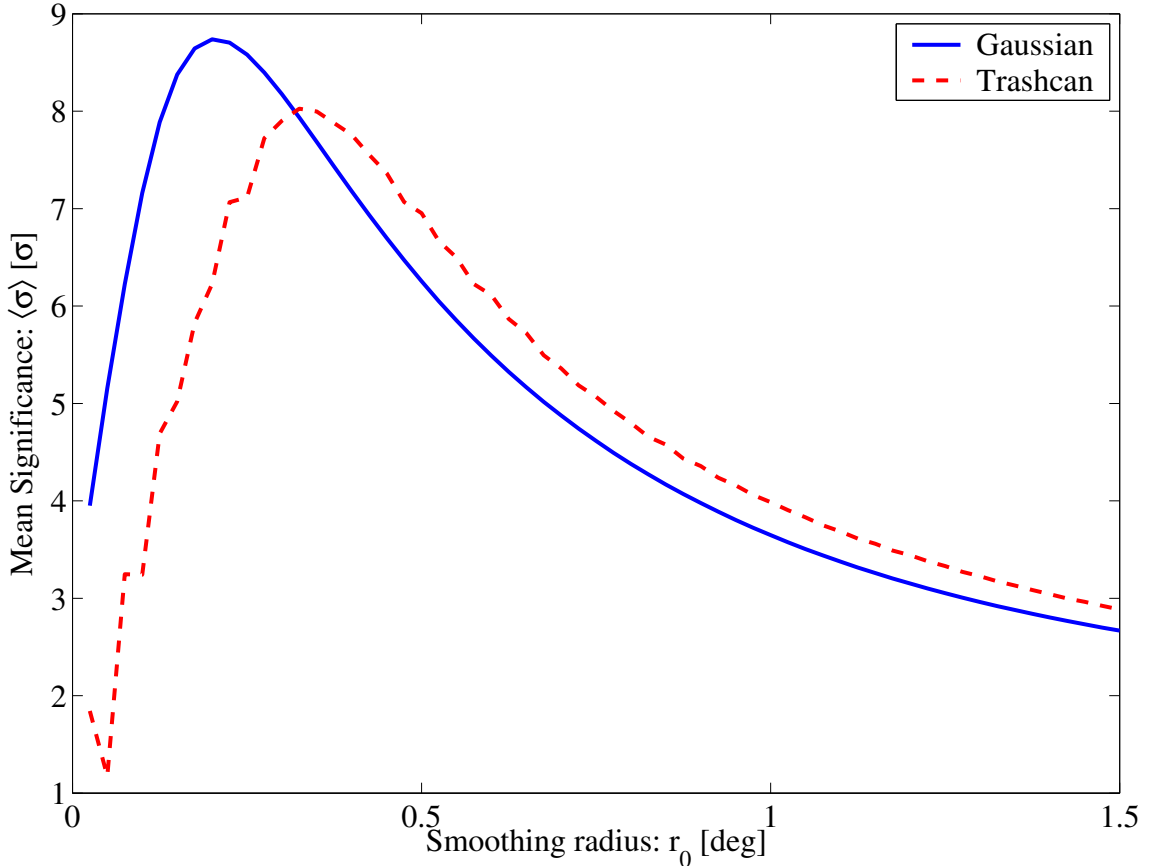


**Figure C.1: Mean significance after smoothing with Gaussian and Trashcan functions with various smoothing radii.**

On average, the Gaussian smoothing function performs slightly better, with  $\langle \sigma \rangle = 8.75\sigma$  for  $r_0 = 0.2^\circ$ , while the Trashcan function has maximum mean significance of  $\langle \sigma \rangle = 8.0\sigma$  for  $r_0 = 0.325^\circ$ .

Finally, by removing the  $\gamma$ -ray source from the Monte Carlo simulations, distributions of the maximum significance in the absence of a source, can be calculated for various regions of the sky-map. The results of this analysis, for regions of  $R < 0.35^\circ$ ,  $< 0.55^\circ$ ,  $< 1.10^\circ$  are presented in figure 4.8, along with experimental distributions and a theoretical curve based on the assumption that the counts are distributed as Gaussian.

## APPENDIX D

### TRACKING SIGNIFICANCE CALCULATION

For data analyzed using the standard TRACKING analysis (section 4.7), a number of different measures of “significance” can be defined. Li and Ma (1983) discuss the derivation and merits of three such measures, reproduced below as eqns. D.1, D.2 and D.3, corresponding to eqns. 5, 9 and 17 respectively in the original paper. As discussed in the paper, the simple propagation of errors calculation,  $S_5$ , is not distributed as Gaussian in the absence of a source, particularly when  $\rho \ll 1$  or  $\rho \gg 1$ . It systematically underestimates the true significance of a detection. An improved model of the background gives,  $S_9$ , which is shown to overestimate the significance. Taking the ratio of the likelihood of the source being present to the null hypothesis being true (no source present) gives  $S_{17}$ , which is shown to be distributed as Gaussian.

$$S_5 = \frac{N_{\text{On}} - \rho N_{\text{Off}}}{\sqrt{N_{\text{On}} + \rho^2 N_{\text{Off}}}} \quad (\text{D.1})$$

$$S_9 = \frac{N_{\text{On}} - \rho N_{\text{Off}}}{\sqrt{\rho(N_{\text{On}} + N_{\text{Off}})}} \quad (\text{D.2})$$

$$\begin{aligned} S_{17} = & \sqrt{2} \left\{ N_{\text{On}} \ln \left[ \frac{1 + \rho}{\rho} \left( \frac{N_{\text{On}}}{N_{\text{On}} + N_{\text{Off}}} \right) \right] \right. \\ & \left. + N_{\text{Off}} \ln \left[ (1 + \rho) \left( \frac{N_{\text{Off}}}{N_{\text{On}} + N_{\text{Off}}} \right) \right] \right\}^{1/2} \end{aligned} \quad (\text{D.3})$$

$$S_{\Delta\rho} = \frac{N_{\text{On}} - \rho N_{\text{Off}}}{\sqrt{N_{\text{On}} + \rho^2 N_{\text{Off}} + \Delta\rho^2 N_{\text{Off}}^2}} \quad (\text{D.4})$$

No attempt was made by Li and Ma (1983) to account for an error in the ON/OFF ratio,  $\rho$ . They concentrated on classes of experiments in which  $\rho$  arose due to differences in the on-source and off-source observing times, which would be known to high accuracy. For the TRACKING analysis, there is a statistical error on the value of  $\rho$  arising from the fact that it must be calculated from dark-field data, with  $N_{\text{On}}^*$

counts with  $\alpha < 15^\circ$  and  $N_{\text{Off}}^*$  counts with  $20^\circ < \alpha < 65^\circ$ :

$$\rho = \frac{N_{\text{On}}^*}{N_{\text{Off}}^*} \pm \frac{N_{\text{On}}^*}{N_{\text{Off}}^*} \sqrt{\frac{1}{N_{\text{On}}^*} + \frac{1}{N_{\text{Off}}^*}}$$

Propagation of errors, including  $\Delta\rho$ , leads to  $S_{\Delta\rho}$  (eqn. D.4), which becomes equal to  $S_5$  as  $\Delta\rho \rightarrow 0$ .

Following Li and Ma (1983), a simple Monte Carlo (MC) simulation was performed to test the four “significance measures”. Random values for  $N_{\text{On}}$  and  $N_{\text{Off}}$  were generated from Poisson distribution with appropriate  $\langle N_{\text{On}} \rangle$  and  $\langle N_{\text{Off}} \rangle$ . It was assumed that there is a true value for the tracking ratio,  $\rho^T = 1/3$  which connects the distributions of ON and OFF counts, i.e. that  $\langle N_{\text{On}} \rangle = \rho^T \langle N_{\text{Off}} \rangle$ . To match the simulation with the exposures used in this study, a value of  $\langle N_{\text{OFF}} \rangle \approx 6300$  counts was used, typical for a ten hour exposure. To calculate of the significances, a random, “measured”, value for the tracking ratio,  $\rho^M$ , was generated, distributed around  $\rho^T$  with  $\Delta\rho^M = 0.0015$ . The size of  $\Delta\rho$  was taken from a calculation of the tracking ratio with real data in 2000/2001 (Horan, 2001).

Figure D.1 shows the frequency of “ $> x\sigma$ ” results with each of the significance measures. In the case of  $\Delta\rho = 0$ , Li and Ma (1983) show, from MC, that  $S_{17}$  is normally distributed. With  $\Delta\rho \neq 0$ , this conclusion is no longer valid, as is expected, since no consideration to  $\Delta\rho$  given in its calculation. It can be seen that the measure which comes closest to a Gaussian distribution is  $S_5$ , at least with the values for  $\rho^T$ ,  $\Delta\rho$  and  $\langle N_{\text{OFF}} \rangle$  used in the simulation. This is attributed to a cancellation of the effect of systematic under-estimation the absence of  $\Delta\rho$  (seen by Li and Ma (1983)) with the overestimation due to  $\Delta\rho \neq 0$ . It is expected that, as  $\Delta\rho$  increases,  $S_{\Delta\rho}$  would become the only significance measure, of the four listed above, representative of a Gaussian distribution.

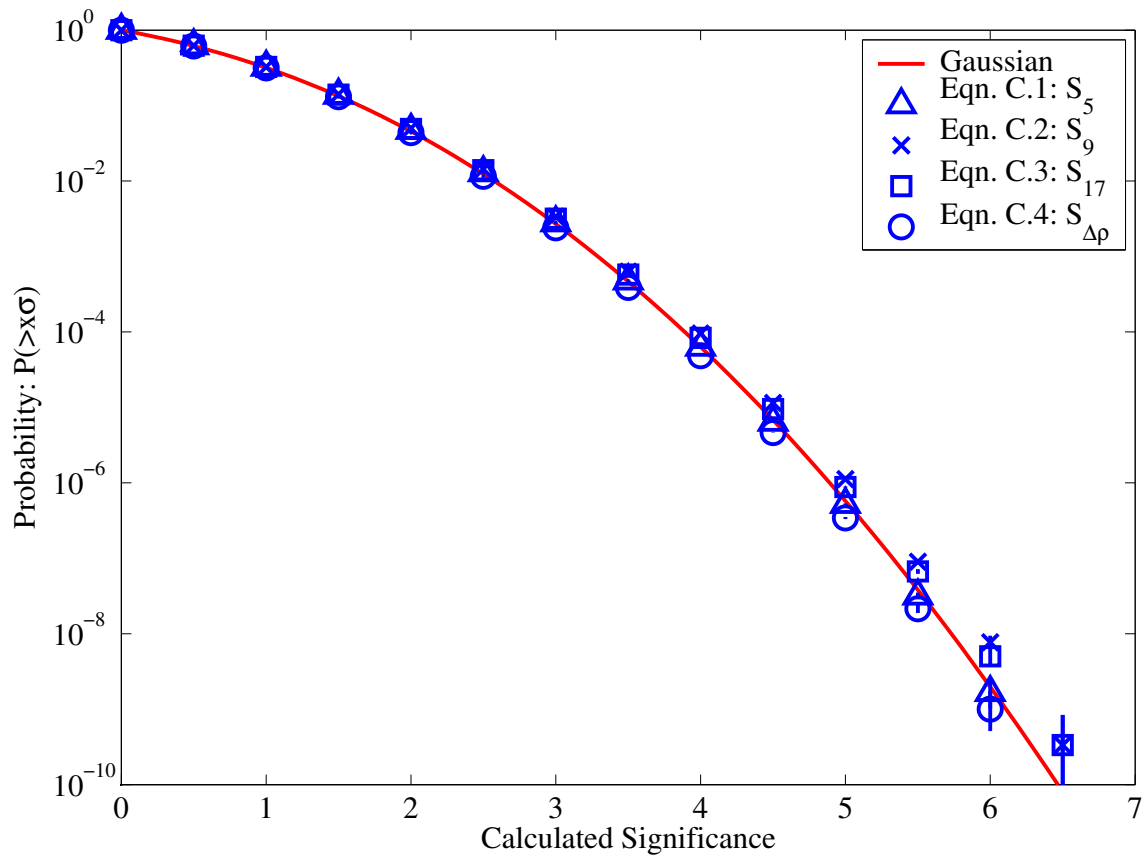


Figure D.1: Monte Carlo evaluation of frequency of  $> x\sigma$  results with different “significance measures”. Only positive excesses are considered in the simulation, so  $P(> 0\sigma) = 1$ .

## REFERENCES

- G. O. Abell, H. G. Corwin, and R. P. Olowin. A catalog of rich clusters of galaxies. *ApJS*, 70:1–138, May 1989.
- F. Aharonian et al. The HEGRA Experiment - Status and Recent Results. In *Proc. 15th European Cosmic Ray Symposium*, volume 60B of *Nuclear Physics Proceedings Supplement*, pages 193–198, August 1996.
- F. Aharonian et al. Evidence for TeV gamma ray emission from Cassiopeia A. *A&A*, 370:112–120, April 2001.
- F. Aharonian et al. An unidentified TeV source in the vicinity of Cygnus OB2. *A&A*, 393:L37–L40, October 2002a.
- F. Aharonian et al. Is the giant radio galaxy M 87 a TeV gamma-ray emitter? *A&A*, 403:L1–L5, May 2003.
- F. A. Aharonian et al. The temporal characteristics of the TeV gamma-radiation from MKN 501 in 1997. I. Data from the stereoscopic imaging atmospheric Cherenkov telescope system of HEGRA. *A&A*, 342:69–86, February 1999.
- F. A. Aharonian et al. A search for TeV gamma-ray emission from SNRs, pulsars and unidentified GeV sources in the Galactic plane in the longitude range between -2 deg and 85 deg. *A&A*, 395:803–811, December 2002b.
- P. Albats et al. *Nature*, 240:221, 1972.
- K. M. V. Apparao et al. 4U0241+61 - A luminous low-redshift QSO. *Nature*, 273: 450–453, June 1978.
- W. I. Axford, E. Leer, and G. Skadron. The acceleration of cosmic rays by shock waves. In *Proc. 15th International Cosmic Ray Conference*, volume 11, pages 132–137, 1977.
- H. Böhringer et al. The Northern ROSAT All-Sky (NORAS) Galaxy Cluster Survey. I. X-Ray Properties of Clusters Detected as Extended X-Ray Sources. *ApJS*, 129: 435–474, August 2000.
- A. R. Bell. The acceleration of cosmic rays in shock fronts. I. *MNRAS*, 182:147–156, January 1978.

- P. Benaglia, G. E. Romero, I. R. Stevens, and D. F. Torres. Can the gamma-ray source 3EG J2033+4118 be produced by the stellar system Cygnus OB2 No. 5? *A&A*, 366:605–611, February 2001.
- K. Bennett. COS-B: The highlights. *Nuclear Physics B - Proceedings Supplements*, 14(2):23–34, 1990.
- D. L. Bertsch et al. Pulsed high-energy gamma-radiation from Geminga (1E0630 + 178). *Nature*, 357:306, May 1992.
- D. Bhattacharya et al. Gamma-ray observations of NGC 253 and M82 with OSSE. *ApJ*, 437:173–178, December 1994.
- G. F. Bignami and P. A. Caraveo. Geminga - New Period Old Gamma-Rays. *Nature*, 357:287, May 1992.
- G. F. Bignami, P. A. Caraveo, and R. C. Lamb. An identification for 'Geminga' (2CG 195+04) 1E 0630+178 - A unique object in the error box of the high-energy gamma-ray source. *ApJ*, 272:L9–L13, September 1983.
- R. D. Blandford and J. P. Ostriker. Particle acceleration by astrophysical shocks. *ApJ*, 221:L29–L32, April 1978.
- J. J. Blom, D. T. A. Paglione, and A. Carramiñana. Gamma-Rays from Starbursts and M31. *Astrophysical Letters Communications*, 39:169, 1999.
- M. Boettcher. Leptonic Jet Models of Blazars: Broadband Spectra and Spectral Variability. In Dingus, Salamon, and Kieda, editors, *GeV-TeV Gamma Ray Astrophysics Workshop, Towards a Major Atmospheric Cherenkov Detector VI*, volume 515 of *AIP Conference Proceedings*, 1999.
- S.M. Bradbury et al. Whipple telescope observations of the crab nebula with a pattern selection trigger. In Dingus, Salamon, and Kieda, editors, *Proc. 26th International Cosmic Ray Conference*, volume 5, page 263, 1999.
- T. M. Braje, R. W. Romani, M. S. E. Roberts, and N. Kawai. Chandra Imaging of the Gamma-Ray Source GeV J1809-2327. *ApJ*, 565:L91–L95, February 2002.
- K. T. S. Brazier, O. Reimer, G. Kanbach, and A. Carramiñana. A candidate gamma-ray pulsar in the supernova remnant CTA 1. *MNRAS*, 295:819–824, April 1998.
- R. Browning, Ramsden D., and P. J. Wright. *Nature*, 232:99, 1971.
- Y. Butt et al. CHANDRA/VLA Follow-up of TeV J2032+4131, the Only Unidentified TeV Gamma-ray Source. *ApJ*, 597:494–512, November 2003.

- Y. M. Butt et al. Supernova-Remnant Origin of Cosmic Rays? *Nature*, 418:499, August 2002.
- A. Carramiñana et al. An upper limit to 300 GeV gamma ray emission from Centaurus A. *A&A*, 228:327–330, February 1990.
- M.F. Cawley. In R.C. Lamb, editor, *Towards a Major Atmospheric Cherenkov Detector II*, pages 176–181, 1993.
- P.A. Čerenkov. *C. R. Ac. Sci. U.S.S.R.*, 8:451, 1934.
- P. M. Chadwick et al. Centaurus X-3: A Source of High-Energy Gamma Rays. *ApJ*, 503:391, August 1998a.
- P. M. Chadwick et al. Centaurus X-3: A Source of High-Energy Gamma Rays. *ApJ*, 503:391, August 1998b.
- R. A. Chevalier. A Model for the X-Ray Luminosity of Pulsar Nebulae. *ApJ*, 539: L45–L48, August 2000.
- A. E. Chudakov, V. L. Dadykin, V. I. Zatsepin, and N. M. Nesterova. On the high energy photons from local sources. In *Proc. 8th International Cosmic Ray Conference*, volume 4, page 199, 1963.
- G. W. Clark, G. P. Garmire, and W. L. Kraushaar. Observation of High-Energy Cosmic Gamma Rays. *ApJ*, 153:L203, September 1968.
- S. Colafrancesco. Gamma-Rays from Galaxy Clusters: Preliminary Evidences and Future Expectations. In *AIP Conf. Proc. 587: Gamma 2001: Gamma-Ray Astrophysics*, page 427, 2001.
- S. Colafrancesco. First gamma-rays from galaxy clusters. Preliminary evidence of the association of galaxy clusters with EGRET unidentified gamma-ray sources. *A&A*, 396:31–51, December 2002.
- J. A. Combi et al. Detection of a new, low-brightness supernova remnant possibly associated with EGRET sources. *A&A*, 366:1047–1052, February 2001.
- J. A. Combi et al. Discovery of a New Radio Galaxy within the Error Box of the Unidentified Gamma-Ray Source 3EG J1735-1500. *ApJ*, 588:731–735, May 2003.
- C. E. Covault et al. The Status of the STACEE Observatory. In Simon, Lorenz, and Pohl, editors, *Proc. 27th International Cosmic Ray Conference*, 2001.
- C. Cruz-González et al. A catalogue of galactic O stars. The ionization of the low density interstellar medium by runaway stars. , 1:211–259, November 1974.

- N. D'Amico et al. Two Young Radio Pulsars Coincident with EGRET Sources. *ApJ*, 552:L45–L48, May 2001.
- S. Danaher, D. J. Fegan, N. A. Porter, T. C. Weekes, and T. Cole. Possible applications of large solar arrays in astronomy and astrophysics. *Solar Energy*, 28:335–343, 1982.
- J.M. Davies and E.S. Cotton. Design of the quartermaster solar furnace. *Journal of Solar Energy, Science and Engineering*, 1(2):16–22, April 1957.
- B. L. Dingus. private communication, 2001.
- B. L. Dingus and D. L. Bertsch. The Highest Energy Emission Detected by EGRET from Blazars. In Gehrels Ritz and Shrader, editors, *AIP Conf. Proc. 587: Gamma 2001: Gamma-Ray Astrophysics*, page 251, 2001.
- L. O. Drury, F. A. Aharonian, and H. J. Völk. The gamma-ray visibility of supernova remnants. A test of cosmic ray origin. *A&A*, 287:959–971, July 1994.
- L. O'C. Drury. An introduction to the theory of diffusive shock acceleration of energetic particles in tenuous plasmas. *Reports on Progress in Physics*, 46:973–1027, August 1983.
- R. Enomoto et al. Design study of CANGAROO-III, stereoscopic imaging atmospheric Cherenkov telescopes for sub-TeV / $\gamma$ -ray detection. , 16:235–244, January 2002a.
- R. Enomoto et al. The acceleration of cosmic-ray protons in the supernova remnant RX J1713.7-3946. *Nature*, 416:823–826, April 2002b.
- J. A. Esposito et al. In-flight Calibration Of EGRET On The Compton Gamma-Ray Observatory. *ApJS*, 123:203–217, July 1999.
- J. A. Esposito, S. D. Hunter, G. Kanbach, and P. Sreekumar. EGRET Observations of Radio-bright Supernova Remnants. *ApJ*, 461:820, April 1996.
- D. J. Fegan. The Art and Power of Cerenkov Imaging. *Space Sci. Rev.*, 75:137–151, January 1996.
- D. J. Fegan et al. Fast large aperture camera and data acquisition system with applications in astrophysics, particle physics and nuclear medicine. , 211(1):179–191, June 1983.
- E. Fermi. On the Origin of the Cosmic Radiation. , 75:1169–1174, 1949.
- C. Fichtel. EGRET overview: Achievements in the light of expectations. *A&AS*, 120: 23–29, 1996.

- C. E. Fichtel et al. High-energy gamma-ray results from the second small astronomy satellite. *ApJ*, 198:163–182, May 1975.
- C. E. Fichtel et al. The first energetic gamma-ray experiment telescope (EGRET) source catalog. *ApJS*, 94:551–581, October 1994.
- Frank and Tamm. *C. R. Ac. Sci. U.S.S.R.*, 14:109, 1937.
- B. M. Gaensler et al. XMM-Newton Observations of PSR B1823-13: An Asymmetric Synchrotron Nebula around a Vela-like Pulsar. *ApJ*, 588:441–451, May 2003.
- J. A. Gaidos et al. Very Rapid and Energetic Bursts of TeV Photons from the Active Galaxy Markarian 421. *Nature*, 383:319, 1996.
- W. Galbraith and J.V. Jelley. *Nature*, 171:349, 1953.
- W. Galbraith and J.V. Jelley. *Journal of Atmospheric and Terrestrial Physics*, 250: 304, 1955.
- N. Gehrels, D. J. Macomb, D. L. Bertsch, D. J. Thompson, and R. C. Hartman. Discovery of a new population of high-energy  $\gamma$ -ray sources in the Milky Way. *Nature*, 404:363–365, March 2000.
- V. L. Ginzburg and S. I. Syrovatskii. *The Origin of Cosmic Rays*. Macmillan, New York, 1964.
- P. Goldreich and W. H. Julian. Pulsar Electrodynamics. *ApJ*, 157:869, August 1969.
- R. J. Gould and G. Schréder. Opacity of the Universe to High-Energy Photons. *Phys. Rev. Lett.*, 16(6):252–254, February 1966.
- R. J. Gould and G. Schréder. Opacity of the Universe to High-Energy Photons. , 155 (5):1408–1411, March 1967.
- D. A. Green. *A Catalogue of Galactic Supernova Remnants (2001 December version)*. Mullard Radio Astronomy Observatory, Cavendish Laboratory, Cambridge, United Kingdom (Available on the World-Wide-Web), 2001. URL <http://www.mrao.cam.ac.uk/surveys/snrs/>.
- P. C. Gregory. Bayesian Analysis of Radio Observations of the Be X-Ray Binary LSI +61°303. *ApJ*, 575:427–434, August 2002.
- P. C. Gregory et al. The radio, optical, X-ray, gamma-ray star LSI +61°303. *AJ*, 84: 1030–1036, July 1979.
- P. C. Gregory and C. Neish. Density and Velocity Structure of the Be Star Equatorial Disk in the Binary LS I +61°303, a Probable Microquasar. *ApJ*, 580:1133–1148, December 2002.

- P. C. Gregory, M. Peracaula, and A. R. Taylor. Bayesian Periodic Signal Detection. II. Discovery of Periodic Phase Modulation in LS I +61 deg303 Radio Outbursts. *ApJ*, 520:376–390, July 1999.
- P. C. Gregory and A. R. Taylor. New highly variable radio source, possible counterpart of gamma-ray source CG135+1. *Nature*, 272:704–706, April 1978.
- I. A. Grenier. Unidentified EGRET sources in the Galaxy. In *Proc. XXI Texas Symposium on Relativistic Astrophysics*, volume in press. World Scientific, 2002.
- J. E. Grindlay et al. Evidence for the detection of gamma rays from Centaurus A at gamma-ray energies above 300 GeV. *ApJ*, 197:L9–L12, April 1975.
- T. A. Hall et al. Observations of galactic pulsars and supernova remnants with the Whipple 10m Imaging Atmospheric Cherenkov Telescope. In *Proc. 27th International Cosmic Ray Conference*, pages 2485–2488. Copernicus Gesellschaft, 2001.
- T. A. Hall et al. Search for TeV Emissions from Pulsars in Binary Systems. *ApJ*, 583:853–860, February 2003a.
- T. A. Hall et al. Very High Energy Observations Of PSR B1823–13. In *Proc. 28th International Cosmic Ray Conference*, pages 2497–2500. Universal Acadamy Press, Inc., 2003b.
- J. P. Halpern, M. Eracleous, and J. R. Mattox. Redshifts of Candidate Gamma-Ray Blazars. *AJ*, 125:572–579, February 2003.
- J. P. Halpern, M. Eracleous, R. Mukherjee, and E. V. Gotthelf. 3EG J2016+3657: Confirming an EGRET Blazar behind the Galactic Plane. *ApJ*, 551:1016–1023, April 2001a.
- J. P. Halpern et al. PSR J2229+6114: Discovery of an Energetic Young Pulsar in the Error Box of the EGRET Source 3EG J2227+6122. *ApJ*, 552:L125–L128, May 2001b.
- J. P. Halpern, E. V. Gotthelf, K. M. Leighly, and D. J. Helfand. A Possible X-Ray and Radio Counterpart of the High-Energy Gamma-Ray Source 3EG J2227+6122. *ApJ*, 547:323–333, January 2001c.
- J. P. Halpern, E. V. Gotthelf, N. Mirabal, and F. Camilo. The Next Geminga: Deep Multiwavelength Observations of a Neutron Star Identified with 3EG J1835+5918. *ApJ*, 573:L41–L44, July 2002.
- J. P. Halpern and S. S. Holt. Discovery of soft X-ray pulsations from the gamma-ray source Geminga. *Nature*, 357:222–224, May 1992.

- A. K. Harding. Gamma-ray Pulsars: Models and Predictions. In *High Energy Gamma-Ray Astronomy*, page 115, 2001.
- A. K. Harding et al. Pulsar Populations and Unidentified Gamma-Ray Sources. In *Proceedings of 34th COSPAR Scientific Assembly, Symposium on Supernova Remnants and Neutron Stars*, volume in press, 2003. URL <http://www.arxiv.org/pdf/astro-ph/0308215>.
- R. C. Hartman et al. Galactic plane gamma-radiation. *ApJ*, 230:597–606, June 1979.
- R. C. Hartman et al. The Third EGRET Catalog of High-Energy Gamma-Ray Sources. *ApJS*, 123:79–202, July 1999.
- O. Helene. Upper limit of peak area. , 212:319–322, July 1983.
- W. Hermsen et al. New high energy gamma-ray sources observed by COS B. *Nature*, 269:494, October 1977.
- HESS collaboration. New Frontiers of Astronomy the High Energy Stereoscopic System (H.E.S.S.) in Namibia. Available only on the Web, 2002. URL [http://www.mpi-hd.mpg.de/hfm/HESS/public/f1c/HESS\\_Brochure.pdf](http://www.mpi-hd.mpg.de/hfm/HESS/public/f1c/HESS_Brochure.pdf).
- A. M. Hillas et al. The spectrum of TeV gamma rays from the Crab Nebula. *ApJ*, 503:744, 1998.
- W. Hofmann et al. Measuring  $\gamma$ -Ray Energy Spectra with the HEGRA IACT System. In O.C. De Jager, editor, *Towards a Major Atmospheric Cherenkov Detector V*, 1997.
- D. Horan. *The Discovery of TeV  $\gamma$ -rays from the BL Lacertae object, 1H1426+428*. PhD thesis, University College Dublin, IRELAND, September 2001.
- D. Horan and T. C. Weekes. Extragalactic Sources of TeV Gamma Rays: A Summary. In S. Swordy and L. Fortson, editors, *New Astronomy Review, Proceedings of the 2nd VERITAS Symposium on TeV Astrophysics of Extragalactic Sources*, volume 48, pages 527–535, April 2004.
- C. Itoh et al. Evidence of TeV gamma-ray emission from the nearby starburst galaxy NGC 253. *A&A*, 402:443–455, May 2003.
- J.D. Jackson. *Classical Electrodynamics*, chapter 13. John Wiley & Sons, Inc., second edition, 1975.
- T. R. Jaffe, D. Bhattacharya, D. D. Dixon, and A. D. Zych. Evidence for Extended High Energy Gamma-Ray Emission from the Rosette/Monoceros Region. *ApJ*, 484:L129, August 1997.

- J. V. Jelley. *Čerenkov Radiation and its Applications*. Pergamon Press, 1958.
- J. V. Jelley. High-Energy  $\gamma$ -Ray Absorption in Space by a  $3.5^{\circ}\text{K}$  Microwave Field. *Phys. Rev. Lett.*, 16(11):479–481, March 1966.
- J. V. Jelley and N. A. Porter. Čerenkov Radiation from the Night Sky, and its Application to  $\gamma$ -Ray Astronomy. *QJRAS*, 4:275, September 1963.
- P. Kaaret and J. Cottam. Do the Unidentified EGRET Sources Lie in Star-forming Regions? *ApJ*, 462:L35, May 1996.
- P. Kaaret, G. Cusumano, and B. Sacco. X-Ray Timing of the 34 Millisecond Binary Pulsar SAX J0635+0533. *ApJ*, 542:L41–L43, October 2000.
- P. Kaaret, S. Piraino, J. Halpern, and M. Eracleous. Discovery of a Hard X-Ray Source, SAX J0635+0533, in the Error Box of the Gamma-Ray Source 2EG 0635+0521. *ApJ*, 523:197–202, September 1999.
- G. Kanbach et al. The Project EGRET - Energetic Gamma-Ray Experiment Telescope - on Nasa's Gamma-Ray Observatory GRO. *Space Sci. Rev.*, 49:61, 1988.
- V. M. Kaspi et al. High-Energy Gamma-Ray Observations of Two Young, Energetic Radio Pulsars. *ApJ*, 528:445–453, January 2000.
- W. Kawasaki and T. Totani. Positional Coincidence between the High-Latitude Steady Unidentified Gamma-Ray Sources and Possibly Merging Clusters of Galaxies. *ApJ*, 576:679–687, September 2002.
- M. P. Kertzman and G. H. Sembroski. Computer simulation methods for investigating the detection characteristics of TeV air Cherenkov telescopes. , 343, 1994.
- J. G. Kirk, L. Ball, and O. Skjæraasen. Inverse Compton emission of TeV gamma rays from PSR B1259-63. , 10:31–45, January 1999.
- D. A. Kniffen et al. EGRET Observations of the Gamma-Ray Source 2CG 135+01. *ApJ*, 486:126, September 1997.
- A. K. Konopelko. Design studies for the future 50 GeV arrays of imaging air Čerenkov telescopes. , 11:263–266, June 1999.
- W. Kraushaar et al. Explorer XI Experiment on Cosmic Gamma Rays. *ApJ*, 141: 845, April 1965.
- F. Krennrich et al. Discovery of Spectral Variability of Markarian 421 at TeV Energies. *ApJ*, 575:L9–L13, August 2002.
- G. F. Krymskii. A regular mechanism for the acceleration of charged particles on the front of a shock wave. *Akademii Nauk SSSR Doklady*, 234:1306–1308, June 1977.

- L. Kuiper et al. The likely detection of pulsed high-energy gamma-ray emission from millisecond pulsar PSR J0218+4232. *A&A*, 359:615–626, July 2000.
- R. C. Lamb and D. J. Macomb. Point Sources of GeV Gamma Rays. *ApJ*, 488: 872–880, October 1997.
- S. A. Laurent-Muehleisen et al. Radio-loud active galaxies in the northern ROSAT All-Sky Survey. I. Radio identifications. *A&AS*, 122:235–247, April 1997.
- Glenn LeDrew. Gould’s Belt (Part I). In *AstroNotes, The Newsletter of the Ottawa Centre*, volume 38, 10. Royal Astronomical Society of Canada, December 1999. URL <http://ottawa.rasc.ca/observers/1999/an9912p8.html>.
- R. W. Lessard, J. H. Buckley, V. Connaughton, and S. Le Bohec. A new analysis method for reconstructing the arrival direction of TeV gamma rays using a single imaging atmospheric Cherenkov telescope. , 15:1–18, March 2001.
- R. W. Lessard et al. Search for TeV Gamma-Rays from Shell-Type Supernova Remnants. In Dingus, Salamon, and Kieda, editors, *Proc. 26th International Cosmic Ray Conference*, volume 3, page 488, 1999.
- T.-P. Li and Y.-Q. Ma. Analysis methods for results in gamma-ray astronomy. *ApJ*, 272:317–324, September 1983.
- E. Lorenz. The MAGIC telescope project for gamma ray astronomy in the 15 to 300 GeV energy range. *Nuclear Physics B - Proceedings Supplements*, 48(1-3), May 1996. URL <http://www.sciencedirect.com/science/article/B6TVD-3VTHYFM-3S/1/0d6c0d97a09562b554c4f73d5905509b>.
- F. Lucarelli et al. Observations of the Monoceros/Rosette Nebula with the HEGRA System of IACTs. In *High Energy Gamma-Ray Astronomy*, pages 779–, 2001.
- D. J. Macomb and R. C. Lamb. Exploring the Universe above 1 GeV. In Dingus, Salamon, and Kieda, editors, *Proc. 26th International Cosmic Ray Conference*, volume 4, page 107, 1999.
- R. N. Manchester et al. The Parkes multi-beam pulsar survey - I. Observing and data analysis systems, discovery and timing of 100 pulsars. *MNRAS*, 328:17–35, November 2001.
- R. N. Manchester et al. Young Pulsars from the Parkes Multibeam Pulsar Survey and their Associations. In *ASP Conf. Ser. 271: Neutron Stars in Supernova Remnants*, page 31, 2002.
- L. Maraschi et al. Possible X-ray counterparts of gamma-ray sources. *Nature*, 272: 679–681, April 1978.

- L. Maraschi et al. Correlated variability of MKN 421 at X-ray and TeV wavelengths on time scales of hours. , 11:189–192, June 1999.
- M. Massi et al. One-sided jet at milliarcsecond scales in LSI +61°303. A&A, 376: 217–223, September 2001.
- J. R. Mattox. Further Examination of the SAS 2 and COS B Cygnus X-3 Data. , 22: 1230, September 1990.
- J. R. Mattox et al. SAS 2 observation of pulsed high-energy gamma radiation from Geminga. ApJ, 401:L23–L26, December 1992.
- J. R. Mattox et al. The Likelihood Analysis of EGRET Data. ApJ, 461:396, April 1996.
- J. R. Mattox, R. C. Hartman, and O. Reimer. A Quantitative Evaluation of Potential Radio Identifications for 3EG EGRET Sources. ApJS, 135:155–175, August 2001.
- B. McBreen et al. Pulsed high-energy gamma rays from the Crab Nebula. ApJ, 184: 571–580, September 1973.
- A. M. Mel’Nik and Y. N. Efremov. A new list of OB associations in our galaxy. , 21: 10–26, January 1995.
- N. Mirabal and J. P. Halpern. A Neutron Star Identification for the High-Energy Gamma-Ray Source 3EG J1835+5918 Detected in the ROSAT All-Sky Survey. ApJ, 547:L137–L140, February 2001.
- N. Mirabal, J. P. Halpern, M. Eracleous, and R. H. Becker. Search for the Identification of 3EG J1835+5918: Evidence for a New Type of High-Energy Gamma-Ray Source. ApJ, 541:180–193, September 2000.
- R. Mukherjee. EGRET (GeV) Blazars. In *High Energy Gamma-Ray Astronomy*, page 324, 2001.
- R. Mukherjee et al. EGRET Observations of High-energy Gamma-Ray Emission from Blazars: an Update. ApJ, 490:116, November 1997.
- R. Mukherjee, E. V. Gotthelf, J. Halpern, and M. Tavani. Multiwavelength Examination of the COS B Field 2CG 075+00 Yields a Blazar Identification for 3EG J2016+3657. ApJ, 542:740–749, October 2000.
- R. Mukherjee, J. Halpern, N. Mirabal, and E. V. Gotthelf. Is the EGRET Source 3EG J1621+8203 the Radio Galaxy NGC 6251? ApJ, 574:693–700, August 2002.
- R. Mukherjee, J. P. Halpern, E. V. Gotthelf, M. Eracleous, and N. Mirabal. Search for a Point-Source Counterpart of the Unidentified Gamma-Ray Source TeV J2032+4130 in Cygnus. ApJ, 589:487–494, May 2003.

- H. Muraishi et al. Evidence for TeV gamma-ray emission from the shell type SNR RX J1713.7-3946. *A&A*, 354:L57–L61, February 2000.
- NASA. GLAST, Exploring Nature’s Highest Energy Processes with the Gamma-ray Large Area Space Telescope. Available on the Web, February 2001. URL [http://glast.gsfc.nasa.gov/resources/brochures/gsd/GSD\\_print.pdf](http://glast.gsfc.nasa.gov/resources/brochures/gsd/GSD_print.pdf).
- A. I. Nikishov. Absorption of High-Energy Photons in the Universe. *Soviet Physics JETP*, 14(2):393–394, February 1961.
- P. L. Nolan et al. EGRET observations of pulsars. *A&AS*, 120:C61, November 1996.
- P. L. Nolan, W. P. Tompkins, et al. Variability of EGRET Gamma-Ray Sources. *ApJ*, 597:615–627, November 2003.
- N. Odegard. 57.5 MHz observations of extended nonthermal sources in the galactic plane. *AJ*, 92:1372–1380, December 1986.
- J. M. Paredes, J. Martí, M. Peracaula, and M. Ribo. Evidence of X-ray periodicity in LSI +61°303. *A&A*, 320:L25–L28, April 1997.
- B. Parlier et al. Gamma-ray emission above 20 MeV from the Crab Nebula and NP-0532. *Nature Physical Science*, 242:117, 1973.
- D. Petry. A First EGRET-UNID-Related Agenda for Cherenkov Telescopes. In *ASSL Vol. 267: The Nature of Unidentified Galactic High-Energy Gamma-Ray Sources*, pages 299–319, 2001.
- M. Punch et al. Detection of TeV photons from the active galaxy Markarian 421. *Nature*, 358:477, August 1992.
- P. V. Ramanamurthy et al. EGRET Detection of Pulsed Gamma Radiation from PSR B1951+32. *ApJ*, 447:L109, July 1995.
- P. V. Ramanamurthy et al. Possible Evidence for Pulsed Emission of High-Energy Gamma Rays by PSR B0656+14. *ApJ*, 458:755, February 1996.
- O. Reimer et al. Chasing the second gamma-ray bright isolated neutron star: 3EG J1835+5918/RX J1836.2+5925. In *Neutron Stars, Pulsars, and Supernova Remnants*, pages 100–, 2002.
- O. Reimer and M. Pohl. No evidence yet for hadronic TeV gamma-ray emission from SNR RX J1713.7-3946. *A&A*, 390:L43–L46, July 2002.
- O. Reimer, M. Pohl, P. Sreekumar, and J. R. Mattox. EGRET Upper Limits on the High-Energy Gamma-Ray Emission of Galaxy Clusters. *ApJ*, 588:155–164, May 2003.

- P. T. Reynolds et al. Survey of candidate gamma-ray sources at TeV energies using a high-resolution Cerenkov imaging system - 1988-1991. *ApJ*, 404:206–218, February 1993.
- M. S. E. Roberts et al. PSR J2021+3651: A Young Radio Pulsar Coincident with an Unidentified EGRET  $\gamma$ -Ray Source. *ApJ*, 577:L19–L22, September 2002a.
- M. S. E. Roberts, B. M. Gaensler, and R. W. Romani. Pulsar Wind Nebulae as High Energy gamma-Ray Emitters. In *ASP Conf. Ser. 271: Neutron Stars in Supernova Remnants*, page 213, 2002b.
- M. S. E. Roberts, R. W. Romani, and S. Johnston. Multiwavelength Studies of PSR J1420-6048, a Young Pulsar in the Kookaburra. *ApJ*, 561:L187–L190, November 2001a.
- M. S. E. Roberts, R. W. Romani, and N. Kawai. The ASCA Catalog of Potential X-Ray Counterparts of GEV Sources. *ApJS*, 133:451–465, April 2001b.
- G. E. Romero, P. Benaglia, and D. F. Torres. Unidentified 3EG gamma-ray sources at low galactic latitudes. *A&A*, 348:868–876, August 1999.
- G. Rowell et al. TeV Observations of Selected GeV Sources with the HEGRA IACT-System. In *Proc. 28th International Cosmic Ray Conference*, pages 2329–2332. Universal Acadamy Press, Inc., 2003.
- M. A. Ruderman and P. G. Sutherland. Theory of pulsars - Polar caps, sparks, and coherent microwave radiation. *ApJ*, 196:51–72, February 1975.
- M. H. Salamon and F. W. Stecker. Absorption of High-Energy Gamma Rays by Interactions with Extragalactic Starlight Photons at High Redshifts and the High-Energy Gamma-Ray Background. *ApJ*, 493:547–, January 1998.
- V. Schönfelder et al. The first COMPTEL source catalogue. *A&AS*, 143:145–179, April 2000.
- C. A. Scharf and R. Mukherjee. A Statistical Detection of Gamma-Ray Emission from Galaxy Clusters: Implications for the Gamma-Ray Background and Structure Formation. *ApJ*, 580:154–163, November 2002.
- M. Schroedter. private communication, 2002.
- M. Schroedter et al. Improvements to the Optics of the Whipple 10 m Telescope. In , volume 47, 2, 2002.
- F. D. Seward, B. Schmidt, and P. Slane. X-Ray Emission from the Supernova Remnant CTA 1. *ApJ*, 453:284, November 1995.

- P. Slane et al. Nonthermal X-Ray Emission from CTA 1. *ApJ*, 485:221, August 1997.
- P. Slane et al. X-Ray Observations of the Compact Source in CTA 1. *ApJ*, 601: 1045–1049, February 2004.
- D. A. Smith et al. CELESTE experimental proposal. Available only on the Web, 1996. URL <ftp://ftpcenbg.in2p3.fr/pub/astropart/celeste/cxp.ps>.
- F. W. Stecker and O. C. de Jager. Absorption of High Energy Gamma-Ray by Low Energy Intergalactic Photons. *Space Sci. Rev.*, 75:401–412, January 1996.
- F. W. Stecker and O. C. de Jager. Absorption of very high energy gamma-rays by intergalactic infrared radiation: A new determination. *A&A*, 334:L85–L87, June 1998.
- F. W. Stecker, O. C. de Jager, and M. H. Salamon. TeV gamma rays from 3C 279 - A possible probe of origin and intergalactic infrared radiation fields. *ApJ*, 390: L49–L52, May 1992.
- R. Stothers and J. A. Frogel. The local complex of O and B stars. I. Distribution of stars and interstellar dust. *AJ*, 79:456, April 1974.
- S. J. Sturner and C. D. Dermer. Association of unidentified, low latitude EGRET sources with supernova remnants. *A&A*, 293:L17–L20, January 1995.
- B. N. Swanenburg et al. COS B observation of high-energy gamma radiation from 3C273. *Nature*, 275:298, September 1978.
- B. N. Swanenburg et al. Second COS B catalog of high-energy gamma-ray sources. *ApJ*, 243:L69–L73, January 1981.
- T. Tanimori et al. Discovery of TeV Gamma Rays from SN 1006: Further Evidence for the Supernova Remnant Origin of Cosmic Rays. *ApJ*, 497:L25, April 1998.
- A. R. Taylor and P. C. Gregory. Periodic radio emission from LS I +61 deg 303. *ApJ*, 255:210–216, April 1982.
- The Auger collaboration. Pierre Auger Project Design Report. Available only on the Web, 1996. URL <http://www.auger.org/admin/DesignReport/index.html>.
- D. J. Thompson, D. L. Bertsch, and R. C. Hartman. Artifact Sources Near Bright EGRET Pulsars. In Gehrels Ritz and Shrader, editors, *AIP Conf. Proc. 587: Gamma 2001: Gamma-Ray Astrophysics*, page 668, 2001.
- D. J. Thompson et al. Final SAS-2 gamma-ray results on sources in the galactic anticenter region. *ApJ*, 213:252–262, April 1977.

- D. J. Thompson et al. Calibration Of The Energetic Gamma-Ray Experiment Telescope (EGRET) For The Compton Gamma-Ray Observatory. *ApJS*, 86:629–656, June 1993.
- Diego. F. Torres. Gamma-ray sources at high latitudes. In K. S. Cheng and G. E. Romero, editors, *Cosmic Gamma-ray Sources*, volume in press. Kluwer Academic Press, 2003.
- Diego F. Torres et al. Supernova remnants and  $\gamma$ -ray sources. *Physics Reports*, 382(6):303–380, August 2003.
- M. P. Ulmer. Gamma-ray observations of pulsars. *ApJS*, 90:789–795, February 1994.
- C. M. Urry and P. Padovani. Unified Schemes for Radio-Loud Active Galactic Nuclei. *Proceedings of the Astronomical Society of the Pacific*, 107:803, September 1995.
- V. V. Vassiliev. Extragalactic background light absorption signal in the TeV gamma-ray spectra of blazars. , 12:217–238, January 2000.
- VERITAS collaboration. The VERITAS proposal. Available only on the Web, 1999. URL [http://veritas.sao.arizona.edu/Proposal/veritas\\_full.pdf](http://veritas.sao.arizona.edu/Proposal/veritas_full.pdf).
- José R. Vieira. Milky Way Outline Catalogs. Available on the Web: [http://www.skymap.com/milkyway\\_cat.htm](http://www.skymap.com/milkyway_cat.htm), 2000. URL <http://www.skymap.com/milkyway\protect\unhbox\voidb@x\kern.06em\vbox{\hrulewidth.3em}cat.htm>.
- H. J. Völk. Energetic Particles in Clusters of Galaxies and Starburst Galaxies. In *The Universe Viewed in Gamma-Rays*, volume in press, 2003. URL <http://www.arxiv.org/pdf/astro-ph/0303078>.
- C. von Montigny et al. High-Energy Gamma-Ray Emission from Active Galaxies: EGRET Observations and Their Implications. *ApJ*, 440:525, February 1995.
- P. M. Wallace, M. Eracleous, J. V. Foreman, J. P. Halpern, O. Reimer, and D. J. Thompson. Multiwavelength Observations of 3EG J2006-2321 and 3EG J0433+2908. In *AIP Conf. Proc. 587: Gamma 2001: Gamma-Ray Astrophysics*, pages 319–, 2001.
- T. Weekes, H. Helmken, and J. Grindlay. The Mt. Hopkins Sky Survey for gamma rays of energy 100-1000 GeV III, galactic plane and extended sources. In *Proc. 16th International Cosmic Ray Conference*, volume 1, 1979.
- T. C. Weekes. *Very high energy gamma-ray astronomy*. IoP Series in astronomy and astrophysics. The Institute of Physics Publishing, Bristol, UK, 2003. ISBN 0750306580.

- T. C. Weekes et al. Observation of TeV gamma rays from the Crab nebula using the atmospheric Cerenkov imaging technique. *ApJ*, 342:379–395, July 1989.
- T. C. Weekes et al. VERITAS: the Very Energetic Radiation Imaging Telescope Array System. , 17:221–243, May 2002.
- T. C. Weekes and K. E. Turver. Gamma-ray astronomy from 10-100 GeV: A new approach. In *ESA Recent Advan. in Gamma-Ray Astronomy p 279-286 (SEE N78-11899 02-88)*, pages 279–286, July 1977.
- T.C. Weekes. VHE Astronomy before the New Millenium. In Dingus, Salamon, and Kieda, editors, *GeV-TeV Gamma Ray Astrophysics Workshop, Towards a Major Atmospheric Cherenkov Detector VI*, volume 515 of *AIP Conference Proceedings*, pages 3–15, 1999.
- L. Woltjer. Supernova Remnants. *Annual Reviews of Astronomy and Astrophysics*, 10:129, 1972.
- L. Zhang, Y. J. Zhang, and K. S. Cheng. Young pulsars and unidentified gamma-ray sources at the Galactic plane. *A&A*, 357:957–967, May 2000.